Natural Resources Canada | Ressources naturelles Canada

GEOLOGICAL SURVEY OF CANADA
OPEN FILE 8660

Geotechnical characteristics of marine sediments, Baffin Bay, offshore Nunavut: methodology and results

K. MacKillop, M. Macquarrie, D.C. Campbell, and K.A. Jenner

2020

Canada

GEOLOGICAL SURVEY OF CANADA
OPEN FILE 8660

Geotechnical characteristics of marine sediments, Baffin Bay, offshore Nunavut: methodology and results

K. MacKillop, M. Macquarrie, D.C. Campbell, and K.A. Jenner

Geological Survey of Canada, 1 Challenger Drive, Dartmouth, Nova Scotia B2Y 4A2

2020

© Her Majesty the Queen in Right of Canada, as represented by the Minister of Natural Resources, 2020

Information contained in this publication or product may be reproduced, in part or in whole, and by any means, for personal or public non-commercial purposes, without charge or further permission, unless otherwise specified.
You are asked to:
- exercise due diligence in ensuring the accuracy of the materials reproduced;
- indicate the complete title of the materials reproduced, and the name of the author organization; and
- indicate that the reproduction is a copy of an official work that is published by Natural Resources Canada (NRCan) and that the reproduction has not been produced in affiliation with, or with the endorsement of, NRCan.

Commercial reproduction and distribution is prohibited except with written permission from NRCan. For more information, contact NRCan at nrcan.copyrightdroitdauteur.rncan@canada.ca.

Permanent link: https://doi.org/10.4095/321818

This publication is available for free download through GEOSCAN (https://geoscan.nrcan.gc.ca/).

Recommended citation

MacKillop, K., Macquarrie, M., Campbell, D.C., and Jenner, K.A., 2020. Geotechnical characteristics of marine sediments, Baffin Bay, offshore Nunavut: methodology and results; Geological Survey of Canada, Open File 8660, 1 .zip file. https://doi.org/10.4095/321818

Publications in this series have not been edited; they are released as submitted by the author.

Authors' e-mails

Kevin.MacKillop@canada.ca

Meaghan.Macquarrie@canada.ca

Calvin.Campbell@canada.ca

Kimberley.Jenner@canada.ca

Contents

1.0 Introduction 11
2.0 Core Processing Methods 12
2.1 Shipboard operations 12
2.2 Multi Sensor Core Logger 12
2.3 Compressional Wave Velocity (PWL) 13
2.4 Gamma Ray Attenuation (GRA) 13
2.5 Magnetic Susceptibility (MS) 14
2.6 Geotechnical Whole Round Sampling 15
2.7 Split Core 15
2.8 Core Photography 15
2.9 Sample Description 16
2.10 Laboratory Mini Vane Shear Strength Measurements 16
2.11 Constant volume sampling 16
2.12 Grain Size 17
3.0 Atterberg Limits 17
3.1 Introduction 17
3.2 Liquid Limit Test 19
3.3 Plastic Limit Test 19
3.4 Soil Classification 19
3.5 Liquidity Index 20
4.0 Soil Stresses 21
4.1 Introduction 21
4.2 Total Stress 21
4.3 Hydrostatic Pore Water Pressure 22
4.4 Effective Stress 22
4.5 Excess Pore Water Pressure 23
5.0 Consolidation 24
5.1 Introduction 24
5.2 Stress History 24
5.3 Consolidation Testing 26
5.3.1 Introduction 26
5.3.2 Consolidation Equipment 27
5.3.3 Sample Preparation 27
5.3.4 Sample Saturation 28
5.3.5 Loading/Unloading 28
5.3.6 Data analysis 29
6.0 Shear Strength Properties 31
6.1 Introduction 31
6.2 Strength Profiles 32
6.2.1 Introduction 32
6.2.2 SHANSEP Method 32
6.3 Triaxial Testing 33
6.3.1 Introduction 33
6.3.2 Triaxial Test Equipment 34
6.3.3 Triaxial Test Procedure 35
6.3.4 Data Analysis 37
7.0 Slope Stability 38

7.1 Introduction 38
7.2 Slope Analysis 38
7.2.1 Gravitation Loading 39
7.2.2 Earthquake Seismic Loading 40
8.0 Results 41
8.1 Introduction 41
8.2 Piston Core 20130290048 43
8.2.1 Introduction 43
8.2.2 Atterberg Limits 44
8.2.3 Consolidation Test Results 44
8.2.4 Triaxial Test Results 44
8.2.5 Slope Stability 44
8.2.6 Geotechnical Profile 45
8.3 Piston Core 20130290060 46
8.3.1 Introduction 46
8.3.2 Atterberg Limits 46
8.3.3 Consolidation Test Results 46
8.3.4 Triaxial Test Results 46
8.3.5 Slope Stability 47
8.3.6 Geotechnical Profile 47
8.4 Piston Core 20130290075 48
8.4.1 Introduction 48
8.4.2 Atterberg Limits 48
8.4.3 Consolidation Test Results 48
8.4.4 Triaxial Test Results 49
8.4.5 Slope Stability 49
8.4.6 Geotechnical Profile 49
8.5 Piston Core 20130290077 50
8.5.1 Introduction 50
8.5.2 Atterberg Limits 51
8.5.3 Consolidation Test Results 51
8.5.4 Triaxial Test Results 51
8.5.5 Slope Stability 51
8.5.6 Geotechnical Profile 52
8.6 Piston Core 20130290082 53
8.6.1 Introduction 53
8.6.2 Atterberg Limits 53
8.6.3 Consolidation Test Results 53
8.6.4 Triaxial Test Results 54
8.6.5 Slope Stability 54
8.6.6 Geotechnical Profile 54
9.0 Geotechnical units 55
9.1 Introduction 55
9.2 Geotechnical Units 56
9.2.1 Unit 1A and 1B 56
9.2.2 Unit 2 58
9.2.3 Unit 3 59
9.2.4 Unit 4 60
9.2.5 Unit 5A and 5B 61

9.2.6 Unit 6A and 6B 62
10.0 Summary 64
References 65

List of Figures

Figure 1.1. Location map of the 5 geotechnical core collected during cruise 2013029 (from Google Earth).

Figure 3.1. Liquid limit test apparatus.

Figure 3.2. Laboratory data for determining the LL of the soil.

Figure 3.3. Crumbing of the soil threads at the plastic limit.

Figure 3.4. British Standard plasticity chart with A and U lines defined.

Figure 3.5. Plasticity Chart with liquefaction potential zones (Seed et al., 2003).

Figure 4.1. Schematic representation of normal (N) and tangential (T) force transmission through soil under an applied vertical load (σ'_v) (after Lamb and Whitman, 1969).

Figure 4.2. The total normal stress acting on sediment below the seafloor is a combination of effective stress and pore water pressure.

Figure 5.1. Normal and overconsolidated clays by gravitational compaction (Skempton, 1970).

Figure 5.2. Typical consolidation e-log effective stress curve. Point A marks the end of the reloading point A to B marks the transition from reloading to new stresses, point B to C defines the virgin compression line and point C to D defines the expansion index.

Figure 5.3. The GDS CRS consolidation system includes (A) back pressure controller, (B) 50 kN load frame, (C) axial displacement transducer, (D) CRS consolidation cell, (E) submersible load cell, (F) pore pressure transducer and (G) DAQ system.

Figure 5.4. The GDS Rowe consolidation system includes (A) back pressure controller, (B) load chamber controller, (C) Rowe consolidation cell, (D) DAQ system and (E) pore pressure transducer.

Figure 5.5. Sediment extruded into CRS consolidation ring (A) and a trimmed sample on the CRS cell base (B).

Figure 5.6. Sediment being extruded into the Rowe cell consolidation ring (A) and a trimmed sample on the Rowe cell base (B).

Figure 5.7. Sample pore pressure response measured at the base of the sample to a new load increment.

Figure 5.8. Sample pore pressure response measured at the base of the sample to a new unload increment.

Figure 6.1. Maximum shear strength related to effective normal stress from triaxial tests.

Figure 6.2. Example of a SHANSEP analysis for plastic marine clay showing the OCR vs undrained strength ratio (S_u/σ'_v) relationship (after Ladd and DeGroot, 2003).

Figure 6.3. A comparison of the undrained shear strength (S_u) with depth calculated using the S and MV shear strength data.

Figure 6.4. General set-up of a soil sample in a triaxial cell.

Figure 6.5. Sample stress during the shear stage where σ_c is the confining pressure that remains constant during the shear stage.

Figure 6.6. The GDS triaxial system at the GSCA geomechnical lab includes 3 2 MPa GDS pressure/volume controllers (A, B, C), submersible load cell (D), pore pressure transducer (E), linear displacement transducer (F), DAQ system (G) and Bishop & Wesley stress path triaxial cell (H).

Figure 6.7. Placement of the sample into the rubber membrane in the B&W triaxial cell. A) Sampling ring with sample and split form with rubber membrane. B) Soil sample in the rubber membrane with top cap attached.

Figure 6.8. Triaxial test data illustrating pore pressure dissipation during the isotropic consolidation stage.

Figure 6.9. Consolidation test data illustrating the procedure for selecting 3 confining pressures for CIU triaxial testing. Note that confining pressures 2 and 3 are in the normal consolidation stress range for the sample.

Figure 6.10. Triaxial test data illustrating the stress-strain for the 3 shear stages.

Figure 6.11. Relationship between A_f and OCR values.

Figure 7.1. Triggering mechanisms for 534 submarine slides (Hance, 2003).

Figure 7.2. The equilibrium of an infinite slope under undrained conditions, with gravity forces, T (after Morgenstren, 1967). Only the forces used in the FS calculation are shown.

Figure 7.3. The equilibrium of an infinite slope under undrained conditions, with an earthquake force (kW, after Morgenstren, 1967). Only the forces used in the FS calculation are shown.

Figure 8.1. Location map of geotechnical cores used in this study.

Figure 8.2. Location map of piston core 20130290048.

Figure 8.3. Plasticity chart showing Atterberg limit results of piston core 20130290048.

Figure 8.4. Consolidation plots for piston core 20130290048.

Figure 8.5. Stress paths and failure envelopes from triaxial test results for piston core 20130290048.

Figure 8.6. FS at various slope angles for piston core 20130290048.

Figure 8.7. Geotechnical profile for core 20130290048 from the slope off Qikiqtarjuaq. (ρ_{sat}= saturated bulk density, w_c = water content, w_n = natural in-situ water content, PL = plastic limit, LL = liquid limit, LI = liquidity index, S_u = undrained shear strength, MV = laboratory miniature vane shear strength, S = shear strength calculated from the normalized strength ratio, σ'_v = effective overburden stress, P'_c = past maximum stress, FS = factor of safety).

Figure 8.8. Location map of piston core 20130290060.

Figure 8.9. Plasticity chart showing Atterberg limit results of piston core 20130290060.

Figure 8.10. Consolidation plot for piston core 20130290060.

Figure 8.11. Stress paths and failure envelopes from triaxial test results for piston core 20130290060.

Figure 8.12. FS at various slope angles for piston core 20130290060.

Figure 8.13. Geotechnical profile for core 20130290060 from the slope off Scott Trough. (ρ_{sat}= saturated bulk density, w_c = water content, w_n = natural in-situ water content, PL = plastic limit, LL = liquid limit, LI = liquidity index, S_u = undrained shear strength, MV = laboratory miniature vane shear strength, S = shear strength calculated from the normalized strength ratio, σ'_v = effective overburden stress, P'_c = past maximum stress, FS = factor of safety).

Figure 8.14. Location map of piston core 20130290075.

Figure 8.15. Plasticity chart showing Atterberg limit results of piston core 20130290075.

Figure 8.16. Consolidation plots for piston core 20130290075.

Figure 8.17. Stress paths and failure envelopes from triaxial test results for piston core 20130290075.

Figure 8.18. FS at various slope angles for piston core 20130290075.

Figure 8.19. Geotechnical profile for core 20130290075 from the slope off Clyde River. (ρ_{sat}= saturated bulk density, w_c = water content, w_n = natural in-situ water content, PL = plastic limit, LL = liquid limit, LI = liquidity index, S_u = undrained shear strength, MV = laboratory miniature vane shear strength, S = shear strength calculated from the normalized strength ratio, σ'_v = effective overburden stress, P'_c = past maximum stress, FS = factor of safety).

Figure 8.20. Location map of piston core 20130290077.

Figure 8.21. Plasticity chart showing Atterberg limit results of piston core 20130290077.

Figure 8.22. Consolidation plot for piston core 20130290077.

Figure 8.23. Stress path and failure envelope from triaxial test results for piston core 20130290077.

Figure 8.24. FS at various slope angles for piston core 20130290077.

Figure 8.25. Geotechnical profile for core 20130290077 from the slope off Alexander Bank. (ρ_{sat}= saturated bulk density, w_c = water content, w_n = natural in-situ water content, PL = plastic limit, LL = liquid limit, LI = liquidity index, S_u = undrained shear strength, MV = laboratory miniature vane shear strength, S = shear strength calculated from the normalized strength ratio, σ'_v = effective overburden stress, P'_c = past maximum stress, FS = factor of safety).

Figure 8.26. Location map of piston core 20130290082.

Figure 8.27. Plasticity chart showing Atterberg limit results of piston core 20130290082.

Figure 8.28. Consolidation plots for piston core 20130290082.

Figure 8.29. Stress paths and failure envelopes from triaxial test results for piston core 20130290082.

Figure 8.30. FS at various slope angles for piston core 20130290082.

Figure 8.31. Geotechnical profile for core 20130290082 from the slope off Disko Bugt. (ρ_{sat}= saturated bulk density, w_c = water content, w_n = natural in-situ water content, PL = plastic limit, LL = liquid limit, LI = liquidity index, S_u = undrained shear strength, MV = laboratory miniature vane shear strength, S = shear strength calculated from the normalized strength ratio, σ'_v = effective overburden stress, P'_c = past maximum stress, FS = factor of safety).

Figure 9.1. Lithofacies legend for the 5 geotechnical cores.

Figure 9.2. Lithology and MSCL bulk density (g/cm^3) profiles with geotechnical units.

Figure 9.3. Plasticity chart showing Atterberg limit results for the geotechnical units.

Figure 9.4. Activity chart showing results for the geotechnical units.

Figure 9.5. Lithology and MSCL bulk density (g/cm^3) profiles with geotechnical Unit 1A and 1B.

Figure 9.6. Plasticity chart showing Atterberg limit results for Unit 1A and 1B. The data are identified by core number and down core test sequence.

Figure 9.7. Activity chart showing results for Unit 1A and 1B. The data are identified by core number and down core test sequence.

Figure 9.8. Lithology and MSCL bulk density (g/cm^3) profiles with geotechnical Unit 2.

Figure 9.9. Plasticity chart showing Atterberg limit results for Unit 2. The data are identified by core number and down core test sequence.

Figure 9.10. Activity chart showing results for Unit 2. The data are identified by core number and down core test sequence.

Figure 9.11. Lithology and MSCL bulk density (g/cm^3) profiles with geotechnical Unit 3.

Figure 9.12. Plasticity chart showing Atterberg limit results for Unit 3. The data are identified by core number and down core test sequence.

Figure 9.13. Activity chart showing results for Unit 3. The data are identified by core number and down core test sequence.

Figure 9.14. Lithology and MSCL bulk density (g/cm^3) profiles with geotechnical Unit 4.

Figure 9.15. Plasticity chart showing Atterberg limit results for Unit 4. The data are identified by core number and down core test sequence.

Figure 9.16. Activity chart showing results for Unit 4. The data are identified by core number and down core test sequence.

Figure 9.17. Lithology and MSCL bulk density (g/cm^3) profiles with geotechnical Unit 5A and 5B.

Figure 9.18. Plasticity chart showing Atterberg limit results for Unit 5A and 5B. The data are identified by core number and down core test sequence.

Figure 9.19. Activity chart showing results for Unit 5A and 5B. The data are identified by core number and down core test sequence.

Figure 9.20. Lithology and MSCL bulk density (g/cm^3) profiles with geotechnical Unit 6.

Figure 9.21. Plasticity chart showing Atterberg limit results for Unit 6. The data are identified by core number and down core test sequence.

Figure 9.22. Activity chart showing results for Unit 6. The data are identified by core number and down core test sequence.

List of Tables

Table 8.1. A summary of the number of geotechnical tests conducted for the five cores.

Table 8.2. Summary of Atterberg limit results for piston core 20130290048.

Table 8.3. Summary of consolidation test results for piston core 201390290048.

Table 8.4. Summary of triaxial test results for piston core 20130290048. Initial Young's modulus (ε_i) is calculated for the present day effective overburden stress.

Table 8.5. Summary of FS results for piston core 20130290048.

Table 8.6. Summary of Atterberg limit results for piston core 20130290060.

Table 8.7. Summary of consolidation test results for piston core 201390290060.

Table 8.8. Summary of triaxial test results for piston core 20130290060. Initial Young's modulus (ε_i) is calculated for the present day effective overburden stress.

Table 8.9. Summary of FS results for piston core 20130290060.

Table 8.10. Summary of Atterberg limit results for piston core 20130290075.

Table 8.11. Summary of consolidation test results for piston core 201390290075.

Table 8.12. Summary of triaxial test results for piston core 20130290075. Initial Young's modulus (ε_i) is calculated for the present day effective overburden stress.

Table 8.13. Summary of FS results for piston core 20130290075.

Table 8.14. Summary of Atterberg limit results for piston core 20130290077.

Table 8.15. Summary of consolidation test results for piston core 201390290077.

Table 8.16. Summary of triaxial test results for piston core 20130290077. Initial Young's modulus (ε_i) is calculated for the present day effective overburden stress.

Table 8.17. Summary of FS results for piston core 20130290077.

Table 8.18. Summary of Atterberg limit results for piston core 20130290082.

Table 8.19. Summary of consolidation test results for piston core 201390290082.

Table 8.20. Summary of triaxial test results for piston core 20130290082. Initial Young's modulus (ε_i) is calculated for the present day effective overburden stress.

Table 8.21. Summary of FS results for piston core 20130290082.

Table 9.1. Summary of physical property characteristics.

Table 9.2. Summary of advanced geotechnical data.

List of Symbols

Symbol	Unit	Definition
A	-	Activity (Equation 3.2)
a	-	Ground Accelaration
A_f	-	Skempton's pore pressure paramter A at failure
B	-	Skempton's pore pressure parameter B (Equation 6.4)
C_c	-	Compression index (Equation 5.3)
C_r	-	Recompression index (Equation 5.4)
C_v	-	Coefficient of consolidation (Equation 5.6)
c'	-	Effective cohesion (Equation 6.1)
e	-	Void ratio
F_h	kN	Horizontial Force (Equation 7.4)
FS	-	Factor of safety (Equation 7.1)
g	m/s^2	Gravitational Acceleration of gravity, 9.81 m/s^2
H	m	Depth below seafloor (Equation 7.1)
H_c	m	Critical height (Equation 7.2)
H_s	m	Height of solid soil particles (Equation 5.2)
ΔH	-	Change in height
k	m/s	Hydralic conductivity (Equation 5.7)
k_h	-	Horizontial seismic coefficient
k_{min}	-	Minimum horizontial seismic coefficient (Equation 7.7)
k_o	-	The coefficient of earth pressure at rest
LI	-	Liquidity index (Equation 3.3)
LL	-	Liquid limit
$MSCL$	-	Multisensor core logger
m_v	-	coefficient of volume compressibility (Equation 5.5)
NC	-	Normal consolidation
OCR	-	Overconsolidation ratio
P'_c	kPa	Maximum past effective stress
PI	-	Plasticity index (Equation 3.1)
PL	-	Plastic limit
q	kPa	Deviator stress
R	kPa	Resistance stress
S	-	Ratio of S_u/σ'_v for OCR = 1 (Equation 6.3)
S_u	kPa	Undrained shear strength
t_{90}	s	Time corresponding to 90% primary consolidation (Equation 5.6)

Symbol	Unit	Definition
W	kg	Weight
w_n	%	Natural water content
w_c	%	Water content
z	m	Depth Below Seafloor (Equation 4.2)
ε_a	-	Axial strain
ε_i	MPa	Initial Young's Modulus
β	°	Seafloor Slope Angle
β_c	°	Critical Slope Angle (Equation 7.3)
ρ_{sat}	g/cm^3	Saturated Bulk Density
ρ_{sw}	g/cm^3	Salt Water Density
σ'	kPa	Effective stress (Equation 4.1, 4.5)
σ_c	kPa	Confining stress for triaxial test
σ_3	kPa	Horizontial stress for triaxial test
σ'_c	kPa	Effective consolidation stress for triaxial test
σ_n	kPa	Total normal stress (Equation 4.1)
σ'_n	kPa	Effective normal stress
σ_v	kPa	Total vertical overburden stress (Equation 4.3)
σ'_v	kPa	Effective overburden stress (Equation 4.7)
ϕ'	(°)	Effective internal angle of friction (Equation 6.1)
γ'	kPa	Effective unit overburden stress
μ	kPa	*In-situ* pore water pressure (Equation 4.1)
μ_e	kPa	Excess pore water pressure (Equation 4.8)
μ_h	kPa	Hydrostatic pore water pressure (Equation 4.4)
τ_f	kPa	Shear stress at failure

1.0 Introduction

Baffin Bay forms an elongated ocean basin (1300 km long; 450 km wide) that connects northward to the Arctic Ocean via several Canadian Arctic Channels and southward to the Labrador Sea and the North Atlantic by way of Davis Strait. The continental shelf along the western side of Baffin Bay is 40-60 km wide and up to 300 m deep. Along the eastern side of Baffin Bay the continental shelf width increases to 200-240 km, with an average depth of 500 m, except toward the southern end of the bay where the depth decreases to 300 m. Numerous u-shaped transverse troughs, 20-200 km wide and up to 700 m deep, extend out across the continental shelf to the shelf break as subsea fjord extensions. The continental slope is narrow and steep, passing rapidly out onto the relatively smooth Baffin Bay basin abyssal plain (Aksu and Piper, 1987). Unlike many other passive continental margins, the slope along Baffin Bay does not exhibit well-developed canyon systems. The deepest, central portion of the basin reaches ~2300 m water depth.

The Geological Survey of Canada – Atlantic (GSC-A) collected twenty-eight piston cores onboard the CCGS Hudson during expedition 2013029 as part of a geohazard assessment in Baffin Bay (Campbell, 2014). The cores sampled the surficial (<10 m) sediments predominantly along the western slope of Baffin Bay, but also at the Disko Bugt trough mouth fan, on the southeastern margin of Baffin Bay. Historically, the Baffin region has recorded frequent tremors and earthquakes as great as a 7.3 magnitude (1933) (Bent, 2002).

A comprehensive geotechnical laboratory test program was carried out on five cores collected in Baffin Bay (Figure 1.1). The program was designed to determine the sediment classification, strength parameters, and stress history of the surficial marine sediments. The testing included 1) Multi-Sensor Core Logger (MSCL) density, 2) discrete water content, void ratio and bulk density measurements, 3)

laboratory miniature vane (MV) undrained peak and remoulded shear strength, 4) Atterberg limits, 5) grain size distribution, 6) one dimensional consolidation tests and 7) multi-stage isotropic consolidated undrained (CIU) triaxial tests.

This report presents the detailed methodology applied to marine geotechnical studies at GSC-A as of 2019. It then presents geotechnical results from several long sediment cores collected in Baffin Bay in 2013.

2.0 Core Processing Methods

2.1 Shipboard operations

Piston cores presented in this report were collected in August and September 2013 during CCGS Hudson Expedition 2013029 (Campbell, 2014; Campbell et al., 2017). Core samples were acquired using the AGC Long Coring Facility. On-board processing of core samples entailed sectioning the cores into 1.5 m lengths, measurement of sediment strength using a handheld TorVane on the section ends, and collection of constant volume samples from the section ends. Core sections were then sealed with beeswax and stored upright in refrigerated storage to await further analysis at the Geological Survey of Canada (Atlantic) laboratories.

2.2 Multi Sensor Core Logger

The initial steps in core processing at the GSC-A Core Processing Laboratory are the non-destructive measurements of whole-core X-radiography and physical properties using the Multi Sensor Core Logger (MSCL). Whole-core X-radiography enables the evaluation of core quality and the semi-quantitative assessment of sediment structure and composition. The core is brought to ambient room

temperature after X-radiography is completed and it is run through the MSCL for measurement of whole core sediment physical properties at a standard 1 cm down-core resolution.

The MSCL measures compressional (P) wave velocity in a transverse direction, bulk density and magnetic susceptibility. The sensor stand includes a core detection laser, a gamma ray emitter and detector, two rolling p-wave transducers, and a magnetic susceptibility solenoid. A piece of plastic core liner filled with distilled water is run through the MSCL every four sections of core to check the precision of the MSCL system.

2.3 Compressional Wave Velocity (PWL)

The P-wave logger system consists of two spring-loaded compressional wave transducers (PWT) and two laser distance transducers attached to the PWT mountings. The PWTs are pushed against either side of the core as it moves between the transducers. A short 500 kHz compressional wave pulse is produced at the transmitting transducer at a repetition rate of 1 kHz. This wave pulse travels through the core and is detected by the receiving transducer and the time of flight of the wave pulse is measured. The two laser distance transducers measure the displacement of the active faces of the PWT transducers. The diameter of the sediment core is calculated by subtracting the liner thickness from the measured distance between the distance transducers. This calculation assumes that the core liner is filled with sediment. The P-wave travel time delay caused by the core liner and the electronics of the system is calculated using a distilled water standard of known diameter and temperature. The measured sediment P-wave travel time is corrected for the P-wave travel time delay. The sediment P-wave velocity is calculated as the sediment diameter/corrected P-wave travel time.

2.4 Gamma Ray Attenuation (GRA)

The GRA unit measures the bulk density of the sediment. It comprises a 10 millicurie ^{137}Cesium capsule housed in a 150 mm ø primary lead shield with 2.5 and 5 mm collimators and a sodium iodide

scintillation detector housed in a 100 mm ø collimated lead shielding. The source and detector are mounted on opposite sides of the core as it moves through the central unit assembly. A narrow (pencil size) beam of gamma rays with energies principally at 0.662 MeV is emitted from the ^{137}Cesium source and passes through the diameter of the sediment core. At these energy levels, Compton scattering is the primary mechanism for the attenuation of the gamma rays in most sedimentary material. The incident photons are scattered by collision with electrons encountered in the core and there is a partial energy loss. The attenuated gamma-ray beam is measured by the scintillation detector. The Compton scattering of the photons is directly related to the number of electrons in the path of the gamma ray beam. A two-phase model representing the mineral and interstitial water of fully saturated marine sediment is assumed for the MSCL GRA calibration. Aluminum is assumed to have an attenuation coefficient similar to common minerals found in marine sediments and represents the mineral phase. Distilled water represents the interstitial water phase. A calibration standard consisting of different thicknesses of aluminum and distilled water is used to calibrate the GRA. The measure of density of the sediments assumes that the marine sediment is fully saturated and completely fills the core liner. The diameter of the sediment is determined using the measured displacement between the laser distance transducers and the thickness of the liner. Sediment density is calculated using the calibration coefficients and the measured diameter of the sediment.

2.5 Magnetic Susceptibility (MS)

A Bartington loop sensor (MS2B) measures the magnetic susceptibility of the sediment. It is mounted to minimize the effects of magnetic or metallic components of the MSCL system. An oscillator circuit in the sensor loop produces a low intensity, non-saturating, alternating magnetic field. Changes in the oscillator frequency caused by material that has a magnetic susceptibility is measured and converted into magnetic susceptibility values. Air measurements taken at the beginning and end of each section are used to correct the measurements for equipment drift during each section run.

2.6 Geotechnical Whole Round Sampling

The objective of the whole round sampling was to obtain undisturbed samples to conduct consolidation, triaxial and Atterberg limit tests. The whole round samples were selected to be representative of the different lithologies of the surficial Baffin Bay marine sediments. The quality of the whole round samples were evaluated using the X-radiography images. The X-rays highlighted areas containing materials unsuitable for testing, such as larger clasts and coring disturbance.

2.7 Split Core

The plastic core liner is split longitudinally by pulling a piece of fine wire through the sediment along the cuts in the plastic core liner. The two core halves are designated archive and working and are temporarily covered with plastic wrap. Each half is labelled with an up arrow, cruise number, sample number and section information. Metre tape is placed along the length of the split core section to indicate down-core depth. The archive half is photographed, measured for colour reflectance, and described visually. The working half is immediately measured for physical properties, before the core dries, at intervals of 10 cm for velocity and shear strength and 50 cm for bulk density and water content. Additional samples are taken depending on the specific core-site objectives. The core halves are re-covered with plastic wrap, sealed in labeled plastic core sleeving, placed in labelled plastic D-tubes and stored at 4°C in the GSC-A Marine Geoscience Collection Facility.

2.8 Core Photography

The archive half of the core is photographed using a Nikon D300 12.3 megapixel digital camera. Overlapping digital photographs are taken at two scales. The first is a close up image covering a 30 cm interval with a 5 cm overlap, and the second is a long shot image covering a 90 cm interval with a 25 cm overlap. The images are saved in raw, tiff and jpg formats.

2.9 Sample Description

Written laboratory descriptions for the sediment cores include: 1) condition of sample (e.g. cracks, disturbance, oxidation), 2) consistency of sample (e.g. soft, hard, firm) 3) reaction to 10% hydrochloric acid which indicates the presence of calcium carbonate, 4) colour, based on Munsell soil colour charts and 5) visual core description consisting of colour, texture, grain size, stratification, depositional contacts, bedforms, sedimentary and post-sedimentary structures, presence of organic material, shells, bioturbation and any other visible feature. Lithologic summaries were created on the basis of sedimentary facies developed from visual sediment colour, spectrophotometry data, sediment structures, sediment texture and shear strength.

2.10 Laboratory Mini Vane Shear Strength Measurements

Laboratory miniature vane (MV) shear strength measurements following (ASTM D4648/D4648M) were made using a motorized shear apparatus. A four bladed vane was inserted to constant depths and rotated 90°/min until sediment failure. The difference in rotational strain between the top and bottom of a linear spring is measured, and the torque required to shear the cylindrical surface around the vane is calculated. Peak and remoulded shear strength values were calculated according to ASTM D4648/D4648M. Peak shear strength measurements were taken at standard 10 cm intervals. Two to three measurements of remoulded shear strength were taken per 1.5 m core section.

2.11 Constant volume sampling

Constant volume samples were taken using a stainless steel cylinder of known volume. The cylinder was gently introduced into the sediment at a constant rate. The cylinder was then carefully removed from the core and trimmed using a wire saw. The sediment was extruded from the cylinder, weighed, dried at 105°C for 24 hours and weighed again. Bulk density, water content and void ratio values were calculated according to (ASTM D2216).

2.12 Grain Size

Grain size tests were completed on Atterberg limit and consolidation trimmings. Grain size analysis were completed on samples using the hydrometer method (ASTM D422) and a Beckman Coulter Laser LS-230 laser diffraction analyser at the GSC-A sedimentology laboratory. The Beckman Coulter Laser LS-230 has a grain size analysis range of 0.4 to 2000 μm. Analysis of the >63 μm fraction were manually wet sieved and merged with the <63 μm fraction The hydrometer method used the trimmings from the consolidation or triaxial test sample preparation. The coulter laser method used material from liquid limit test residues.

3.0 Atterberg Limits

3.1 Introduction

Atterberg limits are index property tests applied to fine grained sediments to define the degree of plasticity. A soils degree of plasticity depends on the ratio of silt to clay sized particles within the soil matrix and the mineralogical composition of the colloid particles. Standard testing procedures developed by Atterberg (1911) and Casagrande (1932b) experimentally derive plastic (*PL*) and liquid limits (*LL*) at which a soil changes phase between the solid and liquid states (ASTM D4318). Although Atterberg limits provide no information on the grain size distribution or the type of minerals present, they nevertheless offer quantitative information on the engineering behavior of sediments and a means to classify the soil.

Under a similar principle as water changing phase from a solid, to a liquid, to a gas with increasing temperature, a fine grained soil will change phase from a solid, to a plastic, to a liquid with increasing water content. The *PL* defines the water content at which fine grained sediment, in the remolded (manually reworked to remove soil structure) state, changes between the solid to plastic condition.

Likewise the *LL* defines the water content at which a fine grained sediment, in the remolded state, changes between the plastic to liquid condition. The plasticity index (*PI*) defines the range of water contents in which the sediment behaves in the plastic condition, defined by the difference between the *LL* and *PL* values,

$$PI = LL - PL \qquad \text{Equation 3.1}$$

A sediment classifies as fine grained if the majority has a particle size of less than 420 μm (#40-mesh sieve), which includes silt and clay. Silt particles are spherical in shape between 2 and 60 μm. Clay particles are colloidal, flat plated structures of 2 μm or less and are controlled through electrostatic forces on the surface of the particle. The mineralogical composition of colloidal particles dictates how strongly the particle will bond. Expansive clays, like montmorillonite, can absorb large quantities of water while remaining in the plastic state.

It is widely recognized that the higher the plasticity index the more pronounced the colloidal properties of the clay. A direct relationship is shared between the clay fraction and the *PI*, with *PI* increasing with colloid particles. This relationship is the activity (*A*) and expressed by the ratio of *PI* to the clay fraction (Skempton, 1953),

$$A = \frac{PI}{Clay\ Fraction} \qquad \text{Equation 3.2}$$

The plasticity chart classifies soil as predominantly silt or clay, with the added denotation of fat or lean, and inorganic or organic. The terms fat (i.e. high *LL*) and lean (i.e. low *LL*) describe a soils ability to attract and retain water. Inorganic sediments form from rocks weathering overtime into their basic mineralogy. Due to the highly complex nature of organic chemistry, organic sediments are not well understood by the soil engineer. There is evidence to suggest that organic sediments behave as inorganic particles. This is observed with diatoms that exist in both the size and shape of silt and clay particles.

It is important to note Atterberg limits are empirically derived after the sediment has been reworked into a remolded state. Fine grained sediments with an *in-situ* water content equal to the *LL* have little strength when remolded, but may have considerable *in-situ* strength. Therefore fine grained sediment several metres below the seafloor with water contents above their *LL* do not exist in the form of a fluid mud; however, it would reduce to such a state in the remolded condition (Skempton, 1970).

3.2 Liquid Limit Test

The *LL* defines the water content at which a fine grained sediment changes from a plastic to a liquid state. The *LL* is experimentally derived by placing a remolded soil into a Casagrande's cup (Figure 3.1) and separating the soil into two halves with a standard cutting tool. A lever is turned at a consistent and rapid rate to raise and drop the Casagrande's cup until the gap closes by ½ inch. Each drop of the cup is considered to be a single blow. A water content sample is then taken at the point of closure. The liquid limit test is repeated a minimum of three times, adding or removing water as necessary to achieve blow counts from 15 to 40. The blow count plotted against the water content on a semi-logarithmic graph yields a linear relationship (Figure 3.2). A line of best fit is drawn and the water content at 25 blow counts represents the *LL*.

3.3 Plastic Limit Test

The *PL* is determined through a standard procedure to define the boundary between the plastic and solid state. A soil is remolded and then rolled into a clay thread until the thread begins to crumble at a diameter of ⅛ inch (Figure 3.3). The water content of the broken soil is then determined. This is repeated for a second piece of soil, with the plastic limit reported as the average of the 2 tests.

3.4 Soil Classification

The *LL* and *PL* are used to classify fine grained cohesive soils (Casagrande, 1948). Particle size tests provide quantitative data on the range of sizes of particles and the amount of clay present, but say

nothing about the type of clay (Head, 1992). Fine grained soils with greater than 50% passing the #200 sieve (75 μm) are classified using a plasticity chart plotting *LL* versus *PI* (Figure 3.4). The plasticity chart classifies fine grained sediments through the naming convention displayed on the chart. The A-line separates silts "M" from clays "C". The chart used in this report follows British Standard practice (Head, 1992). The British Standard plasticity chart is divided into 5 zones:

(1) clays of low plasticity (CL) with less than 35 *LL*.
(2) clays of medium plasticity (CI) with *LL* from 35 to 50.
(3) clays of high plasticity (CH) with *LL* from 50 to 70.
(4) clays of very high plasticity (CV) with *LL* from 70 to 90.
(5) clays of very extreme plasticity (CE) with *LL* exceeding 90.

3.5 Liquidity Index

The natural water content (w_n) of fine grained sediments can be compared to their Atterberg limits by using a ratio defined as the liquidity index (*LI*),

$$LI = \frac{w_n - PL}{PI} \qquad \text{Equation 3.3}$$

The *LI* approximates whether a soil is normally consolidated (*LI=1*), underconsolidated (*LI>1*) or overconsolidated (*LI<1)*. The *LI* values generally decrease with depth below seafloor for normally consolidated soils, and therefore *LI* can be used to evaluate trends in water content with depth. For example, consider two samples at different core depths, but with the same *in-situ* water content. Because the water contents are equal, it may be inferred that the deeper sample has not experienced additional compaction due to the greater overburden. However, if the *LI* for the deeper sample is less than the shallow sample, this would imply normal consolidation for both samples.

Seed et al. (2003) suggests that lean silts and clays with high *in-situ* water contents relative to their *LL* may be susceptible to liquefaction under a cyclic load. Atterberg limits have been used by Seed et al. (2003) to identify potentially liquefiable fine grained sediments under cyclic loading (Figure 3.5). It is

recommended that soils that plot within zones A or B (Figure 3.5) undergo a testing program to evaluate further their potential for liquefaction.

4.0 Soil Stresses

4.1 Introduction

Sediment is composed of discrete, individual particles as well as void space, and soil particles are relatively free to move with respect to one another. The cross-sectional area of a soil subject to an applied load is shown in Figure 4.1.

Soil grains transmit forces from one adjacent particle to the next. At each point of contact there is an equal and opposite normal (compressive) force and tangential (shear) force (Figure 4.1). As the load increases, the void space decreases and the contact area between particles increase. This results in greater frictional resistance between soil grains. The intergranular frictional resistance is termed the effective stress (σ'), which is the support system of soils.

The space between the particles is the void space, which contain variable amounts of water or air. Marine sediments are considered to be fully saturated, meaning the void space is entirely filled with water. Water within the void space has a profound effect on the effective stress of sediments. Water pressure above the hydrostatic condition will reduce the frictional resistance between soil particles, thus reducing the effective stress (σ') of soils.

4.2 Total Stress

The total normal stress (σ_n) is simply the vertical pressure exerted by the weight of the materials above the point considered (Skempton, 1970). A saturated soil in equilibrium will support the total stress

partly by the soil grains at their points of contact (σ′) and partly by the water pressure (μ, Figure 4.2) and is represented by,

$$\sigma_n = \sigma' + \mu \qquad \text{Equation 4.1}$$

The total stress is calculated using the saturated bulk density (ρ_{sat}) of the soil and the thickness of the soil layer. The total vertical stress (σ_v) is the sum of the saturated bulk densities of the material at depth (z) multiplied by the gravitational constant (g),

$$\sigma_v = \int_0^z \rho_{sat} z g \qquad \text{Equation 4.2}$$

The σ_v, expressed as kN/m^2 or kPa, is calculated using,

$$\sigma_v = \rho_{sat} z * 9.81 \qquad \text{Equation 4.3}$$

4.3 Hydrostatic Pore Water Pressure

Water in a state of equilibrium is in the hydrostatic condition, meaning there is no pressure differential or fluid flow. Hydrostatic pore water pressure increases proportionally with depth and is calculated using,

$$\mu_h = \mathrm{g} z \rho_{sw} \qquad \text{Equation 4.4}$$

where ρ_{sw} is the density of salt water. Under hydrostatic conditions, water does not impart a stress to the soil grains. This is observed in porous sediments on the seafloor that retain their open structure even at extreme water depths. Intuitively speaking, a change in the water depth would scarcely cause any change in the compaction of clay underlying the seabed (Skempton, 1970).

4.4 Effective Stress

Effective stress is one of the most important concepts in soil mechanics and is the difference between the total stress and pore water pressure. Mechanical loading by deposition of soils reduces the void spaces and increases the grain-to-grain contact and frictional resistance between soil particles. As the void space reduces, there is a corresponding increase in strength as the soil particles rearrange into a

new shape. The study of soil mechanics is exclusively dealt with in terms of effective stress. The effective stress is defined as,

$$\sigma' = \sigma_n - \mu \qquad \text{Equation 4.5}$$

The effective overburden stress, σ'_v is calculated at a depth of z by,

$$\sigma'_v = \int_0^z (\rho_{sat} - \rho_{sw}) z g \qquad \text{Equation 4.6}$$

The σ'_v effective stress in kN/m^2 or kPa is calculated using,

$$\sigma'_v = (\rho_{sat} - \rho_{sw}) z * 9.81 \qquad \text{Equation 4.7}$$

4.5 Excess Pore Water Pressure

When a marine sediment is in a state of equilibrium, the water in the void spaces will be at hydrostatic conditions and the weight of the overburden is entirely supported by grain-to-grain contact. Excess pore water pressures (μ_e) generate when the *in-situ* pressures (μ) rise above hydrostatic conditions (μ_h) and is defined as,

$$\mu_e = \mu - \mu_h \qquad \text{Equation 4.8}$$

Under excess conditions, water applies a pressure in all directions and reduces the frictional resistance between particles. In the special case where μ_e equals the total stress (σ), the effective stress (σ') reduces to zero, resulting in liquefiable conditions. This most often occurs in sands or silty sands where cyclic loading can cause a significant generation in μ_e and removes the strength entirely. Excess pore water pressures generate when there is an imbalance to the system, and these conditions may exist under rapid loading (i.e. delta fronts, landslides or earthquake induced cyclic loading).

5.0 Consolidation

5.1 Introduction

Soils undergo consolidation under a compressive load, which increases the pore pressure above hydrostatic and induces fluid flow through the sediment, resulting in a reduction in volume. As water is squeezed from the voids, pore pressure dissipates and the applied load is transferred to the soil grains. This continues until the pore water pressure returns to hydrostatic conditions.

The rate at which the excess water pressure dissipates is dependent on the hydraulic conductivity and thickness of the soil layer. Coarse-grained soils like sands and gravels have a high hydraulic conductivity, which means excess pore water pressures usually do not develop. Fine grained soils like silts and clays have a low hydraulic conductivity and may require considerable time for pore pressure dissipation.

5.2 Stress History

Soils are said to carry a memory because the arrangement and orientation of the grains remembers its maximum past effective stress, known as the pre-consolidation pressure (P'_c). A comparison of the P'_c to the present day effective overburden (σ'_v) is termed the over consolidation ratio (*OCR*) and used to determine the soils stress history. A soil is normally consolidated if the P'_c is equal to the *in-situ* effective overburden (*OCR*=1), overconsolidated if the *in-situ* effective overburden pressure is less than the P'_c (*OCR>1*), and underconsolidated if the *in-situ* effective overburden stress is greater than P'_c (*OCR*<1).

Knowing the soils geologic history enables a better understanding of the stress history. Consider a recently deposited soil on the sea floor, illustrated by point *(a)* in Figure 5.1. The soil exhibits a high void ratio and low effective stress. As deposition continues and the sediment is buried beneath the sea

floor, gravitational compaction increases the effective overburden stress and decreases the void ratio, represented by point *(a)* through *(c)*. A reduction in effective overburden stress due to erosion allows the grains to expand elastically, represented by point *(c)* to *(d)*. The soils at point *(b)* and *(d)* are under the same present day effective overburden stress and are in all respects identical, except for their stress history (Skempton, 1970). Therefore, two similar soils at different locations with the same *in-situ* effective overburden stress could have a dramatically different stress history, resulting in one soil being normally consolidated *(b)* and the other being overconsolidated *(d)*. Possible mechanisms for overconsolidation include erosion, wave loading, ice loading and cementation (Poulos, 1988).

Marine sediments in the upper 2 m generally have an *OCR* value greater than 1, even though the sediments geological history suggests it was normally consolidated. This is termed apparent overconsolidation and is recorded throughout the world's oceans. Possible causes of apparent overconsolidation include bioturbation, creep or particle bonding (Gourvenec and White, 2010). This phenomenon creates difficulty in distinguishing between true overconsolidation and apparent overconsolidation.

Underconsolidation indicates the sediments have not fully consolidated under the *in-situ* stresses and suggests the presence of excess pore water pressures. Possible causes of underconsolidation include rapid sedimentation or the presence of gas in marine sediments. In either case, the presence of excess pore pressures reduce the frictional resistance between soil particles, resulting in effective stress that is less than the total stress.

5.3 Consolidation Testing

5.3.1 Introduction

Consolidation tests reproduce gravitational compaction in a controlled environment to simulate a soils response to vertical loading. A consolidation plot is developed from a series of increasing incremental loads applied to a soil sample. At each load the soil is exposed to an increase in total normal stress (σ_n), which results in sample deformation and a corresponding decrease in volume as measured by the void ratio. The process is repeated at different vertical stresses until a consolidation plot is defined (Figure 5.2).

The initial portion of the consolidation curve (Figure 5.2) is the reloading of the sample. Little void ratio change occurs over these pressure intervals, since the sample has previously experienced this stress *in-situ.* Beyond the P'_c marks the beginning of the virgin compression line and effective stresses not previously experienced by the soil sample. The slope of the virgin compression line (C_c) represents the reduction in void ratio as a function of effective stress. C_c is a measure of the compressibility of the sediment and defines the void ratio-depth function of the sediment. Each point on the virgin compression line experiences both plastic and elastic deformation. Plastic deformation is an unrecoverable strain caused by the soil skeleton taking on a new shape to support the load. The unloading portion of the curve represents the elastic rebound of the material. The slope of this portion of the curve defines the recompression index (C_r), which characterizes the sediments elastic response to stress relief.

The maximum curvature of the transition between reloading and the application of new loads approximates the past maximum stress experienced by the soil (P'_c). P'_c can be approximated using several procedures (Grozic et al., 2003). The procedure developed by Casagrande (1936b) is the most

widely used. Comparing the P'_c to the present day effective overburden stress, expressed as the over consolidation ratio, determines the degree of consolidation and defines whether the soil is normally consolidated (*OCR=1*), overconsolidated (*OCR>1*) or underconsolidated (*OCR<1*). The consolidation tests followed the general test procedures outlined in ASTM D2435.

5.3.2 Consolidation Equipment

The GSC-A geomechanical laboratory has two GDS Instruments back pressured consolidation testing systems. The constant rate of strain (CRS) system (Figure 5.3) consists of a CRS consolidation cell for 6.35 cm diameter samples, a 50 kN load frame, one GDS 1 MPa standard pressure/volume controller, 25 mm linear displacement transducer, 2 MPa pore pressure transducer, 2 kN submersible load cell, 16 bit DAQ system, computer and GDSLab software. The Rowe cell system (Figure 5.4) consists of two GDS 2 MPa standard pressure/volume controller, 25 mm linear displacement transducer, 2 MPa pore pressure transducer, a linear displacement transducer, 16 bit DAQ system, computer and GDS software. The GDSLab software can perform incremental loading and the constant rate of strain (CRS) consolidation tests. The CRS test can be performed faster than the incremental loading test; however it is more difficult to obtain the hydraulic conductivity for coarser-grained sediments.

5.3.3 Sample Preparation

The samples for the consolidation tests were taken from whole round samples. The CRS cell sample preparation includes extrusion of sediment into a consolidation ring with a sharp cutting edge and an inner diameter of 6.35 cm. The samples are trimmed in the consolidation ring with a wire saw to a height of 2.2 cm. The sample is then placed on the base of the CRS consolidation cell (Figure 5.5). The CRS cell top is secured and filled with de-aired water.

The Rowe cell sample preparation includes pushing a cutting shoe with a sharp cutting edge into the whole round sample which extrudes the sediment into a consolidation ring with an ID of 6.3 cm. The

samples are trimmed in the consolidation ring with a wire saw to a height of 2.58 cm. The consolidation ring is then placed on the Rowe cell base (Figure 5.6) and the cell top is placed over the consolidation ring. Initial measurements of dimension, weight and water contents are taken after the samples are trimmed in the consolidation rings.

5.3.4 Sample Saturation

The removal of the sediment from the marine environment permits the formation of gas bubbles. Gas bubbles may be entrapped in the pore fluid, which can have a considerable effect on the consolidation and permeability of the sediments. The gas bubbles in partially saturated sediment are highly compressible compared with the relatively incompressible pore water and sediment. The gas bubbles also impede the flow of water through the pores, reducing the effective permeability of the sediment.

The saturation stage is designed to ensure all voids within the test sample are filled with de-aired water. The sample saturation involves increasing the axial stress and the pore fluid pressure. The axial stress is set to 2 kPa higher than the backpressure. The duration of the saturation stage ranged from three to six hours. The samples were then allowed to adjust to the back-pressure for a minimum of 12 hours.

5.3.5 Loading/Unloading

Vertical loads were applied until the virgin compression line (*VCL*) was established which enabled the determination of C_c. Load increments increased by 50% of the previous load. The vertical load is initially carried by the pore water, resulting in an increase in pore pressure (Figure 5.7). The dissipation of excess pore pressure to back pressure and corresponding volume change marks the end of primary consolidation. Most volume change occurs in this stage. The time required for excess pore pressures to dissipate depends on the hydraulic conductivity, compressibility, and the length of the drainage path. Once primary consolidation is complete a new load is applied.

Once the *VCL* is defined, the samples are unloaded by applying increments of decreasing load. Load increments decrease by 100% of the previous load. The reduction of the vertical load results in an initial decrease in pore pressure as the soil skeleton expands. The pore pressure will return to the backpressure as water returns to the sample (Figure 5.8). Once the pore pressure returns to the backpressure, the next unload increment is applied.

The effective axial stress (σ') for the CRS cell was calculated as the difference between the pore pressure (μ) and total axial stress (σ). The axial stress for the Rowe cell was calculated using,

$$\sigma_v' = (\sigma_{up} * 0.996) - u_b \qquad \text{Equation 5.1}$$

Where σ_{up} is the load clamber pressure, μ_b is the back pressure and 0.996 is the area correlation for the drainage port on the spindle that is in contact with the sample. The pore pressure in the drainage port remains constant throughout the test and does not apply vertical load on the sample.

5.3.6 Data analysis

The sample volume change is determined using the change in sample height, since the cross-sectional area of the sample is constant throughout the test. The volume is represented as a void ratio and is calculated at the end of each load increment using,

$$e_{end} = e_i - \frac{\Delta H}{H_s} \qquad \text{Equation 5.2}$$

where e_{end} is the void ratio at the end of the load stage, e_i is the void ratio at the start of the load stage, ΔH is the change in height during the load stage and H_s is the height of the solids.

Soil parameters derived from the consolidation plot include the compression index (C_c) and the recompression index (C_r). C_c is calculated from the slope of the *VCL* and defines the compressibility of the soil,

$$C_c = \frac{\Delta e}{\log(P_1'/P_2')}$$ Equation 5.3

C_r is the slope of a straight-line approximation of the unloading portion of the consolidation curve and is calculated by,

$$C_r = \frac{\Delta e}{\log(P_2'/P_1')}$$ Equation 5.4

The compressibility can also be described as the compressibility per unit thickness of the soil. This is known as the coefficient of volume compressibility (m_v) and is defined by,

$$m_v = \frac{1}{1+ e_1}\left(-\frac{\Delta e}{\Delta p}\right)$$ Equation 5.5

where e_1 is the void ratio at the start of the stress increment, Δp is the change in effective axial stress and Δe is the change in void ratio for the stress increment.

The rate at which the sample compresses during each load increment is termed the coefficient of consolidation (C_v) and is dependent on the hydraulic conductivity of the soil. The C_v values were calculated using Taylor's square root of time method (Holtz and Kovacs, 1981). The time versus height compression curves are used to calculate C_v using,

$$C_v = \frac{0.848H^2}{t_{90}}$$ Equation 5.6

where H is the length of the drainage path and t_{90} is the time corresponding to 90% of primary consolidation.

The hydraulic conductivity (k) is calculated using,

$$k = C_v\, m_v \rho_{sw} g$$ Equation 5.7

6.0 Shear Strength Properties

6.1 Introduction

The shear strength of a soil is the maximum resistance a soil displays against failure and is directly controlled by its effective stress. Several sources contribute to a soils shear strength, but gravitational compaction and the accompanying squeezing out of pore water under the weight of overburden sediments by far contributes the most. Other sources of strength include bioturbation, desiccation, and particle bonding. The most common failure criteria applied to soil is the Mohr-Coulomb failure criteria defined as,

$$\tau_f = c' + (\sigma - \mu)\, tan\phi' \qquad \text{Equation 6.1}$$

where τ_f is the shear stress at failure, σ_n is the total normal stress, μ is the pore pressure, c' is effective cohesion and ϕ' is effective internal angle of friction.

The relationship between the shear stress (τ_f) and the effective normal stress (σ'_n) at failure define the Mohr-Coulomb strength parameters, c' and ϕ' (Figure 6.1). The Mohr-Coulomb failure envelope defines the stresses at which failure occurs. At stress conditions below the failure envelope, the soils are stable.

Cohesion marks the bonding strength of fine grained soils. Cohesion typically increases with clay content, but effectively depends on the type of clay minerals and their colloidal activity. While cohesion is negligible in most soils, there are soils where it provides a considerable source of strength, particularly soils containing the clay mineral montmorillonite (Lambe and Whitman, 1969). The internal angle of friction (ϕ') is the frictional resistance of soils grains and depends on their shape and size. Coarse-grained soils like sands have a higher friction angle than clays.

The shear strength of sediments at different depths can be compared by normalizing the shear strength with respect to the effective overburden (S_u/σ'_v). The stress history influences the soils S_u/σ'_v ratios. Overconsolidated soils possess a greater strength than what is suggested by the *in-situ* overburden, which results in a relatively high S_u/σ'_v. Normally consolidated soils generally have S_u/σ'_v values in the range of 0.2-0.5, while overconsolidated clays have a S_u/σ'_v greater than 0.5 (Skempton, 1970).

6.2 Strength Profiles

6.2.1 Introduction

A method to characterize the undrained shear strength of soils was presented by Ladd and Foot in 1974. This is known as the SHANSEP (Stress History And Normalized Soil Engineering Properties) and is the most widely used method. The SHANSEP method was used to create continuous strength profiles for normally consolidated sediment (*OCR=1*). Essentially, the profile's shear strength is the expected shear strength increase with depth for a soil in a normal stress state.

6.2.2 SHANSEP Method

The SHANSEP method is based on the observation that the shear strength (S_u) of most cohesive soils increases with depth below the seafloor and can be normalized with respect to the present-day effective overburden (S_u/σ'_v). A comprehensive analysis of the sediment's undrained shear strength using the SHANSEP method includes the determination of S_u/σ'_v for several *OCR* values (Figure 6.2) and is presented as,

$$\frac{S_u}{\sigma'_v} = S\,(OCR)^m \qquad \text{Equation 6.2}$$

where S_u is the undrained shear strength, S is the S_u/σ'_v ratio for normally consolidated soils and m is a soil constant. For simplicity, S will be used to represent the S_u/σ'_v ratio for normally consolidated soils for the remainder of the report. A continuous strength profile for normally consolidated sediments is plotted using,

$$S_u = S\sigma'_v \qquad \text{Equation 6.3}$$

The stress history of the sediments can be estimated by comparing the shear strengths calculated using Equation 6.3 with the measured laboratory MV data (Figure 6.3). If the measured MV shear strength is greater than the calculated S_u, the sediments are considered overconsolidated. If the MV shear strength data is less than the calculated S_u, the sediments are considered underconsolidated.

Assuming that shear strength is a function of gravitational compaction, a linear correlation can be made between the shear strength and depth below the seafloor. The *S* ratio does not account for other sources of strength, therefore S_u/σ'_v provides only an approximation of predicted shear strength and must be used with caution.

6.3 Triaxial Testing

6.3.1 Introduction

The triaxial test is one of the most versatile and widely performed geotechnical laboratory tests, allowing the shear strength and stiffness of soil to be determined for use in geotechnical design. Advantages over simpler tests include the ability to control specimen drainage and taking measurements of pore fluid pressures. Primary parameters obtained from the test include the Mohr Coulomb failure criteria, ϕ' and c'.

The triaxial test typically involves placing a cylindrical soil sample sealed in a rubber membrane, into a cell that can be pressurised. The specimen is saturated, consolidated, and sheared, allowing the soil response to be observed under conditions that may approximate those *in-situ*. The confining pressures of consolidation strengthen the soil sample by creating a pressure differential between the pore water in the void spaces and the fluid cell pressure which surrounds the sample. This pressure differential

creates an increase in effective stress as the sample consolidates. A general set-up of the triaxial sample is shown in Figure 6.4.

There are three primary types of triaxial tests conducted in the laboratory: unconsolidated undrained (UU), consolidated undrained (CU) and consolidated drained (CD). The CU test is the most common triaxial test and was used for this study following ASTM D4767. In this test method, the soil sample is fully consolidated under a stress applicable to field conditions (i.e. effective overburden stress). The sample is then subjected to a compressive axial stress without allowing further consolidation to take place.

The stresses applied to a soil sample in a triaxial compression test are displayed in Figure 6.5. The confining stress, σ_c is applied by pressurising the cell fluid surrounding the sample during the consolidation stage. The difference between the σ_c and the pore pressure (μ) is the effective stress (σ'_c), which represents the consolidation stress. The deviator stress (q) is generated by applying an axial stress greater than the confining pressure (σ_c) during the shear stage and is equal to σ_1 - σ_3.

6.3.2 Triaxial Test Equipment

The triaxial system used is a GDS computer controlled hydraulic triaxial testing system consisting of a 50 mm Bishop & Wesley stress path triaxial cell, 3 GDS 2 MPa pressure/volume controllers, a 5 kN submersible load cell, pore pressure transducer, linear displacement transducer, a DAQ system, a computer and GDS software (Figure 6.6). The GDS pressure/volume controllers and the 3 transducers control and read the cell's back pressure, pore pressure, back volume, axial displacement, axial load and effective stress.

6.3.3 Triaxial Test Procedure

6.3.3.1 Introduction

The CU triaxial test as described by (ASTM D4767) consists of four main stages: 1) sample and system preparation, 2) sample saturation, 3) consolidation and 4) compressive shear. Generally, three specimens are tested at different effective consolidation stresses to define a strength envelope. The lack of available sediment for this study necessitated conducting multi-stage triaxial tests. This type of test is practical when economizing on soil samples or when limited sample is available. Multi-stage triaxial tests are performed in three consolidation and shear sequences. In each sequence, the sample is consolidated to an increasing consolidation stress and then sheared. The first 2 shear stages are stopped when the deviator stress levels off or at 5% strain. The third shear stage continued until 15-18 % total strain. The stresses at failure define the failure envelope and maximum shear strength.

6.3.3.2 Specimen Preparation

A thin-walled sampling tube (14 cm, 50 cm ID) with a sharp cutting edge is pushed into the whole round core sample to extrude sediment from the core liner. The samples are trimmed in the sampling tube with a wire saw to a height of approximately 12 cm and initial measurements of dimensions and weights for water content are made. The samples are extruded from the sampling tube into a rubber membrane fitted in a split form, which is attached to the base pedestal of the triaxial cell Figure 6.7. Following placement of the sample, the triaxial cell and other system components are assembled. During this stage the cell is filled with de-aired water, pressure/volume controllers connected, and transducer readings set as required.

6.3.3.3 Saturation

The saturation stage is designed to ensure all voids within the test sample are filled with de-aired water. The sample saturation involves increasing the axial stress and the pore fluid pressure. The axial

stress is set to 2 kPa higher than the backpressure. The duration of the saturation stage ranged from 3 to 6 hours. The samples were then allowed to adjust to the back-pressure for a minimum of 12 hours.

The degree of specimen saturation is determined by conducting a *B*-check to determine Skempton's *B*-value (Skempton, 1954) which is defined as,

$$B = \frac{\Delta\mu}{\Delta\sigma_3} \qquad \text{Equation 6.4}$$

The sample is considered to be 100% saturated at a *B* valve of > 0.95. The back pressure required to obtain 100% saturation ranged from 200 kPa to 300 kPa.

6.3.3.4 Consolidation

The consolidation stage is used to bring the sample to the effective stress required for shearing by increasing the confining stress (σ_c) while maintaining a constant pore pressure. The increase in cell pressure results in an initial increase and then dissipation of the sample's pore pressure (Figure 6.8). The consolidation process continues until at least 95% of the excess pore pressure generated has dissipated.

The first consolidation stress is set to the *in-situ* effective overburden stress calculated from MSCL bulk density data. After the sample has consolidated and sheared, a second confining pressure is applied, which is at least 2.5 times greater than the effective overburden stress to remove the effect of stress history (Ladd and Foot, 1974). The third confining pressure is set at twice the second confining pressure. The typical 3 confining pressures chosen are illustrated in Figure 6.9. Confining pressures 2 and 3 become the new P'_c for the sample and the *OCR=1*.

6.3.3.5 Shearing

The samples are sheared by applying an axial stress to the test sample at a constant rate of strain through upward compression by movement of the base pedestal. Sample response during the shear

stage was monitored by plotting the deviator stress (q) against axial strain ($\varepsilon_a = \Delta L/L$). The shear stage was continued until a specified failure criterion was reached. The first two shear stages of the multistage tests were stopped when the deviator stage leveled off or at a maximum 5% axial strain. The third shear stage was stopped at total axial strains ranging between 15 to 18% (Figure 6.10).

6.3.4 Data Analysis

A triaxial test determines the Mohr circle failure envelope to define the shear strength characteristics, cohesion (c') and the internal angle of friction (ϕ'). The strength properties used for Mohr-Coulomb failure theory are determined by defining three Mohr's circles at failure. The Mohr-Coulomb failure envelope of a normally consolidated soil should plot as a straight line, indicating that both cohesion and the internal angle of friction are properties of the soil that remain constant despite the confining pressure.

The A_f value (Skempton, 1954) relates the change in pore pressure to the change in deviator stress and is defined as,

$$A_f = \frac{\Delta\mu}{\Delta\sigma_3} \qquad \text{Equation 6.5}$$

A_f values vary depending on the soil stress state (Figure 6.11). For normally consolidated, saturated soils, the change in pore pressure should be approximately equal to the load applied, reflected by an A_f value approximately equal to 1. Heavily overconsolidated soils, generally dilate when sheared and generates a negative change in pore water pressure, resulting in a negative A_f value.

The normalized shear strength ratio (S_u/σ'_v) in the normally consolidated stress (S) range was estimated using the average of maximum shear strength and confining pressure for the second and third confining pressures.

7.0 Slope Stability

7.1 Introduction

Submarine slides in the Baffin Bay represent a significant potential geohazard for offshore infrastructure and coastal communities. Submarine slides can be triggered by processes including glacial activity, seismic loading (earthquakes), over steepening and excess pore water pressures, and, in some cases, human activities. Other than man-made activity causing submarine slides close to shore, earthquakes are probably the most common trigger of offshore slope instability (Hance, 2003). Hance (2003) reported that among the 534 events in his database, over 40% of the slope failures were attributed to earthquake and faulting mechanisms (Figure 7.1). Assessing slope instability requires information on the frequency of failure, trigger mechanism, soil conditions and the morphology of the area.

7.2 Slope Analysis

Limit equilibrium methods are most commonly used to assess the slope stability in a marine environment. The limit equilibrium analysis evaluates a well-defined body on a slope as if it is about to fail and determines the shear stress induced by varying trigger mechanisms. The shear stresses are then compared to the soils shear strength to determine the Factor of Safety (*FS)* using,

$$FS = \frac{Sediment\ Strength}{Trigger\ Mechanisms\ Stress} \qquad \text{Equation 7.1}$$

A slope is unstable if the $FS \leq 1$.

The infinite slope method was used for the slope stability analysis. It assumes that the failure surface is parallel to the slope and the slope is planar and of infinite length. The analysis was done for undrained conditions. The triggering mechanisms analysed were gravitational loading and seismic earthquake loading. The MV measurements represent the sediment shear strength.

7.2.1 Gravitation Loading

Gravity forces are a mechanism for general downslope movement causing slopes to fail or sediments to consolidate under their own weight. A *FS* can be calculated if the slope angle, bulk density and the undrained shear strength of the sediment are known.

Figure 7.2 illustrates the static conditions under which the slice of soil is loaded. The gravitational force (*T*) parallel to the slope is equal to the effective weight of the soil, and the sediments shear strength (*R*) is the undrained shear strength (S_u) times the length (*l*) along the base of the slice. From consideration of the equilibrium of the slope at the point of failure, the forces parallel to the slope are equal therefore,

$$S_u l = W' sin\beta \qquad \text{Equation 7.2}$$

where W′ is the weight of the slice with width b and height h having a unit dimension into the page and equals,

$$W' = \gamma' bh \qquad \text{Equation 7.3}$$

where γ' is the submerged or effective unit weight of the soil and equates,

$$\gamma' = \gamma_{soil} - \gamma_{sea\ water} \qquad \text{Equation 7.4}$$

Since $l = b/cos\beta$, Equation 7.2 can be rewritten as,

$$S_u = \frac{\gamma' bhsin\beta cos\beta}{b} \qquad \text{Equation 7.5}$$

Using the double trigonometry identity sin 2β = 2 sinβcosβ, Equation 7.5 is reduced to,

$$2S_u = \gamma' hsin2\beta \qquad \text{Equation 7.6}$$

The FS (Equation 7.1) is then calculated using Morgenstern's (1967) basic infinite slope analysis equation,

$$FS = \frac{2}{sin2\beta}\frac{S_u}{\gamma' h} \qquad \text{Equation 7.7}$$

The critical height (H_c) where *FS =1* can be obtained using,

$$H_c = \frac{2S_u}{\gamma' \sin 2\beta} \qquad \text{Equation 7.8}$$

The critical slope angle (β_c) where *FS =1* can is determined by,

$$\beta_c = \left[\frac{1}{2}\left\{sin^{-1}\left(\frac{2S_u}{\gamma' h}\right)\right\}\right] \qquad \text{Equation 7.9}$$

7.2.2 Earthquake Seismic Loading

Stability of a slope can be affected by seismicity. These seismic motions are capable of inducing large destabilizing inertial forces. In general, three methods of analysis have been proposed for the evaluation of slopes response under such conditions including the pseudostatic method, Newmark's displacement method and the dynamic finite element analysis method.

The pseudostatic method is the simplest to use and simulates the earthquake's inertial forces by the inclusion of static horizontal and vertical forces in limit equilibrium. The effect of the vertical pseudostatic force on a sliding mass is ignored as it has very little effect on its slope stability. In pseudostatic slope stability analyses, a factor of safety is computed in which a pseudostatic, horizontal inertial force is added to the triggering mechanism stress.

The pseudostatic method ignores the cyclic nature of the earthquake and assumes that an additional static constant force is applied on the slope due to the earthquake. In the actual analysis, a horizontal force is added to the existing gravitational static load. This pseudostatic horizontal force (F_h) is calculated as follows,

$$F_h = ma = \frac{Wa}{g} = k_h W \qquad \text{Equation 7.10}$$

where *m* is the total mass of slide material, *W* is the total weight of the slide mass, *a* is the ground acceleration due the earthquake, *g* is the acceleration due to gravity and k_h is the horizontal seismic coefficient which is a fraction of gravity.

Figure 7.3 illustrates the pseudostatic condition under which the slice of soil is loaded. The seismic load (k_hW) parallel to the slope is equal to the weight of the soil times the horizontal seismic coefficient. From consideration of the equilibrium of the slope at the point of failure, the forces parallel to the slope are equal and Equation 7.2 becomes,

$$S_u l = W' sin\beta + k_h W cos\beta \qquad \text{Equation 7.11}$$

Since $l = b/cos\beta$ and $W=\gamma bh$, Equation 7.11 can be rewritten as,

$$S_u = \frac{\gamma' bhsin\beta cos\beta}{b} + \frac{k_h \gamma bhcos\beta cos\beta}{b} \qquad \text{Equation 7.12}$$

Rearranging Equation 7.12,

$$\frac{S_u}{\gamma' h} = sin\beta \cos\beta + k_h cos^2\beta \frac{\gamma}{\gamma'} \qquad \text{Equation 7.13}$$

The minimum acceleration (k_{min}) necessary to cause slope sediments to fail can be estimated using,

$$k_{min} = \frac{S_u}{\gamma' hcos^2\beta}\frac{\gamma'}{\gamma} - \frac{\gamma'}{\gamma} tan\beta \qquad \text{Equation 7.14}$$

A considerable limitation of the pseudostatic approach is that the horizontal force representing the effects of seismicity is constant and acts in only one direction. With dynamically applied loads, the force may be applied for only a few tenths of a second before the direction of motion is reversed. The result of these transient forces will be a series of displacement pulses rather than complete failure of the slope.

8.0 Results

8.1 Introduction

Campbell et al. (2017) and Jenner et al. (2018) presented the sedimentlogy and physical properties of a number of cores collected by the GSC-A during the 2013029 CCGS Hudson cruise. Five cores that represent the late Quaternary geology across the Baffin shelf were selected as geotechnical cores (Figure 8.1). Four of the cores were selected from the western shelf of Baffin Island between Scott

Trough and Qikiqtarjuaq, which are approximately 628 km apart, and one core was selected from the Greenland shelf near Disko Bugt. The cores penetrated depths of 5 to 8 meters below the seafloor at slope angles between 0.72 and 3.83 degrees.

The late Quaternary geology of the Baffin Island slope is dominated by trough mouth fans fed by distinct transverse troughs (Campbell et al., 2017). Sediment cores taken from undisturbed sections of seabed along the Baffin Island slope reveal a consistent lithostratigraphy that spans the Late Pleistocene to present and is correlatable along the margin (Jenner et al. 2018). In general, this succession consists of proglacial and glaciomarine deposits composed of basal diamicton overlain by fine grained turbidites and meltwater plume deposits, which in turn are overlain by carbonate-rich ice-rafted gravelly, sandy mud. Proglacial deposits transition upsection to postglacial Holocene hemiplegic silty clay sediments.

Geotechnical testing on the five cores included MSCL bulk density, Atterberg limits, grain size analysis, MV undrained shear strength, back-pressured consolidation tests and isotropically consolidated (CIU) triaxial tests. A summary of the type and number of tests completed for each core are presented in Table 8.1.

MSCL bulk density measurements taken at 1 cm intervals are used to develop a continuous bulk density profile. Natural *in-situ* water contents *(w_n) w*ere measured at 75 cm intervals. Atterberg limit samples are representative of the different lithologies and correspond to natural water content measurements. Stress history, compressibility and hydraulic conductivity were determined from consolidation tests.

MV measurements were taken at 10 cm intervals and remoulded shear strengths at 75 cm intervals. The Mohr-Coulomb failure parameters, and *S* ratios were determined from CIU multi-stage triaxial tests. Continuous undrained strength profiles for normal consolidation were complied using the SHANSEP method. Comparisons of the MV data and the strength profiles estimates the stress history.

Slope instability was determined using the infinite slope method. The trigger mechanisms analyzed were gravitational and earthquake loading. The minimum *FS*, critical height, critical slope angle and minimum horizontal acceleration coefficient were calculated.

The geotechnical data were compiled into geotechnical profiles where the various soil properties are presented as a function of depth. The geotechnical profiles result from many stages of development including natural consolidation due to gravitional compaction and depostional or eroisonal events. The profiles include down core plots of lithology, grain size, density, natural water content, plastic and liquid limits, undrained shear strengths, effective overburden stress and P'_c values. The lithology was obtained from Campbell et al. (2017). The geotechnical results for each core are presented in the following sections.

8.2 Piston Core 20130290048

8.2.1 Introduction

Piston core 20130290048 was collected off the southern coast of Baffin Bay near Qikiqtarjuaq, at a water depth of 935 m and a slope angle of 1.4º (Figure 8.2), determined from GEBCO bathymetry. The core recovered 822 cm of sediment.

8.2.2 Atterberg Limits

Atterberg limit tests were completed on eight samples (Figure 8.3). The samples range from low to high plasticity. The liquid limits range from 20.6 to 53.9%, and the plastic limits range from 13.3 to 28.7%. The plasticity index ranges from 7.2 to 29.1% (Table 8.2). One sample at a depth of 162-172 cm plots in Zone A, while the other four samples at depths of 28-38 cm, 190-200 cm, 481-495 cm and 638-648 cm plot in Zone B.

8.2.3 Consolidation Test Results

Consolidation tests were conducted on three samples at core depths of 200-202.5 cm, 353-355.5 cm, and 500-502.5 cm (Figure 8.4) to assess the compressibility (C_c), hydraulic conductivity (k) and stress history (OCR). The compressibility are moderate with compression indices (C_c) of 0.7 and 0.6 and recompression indices (C_r) of 0.05 and 0.03. The hydraulic conductivities, k, at the void ratio equivalent to the P'_c are 5.99E-08 cm/sec and 1.11E-07 cm/sec. The consolidation tests characterize the sediments as normally to slightly overconsolidated with respect to the effective overburden with OCR values of 0.9, 1.0 and 1.2 (Table 8.3).

8.2.4 Triaxial Test Results

Isotopic CU triaxial tests were conducted on 2 samples at core depths of 332-344 cm and 483-495 cm (Figure 8.5). The Mohr-Coulomb failure envelopes are defined by effective friction angles (ϕ') of 25.6° and 24.9° and effective cohesion values (c') of 2.3 kPa and 5.0 kPa. The pore pressure coefficient at failure (A_f) are 0.63 and 0.48. The S ratios are quite similar at 0.25 and 0.27 (Table 8.4).

8.2.5 Slope Stability

The FS was calculated at slope angles of 1°, 1.4°, 5°, 10°, 15° and 20° (Figure 8.6). The slope is stable under static conditions with a minimum FS of 6.4 at a core depth of 794 cm. The critical height, critical slope angle and minimum acceleration coefficient are 32.7 m, 9.3° and 0.06 (Table 8.5).

8.2.6 Geotechnical Profile

The sediment consists of a clayey silt mud with moderate to extensive bioturbation and a glacially derived tan carbonate bed. Gravitational compaction is the dominant feature of this core, except in the tan carbonate interval where there is a change in physical properties. There is a clear break in the depositional sequence observed in the bulk density and lithology profiles at depths of ~140, 175, 385 and 725 cm (Figure 8.7).

The uppermost stratum consists of a silty clay mud with a variable density. At 140 cm there is a 35 cm tan carbonate bed with a corresponding increase in bulk density. Below the tan carbonate, from 175 to 725 cm, the sediments return to a silty clay mud with a gradual increase in bulk density. At 385 cm there is a slight offset in bulk density, corresponding to the occurrence of shell fragments. At 725 cm, there is an abrupt change in bulk density with higher variability to the base of the core.

The grain size fractions are relatively constant with equal parts silt and clay and little to no sand, except at the top and base of the core where the sand content increases to approximately 20%. The water contents and plasticity show little change with depth except from 175 to 385 cm. At 175 cm there is a decrease in water content and plasticity in the tan carbonate bed. From 185 to 385 cm, there is a distinct increase in water contents accompanied by an increase to high plasticity silts and clays. The *LI* decreases with depth, suggesting the sediments are underconsolidated near the surface and become overconsolidated with depth.

The consolidation tests are in good agreement with effective overburden, suggesting the sediments are normally consolidated to slightly overconsolidated within the limits of accuracy. MV measurements increase in proportion with effective overburden to 700 cm and then decrease to the base of the core. The MV measurements plot above or within the *S* values. The variability in MV measurements shows

a noticeable increase from 150 cm to the base of the core. The high shear strengths within the high water content interval suggest sediment with a relatively open structure. The minimum *FS* near the base of the core may be related to coring disturbance; however, the core is stable with a $FS > 6$.

8.3 Piston Core 20130290060

8.3.1 Introduction

Piston core 20130290060 was collected off the northern coast of Baffin Bay near Scott Trough, at a water depth of 1191 m and a slope angle of 3.83º (Figure 8.8), determined from GEBCO bathymetry. The core recovered 487 cm of sediment.

8.3.2 Atterberg Limits

Atterberg limit tests were completed on seven samples (Figure 8.9). The samples ranged from low to high plasticity. The liquid limits range from 20.2 to 66.6% and the plastic limits range from 11.9 to 26.5%. The plasticity index range from give 8.3 to 40.1% (Table 8.6). Two samples at depths of 17-27 cm and 95-105 cm plot in Zone A and one sample at a depth of 298-314 cm plots in Zone B.

8.3.3 Consolidation Test Results

A consolidation test was performed on one sample at a core depth of 294-296.5 cm (Figure 8.10). The compressibility is low with a compression index (C_c) of 0.3 and recompression index (C_r) of 0.04. The hydraulic conductivity (k) at the void ratio equivalent to the P'_c is 1.08E-07cm/sec. The sediment is characterized as overconsolidated with respect to the effective overburden, with an *OCR* value of 2.2 (Table 8.7).

8.3.4 Triaxial Test Results

Isotopic CU triaxial tests were conducted on two samples at a core depth of 142-154 cm and 300-312 cm (Figure 8.11). The Mohr-Coulomb failure envelopes are defined by effective friction angles (ϕ') of

22.3° and 23.8° and effective cohesion values (c') of 2.2 kPa and 6.8 kPa. The pore pressure coefficients at failure (A_f) are 0.54 and 0.36. The S ratios are 0.26 and 0.32 (Table 8.8).

8.3.5 Slope Stability

The FS was calculated at slope angles of 1°, 3.8°, 5°, 10°, 15° and 20° (Figure 8.12). The slope is stable under static conditions with a minimum FS of 4.5 at a core depth of 420 cm. The critical height, critical slope angle and minimum acceleration coefficient are 11.5 m, 18.3° and 0.08 (Table 8.9).

8.3.6 Geotechnical Profile

The sediment consists of a silty clay mud with three well-defined glacially derived deposits. The glacial deposits consist of a tan carbonate mud and two diamicton beds, resulting in abrupt changes in depositional sequence and physical properties. The abrupt changes in the bulk densities suggest rapid onset or offset of glacial ice sheets. This is observed at approximately 15, 130, 275, 330, and 445 cm (Figure 8.13).

The uppermost 15 cm consists of a hemipelagic mud of low bulk density. Below the hemipelagic mud and extending to a depth of 130 cm is a 115 cm thick tan carbonate bed deposited during the last glacial maximum (Jenner et al, 2018). From 130 to 275 cm the core returns to a silty clay mud with very low bulk densities. At 275 cm, there is a sharp increase in bulk density corresponding to a 55 cm thick diamicton bed. Below the diamicton bed and extending to a depth of 445 cm, the bulk density remains noticeably consistent. Near the base of the core, there is a sharp increase in bulk density corresponding to the second diamicton bed.

The glacially derived sediments have low water contents with low to intermediate plasticity, while the silty clay muds have high water contents and high plasticity. The LI decreases with depth, suggesting the sediment is underconsolidated near the surface and becomes overconsolidated with depth.

The consolidation test at 294 cm indicates the sediments are overconsolidated with an *OCR* value of 2.2. This indicates that it would require an additional load of 26 kPa to the present day overburden, which is equivalent to 6m of subaerial glacial ice or 3.5 m of overburden. This is an estimate; however, it is in reasonable agreement with the P'_c determined from the consolidation test. MV measurements increase with respect to the effective overburden with appreciable strength in the glacially-derived units. MV measurements occur above the *S* values for the entire core. The minimum *FS* occurs in the silty clay mud of uniform bulk densities and high water contents; however, the core is stable with a *FS*>4.

8.4 Piston Core 20130290075

8.4.1 Introduction

Piston core 20130290075 was collected off the northern coast of Baffin Bay near Isabella Bank, at a water depth of 1484 m and a slope angle of 1.71º (Figure 8.14), determined from GEBCO bathymetry. The core recovered 704 cm of sediment.

8.4.2 Atterberg Limits

Atterberg limit tests were completed on 10 samples (Figure 8.15). The samples range from low to extremely high plasticity. The liquid limits range from 17.9 to 99.0%, and the plastic limits range from 12.1 to 32.2%. The plasticity index ranges from 5.8 to 66.8% (Table 8.10). One sample at a depth of 320-330 cm plots in Zone A and one sample at a depth of 285-295 cm plots in Zone B.

8.4.3 Consolidation Test Results

Consolidation tests were conducted on three samples at core depths of 201-203.5 cm, 375-377.5 cm and 668-670.5 cm (Figure 8.16). The compressibilities range from high to low with C_c values of 1.1, 1.1 and 0.3 and C_r values of 0.09, 0.08 and 0.02. The hydraulic conductivities (*k*) at the void ratio

equivalent to the P'_c are 2.50E-07cm/sec, 4.21E-06cm/sec and 1.22E-07cm/sec. The consolidation tests characterize the sediment as slightly under to slightly overconsolidated with respect to the effective overburden, with *OCR* values of 1.2, 0.8 and 0.9 (Table 8.11).

8.4.4 Triaxial Test Results

Isotopic CU triaxial tests were conducted on two samples at core depths of 206-218 cm and 646-658 cm (Figure 8.17). The Mohr-Coulomb failure envelopes are defined by effective friction angles (ϕ') of 18.9° and 24.3° and effective cohesion values (c') of 0.0 and 9.4 kPa. The pore pressure coefficients at failure (A_f) are 0.64 and 0.45. The *S* ratios are 0.19 and 0.32 (Table 8.12).

8.4.5 Slope Stability

The *FS* was calculated at slope angles of 1°, 1.7º, 5°, 10°, 15° and 20° (Figure 8.18). The slope is stable under static conditions with a minimum *FS* of 5.2 at a core depth of 422 cm. The critical height, critical slope angle and minimum acceleration coefficient are 12.2 m, 9.2° and 0.07 (Table 8.13).

8.4.6 Geotechnical Profile

The sediment consists of a silty clay mud with two glacially derived, tan carbonate beds. Gravitational compaction is the dominant feature in this core except in the tan carbonate intervals, where there is a distinct break in depositional sequence accompanied by a change in physical properties. The abrupt changes in the bulk densities suggest rapid changes in the position of the leading edge of the glacial ice sheet. The clear breaks occur at approximately 270, 350, 390 and 430 cm (Figure 8.19).

The uppermost stratum consists of a postglacial hemipelagic mud. The hemipelagic mud provides an excellent example of gravitational compaction showing a linear increase in bulk density and a corresponding decrease in water content. At 270 cm, there is a sharp increase in bulk density corresponding to an 80 cm thick tan carbonate bed. Between 350 and 390 cm is a silty clay mud of

similar bulk density to the hemipelagic mud above, indicating a period of quiescent deposition. Oscillating tan carbonate beds between 390 and 430 cm and interbedded silt layers from 430 to 495 cm result in a variable density profile and complex stratigraphy. Beyond 495 cm and to the base of the core is a silty clay matrix with mud clasts corresponding to a variable density profile.

The grain size analysis show approximately equal parts silt and clay, except in the tan carbonate intervals where the sand content increases to approximately 20%. With few exceptions, the water content decreases with depth. In the tan carbonate beds, a significant drop in water content is accompanied by a decrease to low plasticity silts and clays. The *LI* suggests the sediments are underconsolidated to 500 cm and become normally consolidated with depth.

The consolidation tests are in agreement with effective overburden pressures, suggesting the sediments are under to slightly overconsolidated within the limits of accuracy. An *OCR* value of 0.8 at 375 cm corresponds to an interval of elevated water contents in the clayey silt mud below the tan carbonate bed. MV measurements increase in proportion with effective overburden to 500 cm. At 500 cm, there is a sharp increase in values indicating a possible change in geologic history. The minimum *FS>5* occurs below the tan carbonate at 422 cm. At this depth there is an interval of relatively low shear strength, high water content and a *LI>2*.

8.5 Piston Core 20130290077

8.5.1 Introduction

Piston core 20130290077 was collected off the northern coast of Baffin Bay near Alexander Bank, at a water depth of 1153 m and a slope angle of 0.78º (Figure 8.20), determined from GEBCO bathymetry. The core recovered 649 cm of sediment.

8.5.2 Atterberg Limits

Atterberg limit tests were completed on nine samples (Figure 8.21). The samples range from low to very high plasticity. The liquid limits range from 19.7 to 64.6%, and the plastic limits range from 13.4 to 30.9%. The plasticity indexes range from 6.3 to 41.7% (Table 8.14). One sample at a depth of 142-152 cm plots in Zone A.

8.5.3 Consolidation Test Results

A consolidation test was conducted on one undisturbed sample at a core depth of 613-615.5 cm (Figure 8.22). The compressibility is low with a C_c value of 0.3 and a C_r value of 0.03. The hydraulic conductivity (k) at the void ratio equivalent to the P'_c is 1.83E-07 cm/sec. The consolidation test characterize the sediments as underconsolidated with respect to the effective overburden, with an *OCR* value of 0.6 (Table 8.15).

8.5.4 Triaxial Test Results

An isotopic CU triaxial tests was conducted on one sample at a core depth of 598-610 cm (Figure 8.23). The Mohr-Coulomb failure envelope is defined by an effective friction angle (ϕ') of 25.8° and an effective cohesion value (c') of 2.2 kPa. The pore pressure coefficient at failure (A_f) is 0.56. The *S* ratio is 0.28 (Table 8.16).

8.5.5 Slope Stability

The *FS* was calculated at slope angles of 0.8°, 1°, 5°, 10°, 15° and 20° (Figure 8.24). The slope is stable under static conditions with a minimum *FS* of 15.9 at a core depth of 590 cm. The critical height, critical slope angle and minimum acceleration coefficient are 100.9 m, 12.8° and 0.09 (Table 8.17).

8.5.6 Geotechnical Profile

The sediment consists of a clayey silt mud with two glacially derived tan carbonate beds. Gravitational compaction is the dominant feature in this core, except in the tan carbonate intervals where there is a clear break in depositional sequence and change in physical properties. The abrupt changes in bulk density suggest rapid onset or offset of glacial ice sheets. The clear breaks occur at approximately 125, 160, 180, and 215 cm (Figure 8.25).

The uppermost stratum consists of a postglacial hemipelagic mud. The hemipelagic mud provides an excellent example of gravitational compaction with a linear increase in bulk density and a corresponding decrease in water content. There is a sharp increase in bulk density at 125 cm, corresponding to a 35 cm thick tan carbonate bed. From 160 to 180 cm, there is a silty clay mud of a similar bulk density to the hemipelagic mud above. A sharp increase in bulk density at 180 cm corresponds to a 35 cm thick tan carbonate bed. Below 215 cm the core consists of a laminated silty clay mud with occasional sand lenses corresponding to a moderately variable density profile.

The grain size fractions are uniform with equal parts silt and clay, except in the tan carbonate mud where the sand content increases to approximately 30%. With few exceptions, the water content decreases with depth. A significant change is noticed in the tan carbonate interval where a drop in water content is accompanied by a decrease in plasticity to low plastic silts and clays. The *LI* suggests the sediments are underconsolidated near the surface becoming normally consolidated with depth ($LI<1$).

A consolidation test at 613 cm suggests the sediments are underconsolidated with an *OCR* value of 0.6. MV measurements increase in proportion with effective overburden to a depth of 500 cm and decrease with depth to the base of the core. The MV measurements plot within or above the *S* values.

The decrease in shear strength at the base of the core may be attributed to coring disturbance. The minimum *FS>15* occurs at the base of the core; however, the core is stable.

8.6 Piston Core 20130290082

8.6.1 Introduction

Piston core 20130290082 was collected from the slope seaward of Disko Bugt, at a water depth of 1352 m and a slope angle of 0.72º (Figure 8.26), determined from GEBCO bathymetry. The core recovered 643 cm of sediment.

8.6.2 Atterberg Limits

Atterberg limit tests were completed on seven samples (Figure 8.27). The samples range from low to high plasticity. The liquid limits range from 27.6 to 53.0% and the plastic limits range from 16.9 to 25.0%. The plasticity index ranges from 10.7 to 28.1% (Table 8.18). Two samples at depths of 470-475 cm and 533-543 cm plot in Zone A, and two samples at depths of 180-185 cm and 339-344 cm plot in Zone B.

8.6.3 Consolidation Test Results

Consolidation tests were conducted on three samples at core depths of 182-184.5 cm, 343-345.5 cm and 489-491.5 cm (Figure 8.28). The compressibilities are moderate with C_c values of 0.7, 0.5 and 0.6 and C_r values of 0.5, 0.4 and 0.4. The hydraulic conductivities (k) at the void ratio equivalent to the P'_c are 9.47E-08 cm/sec and 3.84E-07 cm/sec. The hydraulic conductivity at 182-184.5 cm was not determined due to a software issue resulting in the delay of load application. The consolidation tests characterize the sediments as slightly underconsolidated to normally consolidated with respect to the overburden with *OCR* values of 1.0, 0.8 and 1.1 (Table 8.19).

8.6.4 Triaxial Test Results

Isotopic CU triaxial tests were conducted on 2 samples at a core depth of 188-196 cm and 478-486 cm (Figure 8.29). The Mohr-Coulomb failure envelopes are defined by an effective friction angle (ϕ') of 30.3° and effective cohesion values (c') of 0.0 kPa and 1.6 kPa. The pore pressure coefficients at failure (A_f) are 0.50 and 0.70. The *S* ratios are similar at 0.26 and 0.29 (Table 8.20).

8.6.5 Slope Stability

The *FS* was calculated at slope angles of 0.7°, 1°, 5°, 10°, 15° and 20° (Figure 8.30). The slope is stable under static conditions with a minimum *FS* of 15.5 at a core depth of 645 cm. The critical height, critical slope angle and minimum acceleration coefficient are 113.7 m, 11.4° and 0.10 (Table 8.21).

8.6.6 Geotechnical Profile

The sediment consists of a massive clayey silt with two glacially derived tan carbonate beds. Gravitational compaction is the dominant feature in this core with a linear increase in bulk density and a corresponding decrease in water content. The tan carbonate beds at depths of ~220 cm and 285 cm are less defined in lithology and bulk density than those along the Baffin shelf (Figure 8.31).

The uppermost stratum consists of a postglacial hemipelagic mud to 220 cm overlying a 45 cm thick tan carbonate mud. From 265 to 285 cm is a silty clay mud, which appears to be equivalent to the low density, silty clay mud underlying the uppermost tan carbonate interval in cores 0075 and 0077. From 365 cm to the base of the core is a silty clay mud with occasional shell beds corresponding to a variable density.

The grain size fractions have a higher percent silt relative to the Baffin coast with up to 30% sands at the top and base of the core. The water contents and plasticity generally decrease with depth. The *LI* is

constant down core between, remaining between 2 and 3, suggesting underconsolidation. The consolidation tests indicate the sediments are slightly underconsolidated to normally consolidated with *OCR* values between 0.8 and 1.1.

MV measurements increase in proportion to effective overburden to a depth of 500 cm where there is an increase followed by a decrease in shear strength. MV measurements occur slightly above or within the *S* values with the exception of the high strength measurement at 510 cm. This measurement is likely due to an abundance of shells, which occur at the same depth. The drop in shear strength measurements may be attributed to coring disturbance. The core is stable with a minimum $FS>15$ at a depth of 645 cm.

9.0 Geotechnical units

9.1 Introduction

A comprehensive geotechnical characterization was carried out on five piston cores from Baffin Bay using sediment lithology and geotechnical data. The lithology and geotechnical data established six geotechnical units. Campbell et al. (2017) and Jenner et al. (2018) identified several lithofacies from cores collected in a regional stratigraphic survey of Baffin Bay. The relevant lithofacies for this study include: glacial diamicton (L1), laminated red brown mud (L2), carbonate-rich ice rafted debris (L3), hemipelagic mud (L4) and blocky mass transport deposit (L5). The lithofacies for the five geotechnical cores are presented in Figure 9.1. Slight differences in depositional processes within the same lithofacies has resulted in a variation of some geotechnical properties within the same unit. This results in the lithofacies being subdivided into two geotechnical subunits.

Initially, MSCL bulk density and lithology profiles were used to identify trends in the down core profiles (Figure 9.2). Three geotechnical units were correlated to a lithology (Jenner et al., 2018; Campbell et al. 2017) and linked to a geologic process with a well-defined trend in bulk density. The sediments that group in this category are: postglacial Holocene hemiplegic mud (L4) defined as Unit 1, the glacially-derived tan carbonate mud (L3) defined as Unit 2, the glacially-derived diamicton (L1) defined as Unit 6A, and the mass transport deposit (L5) defined as Unit 6B (Figure 9.2).

Geotechnical Units 3, 4 and 5 occur within lithofacies 2. Unit 3 is defined by an abrupt change in density from an otherwise increasing profile. This results in a "U" shape trend in the down core density profile (Figure 9.2). Geotechnical Units 4 and 5 are the least distinct of the 6 geotechnical units. Unit 5 is characterized by low plasticity (Figure 9.3) and activity (Figure 9.4). Unit 4 is distinguished from Unit 5 by its higher plasticity and from Unit 3 by its higher density. A summary of the physical properties, compressibility and strength parameters for each geotechnical unit are presented in Tables 9.1 and 9.2.

9.2 Geotechnical Units

9.2.1 Unit 1A and 1B

Unit 1 coincides with the Late Pleistocene and Holocene bioturbated brown mud (L4) (Campbell et al, 2017). X-ray images show the sediment is a massive, hemiplegic mud with a moderate to high degree of bioturbation. Unit 1 was subdivided into Unit 1A and Unit 1B. Unit 1A is identified along the Baffin shelf in cores 0060, 0075 and 0077. The type section appears in core 0075 from 0 to 285 cm. Unit 1B is identified exclusively on the Greenland shelf in core 0082 from 0 to 220 cm (Figure 9.5).

The similarities in geotechnical properties include clay mineralogy and MV measurements. The clay mineralogy of Unit 1A and 1B are inactive with a value of 0.68 (Figure 9.6), comparable to weald

clays of 0.50 to 0.75 (Skempton, 1953). An outlier exists in core 0075, where the activity is 1.22. MV measurements show a general linear increase with depth and plot slightly above the *S* values in the zone of apparent overconsolidation.

The differences in geotechnical properties between Unit 1A and 1B are attributed to coarser sediments along the Greenland margin, where the silt content is approximately 30% higher. This is reflected by lower plasticity, water contents and compressibility, and higher density and friction angles.

Unit 1A – Holocene (East Baffin Island Margin)

Unit 1A is characterized by clays of high (CH) to extremely high (CE) plasticity (Figure 9.7). The liquid limits range between 59% and 99%, and the plastic limits range between 26% and 32%. Average values are *LL*=75, *PL*=29. There is a noticeable change in *LL* with depth, corresponding to a decrease in water content from approximately 200 to 100%. MSCL bulk densities are well defined with a linear increase with depth from 1.3 to 1.6 g/cm^3.

A consolidation test from core 0075 characterizes Unit 1A as slightly overconsolidated with an *OCR* value of 1.2. The compressibility of 1.1 is comparable to Swedish medium sensitive clays (Holtz and Kovacs, 1981). The Mohr-Coulomb failure criteria, measured from a CIU triaxial test in core 0075, are 18.9° and 0.0 kPa. The pore pressure coefficient at failure A_f is 0.64, typical of normally consolidated sediments. The *S* ratio is 0.19.

Unit 1B – Holocene (West Greenland Margin)

Unit 1B is predominantly characterized by clays of medium (CI) plasticity, with one sample plotting in Zone B (Figure 9.7). The liquid limits range between 40% and 53%, and the plastic limits range between 19% and 25%. Average values are *LL*=45, *PL*=22. Bulk densities show a general increase

with depth from 1.4 to 1.7 g/cm^3 with a corresponding decrease in water contents from approximately 110 to 60%.

A consolidation test characterizes Unit 1B as normally consolidated with an *OCR* value of 1.0. The compressibility of 0.7 is comparable to San Francisco bay mud (Holtz and Kovacs, 1981). The Mohr-Coulomb failure criteria, measured from a CIU triaxial test, are 30.3° and 0.0 kPa. At failure, the pore pressure coefficient A_f is 0.50, typical of slightly overconsolidated sediments. The *S* ratio is 0.26.

9.2.2 Unit 2

Unit 2 coincides with glacially derived tan carbonate sandy mud containing subangular to angular IRD (>2 mm), representing lithofacies 3 (Campbell et al, 2017). Unit 2 appears in all five cores with up to 60% clays, 60% silts and 30% sands. In cores 0060, 0075 and 0077, Unit 2 is thicker and well defined with distinct, sharp changes in bulk density. These thicker, well-defined beds form from rapid melting, plume deposition and ice-rafting from the glacial front (Jenner et al, 2018). The type section is in core 0060 from approximately 20 cm to 130 cm (Figure 9.8).

Unit 2 is characterized by silts and clays of low plasticity (ML & CL) and plot within Zones A and B (Figure 9.9). The liquid limits range between 18% and 34%, and the plastic limits range between 12% and 19%. Average values are *LL*=23, *PL*=14. The clay minerals are inactive with a value of 0.22 (Figure 9.10), comparable to activity of mica at 0.23 (Skempton, 1953). The bulk densities from the Baffin shelf are noticeably high, averaging 2.0 g/cm^3. The bulk densities from the Greenland shelf are less pronounced and average 1.7 g/cm^3. The water contents show an inverse relationship to the bulk densities with lower values on the Baffin shelf and higher values on the Greenland shelf.

One consolidation test from core 0082 characterizes Unit 2 as slightly underconsolidated with an *OCR* value of 0.8. The compressibility of 0.5 is comparable to that of Boston blue clays (Holtz and Kovacs, 1981). No triaxial testing was conducted on sediments from Unit 2. Limited MV measurements show an increase with depth, plotting between or slightly above the *S* values.

The distinct, sharp changes in bulk density suggest a rapid change in depositional environment marking the onset and offset of ice sheets. The interbedded nature of the tan carbonate beds in core 0075, from 390 and 430 cm (Figure 9.8), suggest oscillating ice sheets and a complex stratigraphy.

9.2.3 Unit 3

Unit 3 occurs in all five cores as a homogeneous silty clay deposit underlying tan carbonate or diamicton beds. Unit 3 is identified as a laminated red brown mud and represents lithofacies 2 (Campbell et al, 2017). Unit 3 consists of up to 70% clays, 50% silts and less than 5% sands. The type section appears in core 0060 from approximately 330 to 445 cm (Figure 9.11).

Unit 3 is characterized by clays of medium (CI) to very high (CV) plasticity (Figure 9.12). The liquid limits range between 44% and 73%, and the plastic limits range between 22% and 31%. Average values are *LL*=58, *PL*=26. The clay minerals are inactive with a value of 0.65 (Figure 9.13), comparable to kaolinite minerals at 0.63 (Skempton, 1953). An outlier exists in core 0075 where the activity is 1.67. The MSCL bulk densities are uniform or increase slightly with depth and average approximately 1.6 g/cm^3. Water content measurements are limited, but show little variation with depth and range between 60 to 110%. MV measurements generally plot above the *S* values with little variability. In core 0048 the MV measurements are noticeably higher than the *S* values.

Consolidation tests characterize Unit 3 as normal to slightly underconsolidated, with *OCR* values of 0.8 and 0.9. The compressibilities are 1.1 and 0.7, comparable to Swedish sensitive clays (Holtz and

Kovacs, 1981). The Mohr-Coulomb failure criteria, measured from two CIU triaxial tests, provides a reasonably consistent set of results with internal angles of friction of 22.3º and 25.6° and cohesion of 2.2 kPa and 2.3 kPa. At failure the pore pressure coefficient A_f values are 0.54 and 0.63, typical of normally consolidated sediments. The *S* ratios are 0.26 and 0.25.

9.2.4 Unit 4

Unit 4 occurs as a stratified silty clay with sand layers and IRD. Unit 4 is identified as a laminated red brown mud and represents lithofacies 2 (Campbell et al, 2017). Grain size fractions consist of up 60% clays, 60% silts and 10% sands. Unit 4 is identified in cores 0048, 0075 and 0077. The type section appears in core 0077 from 215 cm to the base of the core (Figure 9.14).

Unit 4 is characterized by clays of medium (CI) to high (CH) plasticity (Figure 9.15). The liquid limits range between 42% and 53%, and the plastic limits range between 19% and 24%. Average values are *LL*=48, *PL*=21. The clay minerals are inactive with a value of 0.56 (Figure 9.16), comparable to weald clays of 0.50 to 0.75 (Skempton, 1953). MSCL bulk densities are moderately variable and increase with depth, averaging 1.83 g/cm^3. Water contents generally decrease with depth and range between 42 to 78%. MV measurements plot within or above the *S* values.

A consolidation test from the base of core 0077 characterizes Unit 4 as underconsolidated with an *OCR* value of 0.6. The compressibility of 0.3 is comparable to normally consolidated medium sensitive clays (Holtz and Kovacs, 1981). The Mohr-Coulomb failure criteria, measured from a CIU triaxial test, are 25.8° and 2.2 kPa. At failure, the pore pressure coefficient A_f is 0.56, typical of normally consolidated sediments. The *S* ratio is 0.28.

9.2.5 Unit 5A and 5B

Unit 5 occurs as a massive clayey silt with minor sands and IRD and is subdivided into Unit 5A and Unit 5B. Unit 5A is identified exclusively on the Baffin shelf in core 0048 from 0 to 140 cm, 175 to 210 cm and 385 to 725 cm. The uppermost interval contains considerably more IRD than the deeper intervals. Unit 5B is identified exclusively on the Greenland shelf in core 0082 from approximately 365 cm to the base of the core. The type unit appears in core 0048 between 385 to 725 cm (Figure 9.17).

The similarities include the activity, stress state and compressibility. The clay minerals of Unit 5A and 5B are inactive with a value of 0.39 and 0.44 (Figure 9.18), comparable to kaolinite minerals at 0.33 to 0.46 (Skempton, 1953). The differences in geotechnical properties between Unit 5A and 5B are attributed to coarser sediments in core 0082, where the sand content is approximately 25% higher. This is reflected by lower plasticity and higher friction angles.

Unit 5A – East Baffin Island Margin

Unit 5A is characterized by clays of low (CL) to medium (CI) plasticity and plot within Zone B (Figure 9.19). The liquid limits range between 29% and 40%, and the plastic limits range between 16% and 21%. Average values are *LL*=35, *PL*=18. Grain size fractions consist of up to 50% silt, 45% clay and 5% sands. MSCL bulk densities are moderately variable and range between 1.75 and 2.0 g/cm^3 with no apparent trend with depth. Water contents range between approximately 48 to 69% and show no trend with depth. MV measurements increase in variability with depth, but typically fall within the boundaries of *S* values.

Consolidation tests characterize Unit 5A as normal to slightly overconsolidated with *OCR* values of 1.0 and 1.2. The compressibilities are 0.6 and 0.7 and are comparable to San Francisco bay mud (Holtz

and Kovacs, 1981). The Mohr-Coulomb failure criteria, measured from a CIU triaxial test, are 24.9° and 5.0 kPa. At failure, the pore pressure coefficient A_f is 0.48, typical of overconsolidated sediments. The *S* ratio is 0.27.

Unit 5B – West Greenland Margin

Unit 5B is characterized by clays of low (CL) plasticity and plot within Zone A (Figure 9.19). The liquid limits range between 28% and 29%, and the plastic limits range between 17% and 18%. Average values are *LL*=28, *PL*=17. Grain size fractions consist of up to 60% silt, 30% clay and 30% sands. MSCL bulk densities are moderately variable and increase from 1.75 to 2.2 g/cm^3. Water contents generally decrease with depth from ~70 to 40%. MV measurements show little variability and correlate well with *S* values.

A consolidation test characterizes Unit 5B as normally consolidated with an *OCR* value of 1.1. The compressibility is 0.6, comparable to San Francisco bay mud (Holtz and Kovacs, 1981). The Mohr-Coulomb failure criteria, measured from a CIU triaxial test, are 30.3° and 1.6 kPa. At failure, the pore pressure coefficient A_f value is 0.70, typical of normally consolidated sediments. The *S* ratio is 0.29.

9.2.6 Unit 6A and 6B

Unit 6 was subdivided into Unit 6A and 6B. Unit 6A is identified in core 0060 as a dark grey-brown diamicton and represents glaciogeninc debris flow deposits of lithofacies L1 (Jenner et al, 2018). Unit 6B is identified in core 0075 at the lower part of the core and appears as inclined (tilted) laminated mud interpreted as an intact block of a blocky mass transport deposit (L5) (Figure 9.20). Unit 6A and 6B have similar geotechnical properties despite having different modes of deposition.

The similarities in geotechnical properties include plasticity, clay mineralogy, compressibility, strength parameters and MV measurements. Unit 6 is characterized by clays of medium plasticity (CI), with one sample plotting in Zone B (Figure 9.21). The liquid limits range between 38% and 50%, and the plastic limits range between 18% and 21%. Average values are *LL*=44, *PL*=20 for Unit 6A and *LL*=40, *PL*=18 for Unit 6B. The clay minerals are inactive with a values of 0.49 and 0.57 (Figure 9.22), comparable to weald clays of 0.50 to 0.75 (Skempton, 1953). The compressibility from two consolidation tests are 0.3, comparable to Chicago silty-clays (Holtz and Kovacs, 2011). The Mohr-Coulomb failure criteria, measured from two CIU triaxial tests, provide internal angles of friction of 23.8º and 24.3° and cohesion values of 6.8 kPa and 9.4 kPa for Unit 6A and 6B. At failure the pore pressure coefficient A_f values are 0.36 and 0.45, typical of overconsolidated sediments. The *S* ratio is 0.32 for both units. MV measurements show an offset from the down core profile and plot well above the *S* values.

The differences in geotechnical properties between Unit 6A and 6B are attributed to the different modes of deposition. Unit 6A is a glacially-derived mass transport deposit, while Unit 6B is a more typical submarine landslide. This is reflected by differences in the MSCL bulk density, grain size, water content and stress history.

Unit 6A – Glacially derived diamicton

Unit 6A consists of 33% silt, 48% clay, 14% sands and 5% gravel. The MSCL bulk density measurements are uniform and range from 1.75 to 2.1 g/cm^3, with an average of 1.85 g/cm^3. Water content measurements from core 0060 are similar and average a value of 35.5%. A consolidation test from Unit 6A, characterizes this sediment as overconsolidated, with an *OCR* value of 2.2.

Unit 6B – Blocky mass transport deposit

Unit 6B consist of 49% silt, 39% clay and 12% sand. In core 0075, bulk densities oscillate between 1.8 to 2.3 g/cm^3, with an average of 1.96 g/cm^3. Water content measurements decrease with depth from ~50 to 35% and average 40.2%. A consolidation test from Unit 6B characterizes this sediment as normal to slightly underconsolidated, with an *OCR* value of 0.9.

10.0 Summary

The GSC-A collected 28 piston cores onboard the CCGS Hudson during expedition 2013029 as part of a geohazard assessment of Baffin Bay. A comprehensive geotechnical testing program was carried out on five of the 28 cores. Four of the cores were selected from the western shelf of Baffin Island between Scott Trough and Qikiqtarjuaq, approximately 628 km apart, and one core was selected from the Greenland shelf near Disko Bugt. The cores penetrated depths of 5 to 8 meters below the seafloor at slope angles between 0.72 and 3.83 degrees.

Geotechnical testing included MSCL bulk density, Atterberg limits, grain size analysis, MV undrained shear strength, back-pressured consolidation tests and isotropically consolidated (CIU) triaxial tests. The plasticity was determined for 41 samples. The plasticity chart (Figure 9.3) shows the sediments range from low to extremely high plasticity and plot on or above the A-line. Eight samples plot as potentially liquefiable (Zone A) as described by Seed et al. (2003). The activity was determined for 41 samples. The majority of the sediments plotted as inactive clays. The data from eleven consolidation tests indicate the sediments are normally consolidated, with the exception of core 60 where the sediment are overconsolidated and core 77 where the sediments are underconsolidated. The data from nine triaxial tests give a range of friction angles between 18.9 to 30.3° and cohesion values between 0.0 to 9.4 kPa. Slope instability was determined for each of the five cores using the infinite slope method. The results indicate the slopes are statically stable within the upper 10 m.

The geotechnical data and lithology were compiled into profiles where the various soil properties are presented as a function of depth. The geotechnical profiles were used to establish six geotechnical units using the lithology, MSCL bulk density and the Atterberg limits. Slight differences in depositional processes within the same lithofacies has resulted in a variation of some geotechnical properties within the same unit. This has resulted in subdivision of some geotechnical units.

References

Aksu, A.E. and Piper, D.J.W. 1987. Late Quaternary sedimentation in Baffin Bay. Can. J. Earth Sci., 24, 1833-1846.

ASTM Standard D422, 1963 (2007)e. Particle-Size Analysis of Soils. ASTM International, West Conshohocken, PA, 2013, DOI: 10.1520/D0422-63R07.

ASTM Standard D2216. (2010). Laboratory Determination of Water (Moisture) Content of Soil and Rock by Mass. ASTM International, West Conshohocken, PA, 2013, DOI: 10.1520/D2216-10.

ASTM D2435/D2435M. (2011). One-Dimensional Consolidation Properties of Soils. Danvers: ASTM International, West Conshohocken, PA, 2013, DOI: 10.1520/D2435_D2435M-11.

ASTM Standard D2487. (2011). Classification of Soils for Engineering Purposes (Unified Soil Classification System). ASTM International, West Conshohocken, PA, 2013, DOI: 10.1520/D2487-11.

ASTM Standard D4318 (2010). Liquid Limit, Plastic Limit, and Plasticity Index of Soils. ASTM International, West Conshohocken, PA, 2013, DOI: 10.1520/D4318-10.

ASTM Standard D4648/D4648M, (2010). Laboratory Miniature Vane Shear Test for Saturated Fine-Grained Clayey Soil. ASTM International, West Conshohocken, PA, 2013, DOI: 10.1520/D4648-10.

ASTM Standard 4767 (2011). Consolidated Undrained Triaxial Compression Test for Cohesive Soils. ASTM International, West Conshohocken, PA, 2013, DOI: 10.1520/D4767-11.

Atterberg, A. (1911). The Behaviour of Clays with Water, their Limits of Plasticity and their Degress of Plasticity. Kunglia Lantbruksakademiens Handlingar och Tidskrift, 132-158.

Bent, A.L., 2002. The 1933 M s= 7.3 Baffin Bay earthquake: strike-slip faulting along the northeastern Canadian passive margin. Geophysical Journal International, 150(3), pp.724-736.

Campbell, D.C., 2014. CCGS Hudson Expedition 2013-029, Geological Hazard Assessment of Baffin Bay and Biodiversity Assessment of Hatton Basin, August 14-September 16, 2013; Geological Survey of Canada, Open File 7594, 124 p. doi:10.4095/293694

Campbell, D.C., Jenner, K.A., Higgins, J., and Piper, D.J.W., 2017. Analysis of piston cores and high-resolution sub-bottom profiler data, Baffin Bay slope, Nunavut; Geological Survey of Canada, Open File 8135, 179 p. doi:10.4095/300835

Casagrande, A. (1936b). "The Determination of Pre-Consolidation Load and Its Practical Significance," Discussion D-34, Proceedings of the First International Conference on Soil Mechanics and Foundation Engineering, Cambridge, Vol. III, pp. 60-64.

Casagrande, A. (1932b). Research on the Atterebrg Limits of Soils. *Public Roads*, 121-136.

Casagrande, A. (1948). Classification and Identification of Soils. Transactions, *ASCE*, 901-930.

Gourvenec, S. and White, D (2010). Gulf of Guinea Deepwater Sediments: Geotechnical Properties, Design Issues and Installation Experiences. Frontiers in Offshore Geotechnics II, CRC Press, Boca Raton, 59-86.

Grozic, J.L.H., Lunne, T. and Pande, S. (2003). An oedometer test study on the preconsolidation stress of glaciomarine clays. Canadian Geotechnical Journal, 40, 857-872.

Head, K. H. (1992). Manual of Soil Laboratory Testing: Volume 1 Soil Classification and Compactions Tests (Second Edition). In Manual of Soil Laboratory Testing: Volume 1 Soil Classification and Compactions Tests, Pentech Press London, 388p.

Holtz, R.D. and Kovacs, W.D. (1981). An Introduction to Geotechnical Engineering. Prentice-Hall, Inc., Englewood Cliffs, N.J., 733 p.

Jenner, K.A., Campbell, D.C. and Piper, D.J.W., 2018. Along-slope variations in sediment lithofacies and depositional processes since the Last Glacial Maximum on the northeast Baffin margin, Canada. Marine Geology, 405, pp.92-107.

Ladd, C., DeGoot, D. (2003). Recommended practice for soft ground site characterization:Arthur Casagrande lecture, 12th Panamerican Conference on soil mechanics and geotechnical engineering, Massachusetts Institute of Technology Cambridge, June 22-25,2003, 60 pages.

Ladd, C. and Foot, R. (1974). New Design Procedure for Stability of Soft Clays, Journal of the Geotechnical Engineering Division, ASCE, vol. 100, No. GT7, pp. 763-786

Lambe, W., Whitman, R. (1969). Soil Mechanics. John Wiley & Sons, New York, 552p.

Lacasse S, Farrokh Nadim, MaartenVanneste, Jean-Sébastien L'Heureux, Carl Fredrik Forsberg and Tore J. Kvalstad (2013). Case Studies of Offshore Slope Stability Geo-Congress 2013, 2379-2417.

Poulos, H. (1988). Marine Geotechnics. Unwin Hyman Ltd., London, 473p.

Seed, R., Cetin, K. Moss, R. Kammerer, A., Wu, J., Pestana, J., Riemer, M., Sanciol, R., Bray, J., Kayen, R.,and Faris, A. (2003). Recent advances in soil liquefaction engineering. 26th Annual ASCE Los Angeles Geotechnical Spring Seminar, Long Beach, California.

Skempton, A.W. (1953). The colloidal activity of clays. Proceedings of the 3rd International Conference on Soil Mechanics and Foundation Engineering, Zurich, 1, 57-61.

Skempton, A.W. (1954). The pore pressure coefficients A and B. Géotechnique, vol. 4, 143-147.

Skempton, A. W. (1970). The consolidation of clays by gravitational compaction. Quarterly Journal of the Geological Society of London, vol. 125, 373-412.

Figure 1.1. Location map of the 5 geotechnical cores collected during cruise 2013029 (from Google Earth).

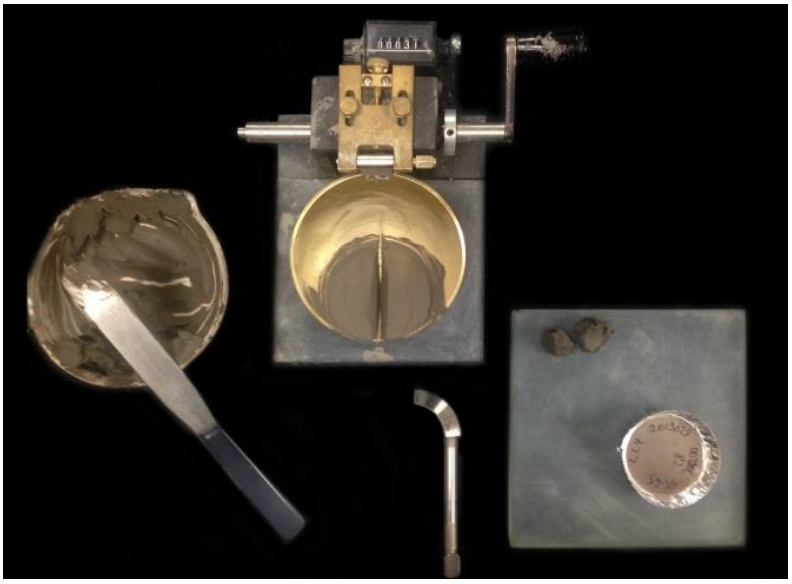

Figure 3.1. Liquid limit test apparatus.

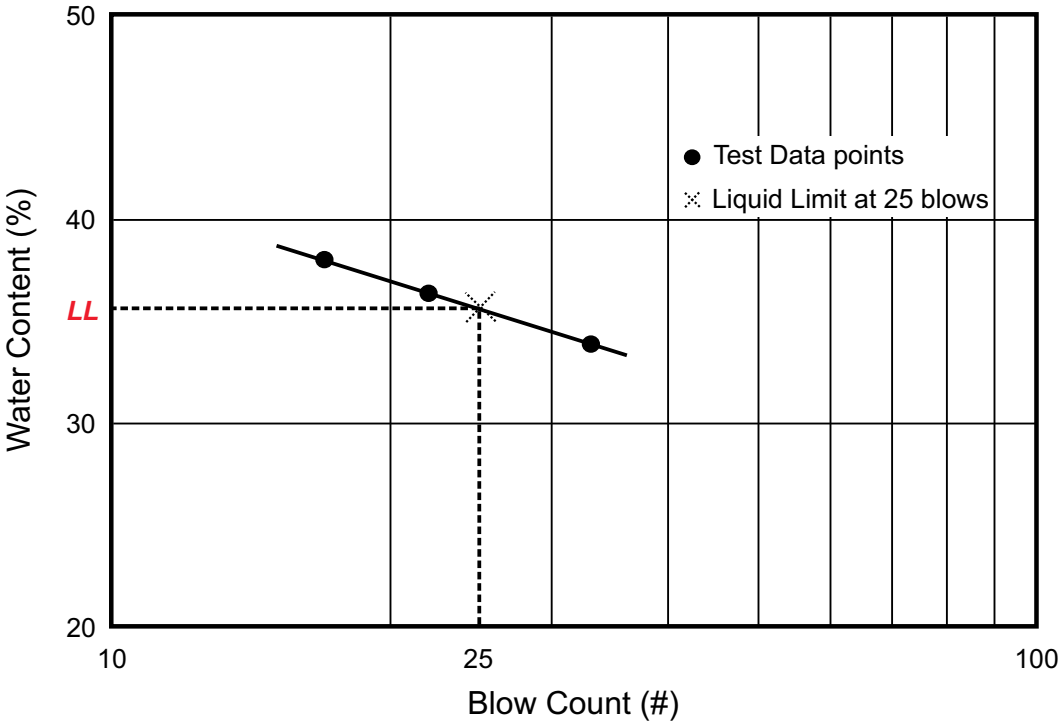

Figure 3.2. Laboratory data for determining the liquid limit of soil.

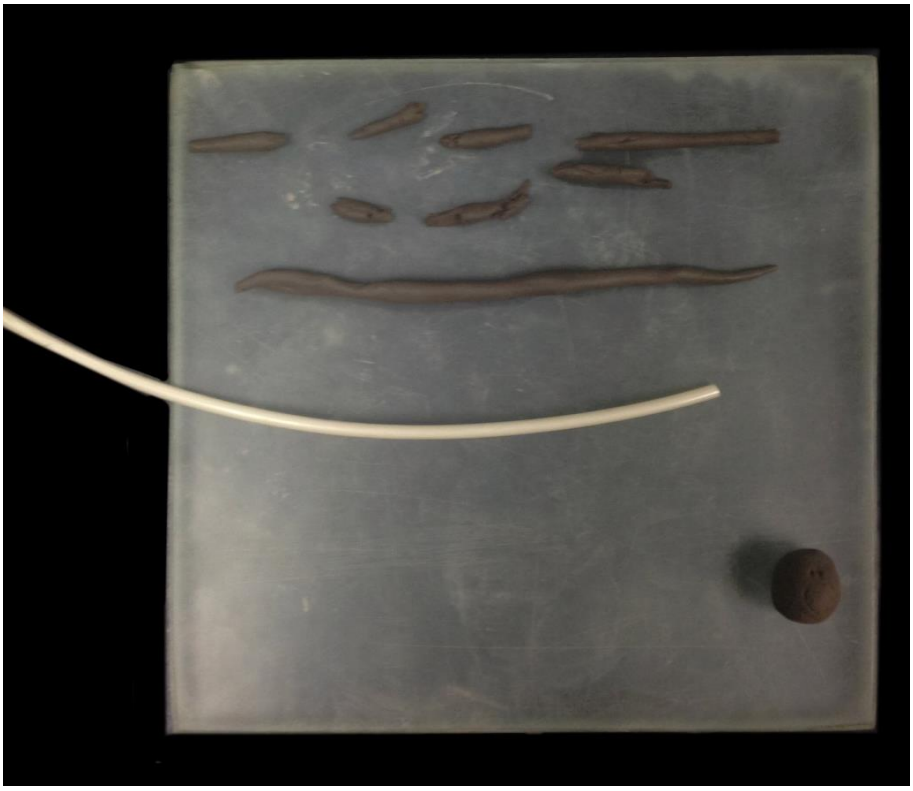

Figure 3.3. Crumbing of the soil threads at the plastic limit.

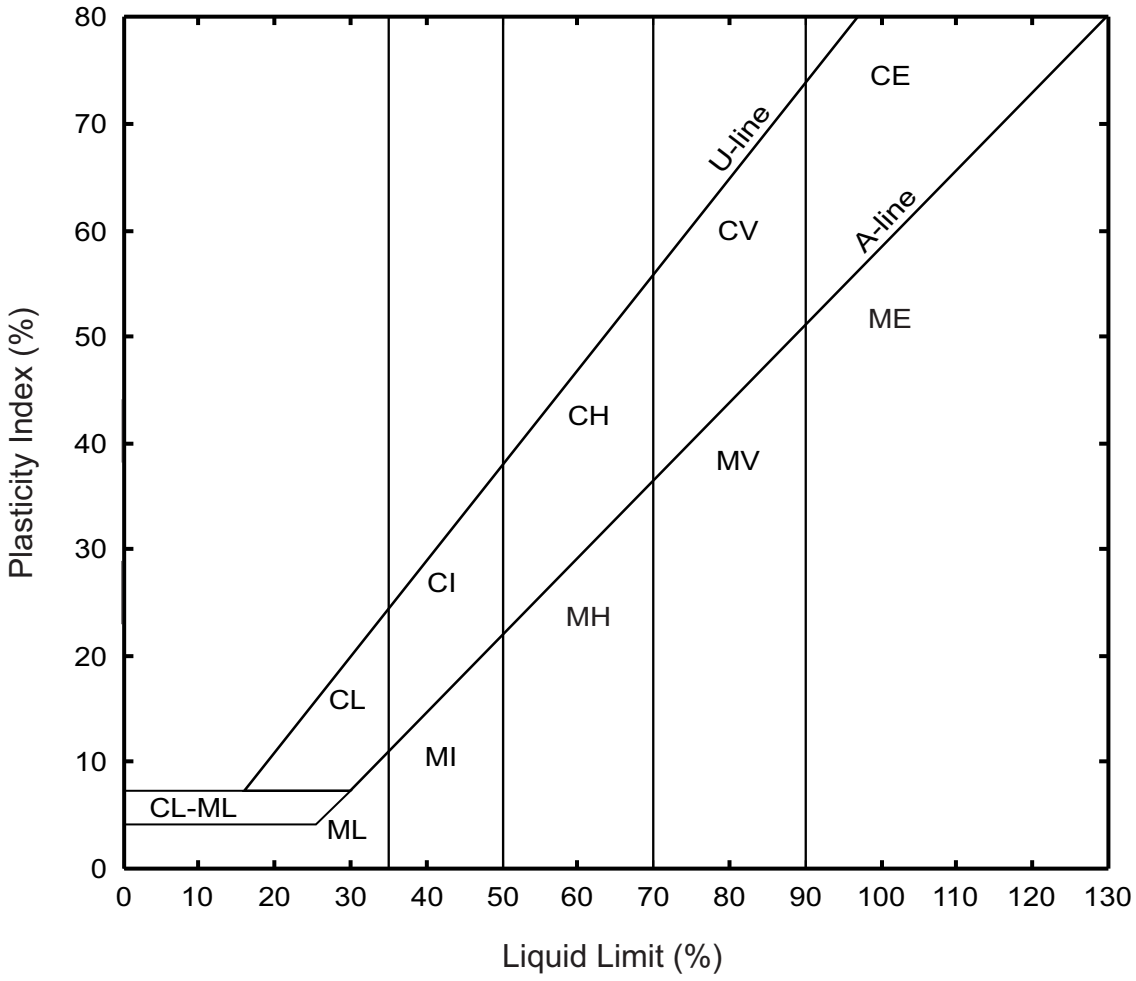

Figure 3.4. British Standard plasticity chart with A and U lines defined.

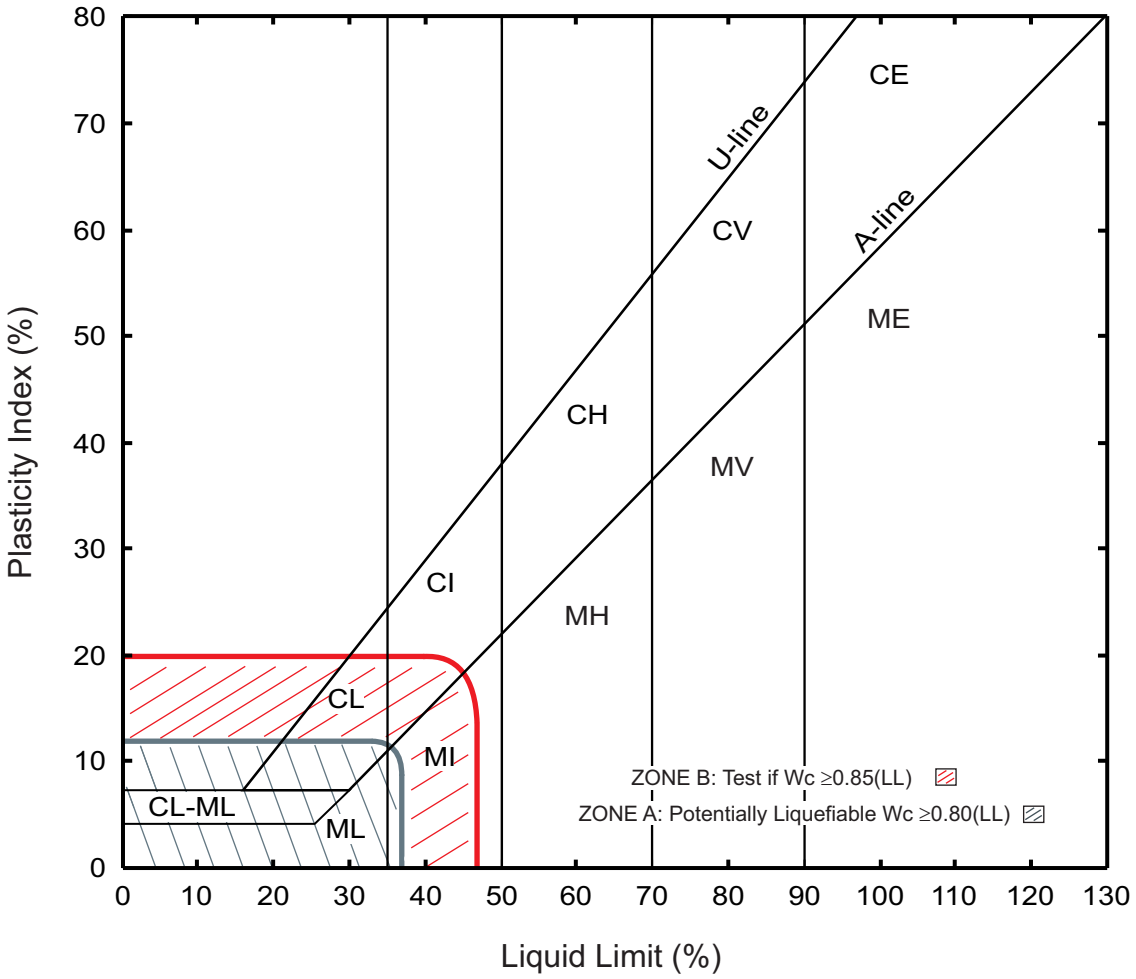

Figure 3.5. Plasticity chart with liquefaction potential zones (Seed et al., 2003).

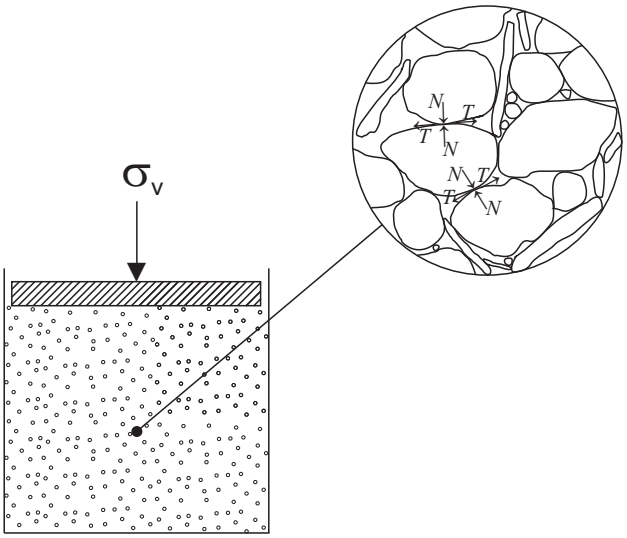

Figure 4.1. Schematic representation of normal (*N*) and tangential (*T*) force transmission through soil under an applied vertical load (σ_v) (after Lamb and Whitman, 1969).

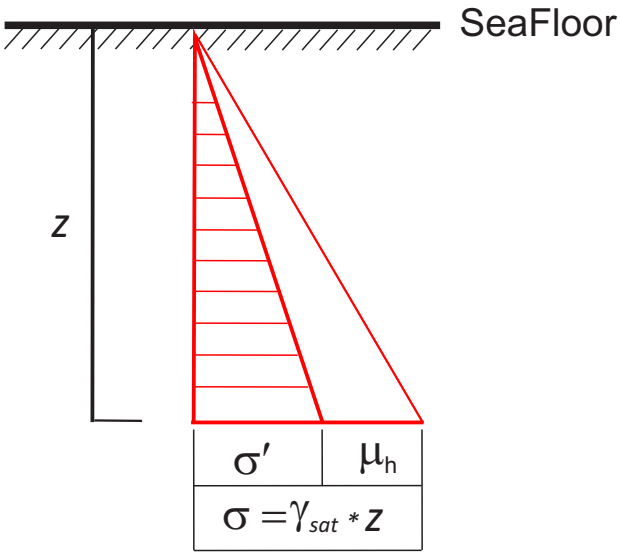

Figure 4.2. The total normal stress acting on sediment below the seafloor is a combination of effective stress and pore water pressure.

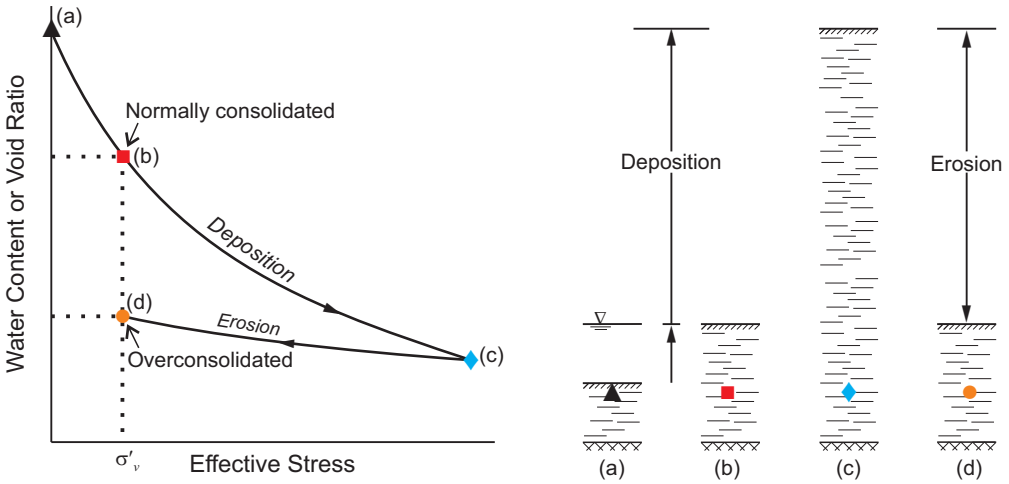

Figure 5.1. Normal and overconsolidated clays by gravitational compaction (Skempton, 1970)

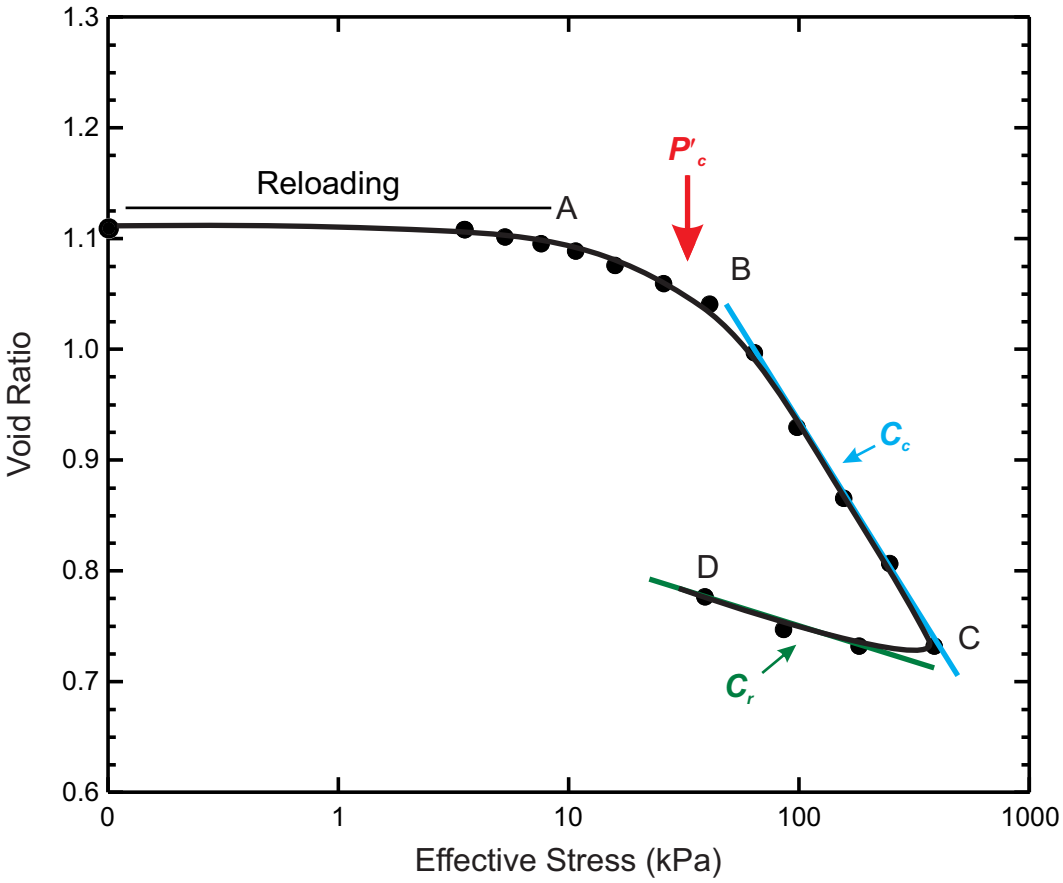

Figure 5.2. Typical consolidation e-log effective stress curve. Point A marks the end of the reloading point A to B marks the transition from reloading to new stresses, point B to C defines the virgin compression line and point C to D defines the expansion index.

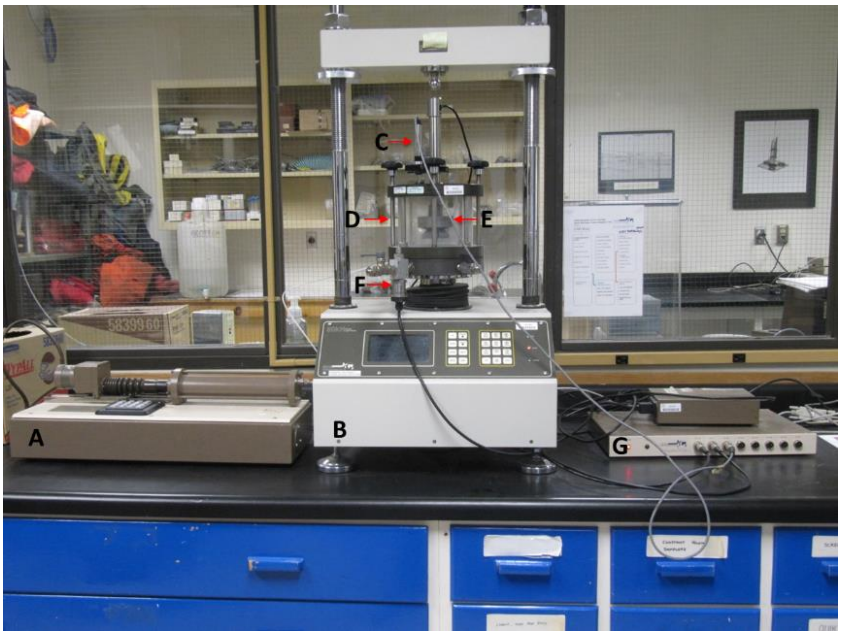

Figure 5.3. The GDS CRS consolidation system includes (A) back pressure controller, (B) 50 kN load frame, (C) axial displacement transducer, (D) CRS consolidation cell, (E) submersible load cell, (F) pore pressure transducer and (G) DAQ system.

Figure 5.4. The GDS Rowe consolidation system includes (A) back pressure controller, (B) load chamber controller, (C) Rowe consolidation cell, (D) DAQ system and (E) pore pressure transducer.

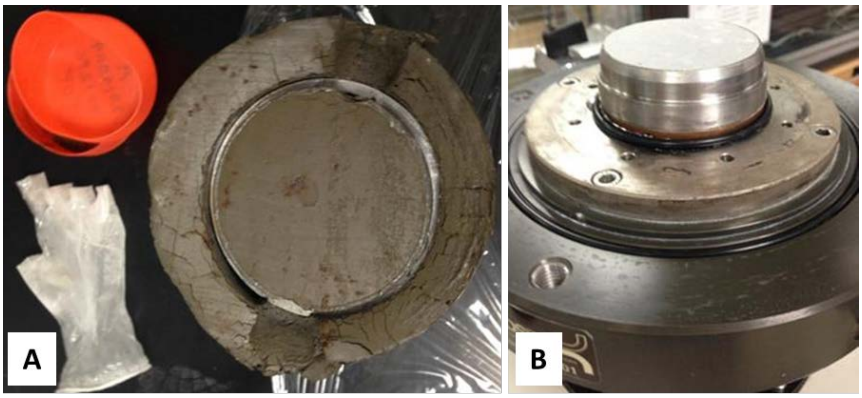

Figure 5.5. Sediment extruded into CRS consolidation ring (A) and a trimmed sample on the CRS cell base (B).

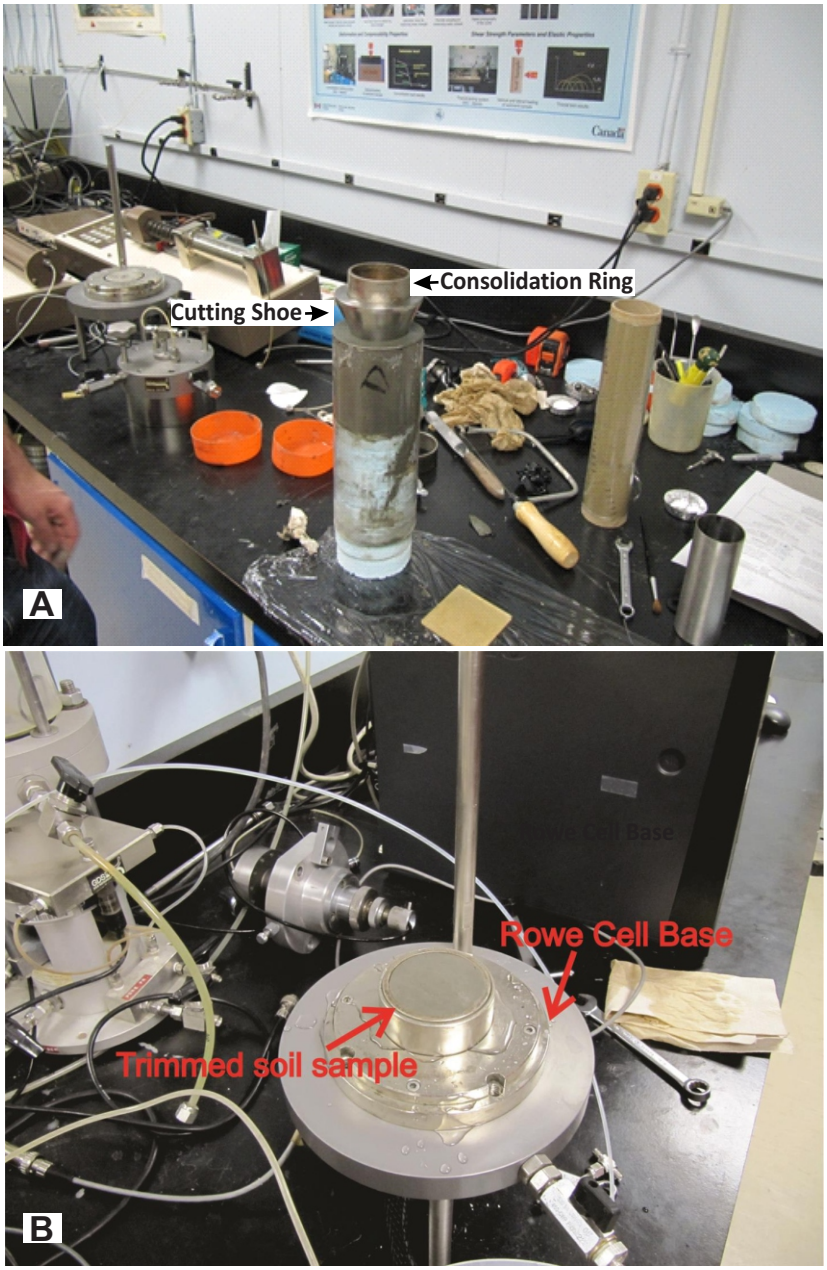

Figure 5.6. Sediment being extruded into the Rowe cell consolidation ring (A) and a trimmed sample on the Rowe cell base (B).

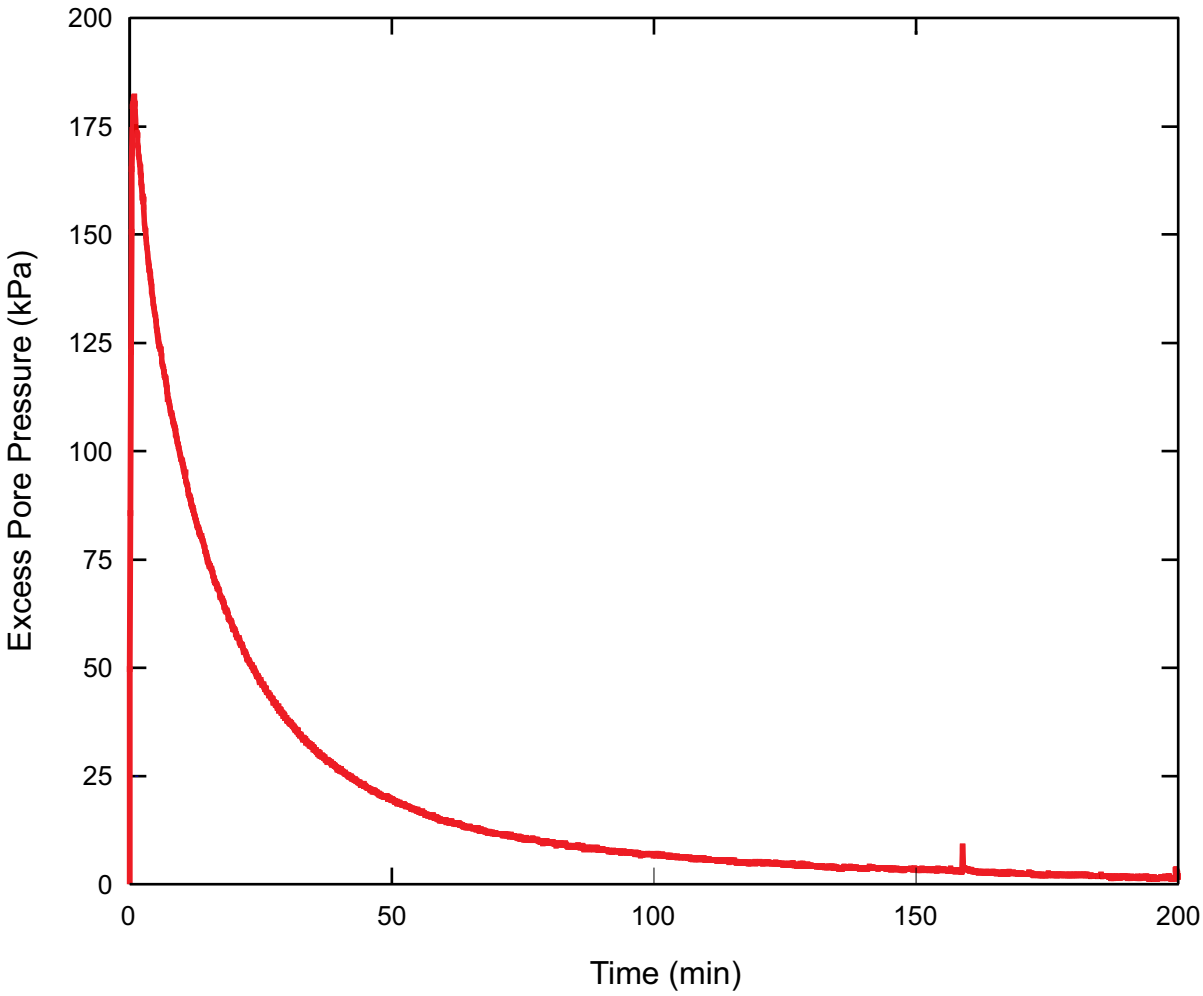

Figure 5.7 Sample pore pressure response measured at the base of the sample to a new load increment.

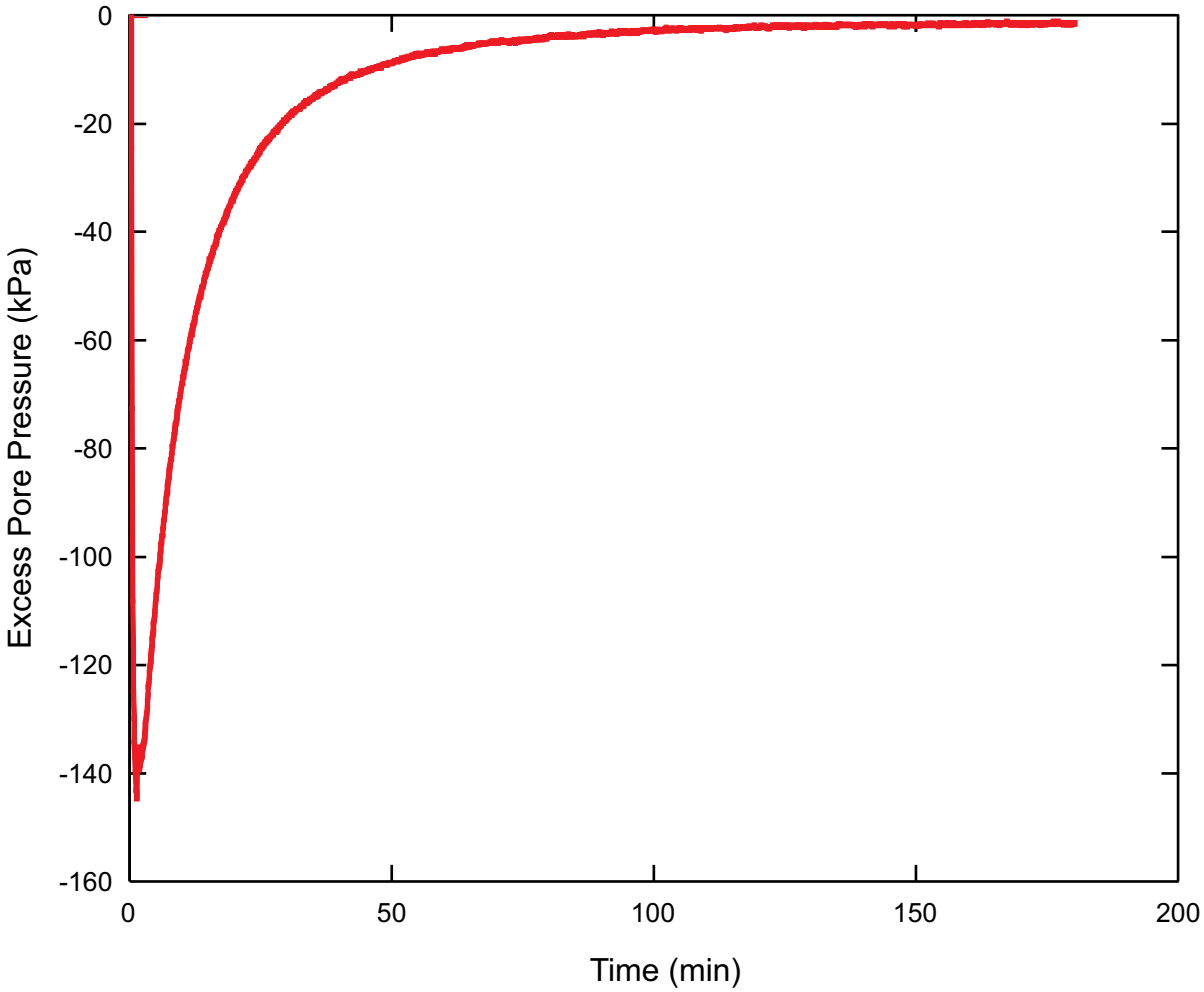

Figure 5.8. Sample pore pressure response measured at the base of the sample to a new unload increment.

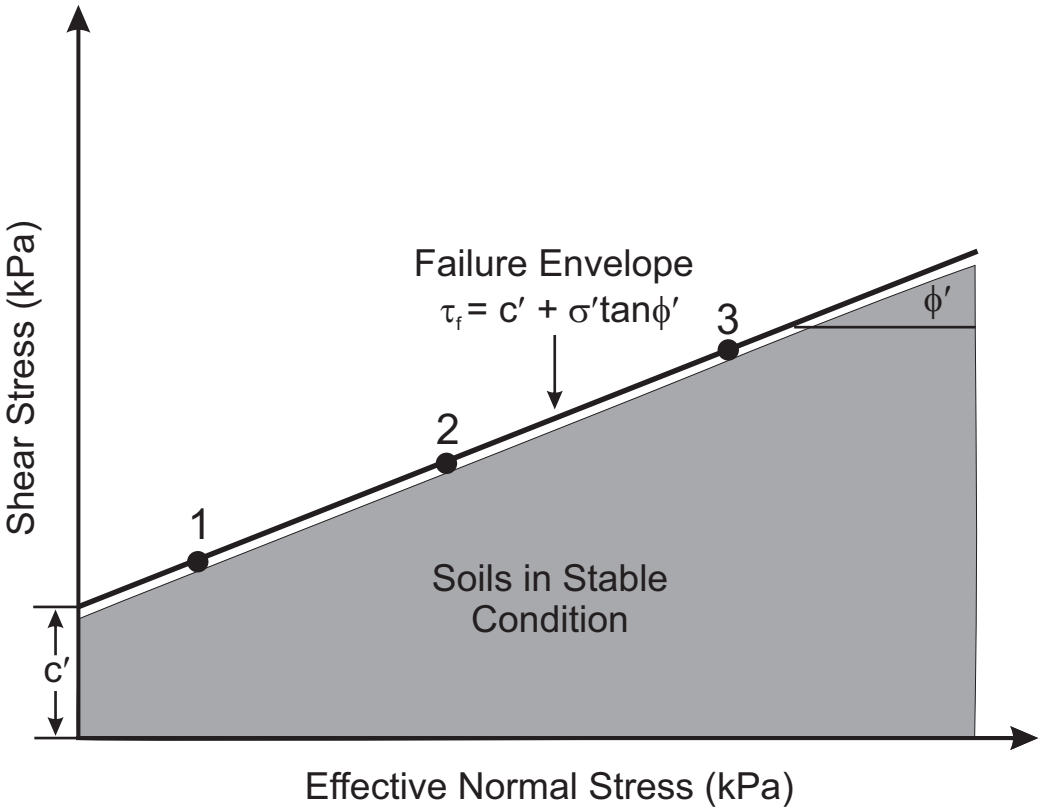

Figure 6.1. Maximum shear strength related to effective normal stress from triaxial tests.

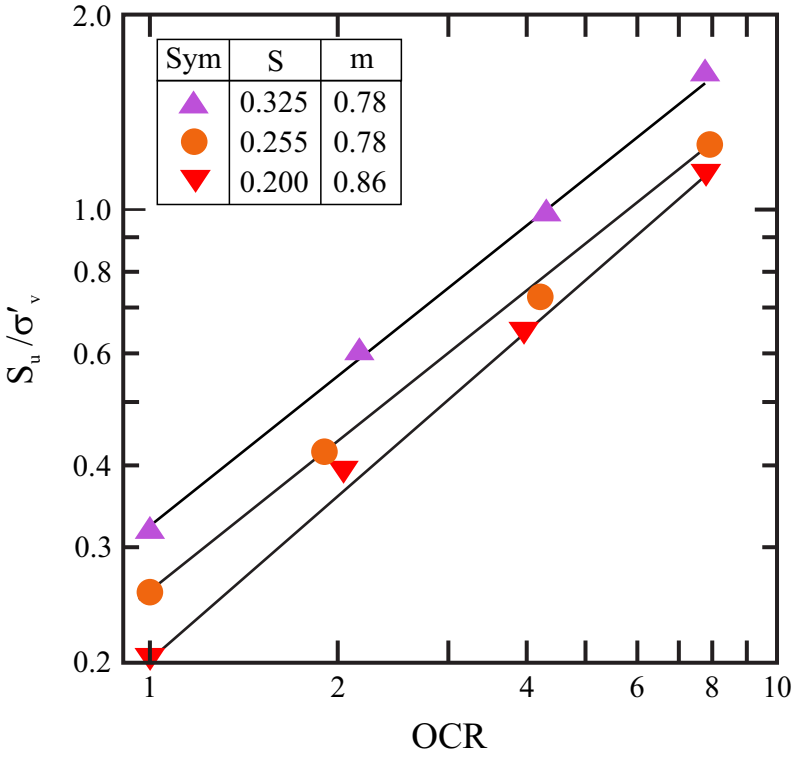

Figure 6.2. Example of a SHANSEP analysis for AGS plastic marine clay showing the OCR vs undrained strength ratio relationship (Su/σ'v) (after Ladd and DeGroot, 2003).

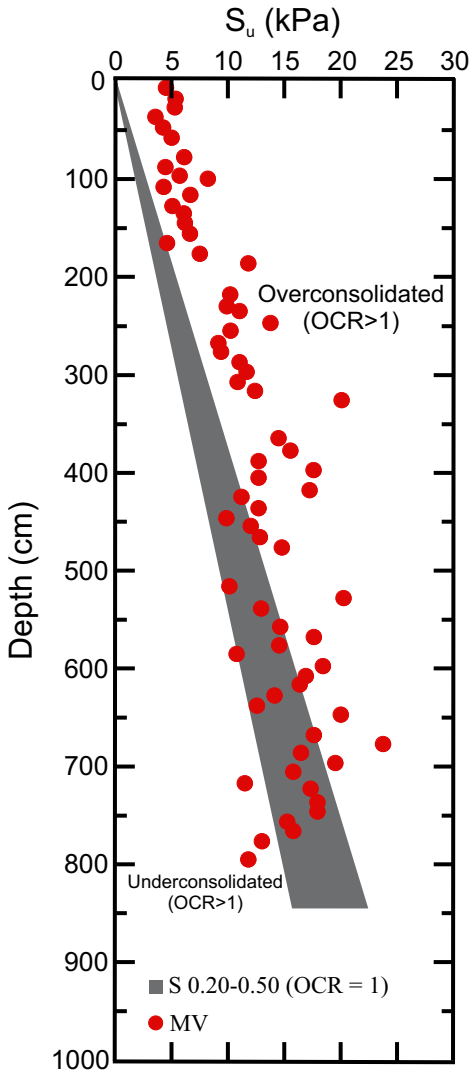

Figure 6.3. A comparison of the undrained shear strength calculated using the S ratio and the MV shear strength data

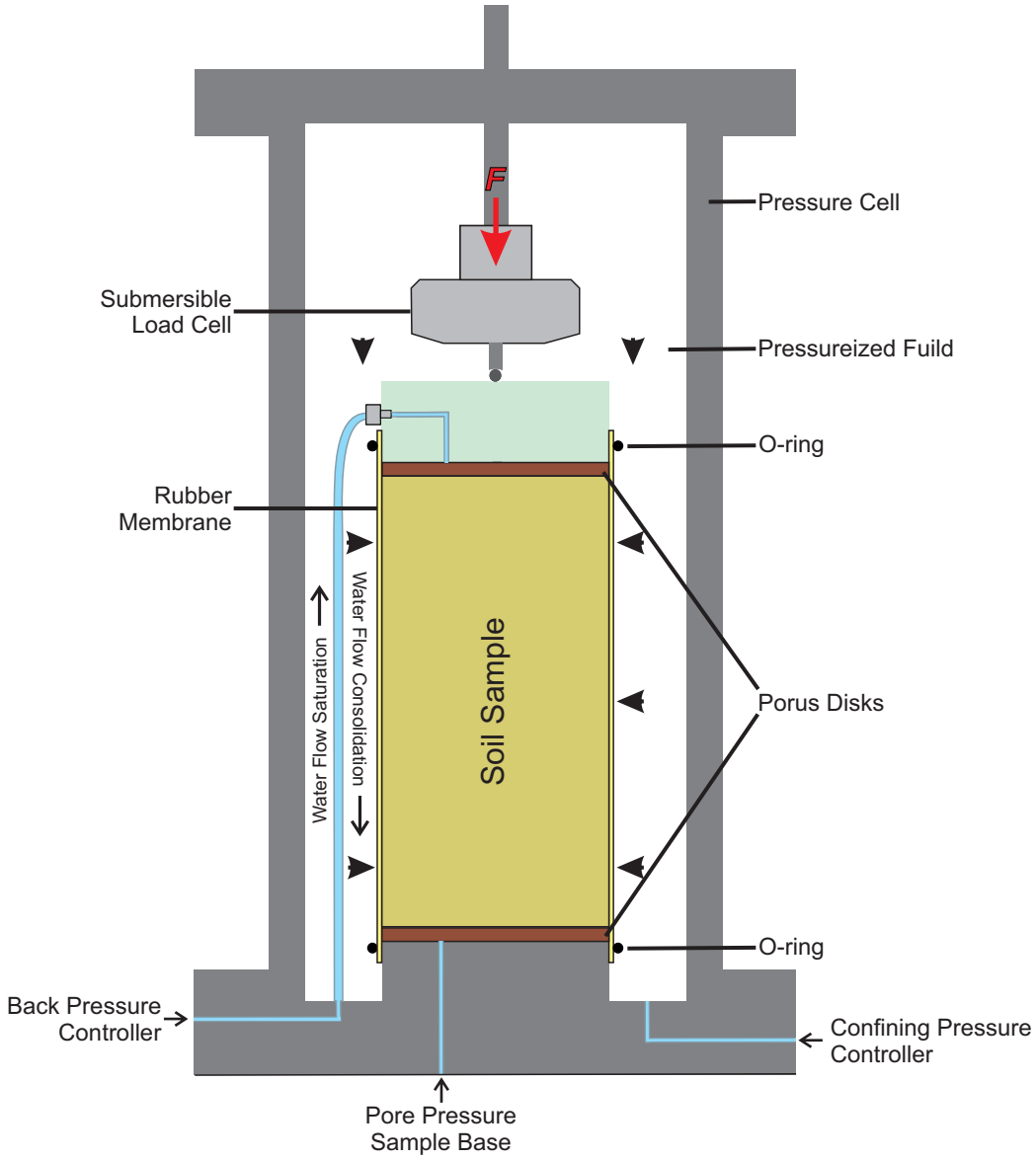

Figure 6.4. General set-up of a soil sample in a triaxial cell.

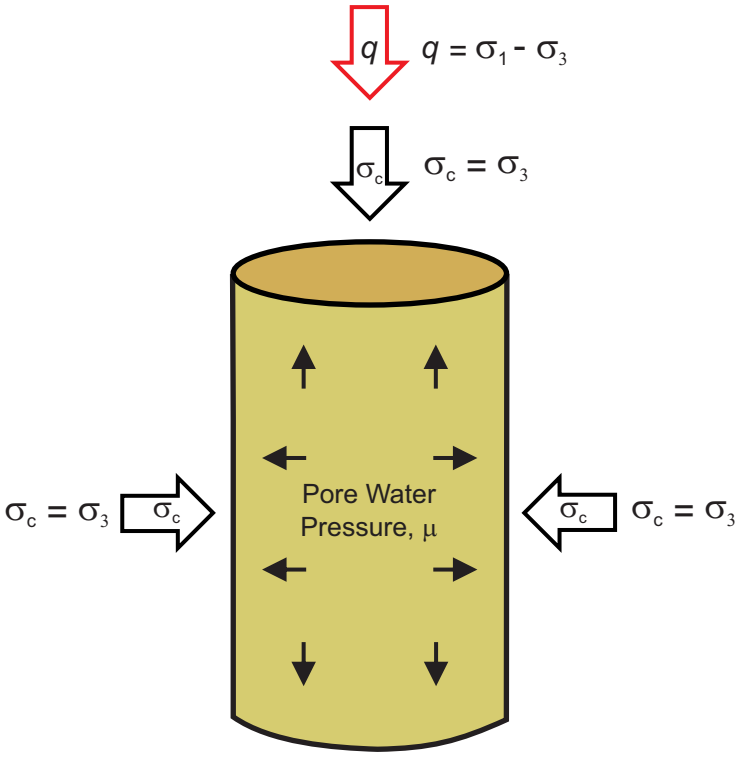

Figure 6.5. Sample stress during the shear stage where σ_c is the confining pressure that remains constant during the shear stage.

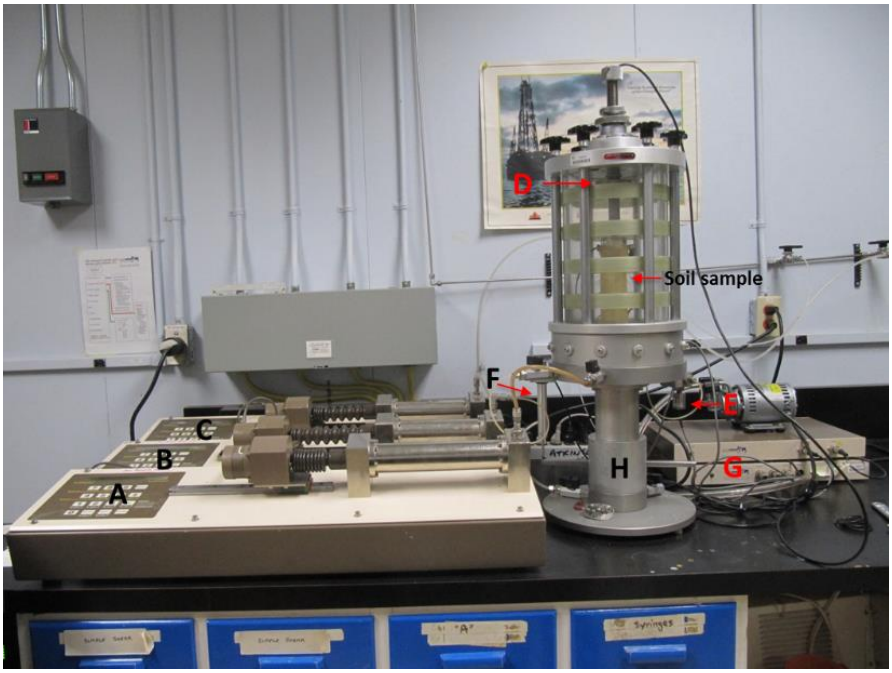

Figure 6.6. The GDS triaxial system at the GSCA geomechnical lab includes 3 2 MPa GDS pressure/volume controllers (A, B, C), submersible load cell (D), pore pressure transducer (E), linear displacement transducer (F), DAQ system (G) and Bishop & Wesley stress path triaxial cell (H).

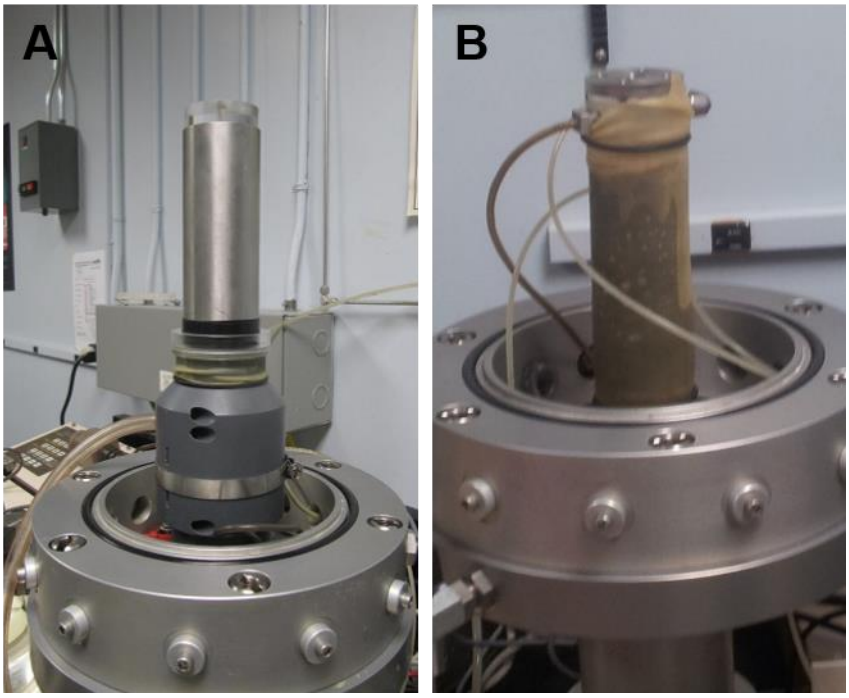

Figure 6.7. Placement of the sample into the rubber membrane in the B&W triaxial cell. A) Sampling ring with sample and split form with rubber membrane. B) Soil sample in the rubber membrane with top cap attached.

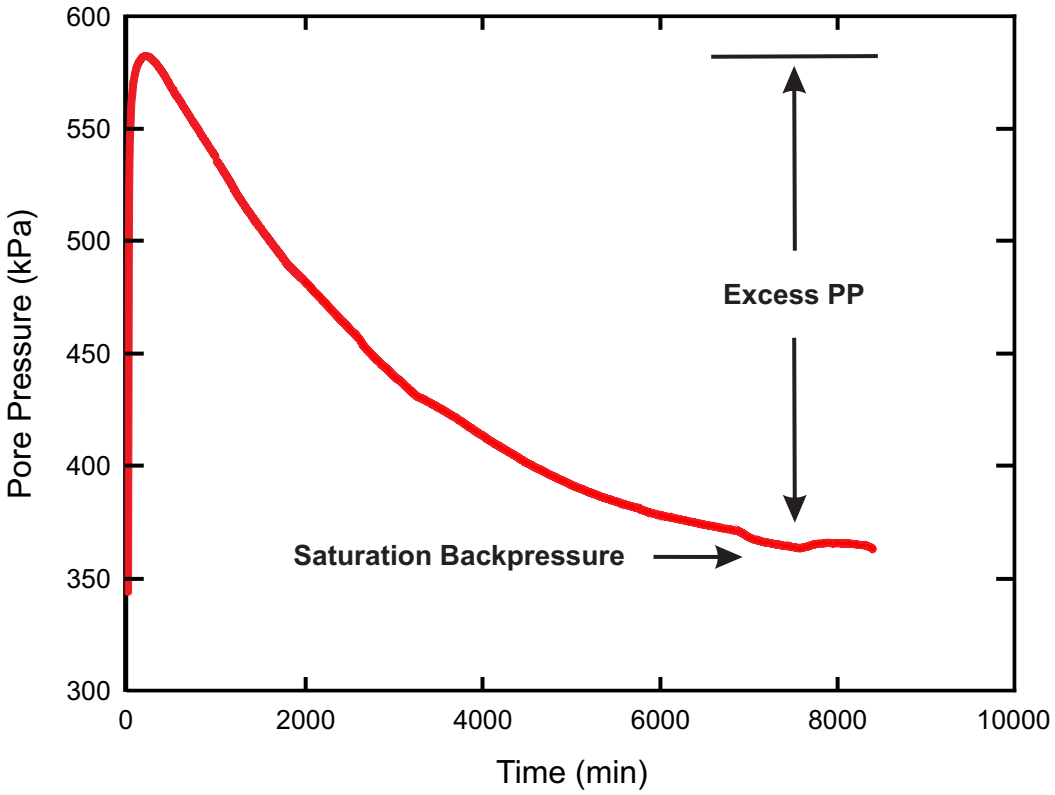

Figure 6.8. Triaxial test data illustrating pore pressure dissipation during the isotropic consolidation stage.

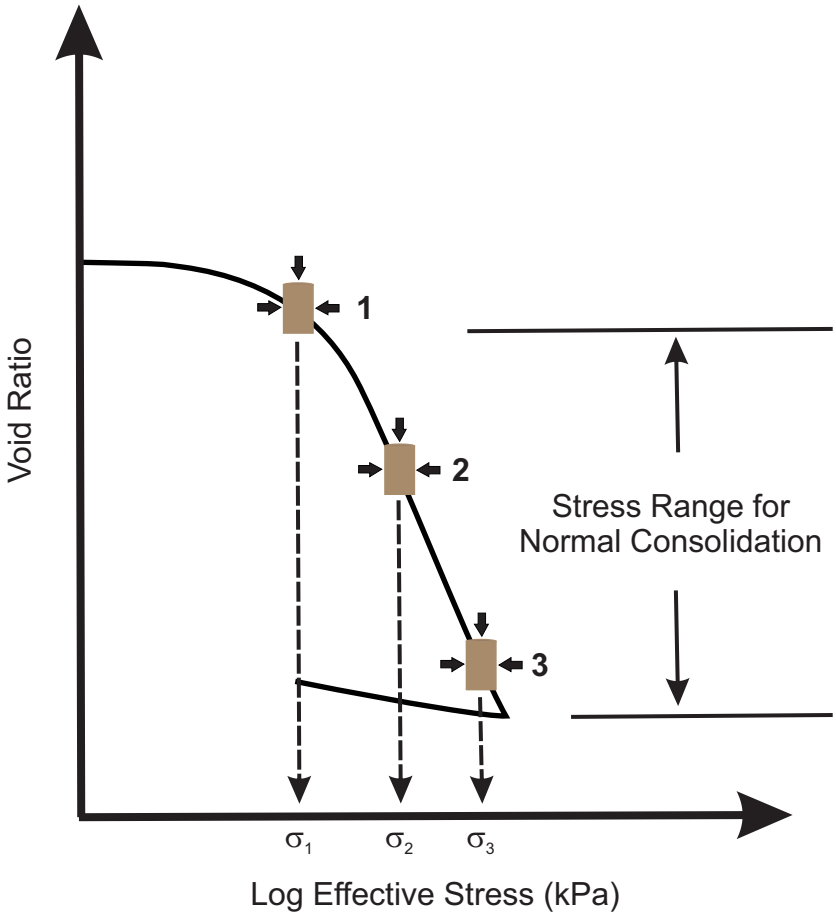

Figure 6.9. Consolidation test data illustrating the procedure for selecting 3 confining pressures for CIU triaxial testing. Note that confining pressures 2 and 3 are in the normal consolidation stress range for the sample.

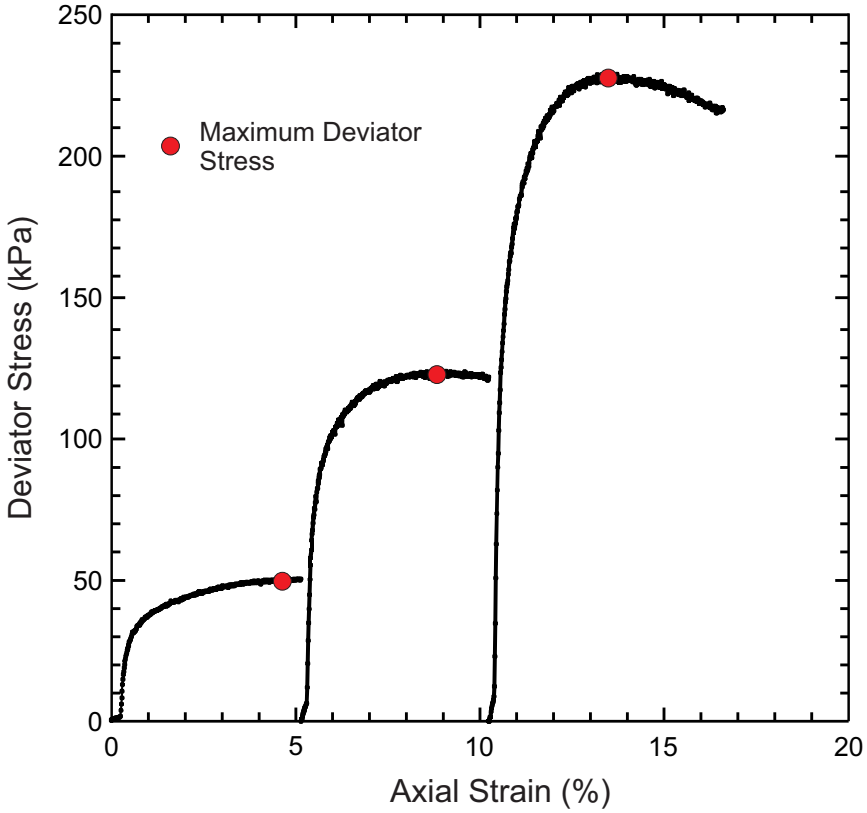

Figure 6.10. Triaxial test data illustrating the stress-strain for the 3 shear stages.

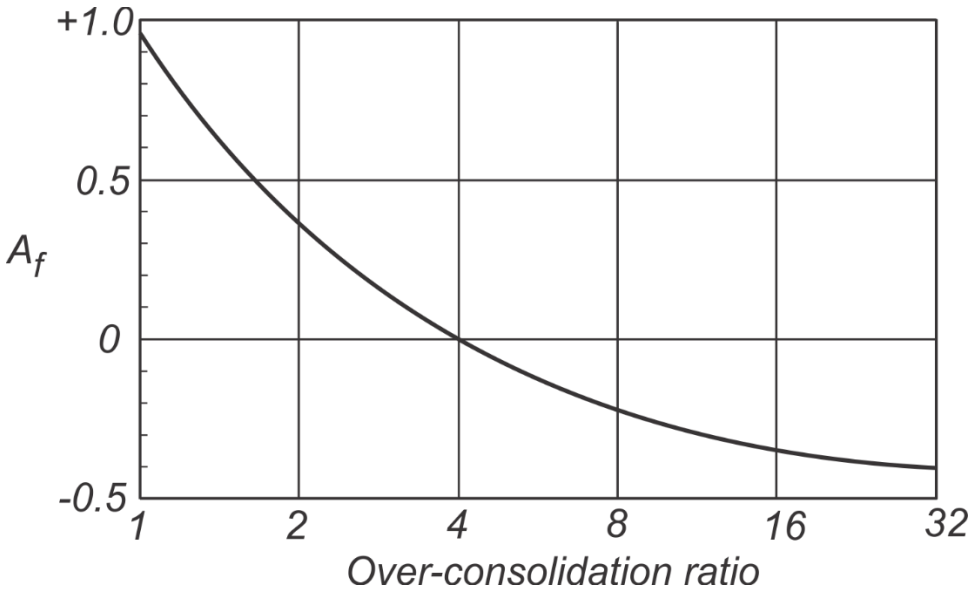

Figure 6.11. Relationship between A_f and OCR values.

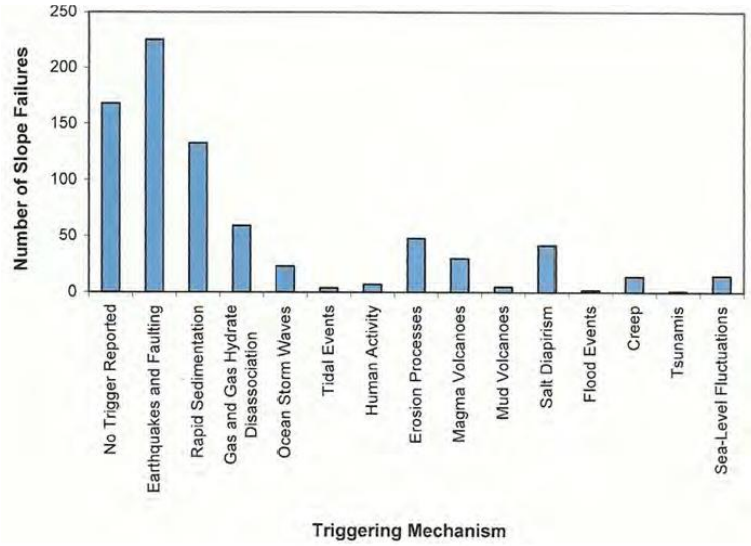

Figure 7.1. Triggering mechanisms for 534 submarine slides (Hance, 2003).

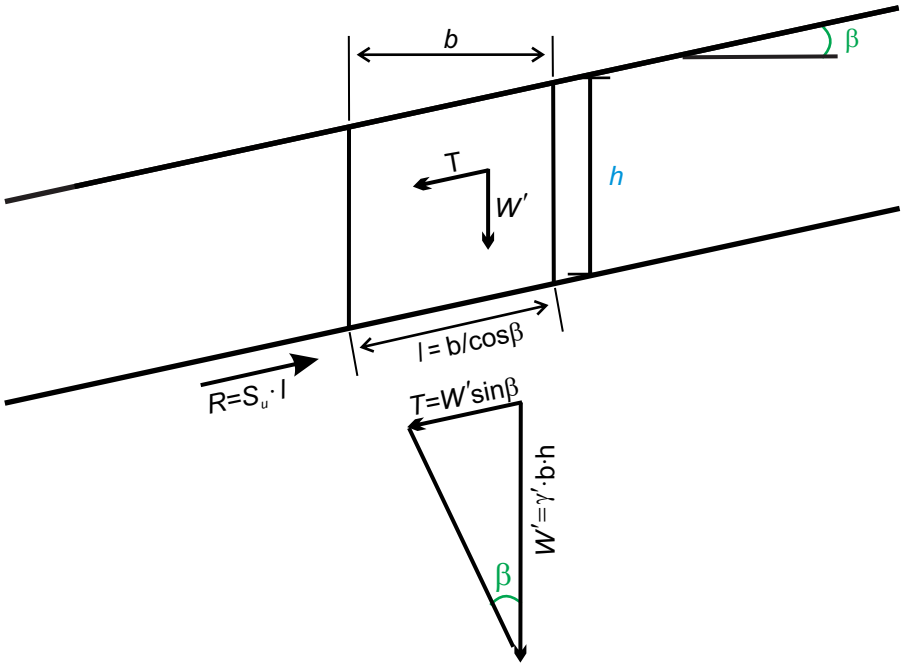

Figure 7.2. The equilibrium of an infinite slope under undrained conditions, with gravity forces, T (after Morgenstren, 1967). Only the forces used in the FS calculation are shown.

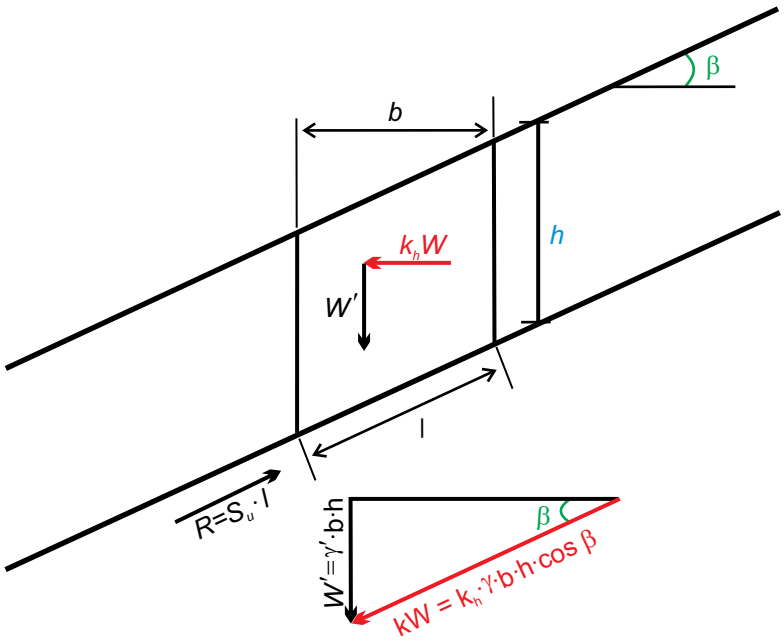

Figure 7.3. The equilibrium of an infinite slope under undrained conditions, with an earthquake force (kW, after Morgenstren, 1967). Only the forces used in the FS calculation are shown.

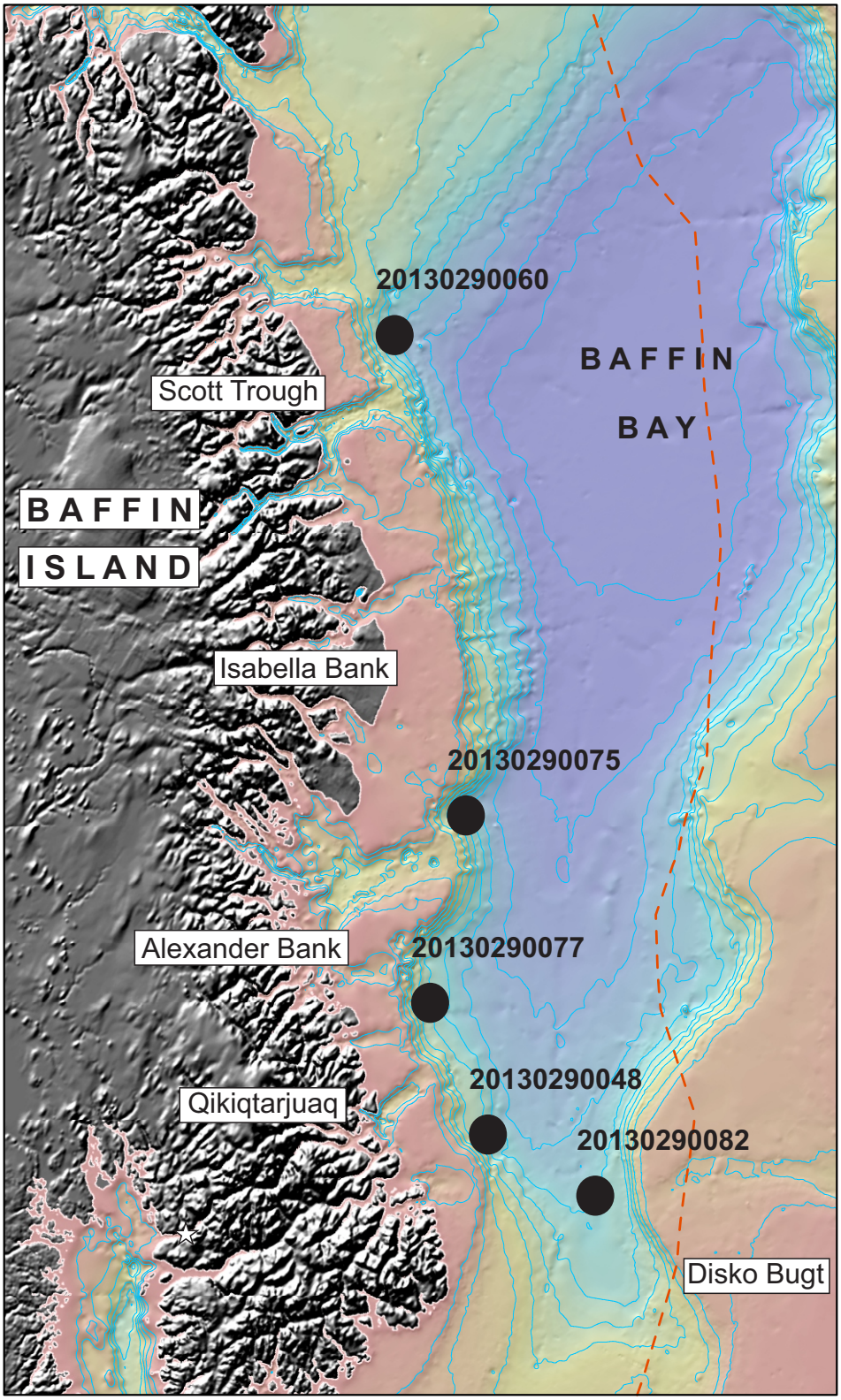

Figure 8.1. Location map of the geotechnical cores used in this study.

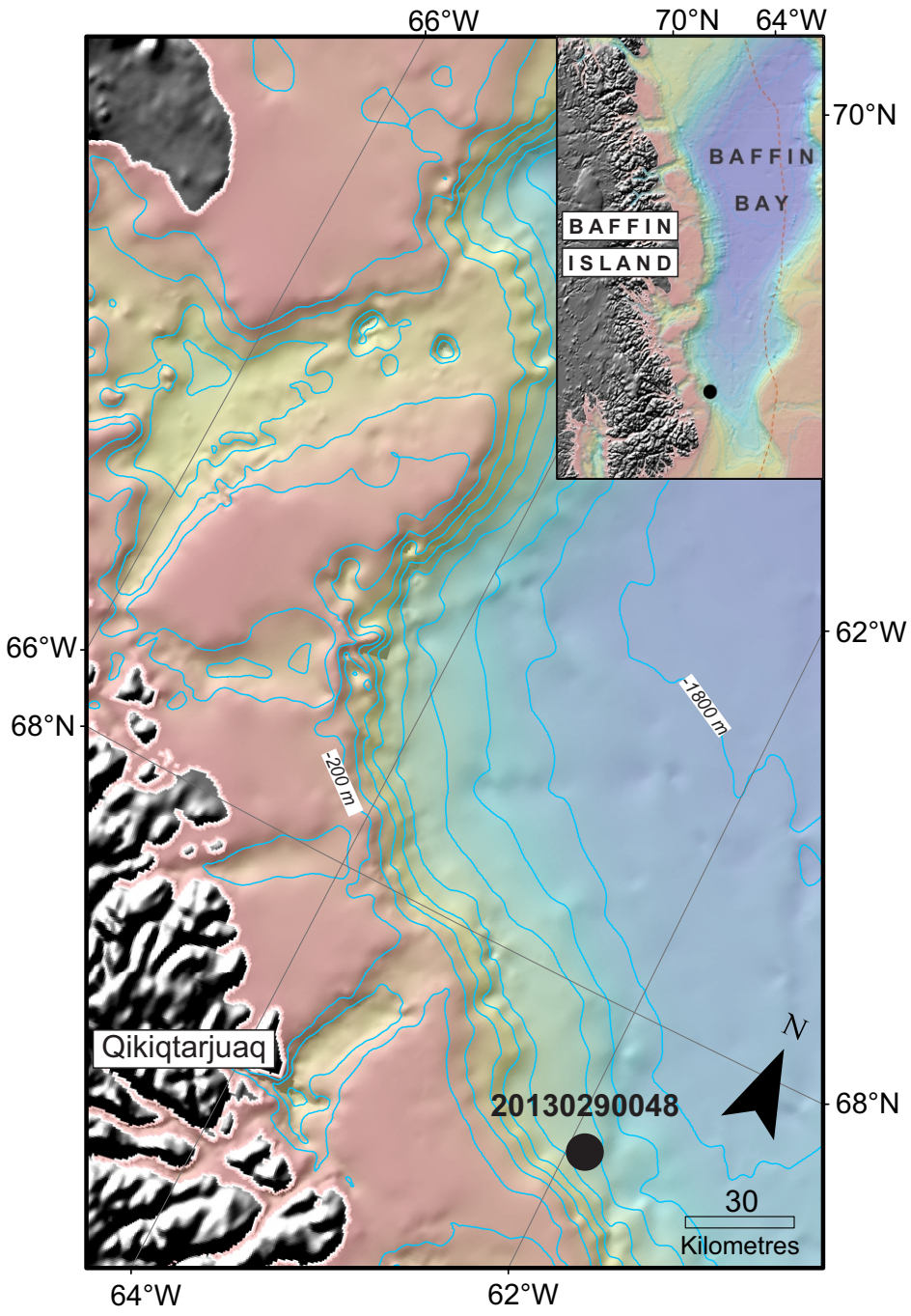

Figure 8.2. Location map of piston core 20130290048.

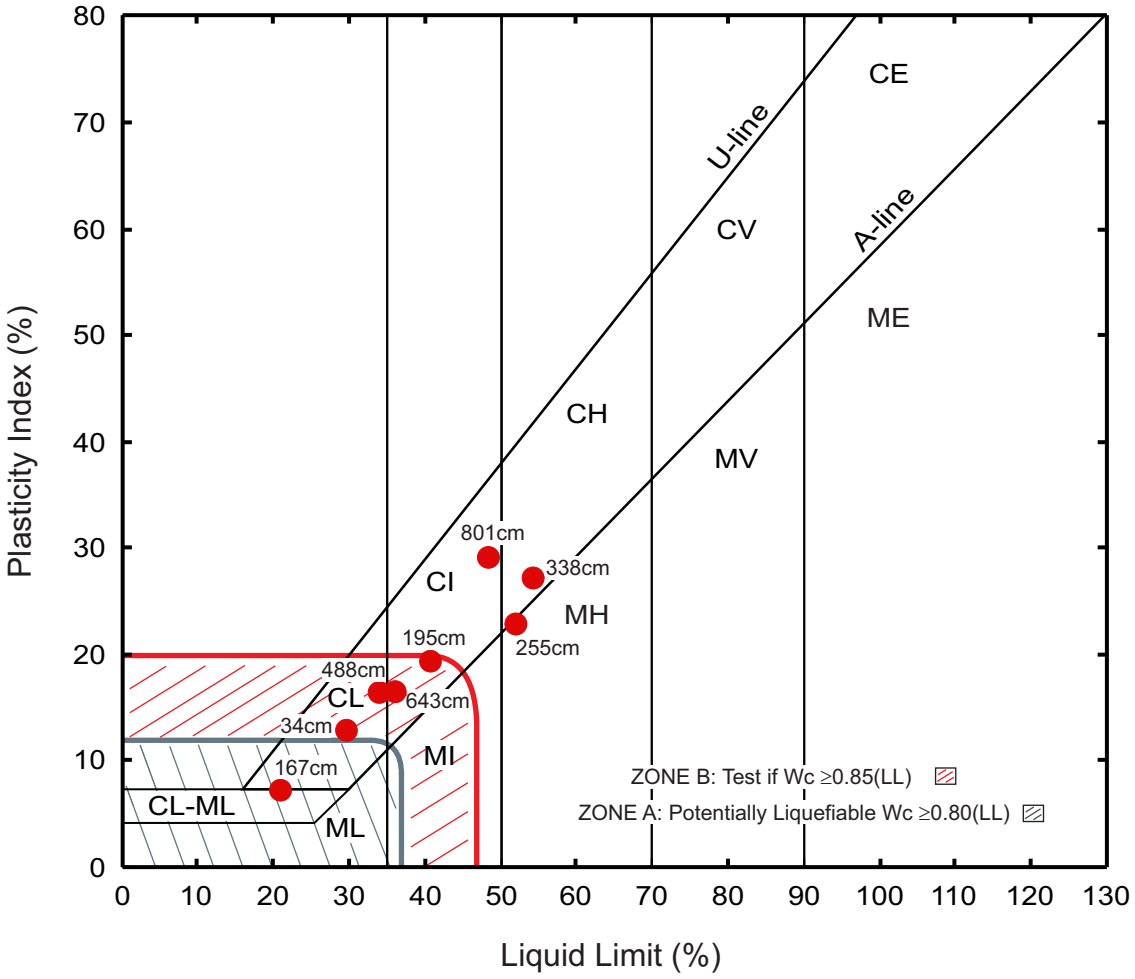

Figure 8.3. Plasticity chart showing Atterberg limit results of piston core 20130290048.

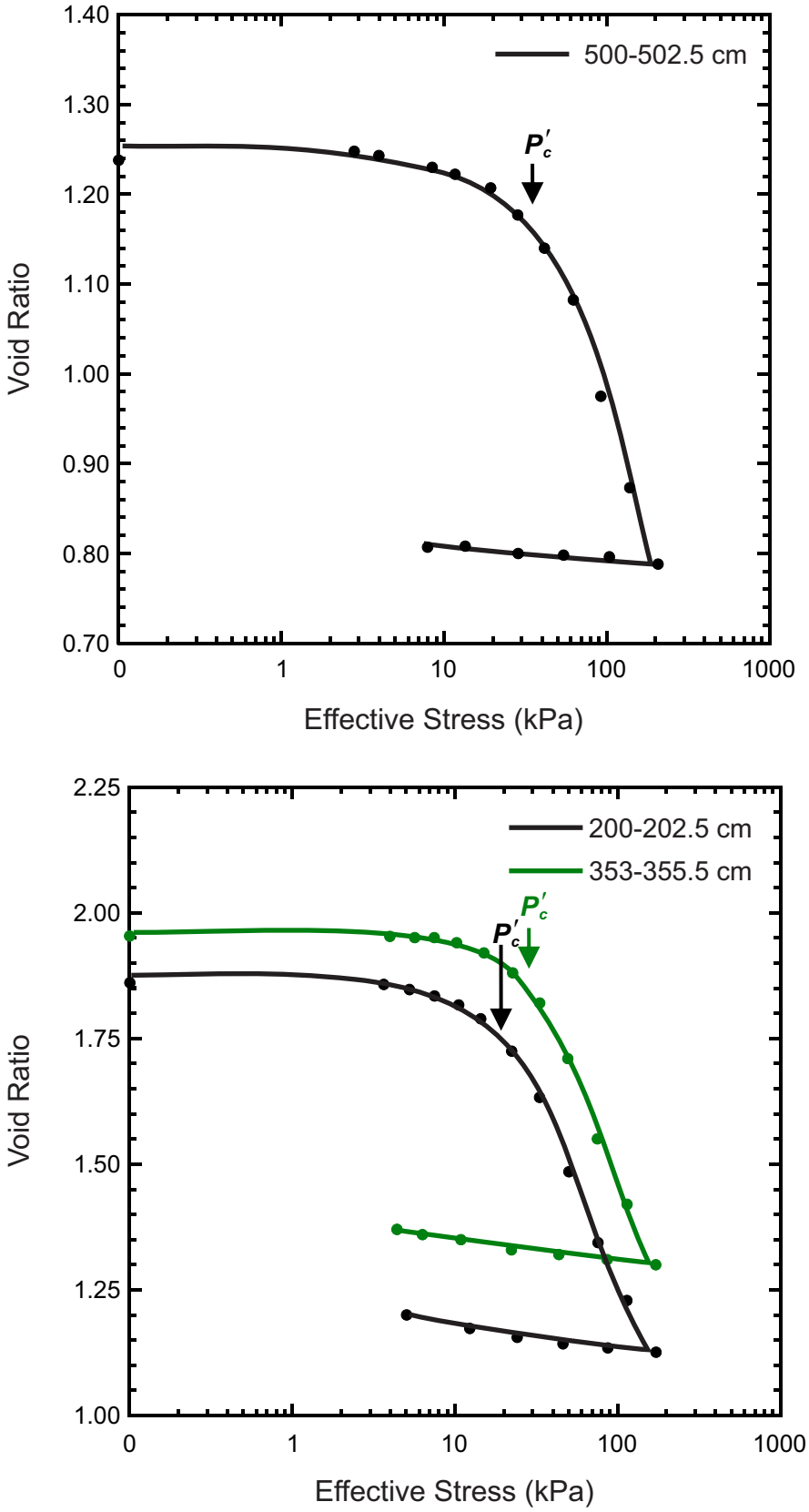

Figure 8.4. Consolidation plots for piston core 20130290048.

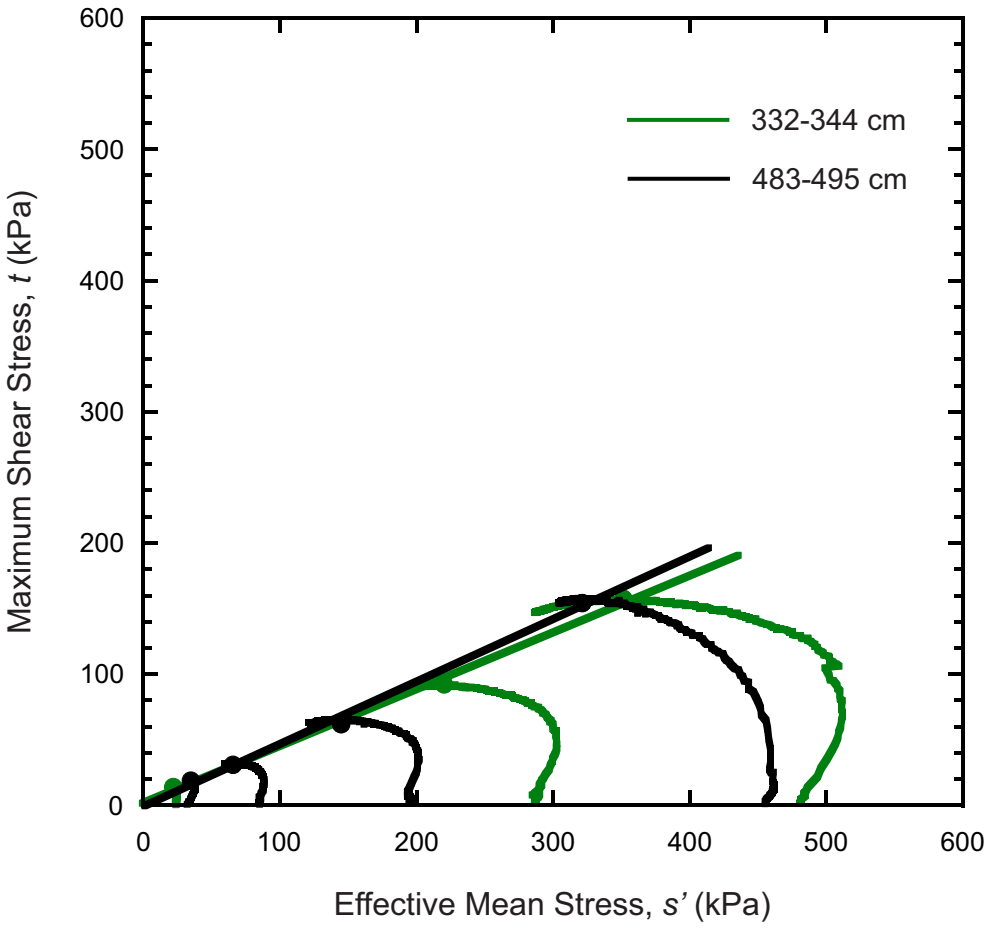

Figure 8.5. Stress paths and failure envelopes from triaxial test results for piston core 20130290048.

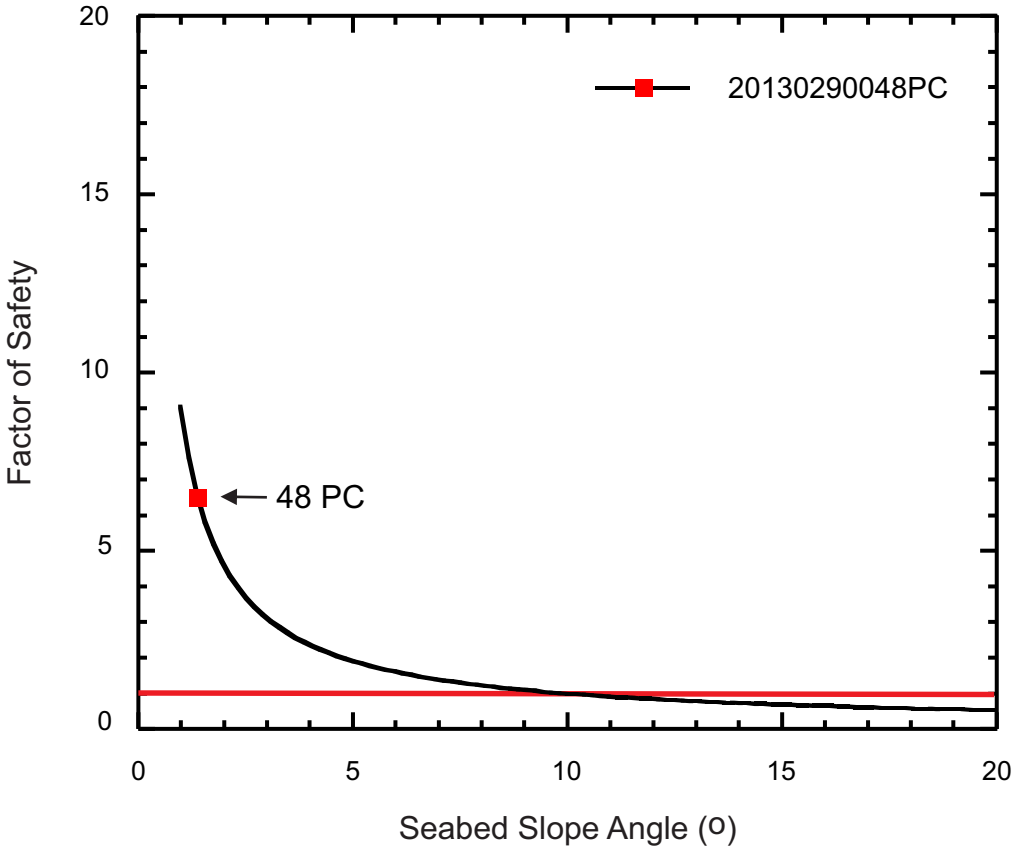

Figure 8.6. FS at various slope angles for piston core 20130290048.

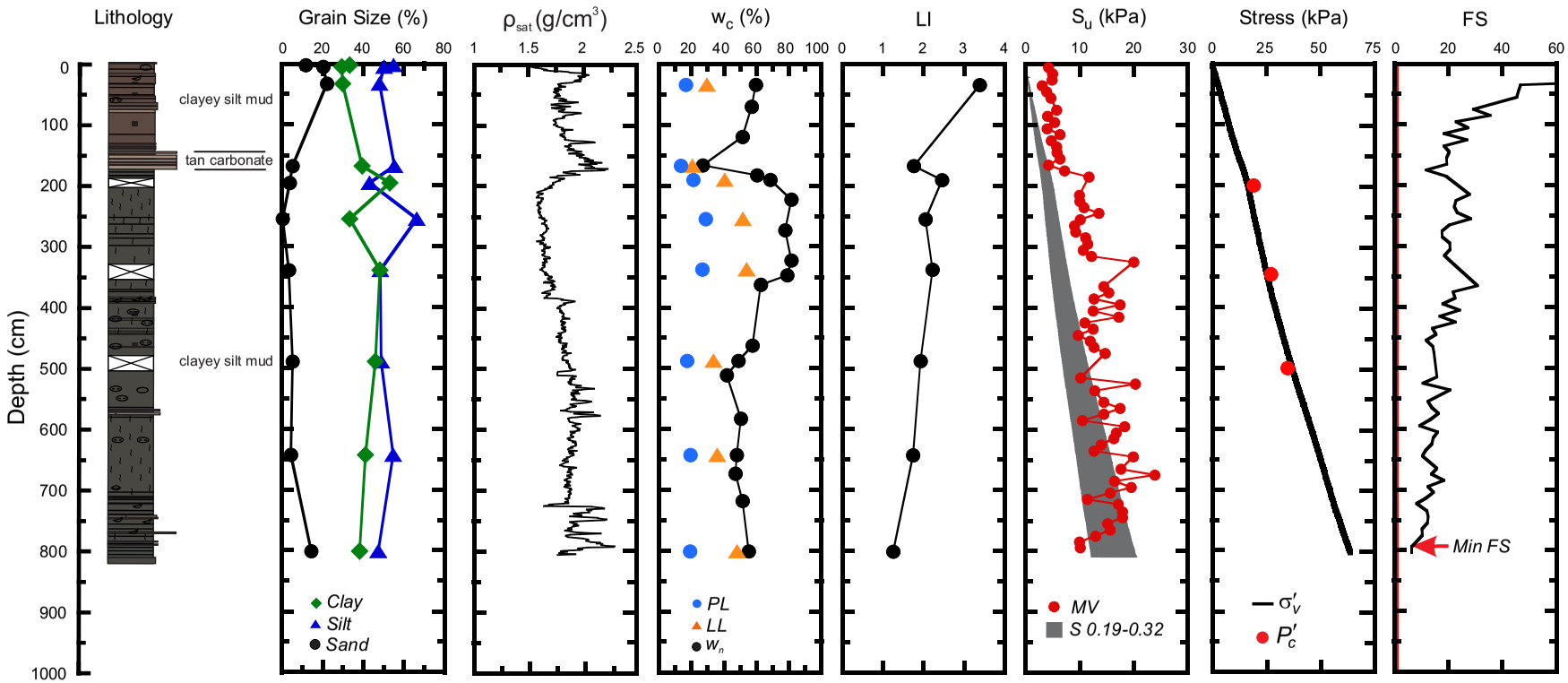

Figure 8.7. Geotechnical profile for core 20130290048 from the slope off Qikiqtarjuaq. (ρ_{sat}= saturated bulk density, w_c = water content, w_n = natural in-situ water content, *PL* = plastic limit, *LL* = liquid limit, *LI* = liquidity index, S_u = undrained shear strength, *MV* = laboratory miniature vane shear strength, *S* = shear strength calculated from the normalized strength ratio, σ'_v = effective overburden stress, P'_c = past maximum stress, *FS* = factor of safety).

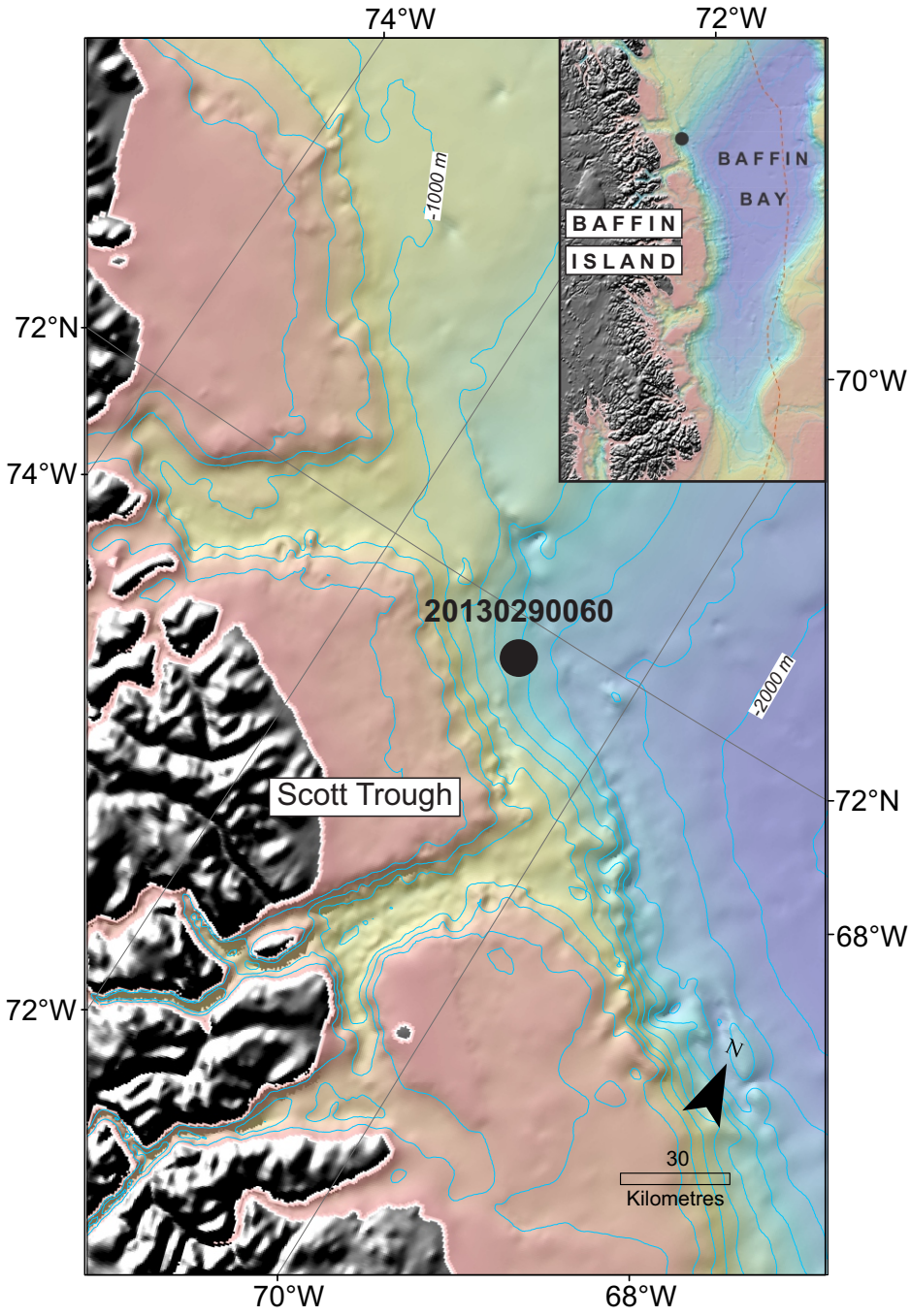

Figure 8.8. Location map of piston core 20130290060.

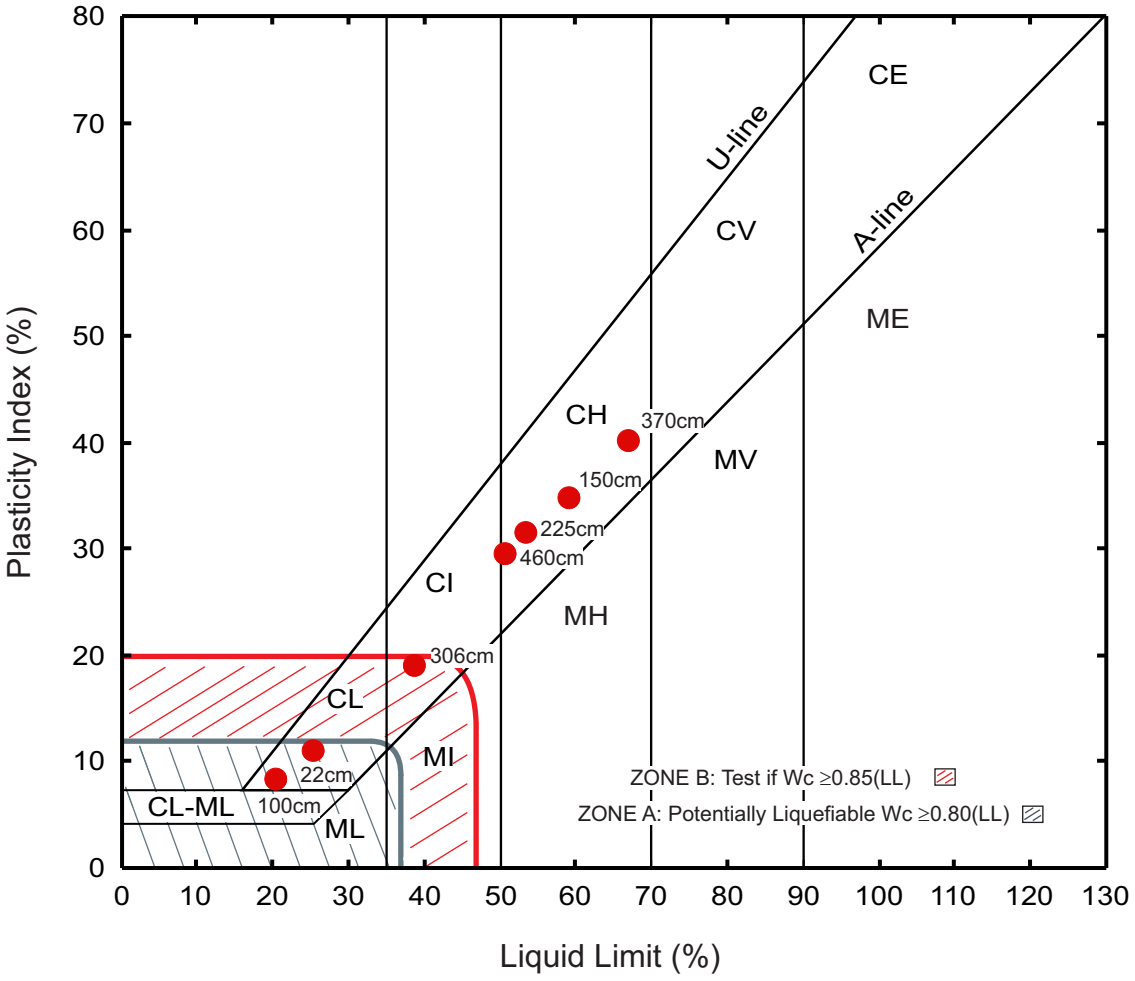

Figure 8.9. Plasticity chart showing Atterberg limit results of piston core 20130290060.

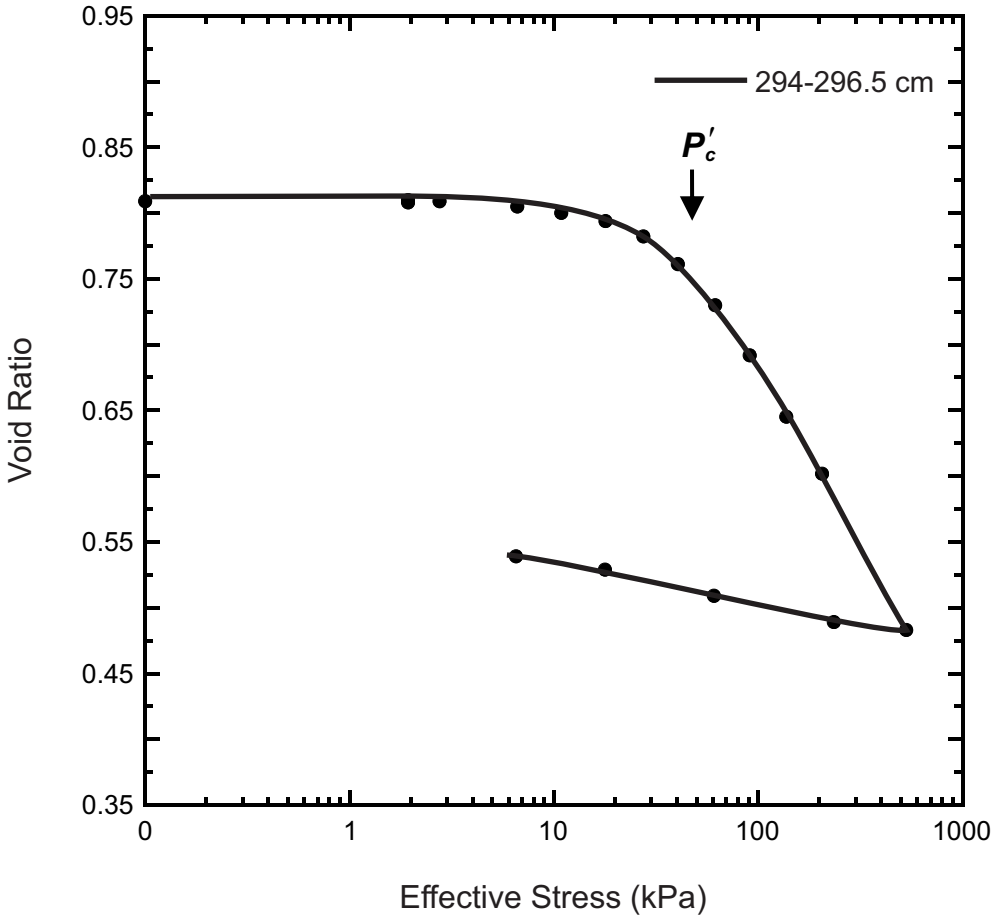

Figure 8.10. Consolidation plot for piston core 20130290060.

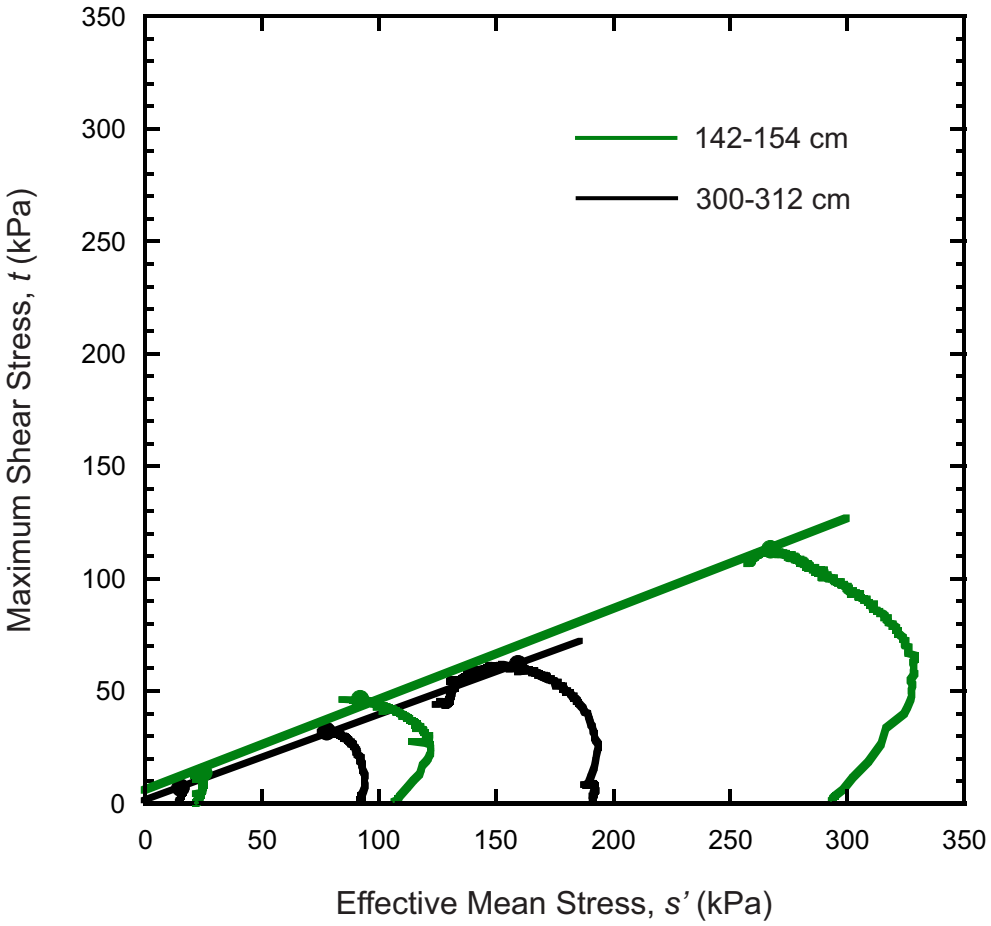

Figure 8.11. Stress paths and failure envelopes from triaxial test results for piston core 20130290060.

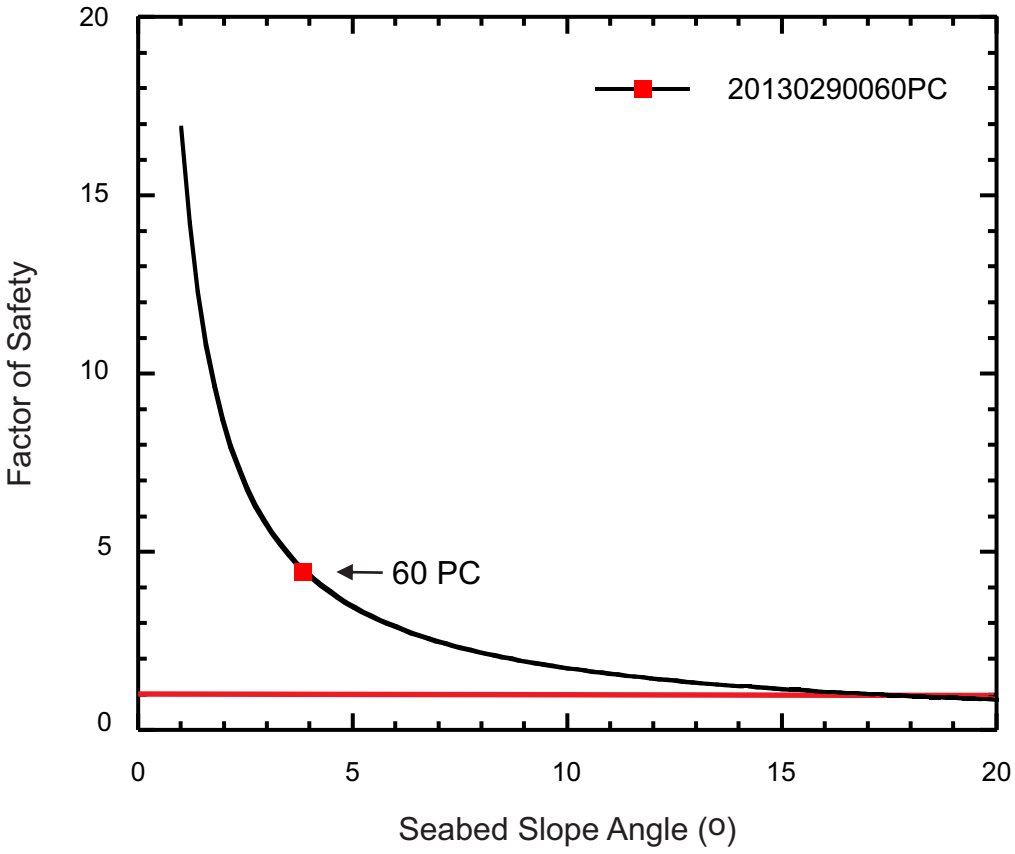

Figure 8.12. FS at various slope angles for piston core 20130290060.

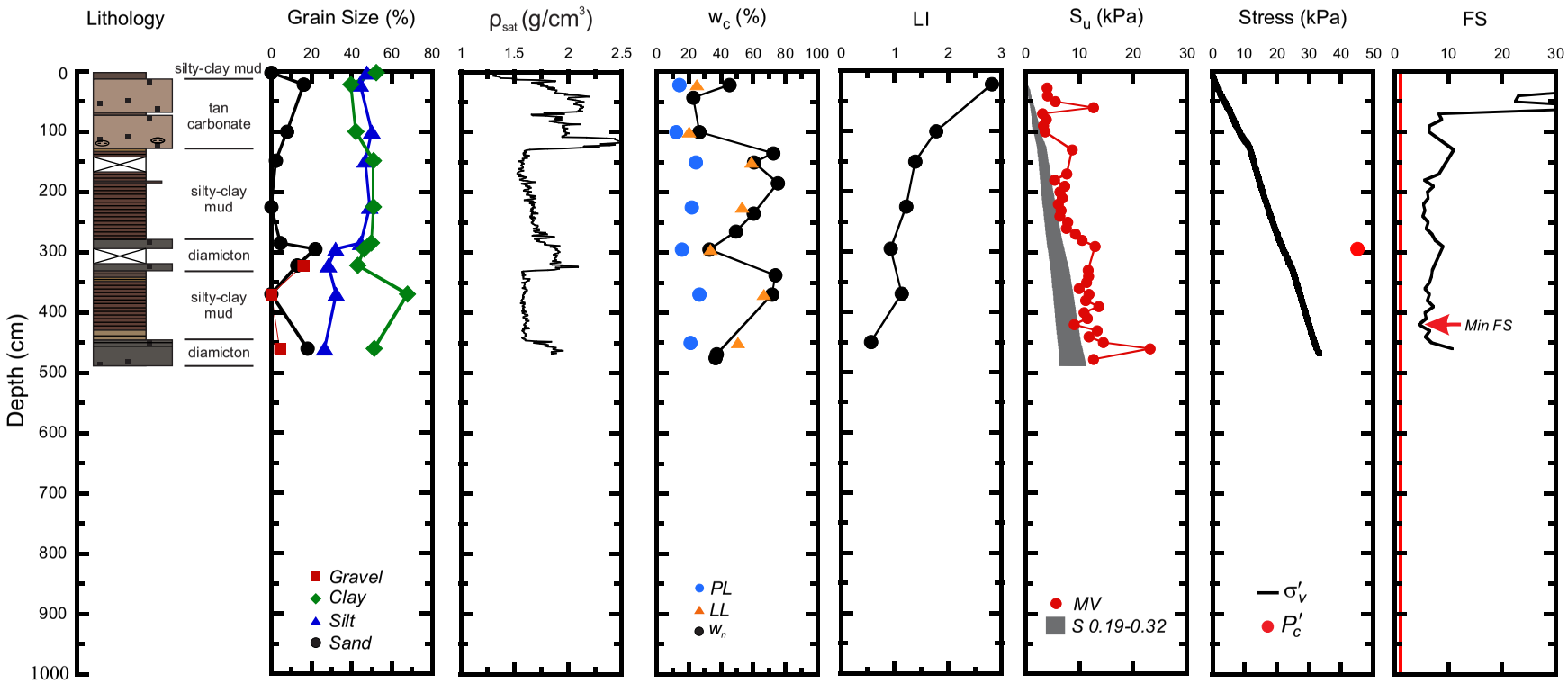

Figure 8.13. Geotechnical profile for core 20130290060 from the slope off Scott Trough. (ρ_{sat}= saturated bulk density, w_c = water content, w_n = natural in-situ water content, *PL* = plastic limit, *LL* = liquid limit, *LI* = liquidity index, S_u = undrained shear strength, *MV* = laboratory miniature vane, *S* = shear strength calculated from the normalized strength ratio, σ'_v = effective overburden stress, P'_c = past maximum stress, *FS* = factor of safety).

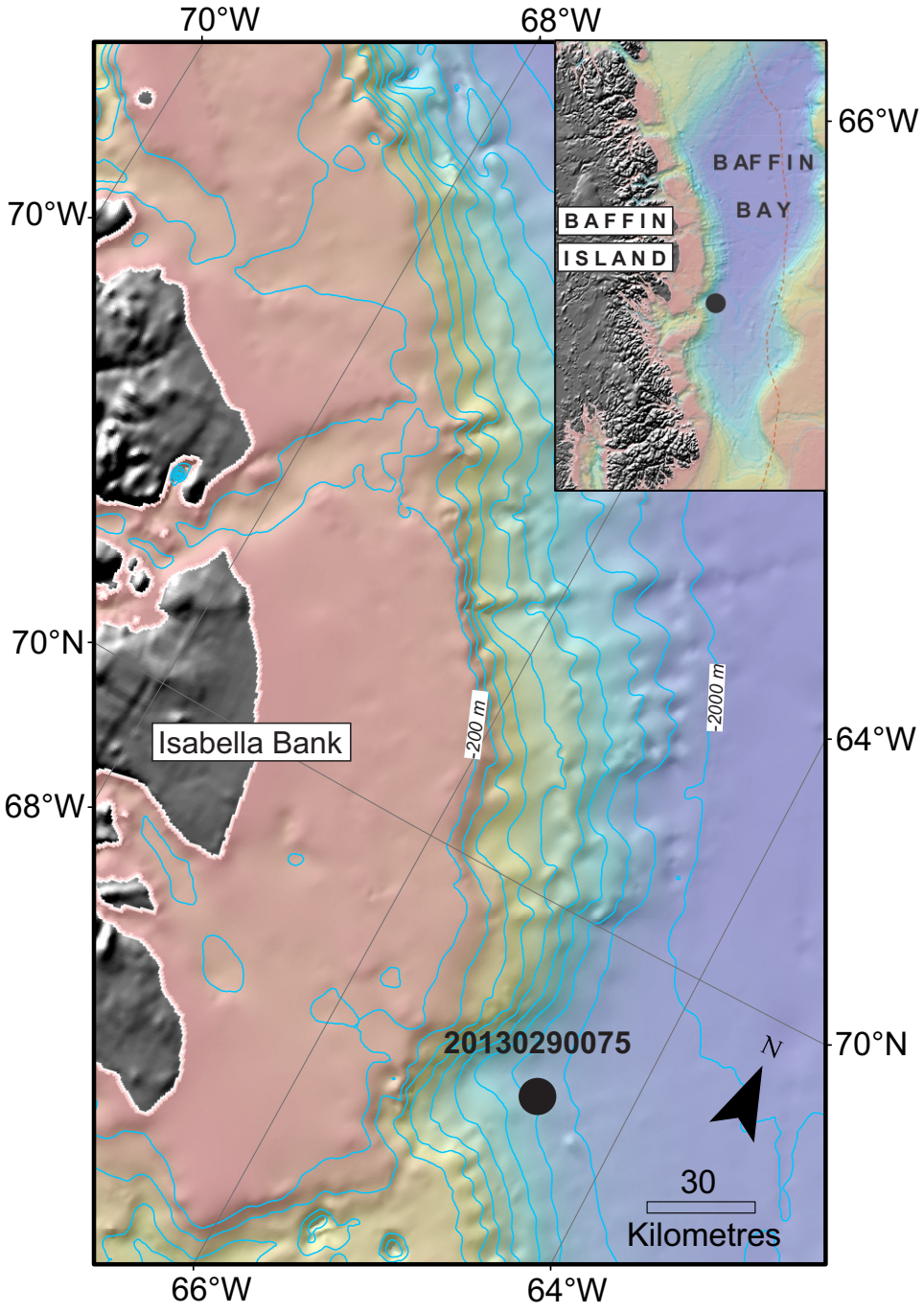

Figure 8.14. Location map of piston core 20130290075.

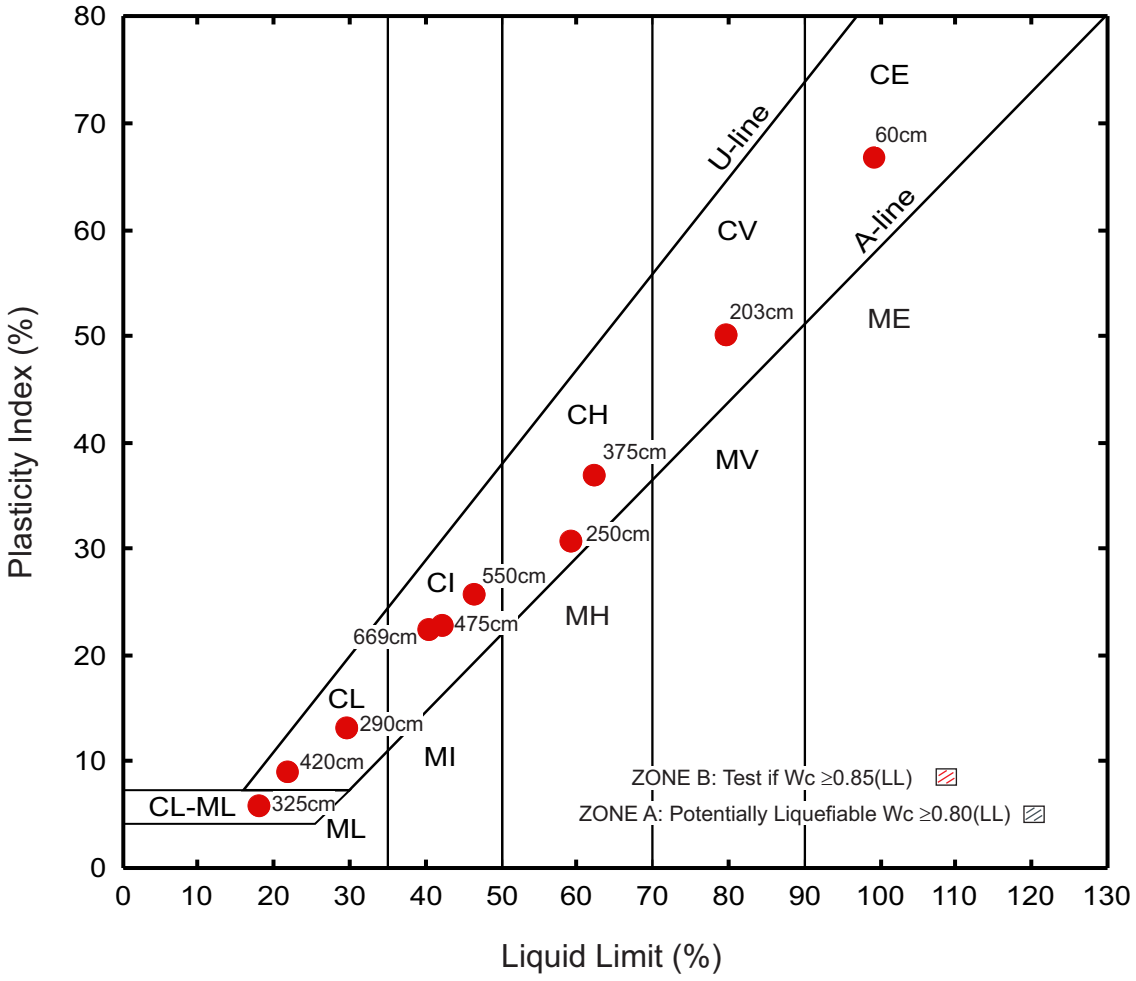

Figure 8.15. Plasticity chart showing Atterberg limit results of piston core 20130290075.

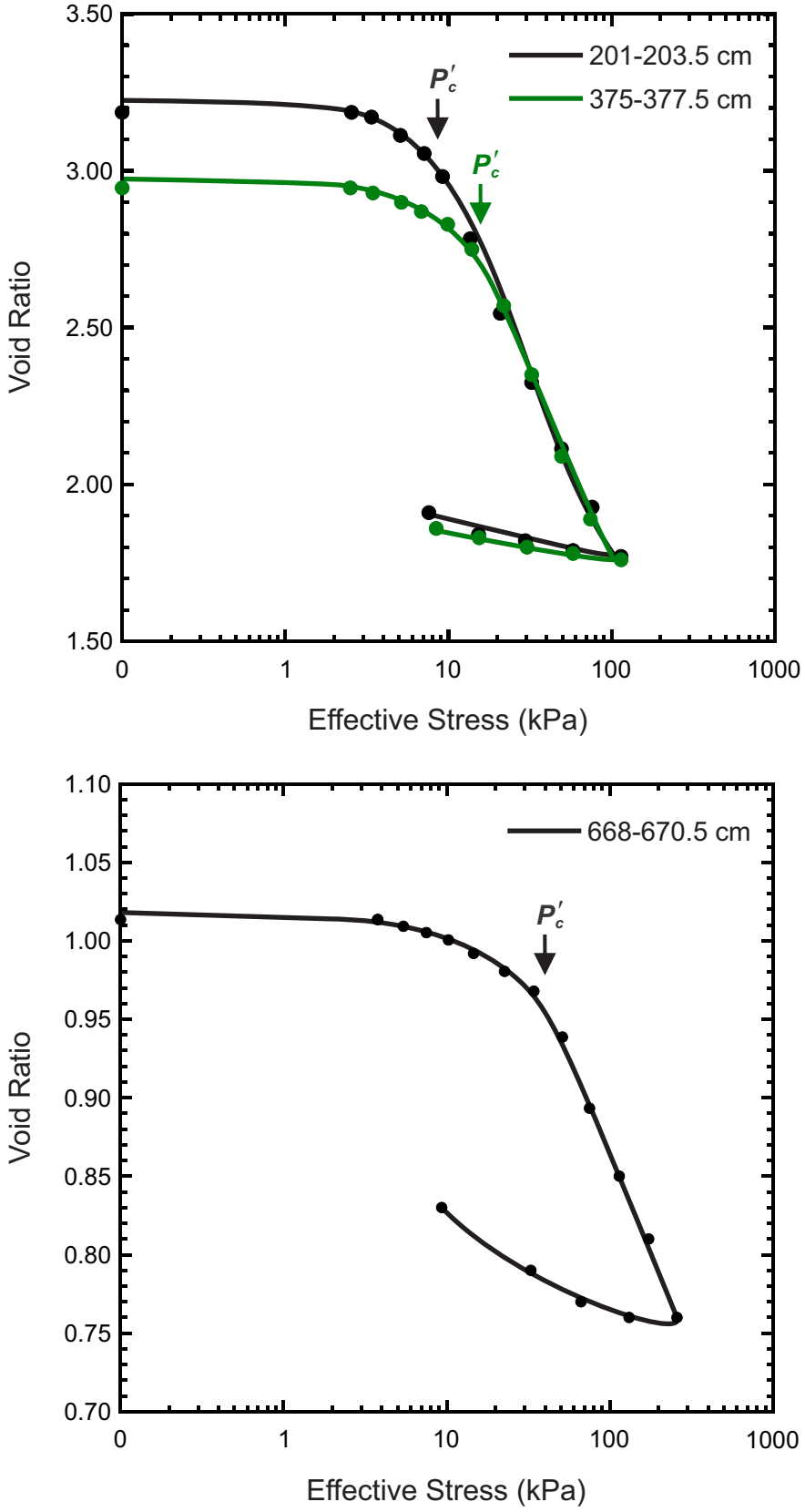

Figure 8.16. Consolidation plots for piston core 20130290075.

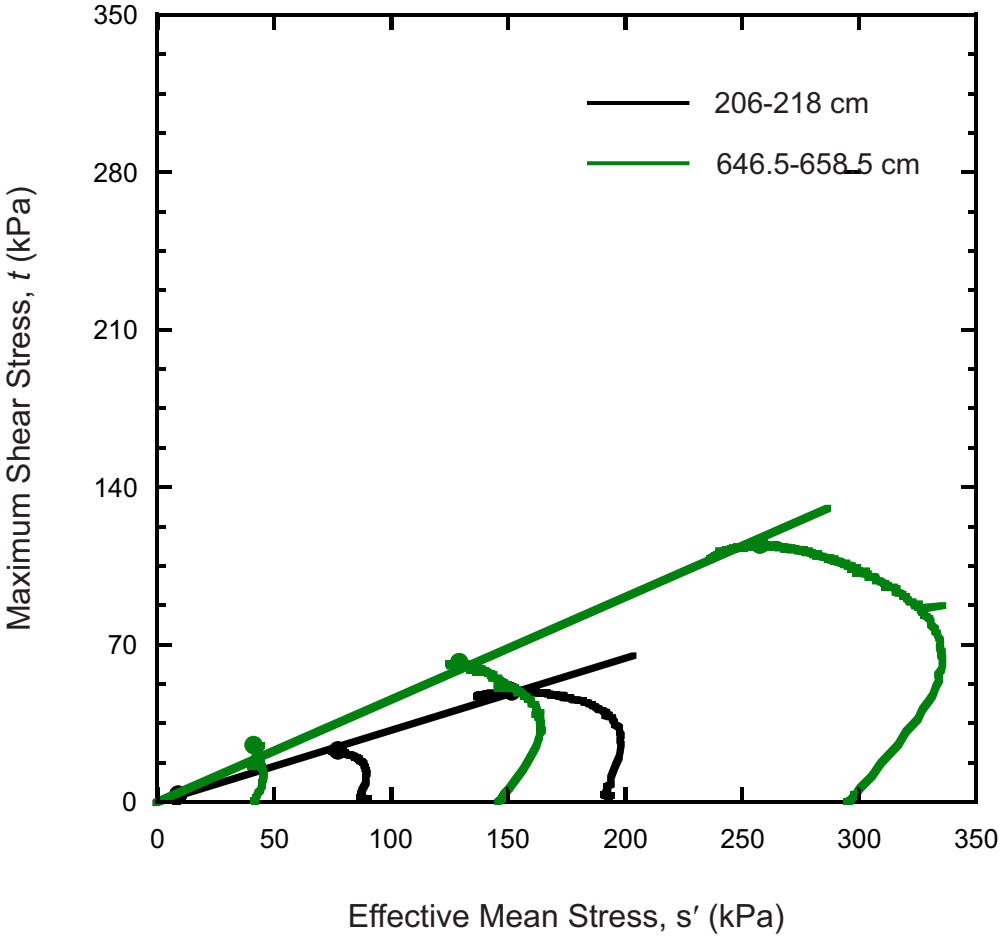

Figure 8.17. Stress paths and failure envelopes from triaxial test results for piston core 20130290075.

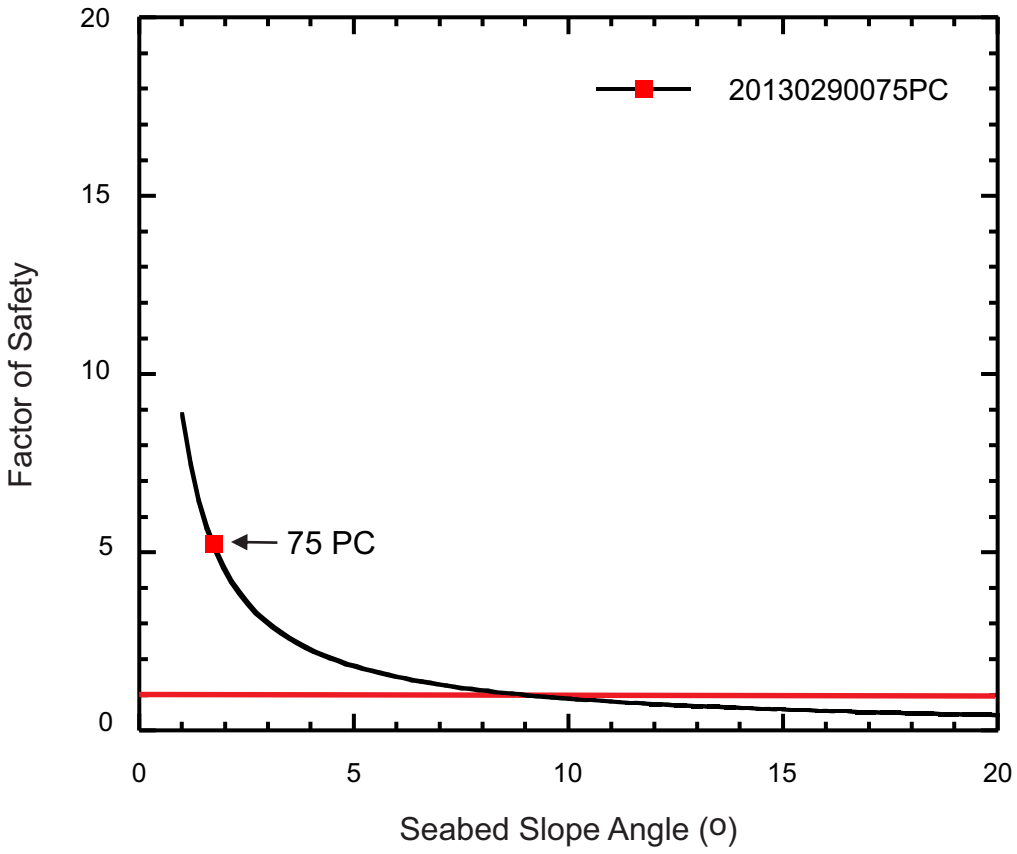

Figure 8.18. FS at various slope angles for piston core 20130290075.

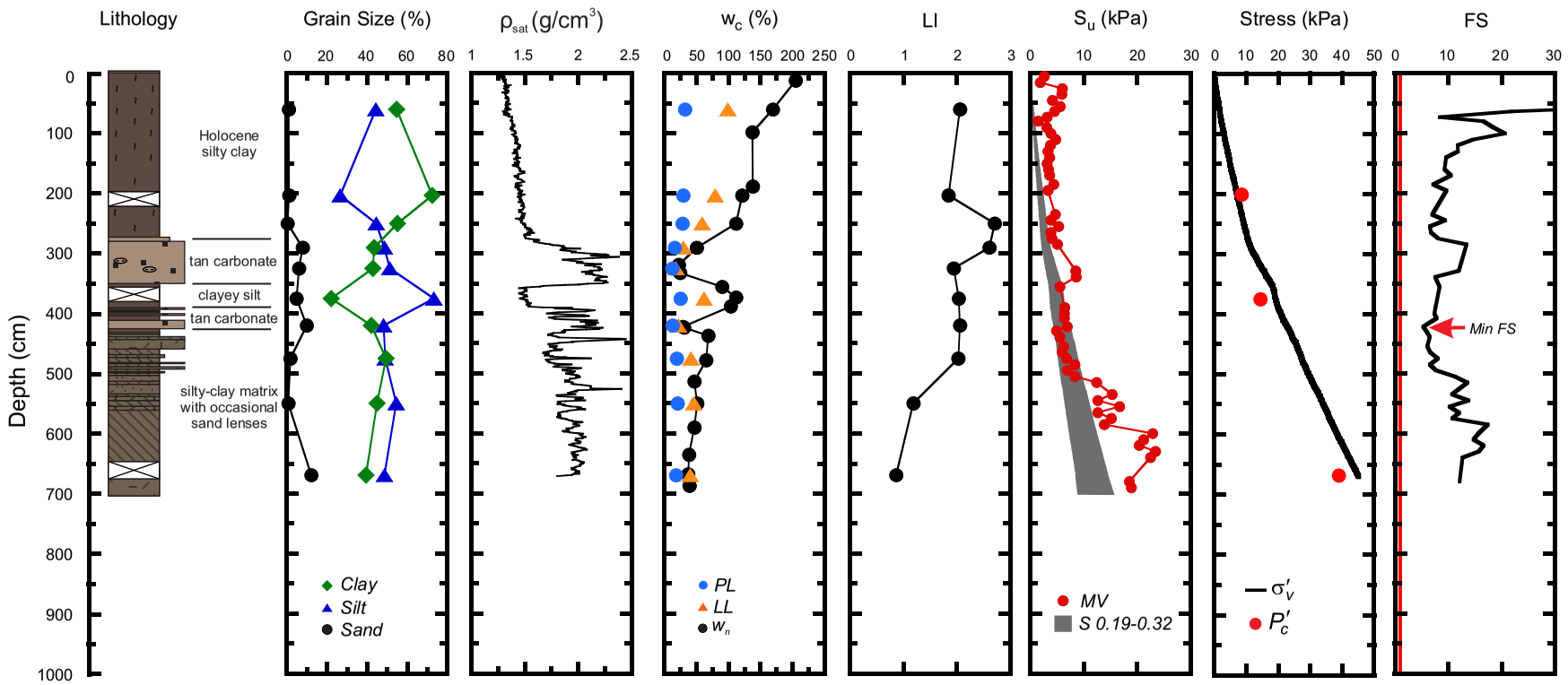

Figure 8.19. Geotechnical profile for core 20130290075 from the slope off Clyde River. (ρ_{sat} = saturated bulk density, w_c = water content, w_n = natural in-situ water content, *PL* = plastic limit, *LL* = liquid limit, *LI* = liquidity index, S_u = undrained shear strength, *MV* = laboratory miniature vane, *S* = shear strength calculated from the normalized strength ratio, σ'_v = effective overburden stress, P'_c = past maximum stress, *FS* = factor of safety).

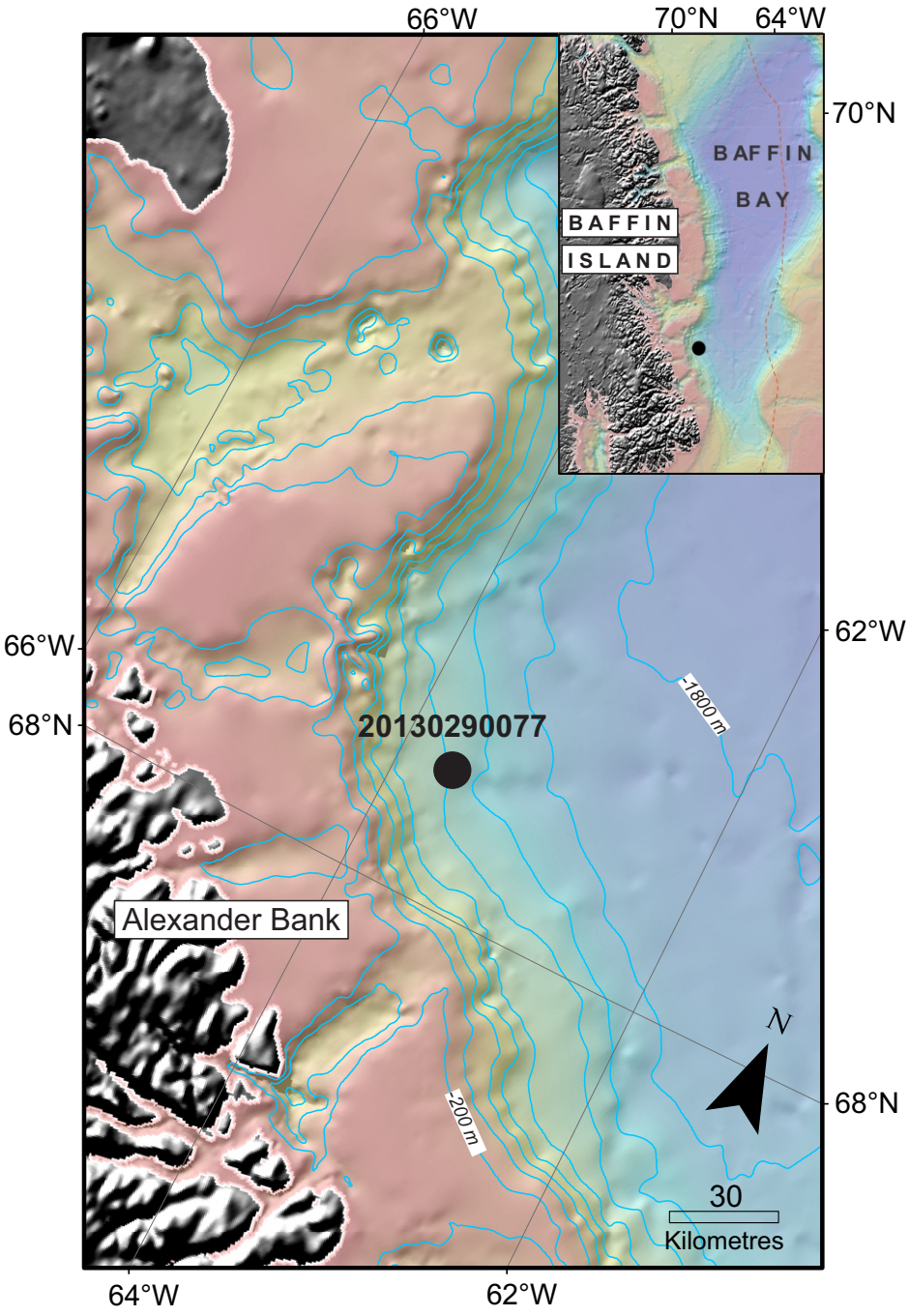

Figure 8.20. Location map of piston core 20130290077.

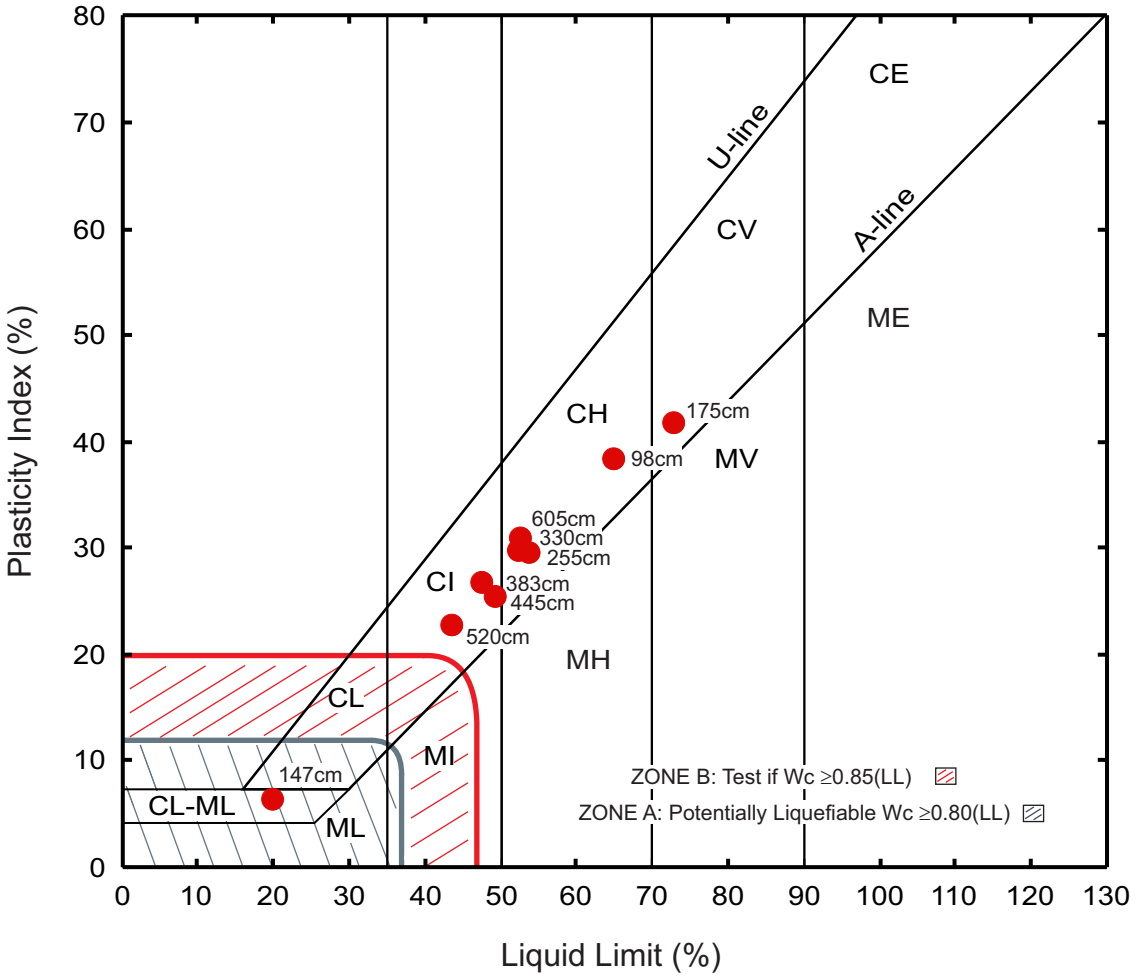

Figure 8.21. Plasticity chart showing Atterberg limit results of piston core 20130290077.

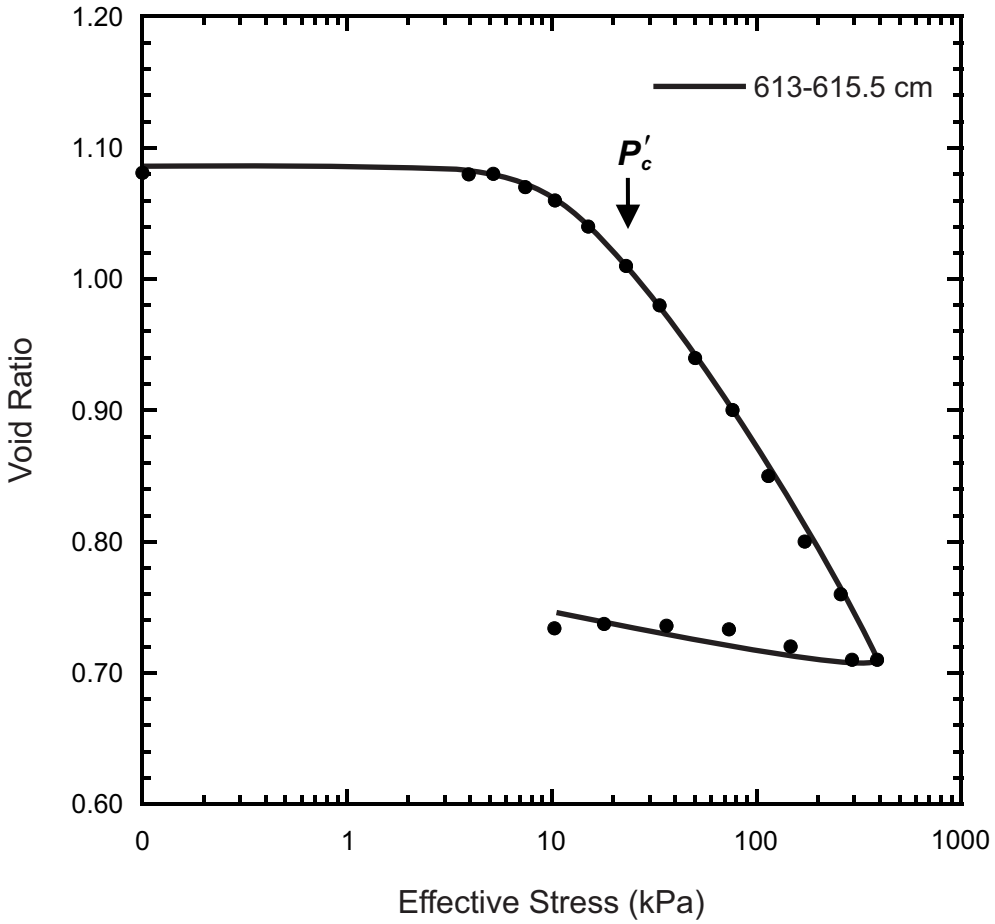

Figure 8.22. Consolidation plot for piston core 20130290077.

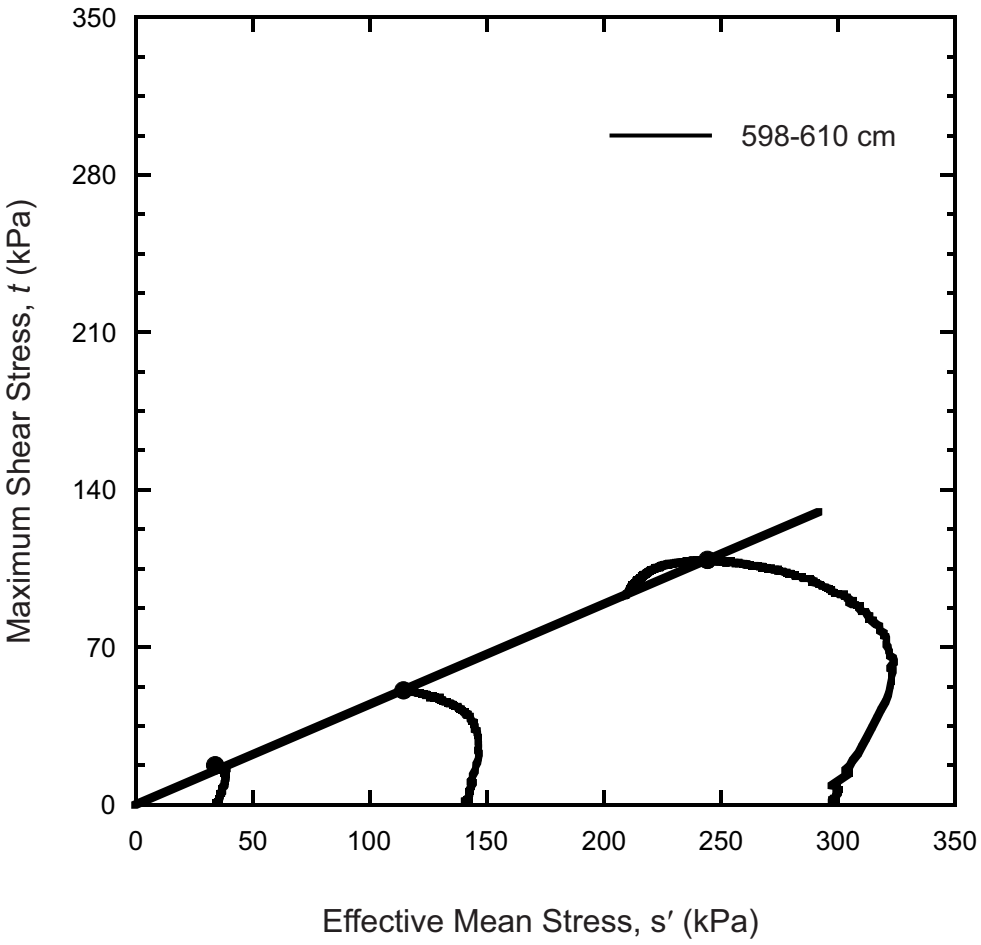

Figure 8.23. Stress path and failure envelope from triaxial test results for piston core 20130290077.

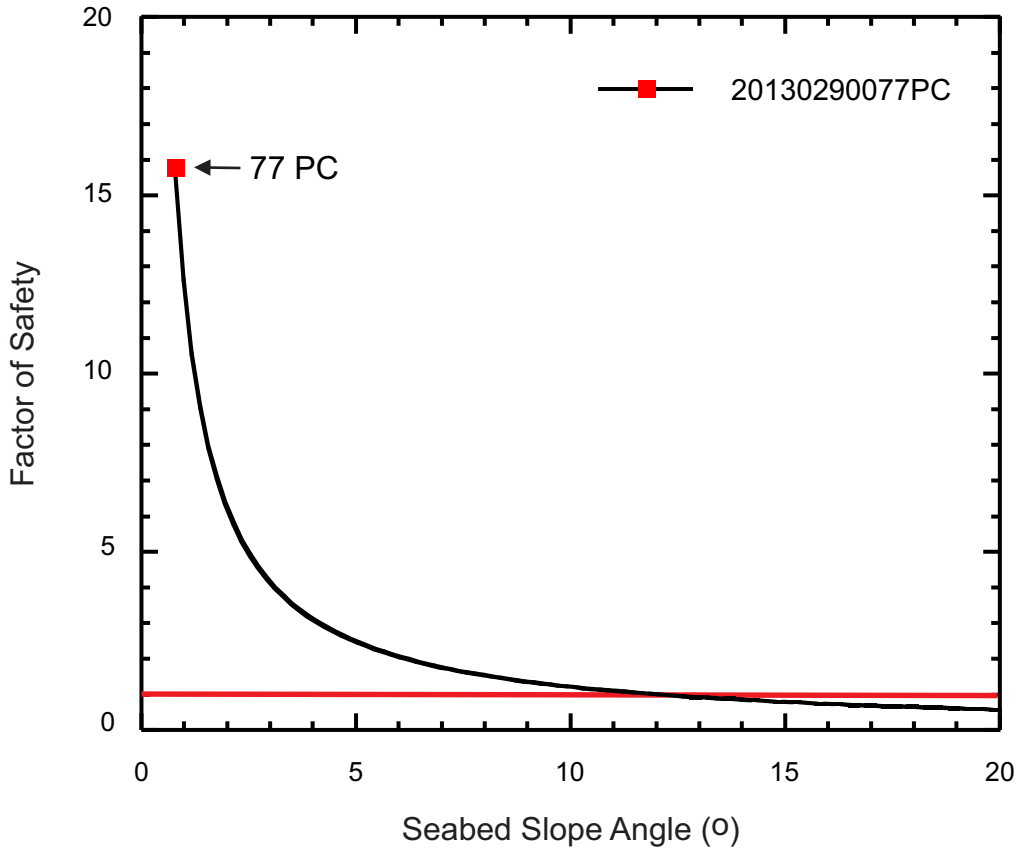

Figure 8.24. FS at various slope angles for piston core 20130290077.

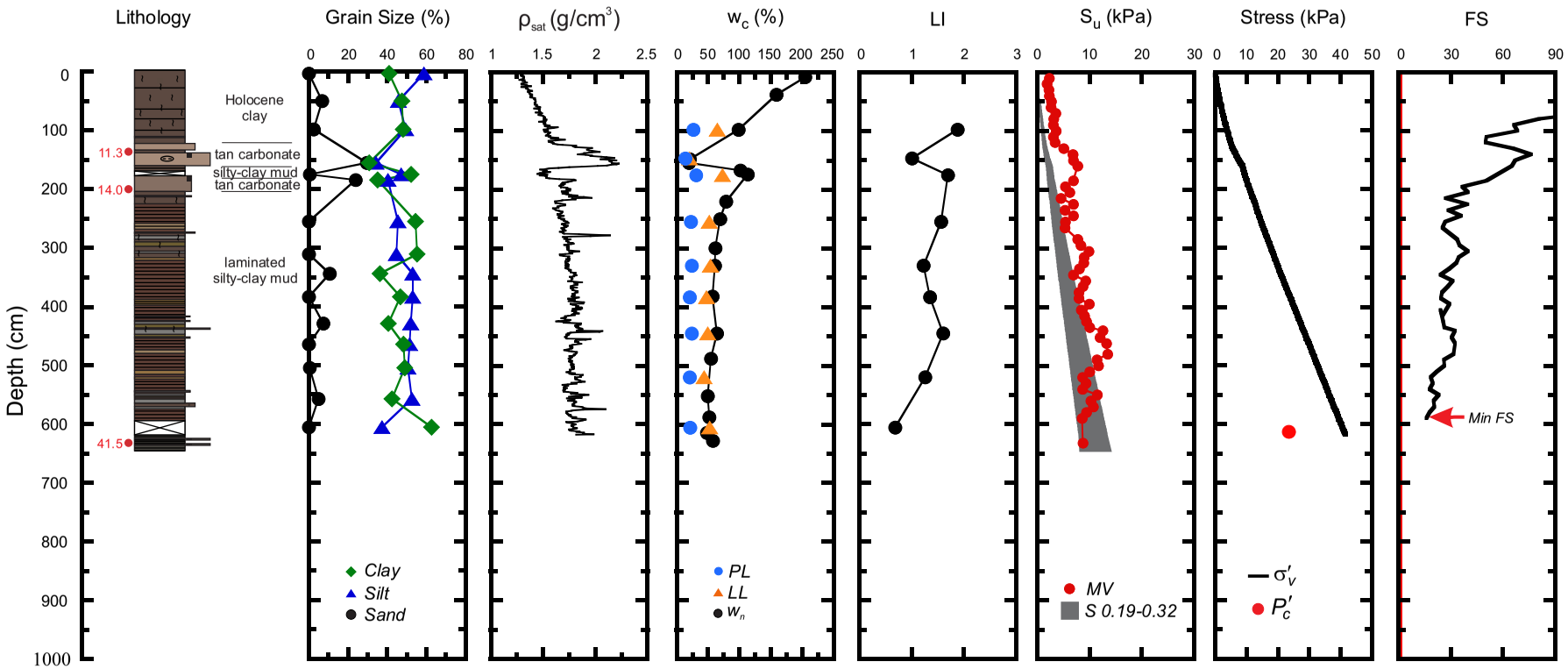

Figure 8.25. Geotechnical profile for core 20130290077 from the slope off Alexander Bank. (ρ_{sat} = saturated bulk density, w_c = water content, w_n = natural in-situ water content, *PL* = plastic limit, *LL* = liquid limit, *LI* = liquidity index, S_u = undrained shear strength, *MV* = laboratory miniature vane, *S* = shear strength calculated from the normalized strength ratio, σ'_v = effective overburden stress, P'_c = past maximum stress, *FS* = factor of safety).

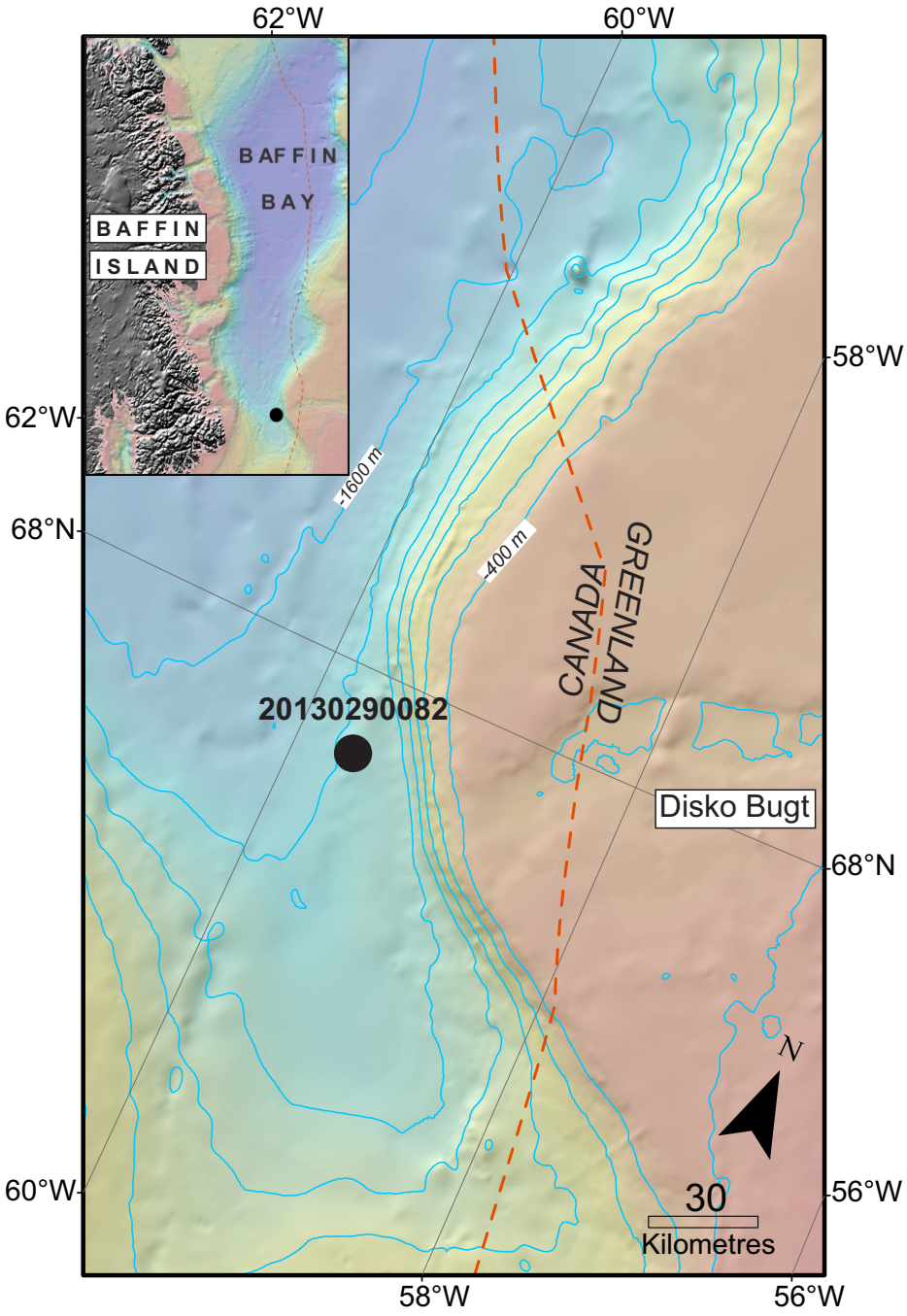

Figure 8.26. Location map of piston core 20130290082.

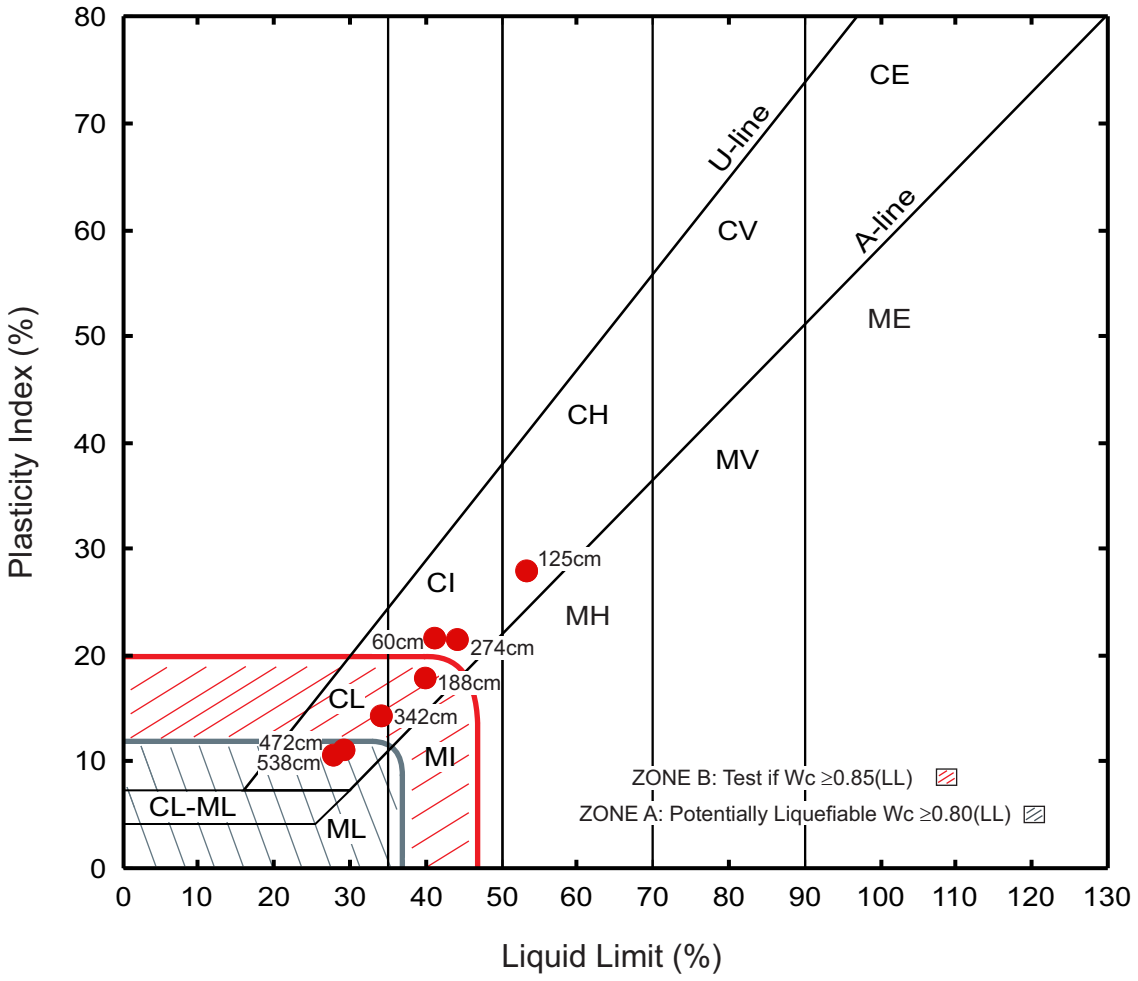

Figure 8.27. Plasticity chart showing Atterberg limit results of piston core 20130290082.

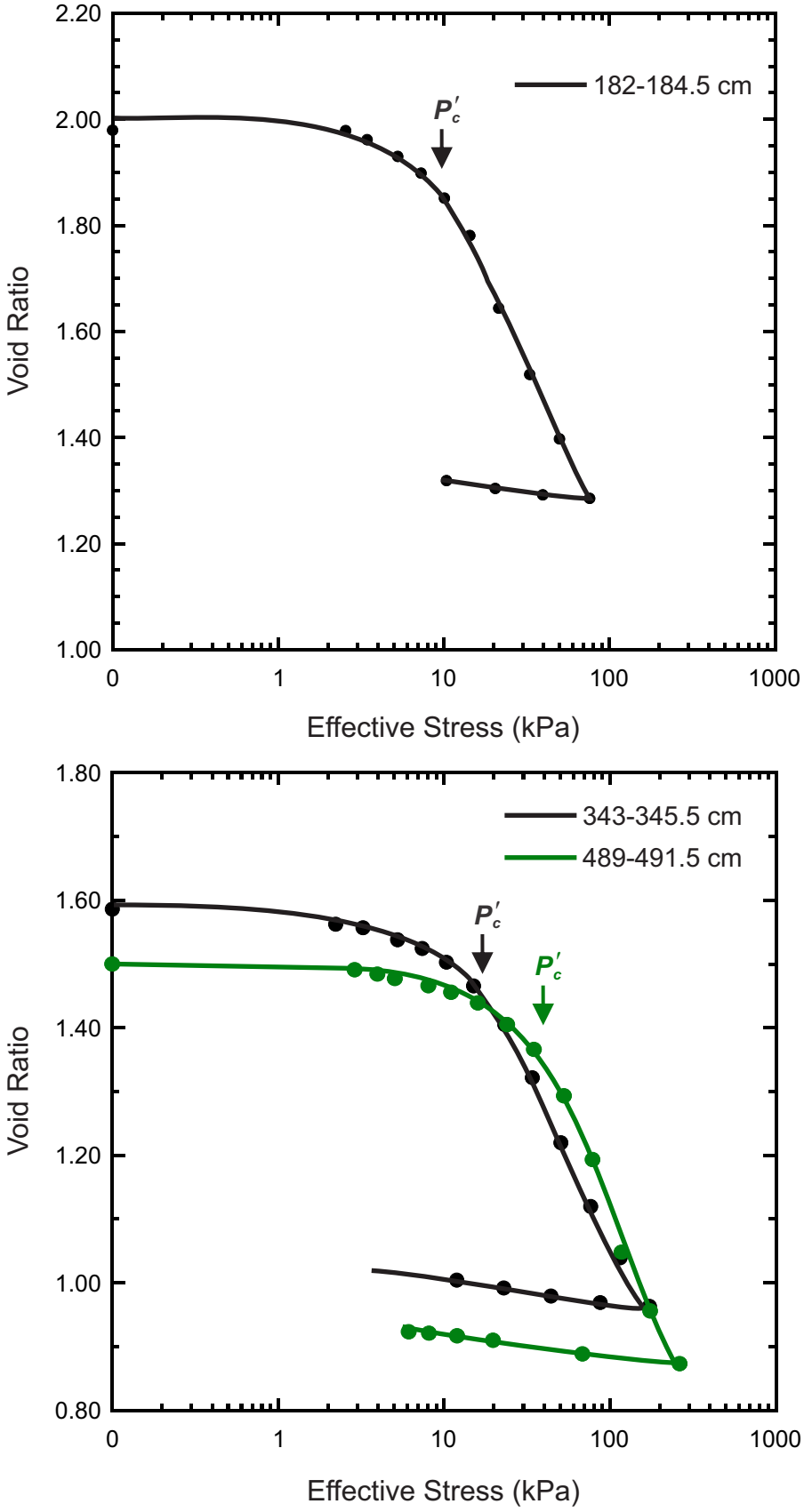

Figure 8.28. Consolidation plots for piston core 20130290082.

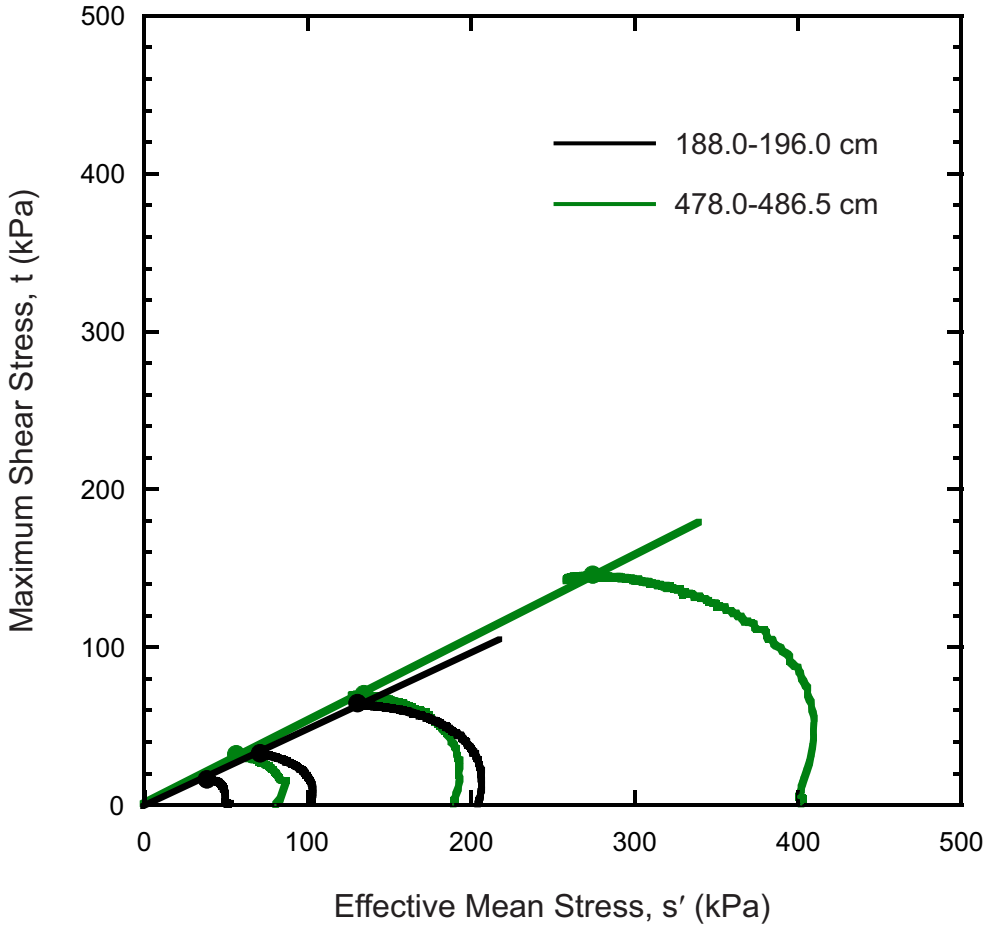

Figure 8.29. Stress paths and failure envelopes from triaxial test results for piston core 20130290082.

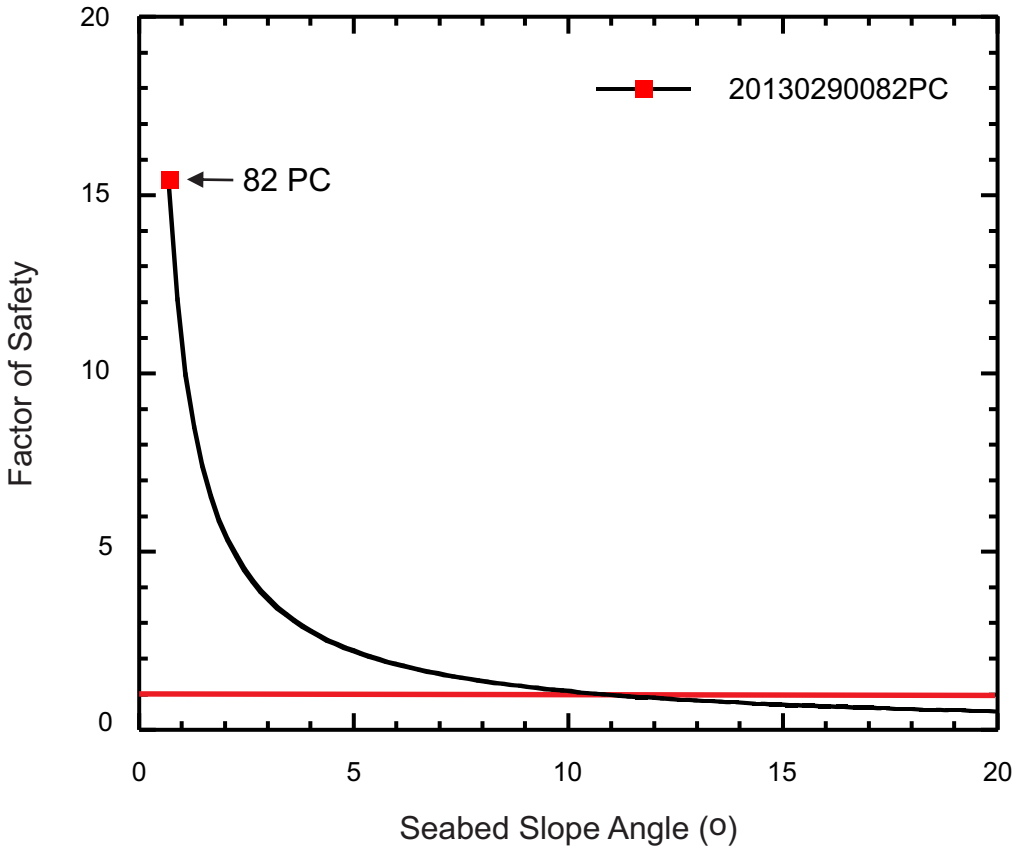

Figure 8.30. FS at various slope angles for piston core 20130290082.

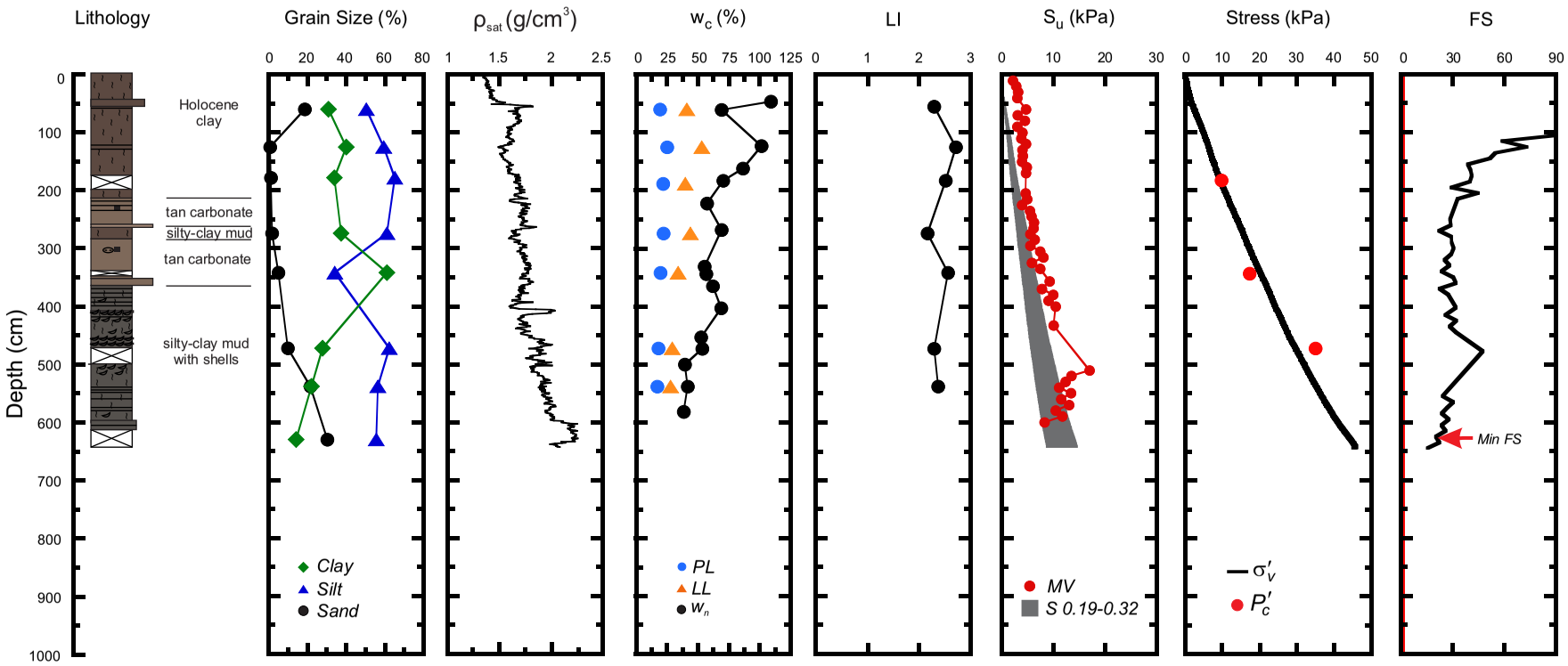

Figure 8.31. Geotechnical profile for core 20130290082 from the slope off Disko Bugt. (ρ_{sat}= saturated bulk density, w_c = water content, w_n = natural in-situ water content, *PL* = plastic limit, *LL* = liquid limit, *LI* = liquidity index, S_u = undrained shear strength, *MV* = laboratory miniature vane, *S* = shear strength calculated from the normalized strength ratio, σ'_v = effective overburden stress, P'_c = past maximum stress, *FS* = factor of safety).

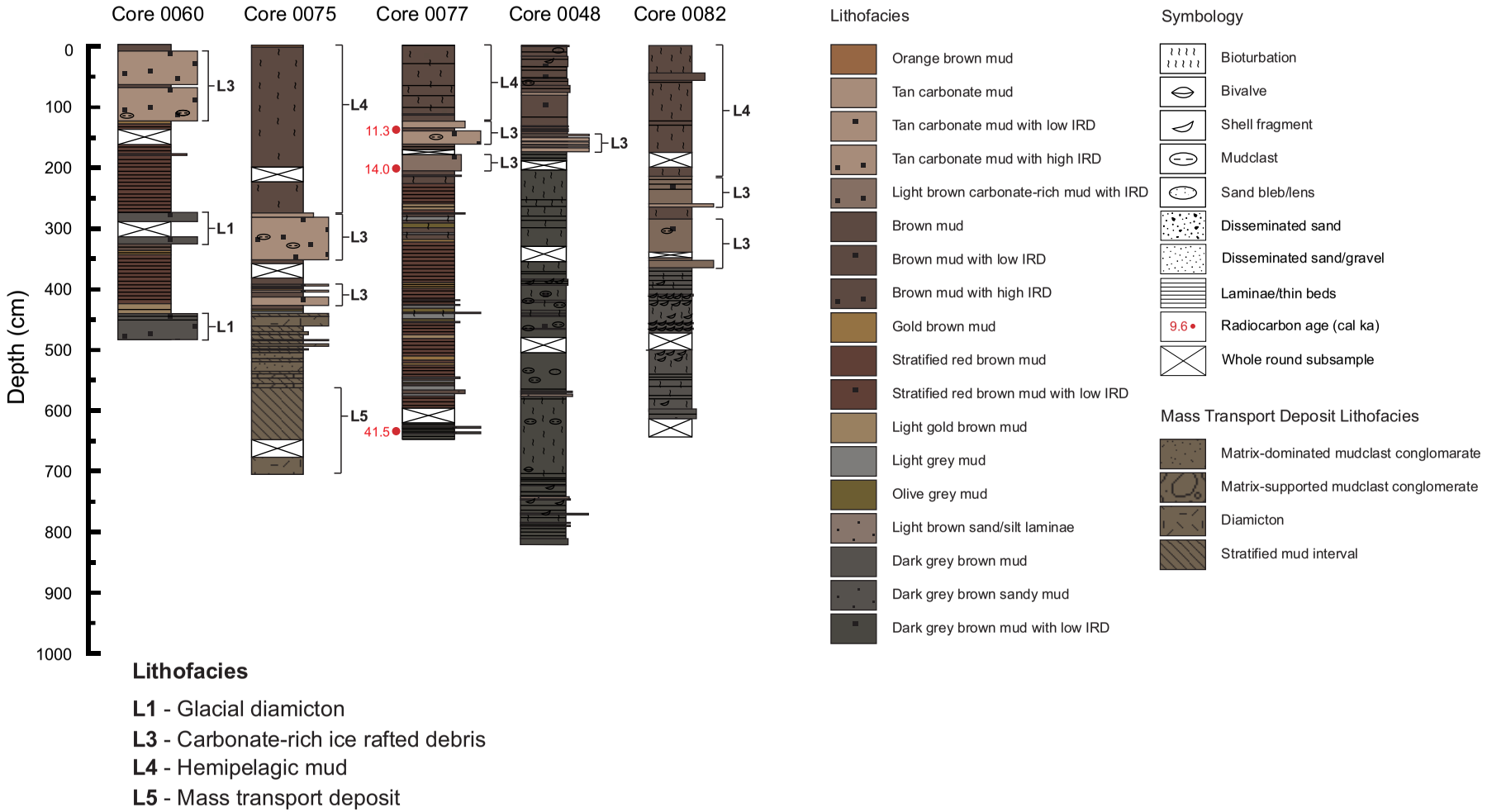

Figure 9.1. Lithofacies for the 5 geotechnical cores.

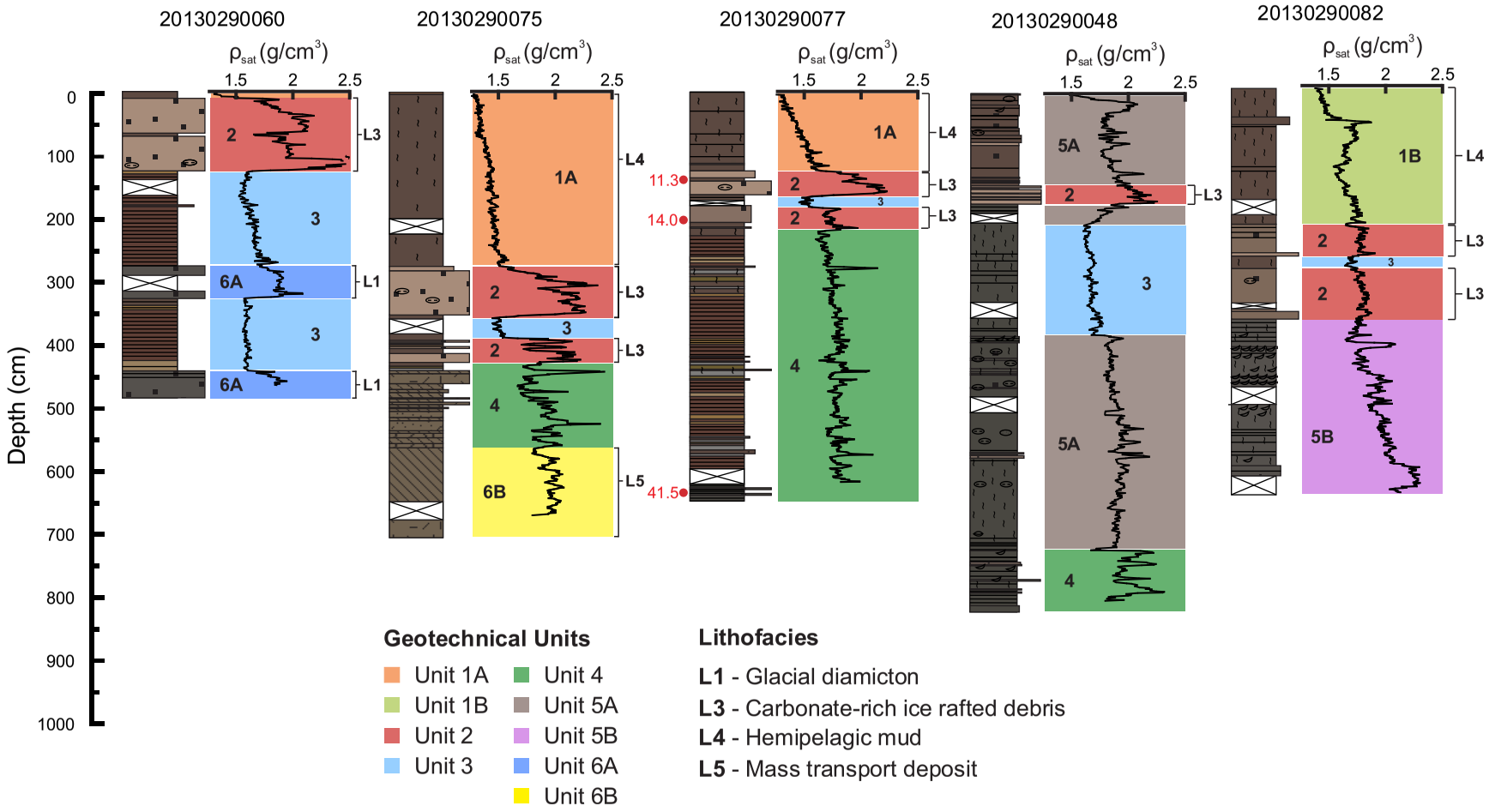

Figure 9.2. Lithologies (Jenner et al, 2018) and associated geotechnical units. Red dots signify radiocarbon age.

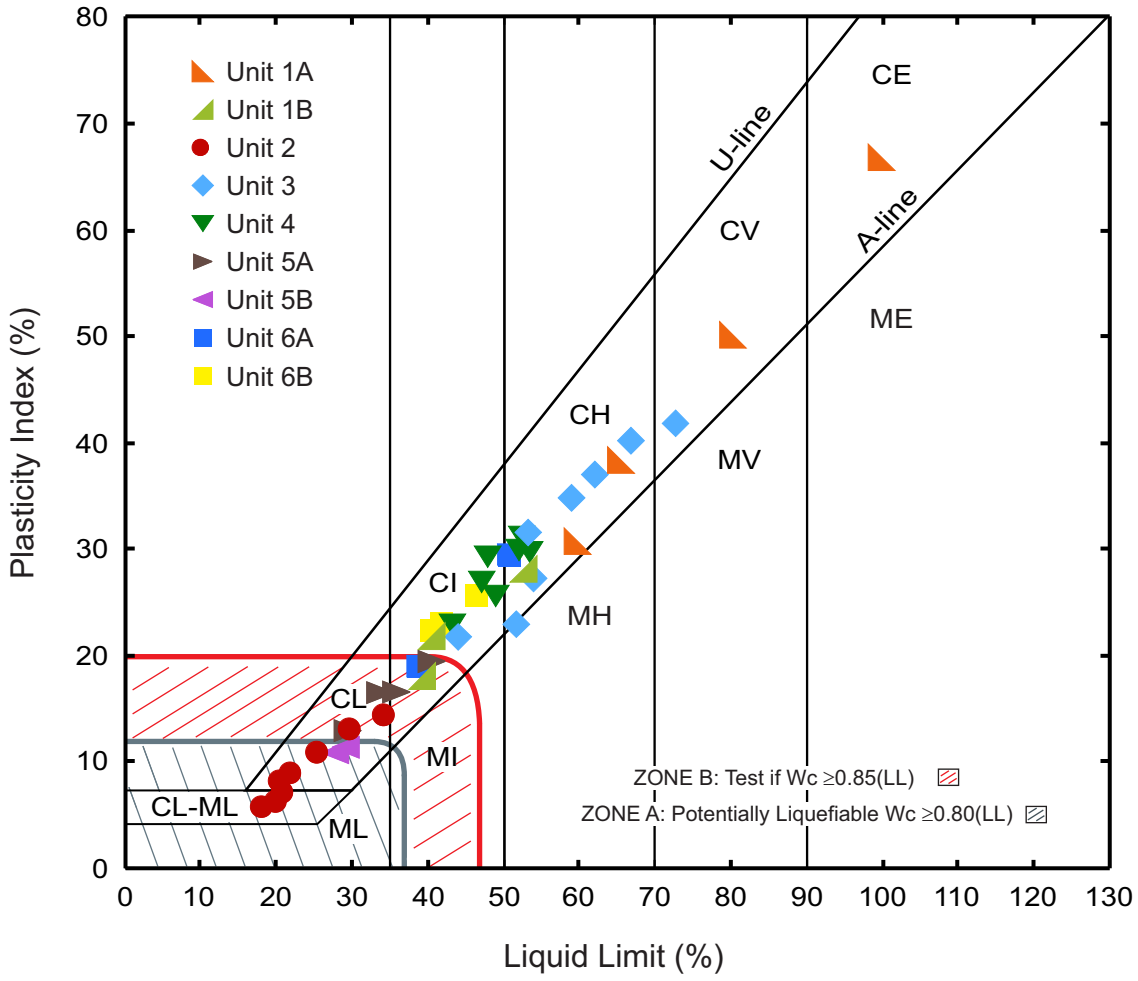

Figure 9.3. Plasticity chart showing Atterberg limit results for the geotechnical units.

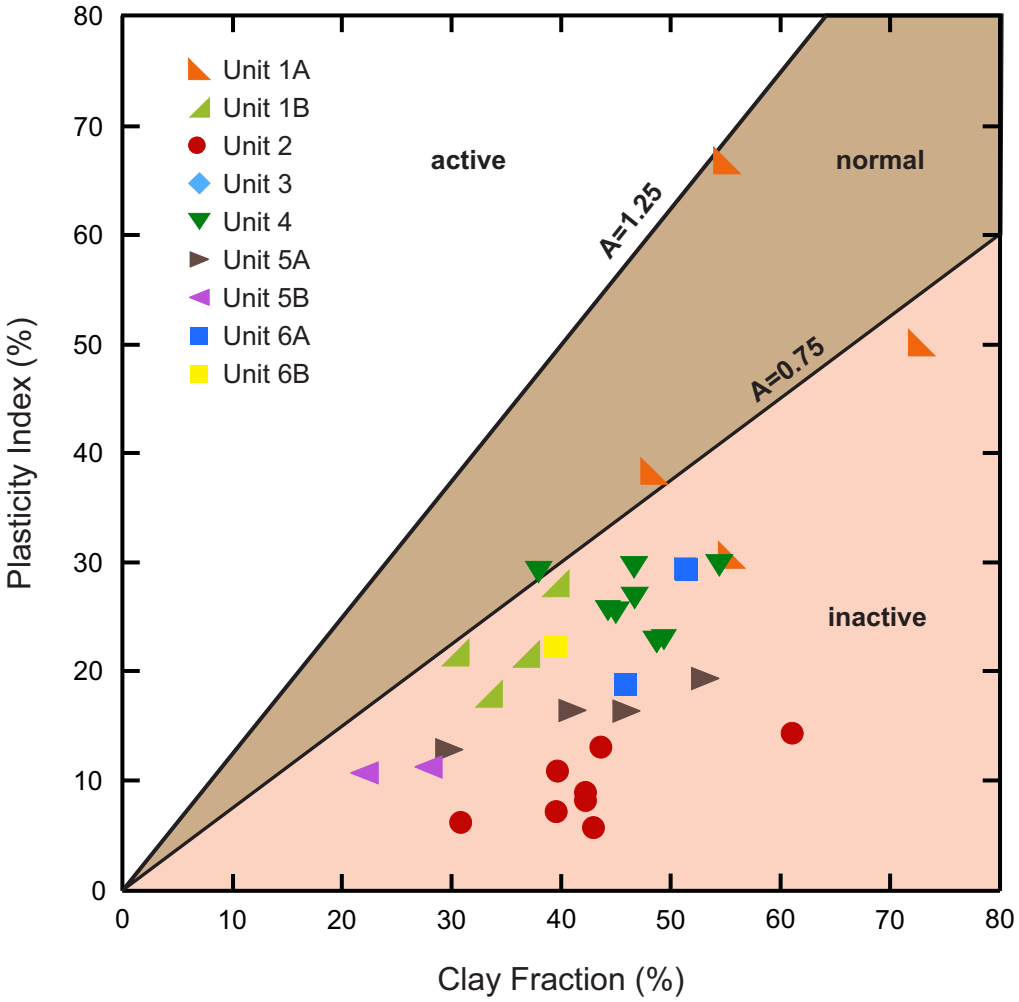

Figure 9.4. Activity chart showing results for the geotechnical units.

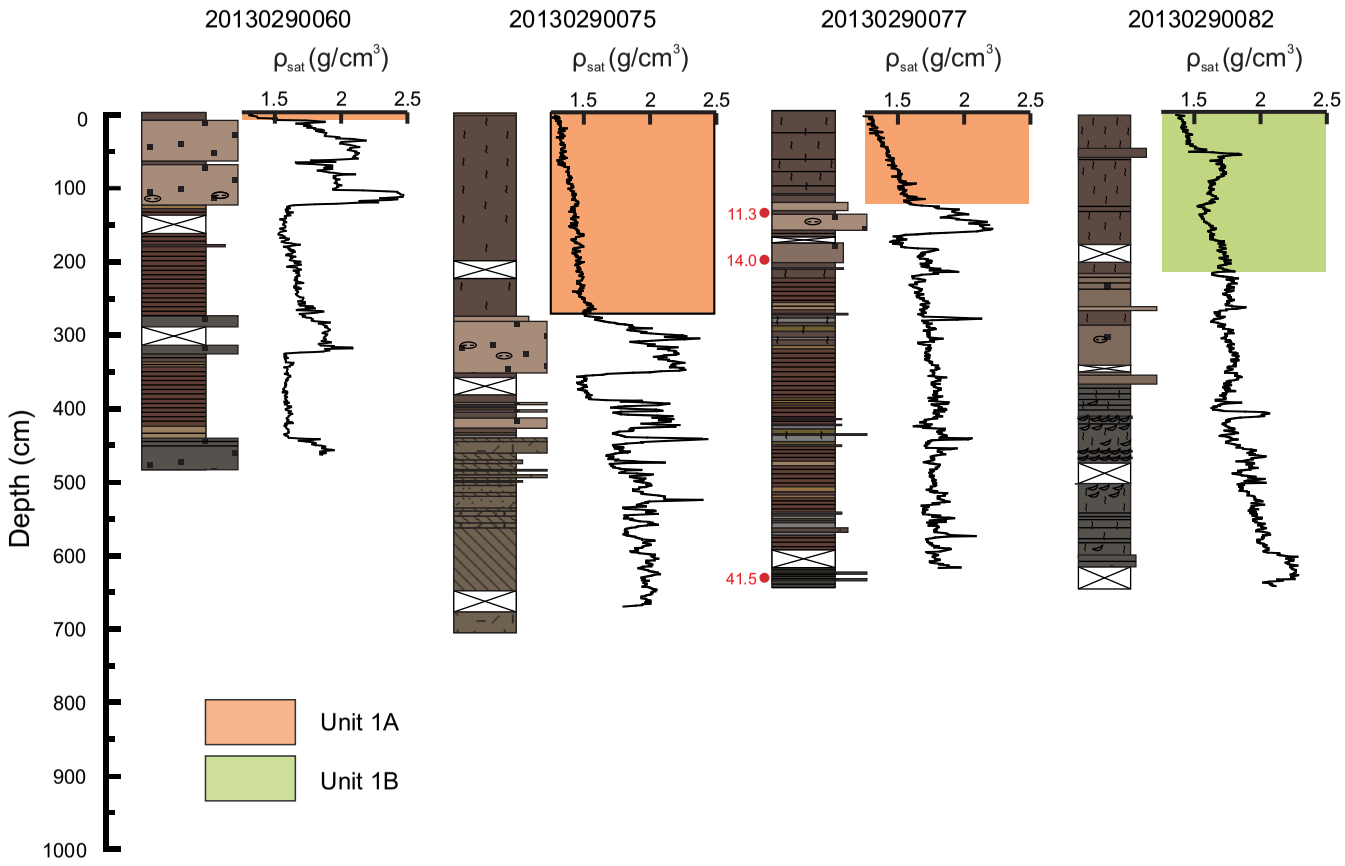

Figure 9.5. Lithology and MSCL bulk density (g/cm^3) profiles with geotechnical Unit 1A (orange rectangles) and 1B (green rectangle). The red dots signify radiocarbon ages.

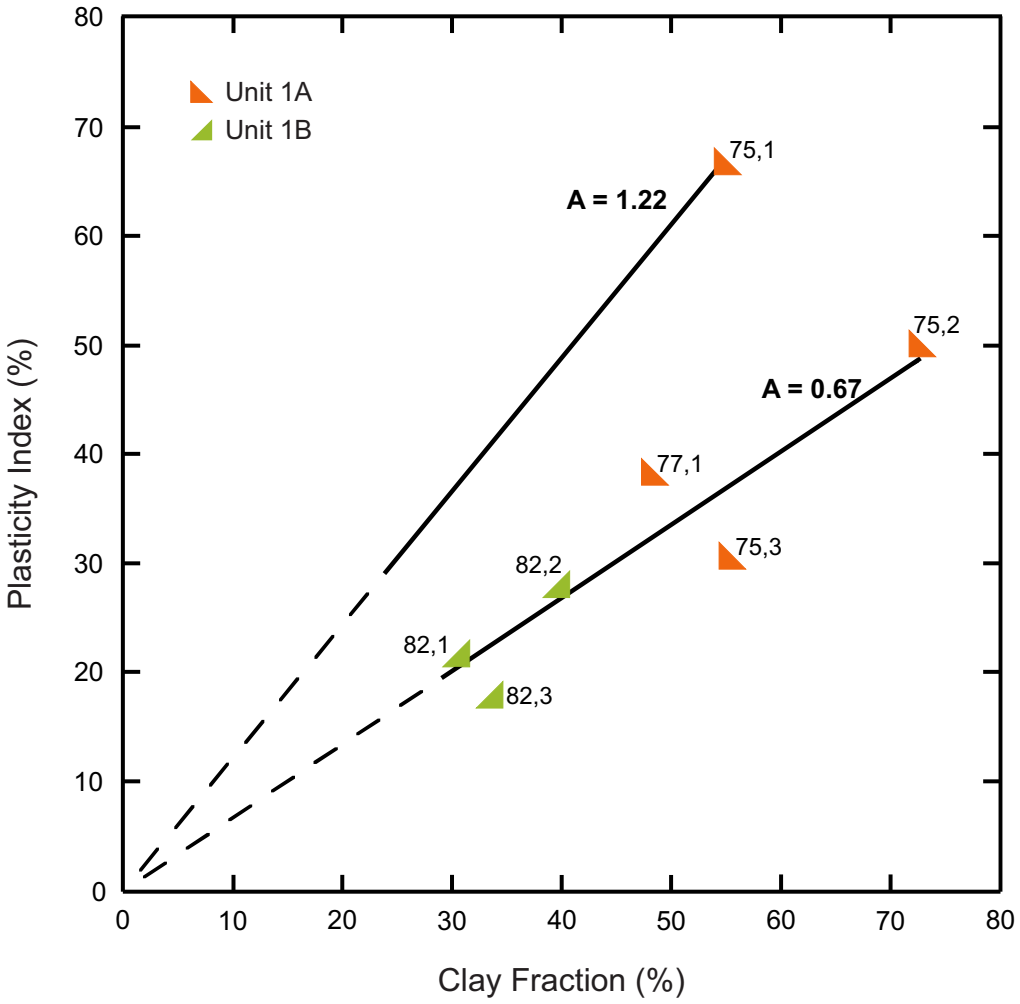

Figure 9.6. Activity chart showing results for Unit 1A and 1B. The first number denotes the core number and the second number denotes the down core Atterberg limit test sequence.

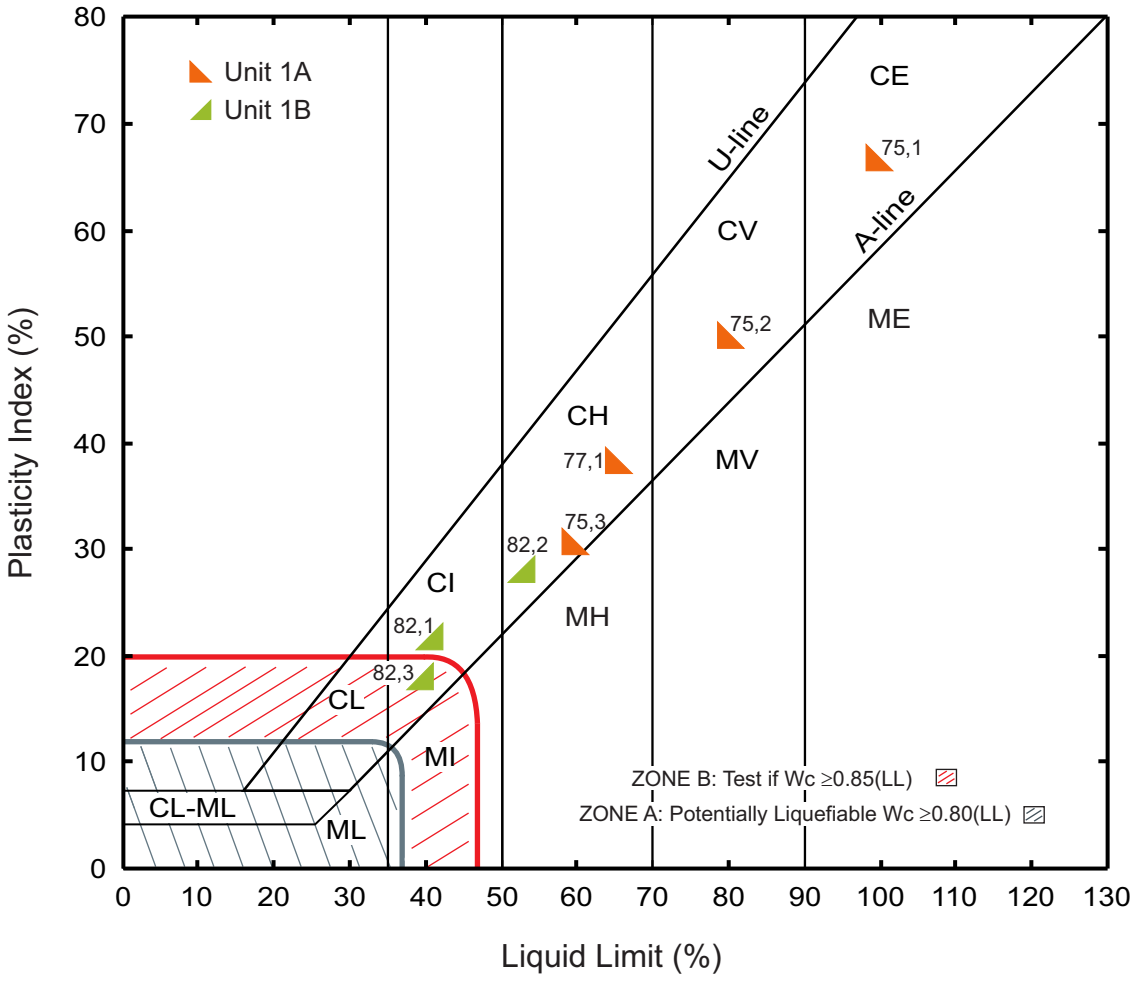

Figure 9.7. Plasticity chart showing Atterberg limit results for Unit 1A and 1B. The first number denotes the core number and the second number denotes the down core Atterberg limit test sequence.

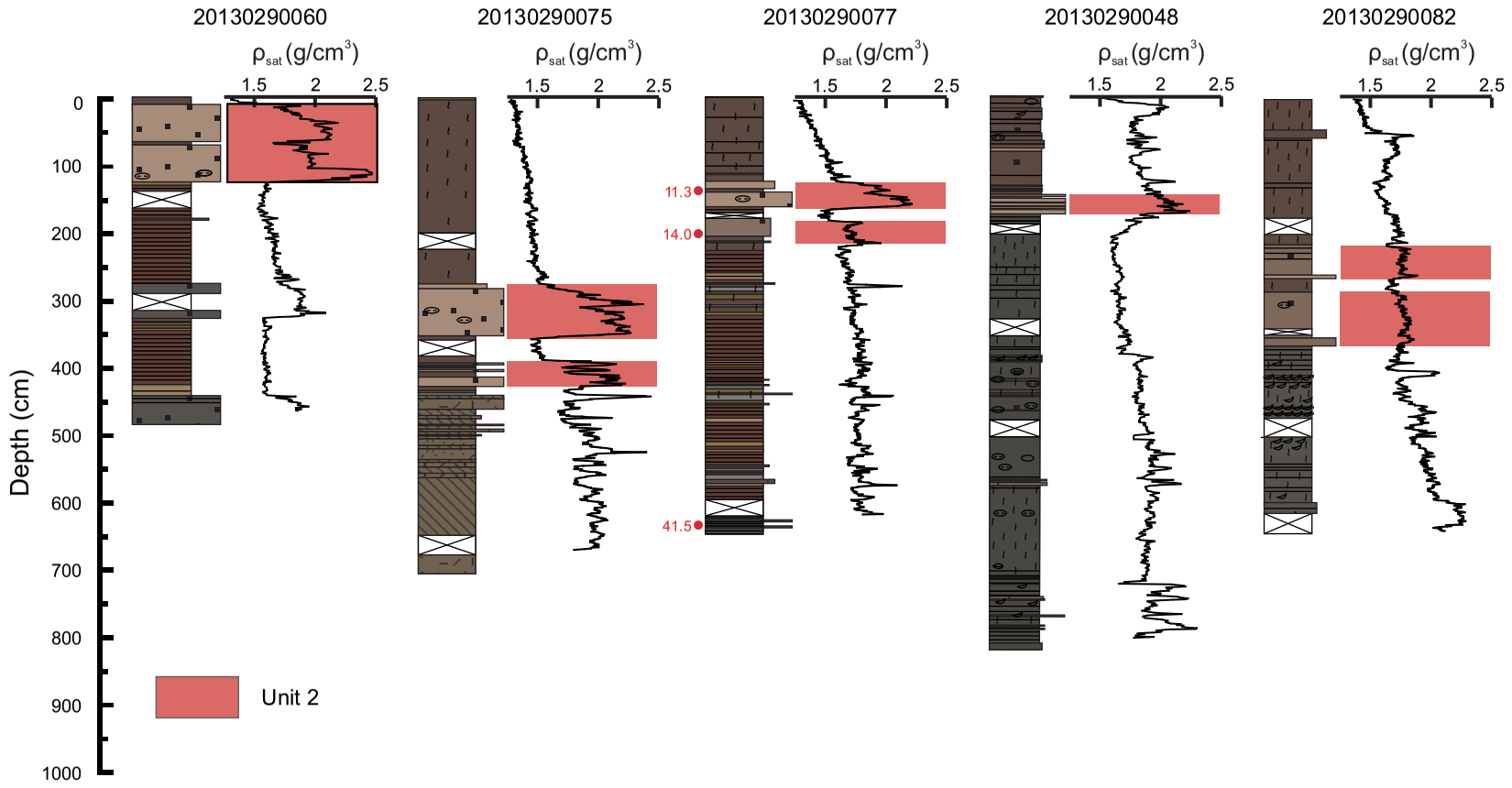

Figure 9.8. Lithology and MSCL bulk density (g/cm^3) profiles with geotechnical Unit 2 shown in red rectangles. Red dots signify radiocarbon age.

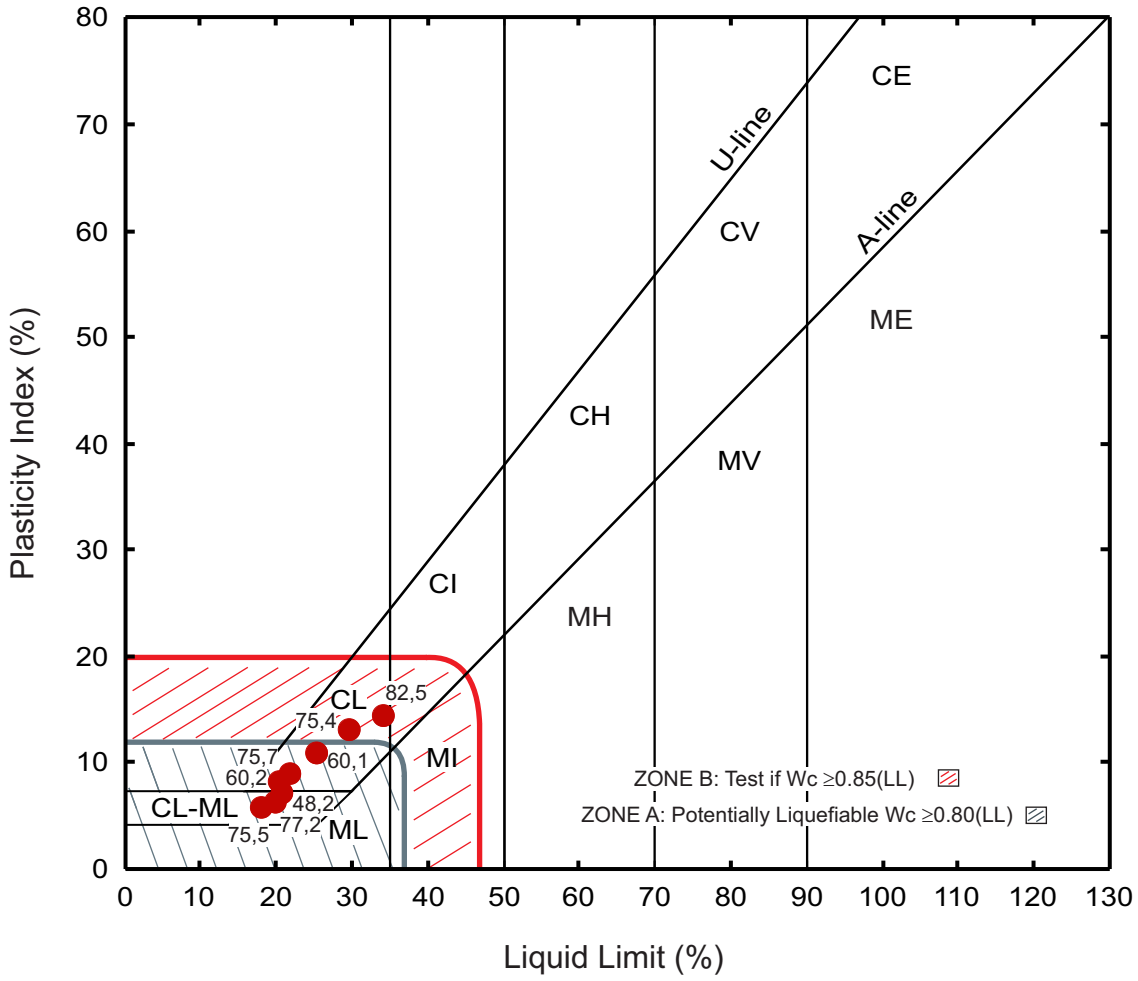

Figure 9.9. Plasticity chart showing Atterberg limit results for Unit 2. The first number denotes the core number and the second number denotes the down core Atterberg limit test sequence.

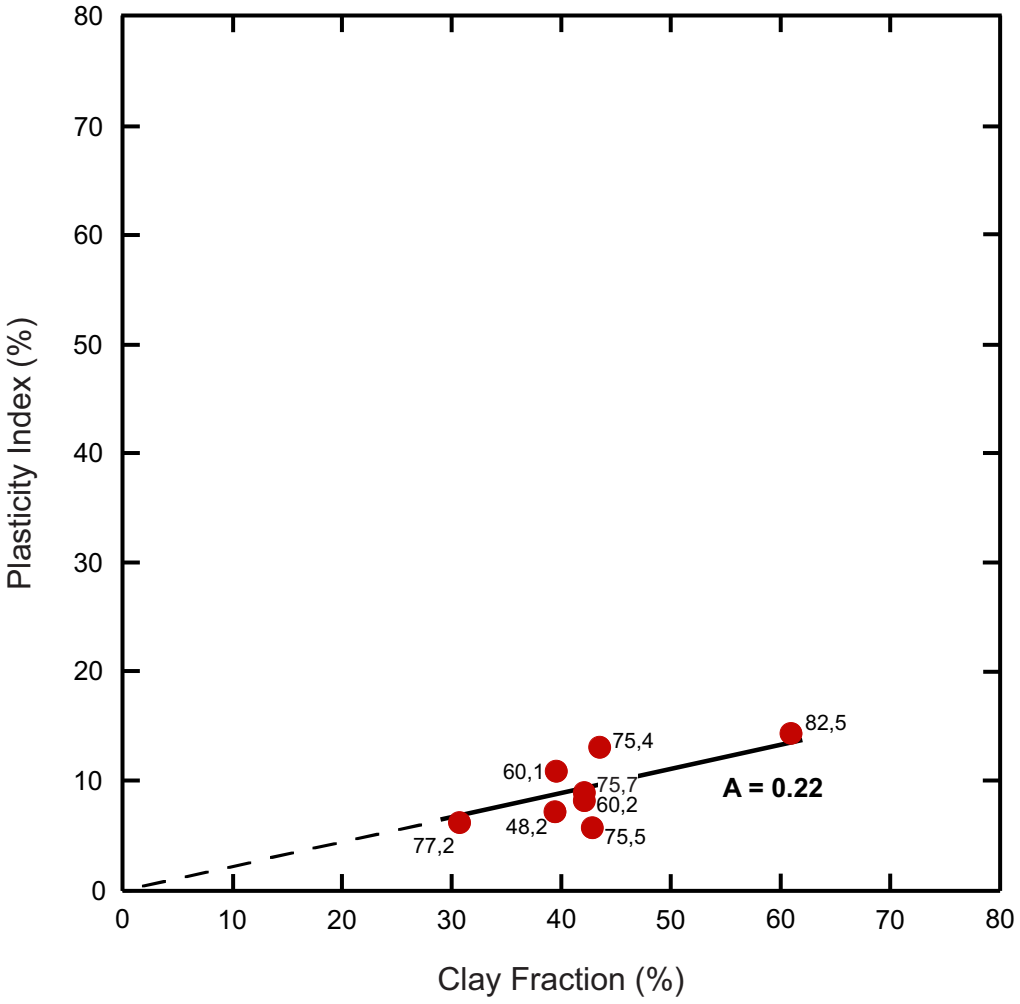

Figure 9.10. Activity chart showing results for Unit 2. The first number denotes the core number and the second number denotes the down core Atterberg limit test sequence.

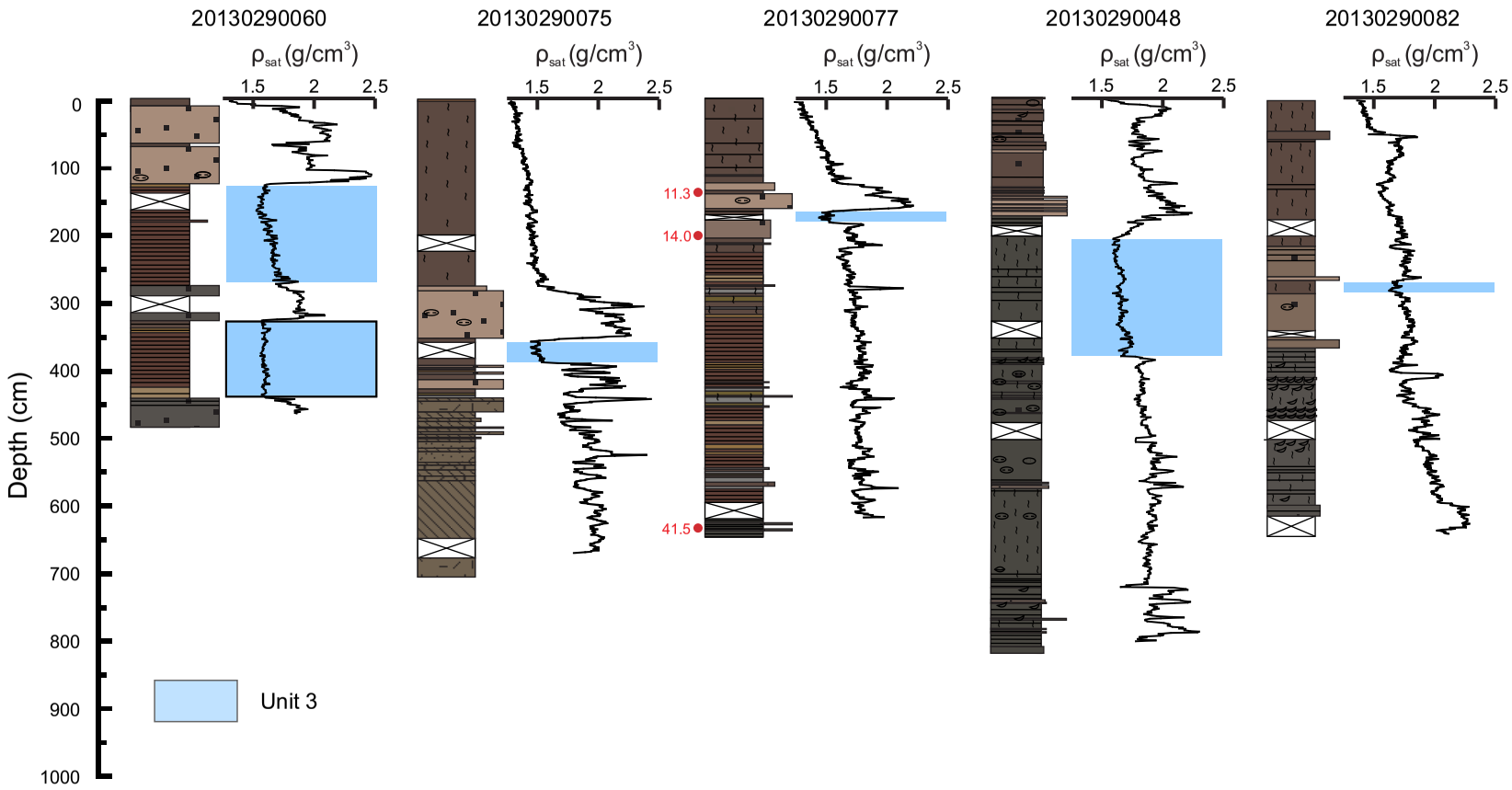

Figure 9.11. Lithology and MSCL bulk density (g/cm^3) profiles with geotechnical Unit 3 shown in blue rectangles. Red dots signify radiocarbon age.

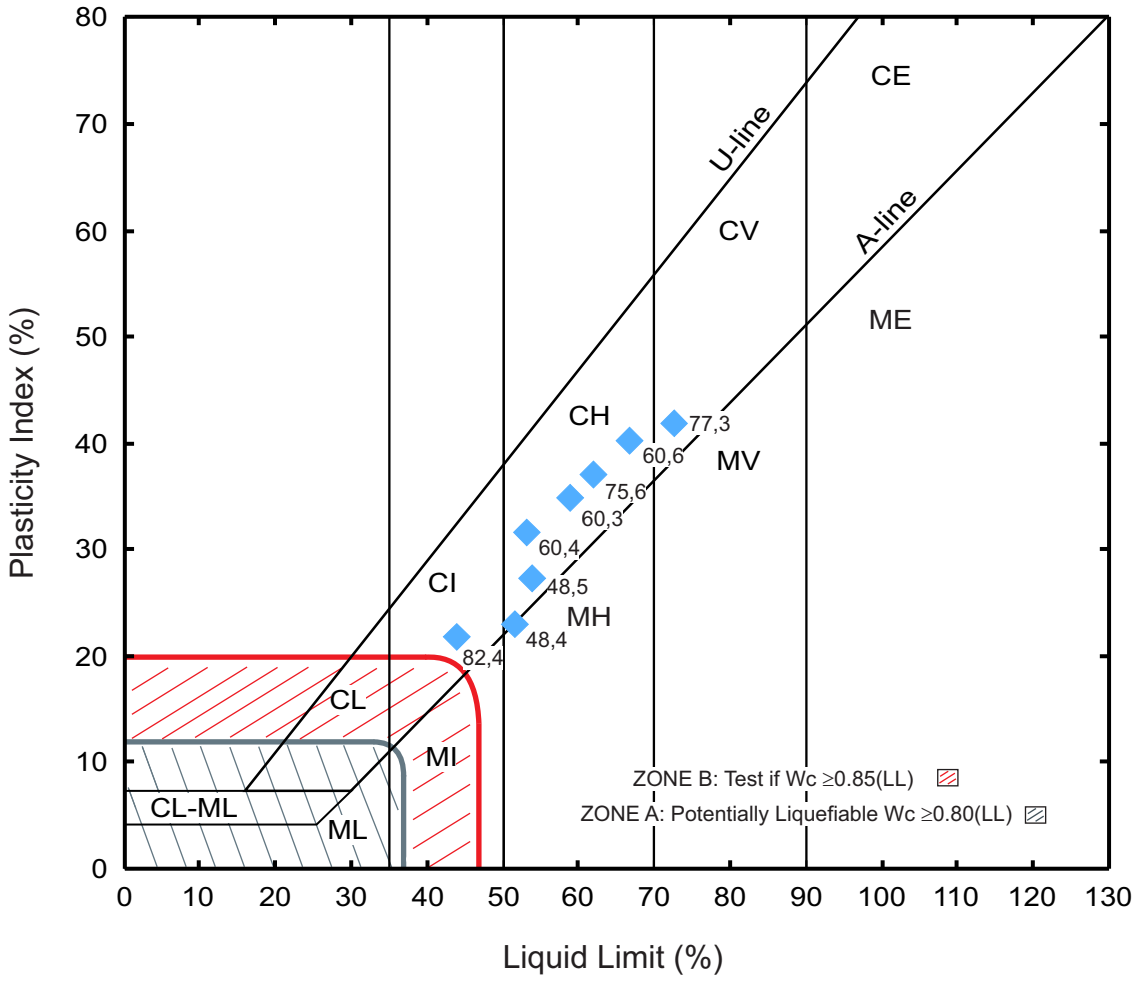

Figure 9.12. Plasticity chart showing Atterberg limit results for Unit 3. The first number denotes the core number and the second number denotes the down core Atterberg limit test sequence.

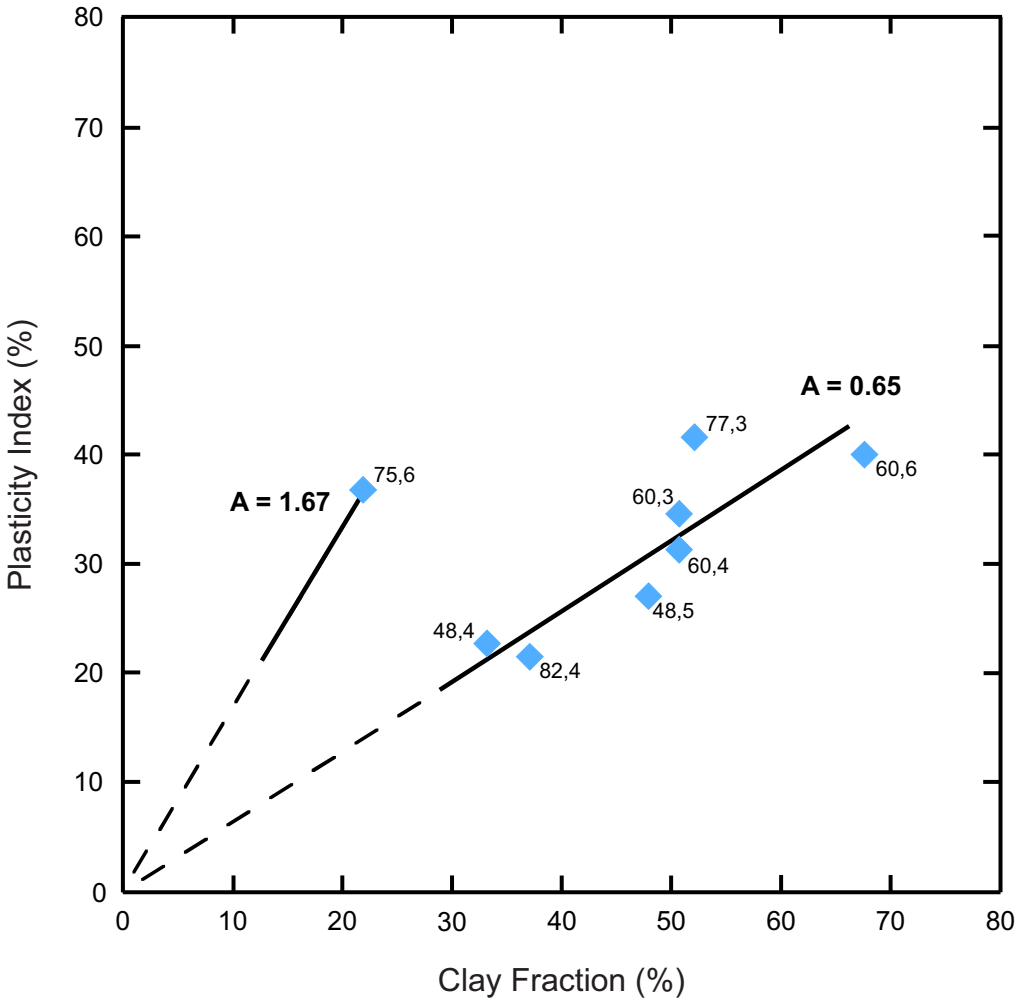

Figure 9.13. Activity chart showing results for Unit 3. The first number denotes the core number and the second number denotes the down core Atterberg limit test sequence.

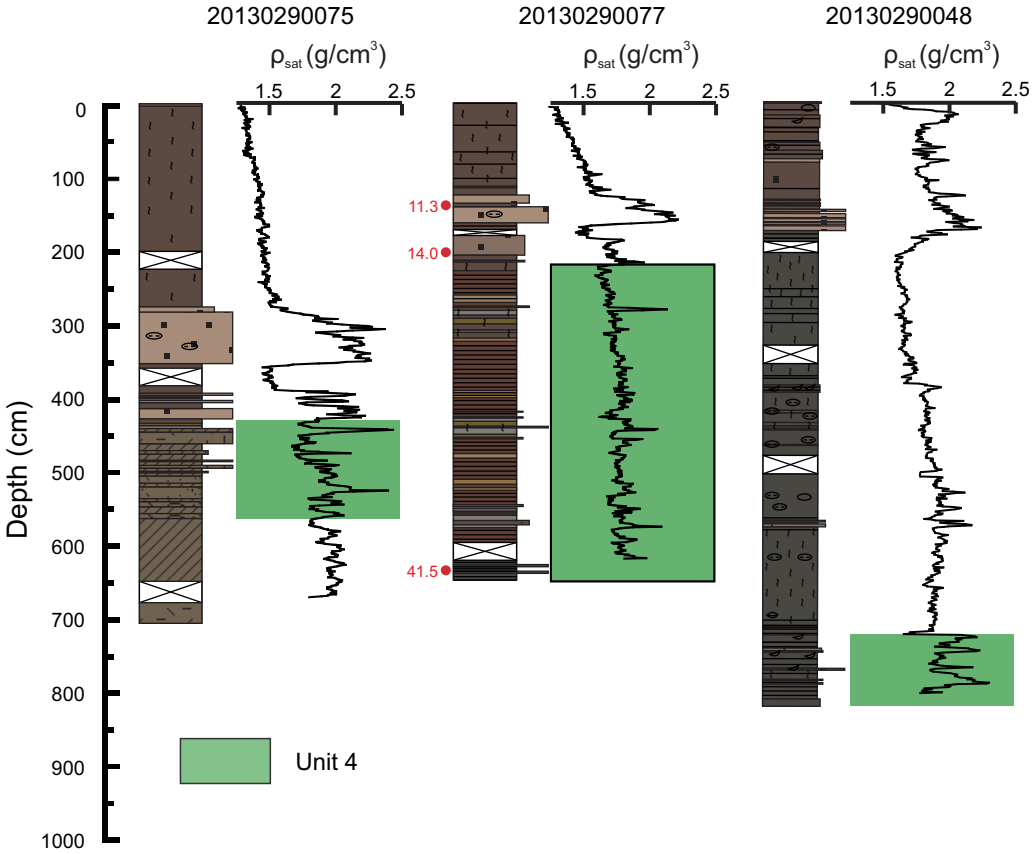

Figure 9.14. Lithology and MSCL bulk density (g/cm^3) profiles with geotechnical Unit 4 shown in green rectangles. Red dots signify radiocarbon age.

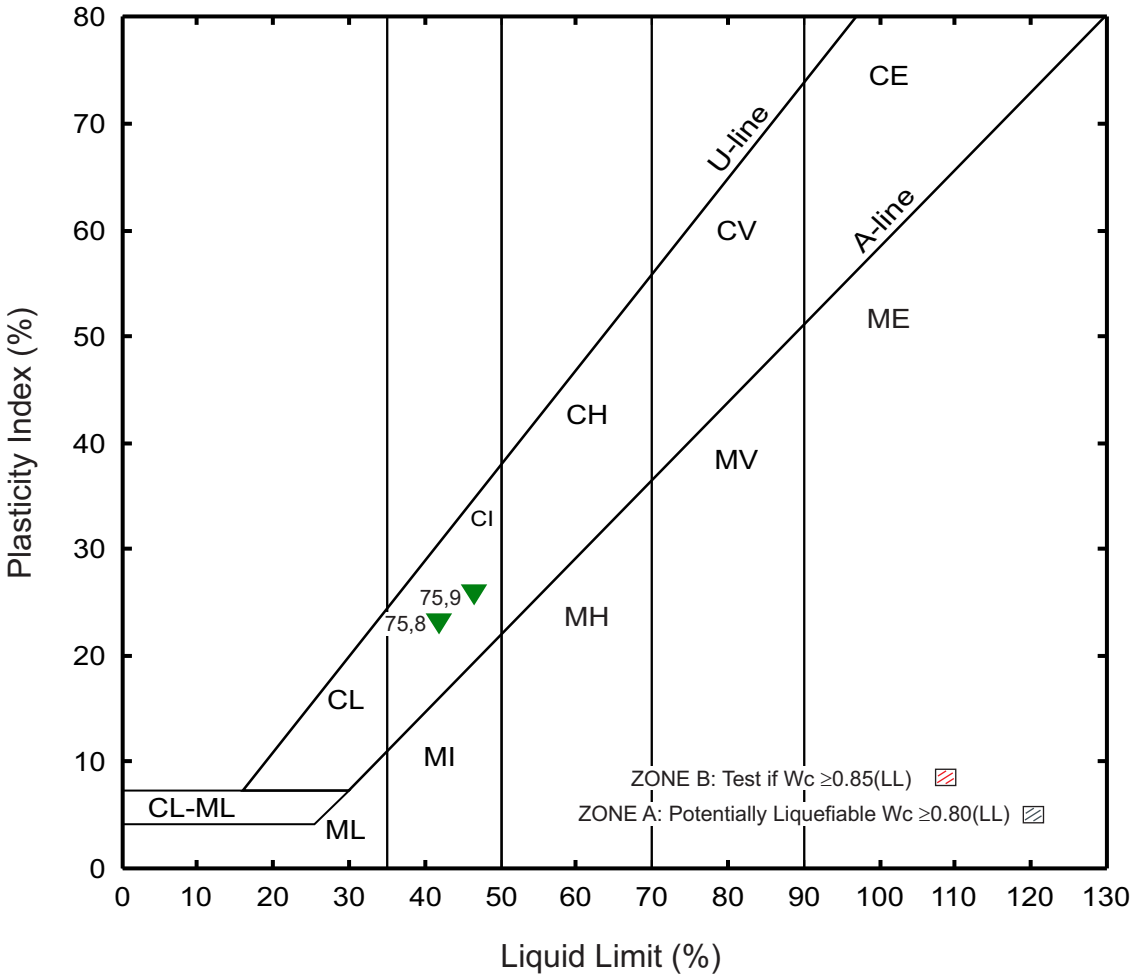

Figure 9.15. Plasticity chart showing Atterberg limit results for Unit 4. The first number denotes the core number and the second number denotes the down core Atterberg limit test sequence.

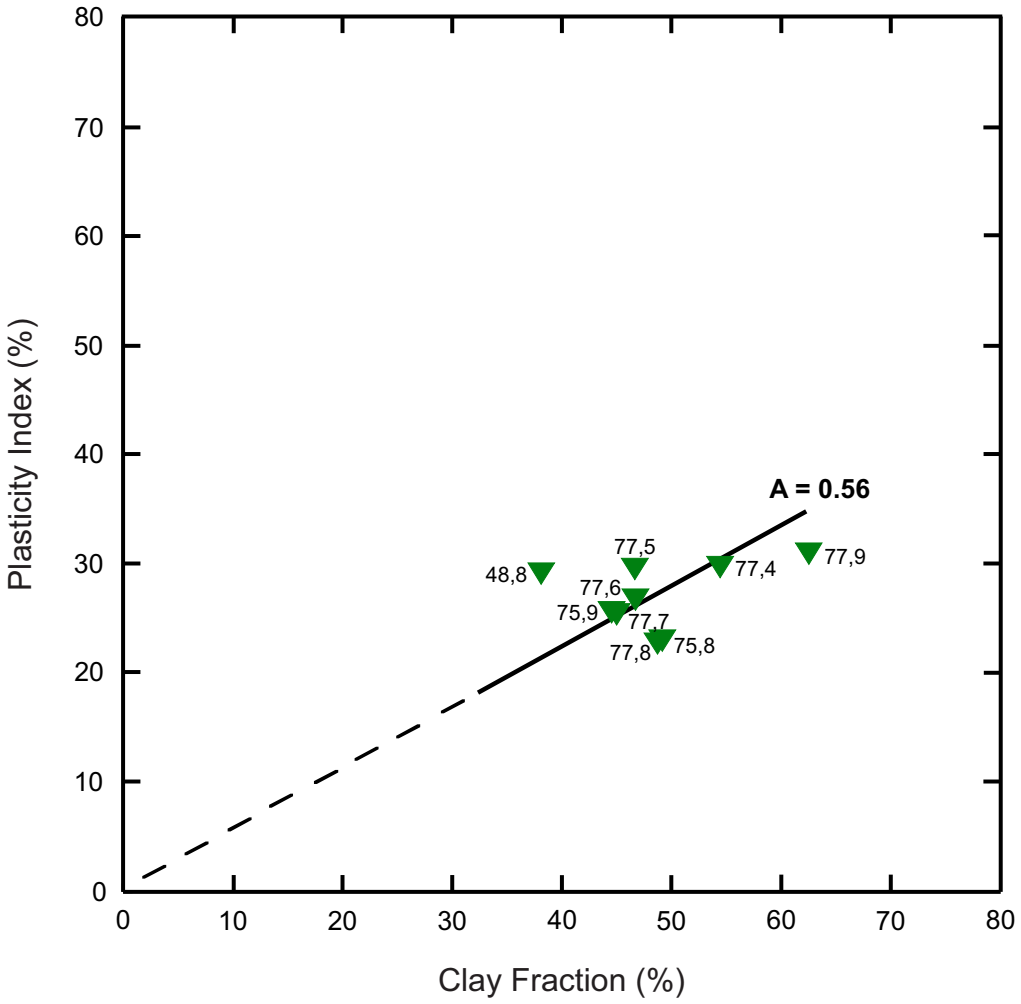

Figure 9.16. Activity chart showing results for Unit 4. The first number denotes the core number and the second number denotes the down core Atterberg limit test sequence.

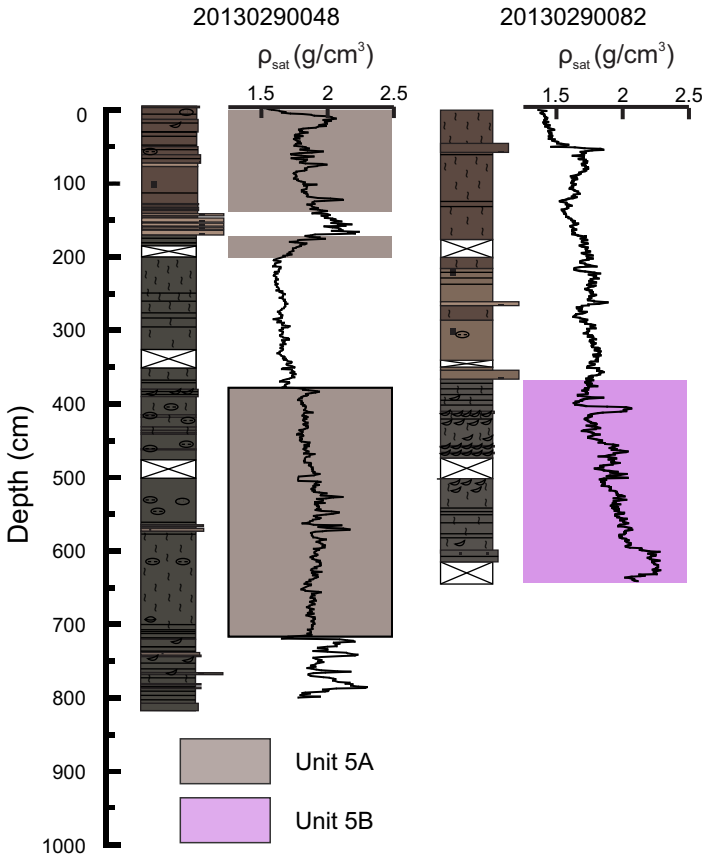

Figure 9.17. Lithology and MSCL bulk density (g/cm^3) profiles with geotechnical Unit 5A (brown rectangles) and 5B (purple rectangle).

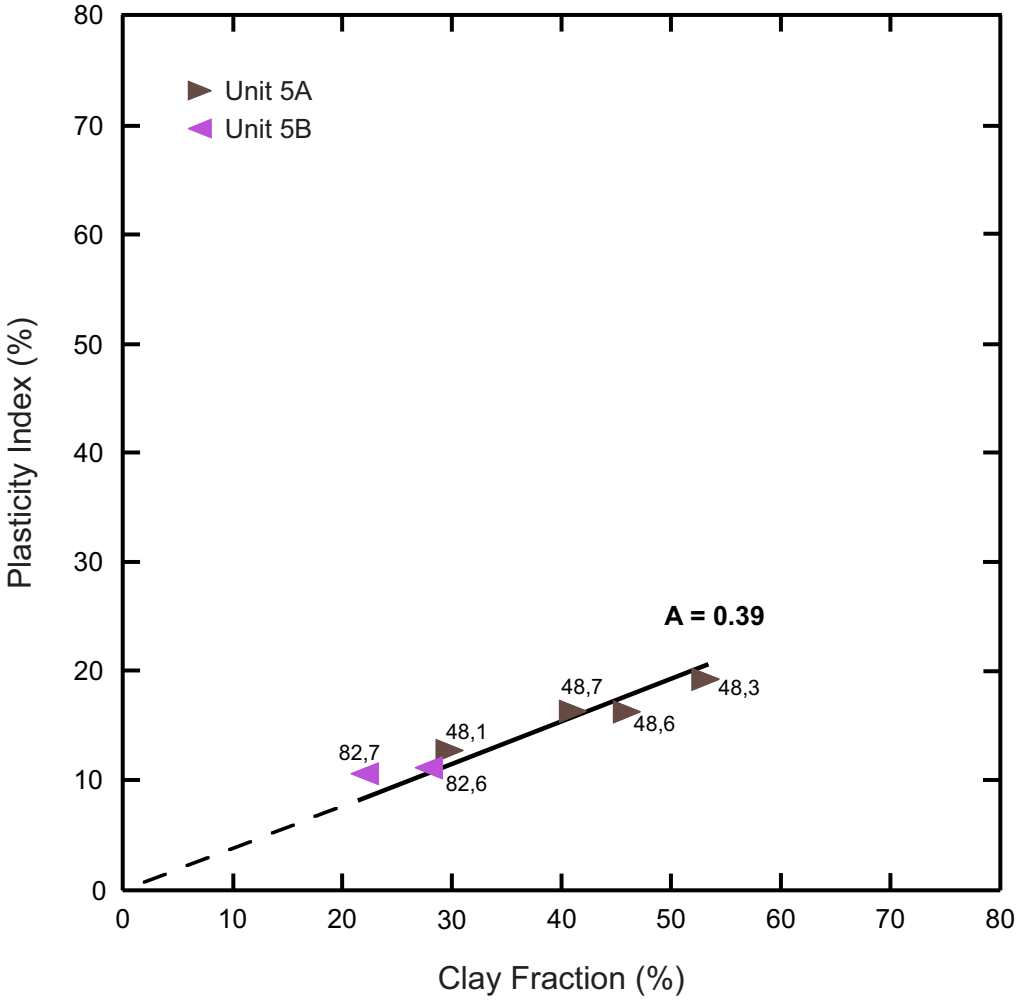

Figure 9.18. Activity chart showing results for Unit 5A and 5B. The first number denotes the core number and the second number denotes the down core Atterberg limit test sequence.

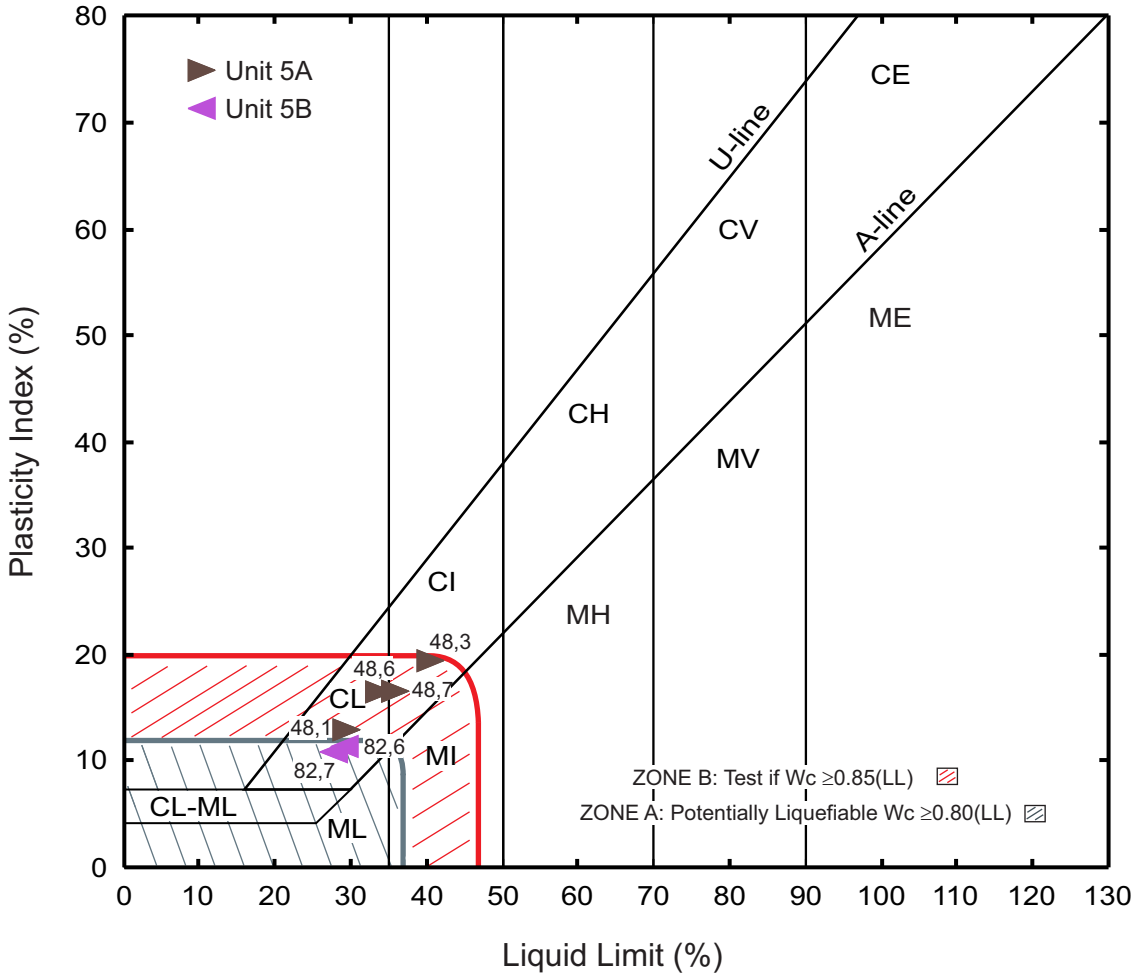

Figure 9.19. Plasticity chart showing Atterberg limit results for Unit 5A and 5B. The first number denotes the core number and the second number denotes the down core Atterberg limit test sequence.

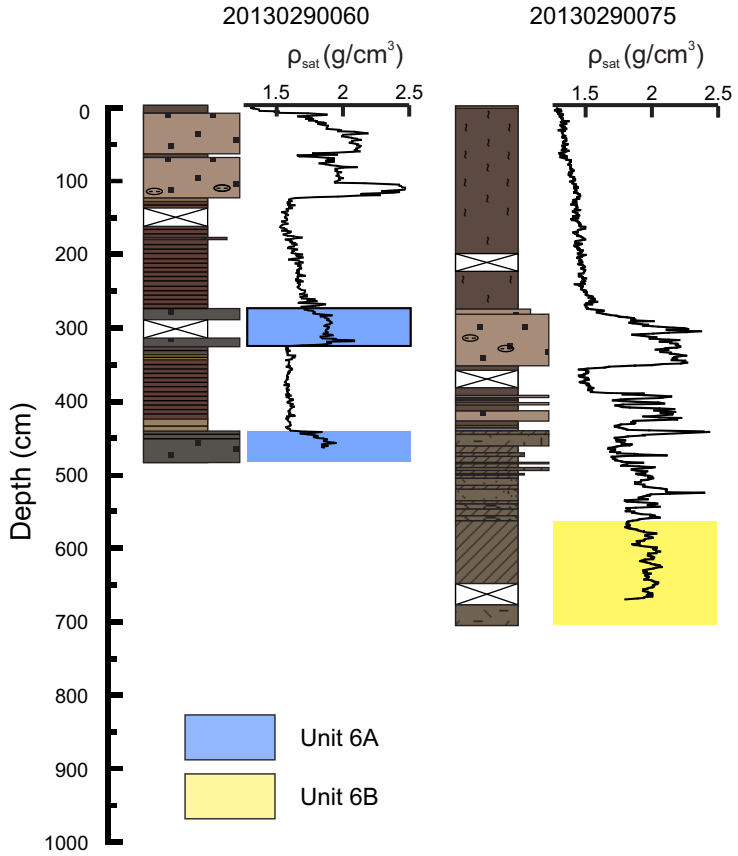

Figure 9.20. Lithology and MSCL bulk density (g/cm^3) profiles with geotechnical Unit 6A (blue rectangles) and 6B (yellow rectangle).

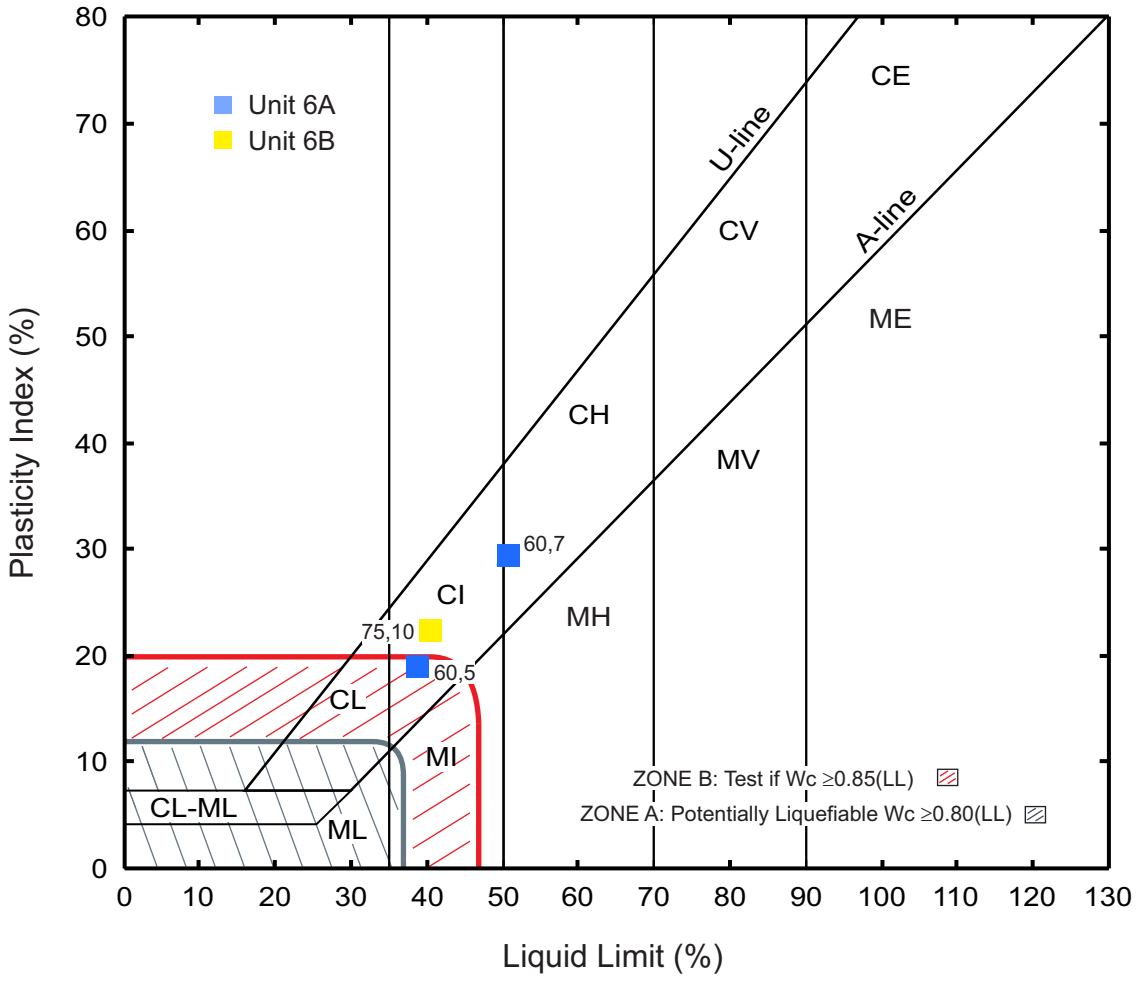

Figure 9.21. Plasticity chart showing Atterberg limit results for Unit 6. The first number denotes the core number and the second number denotes the down core Atterberg limit test sequence.

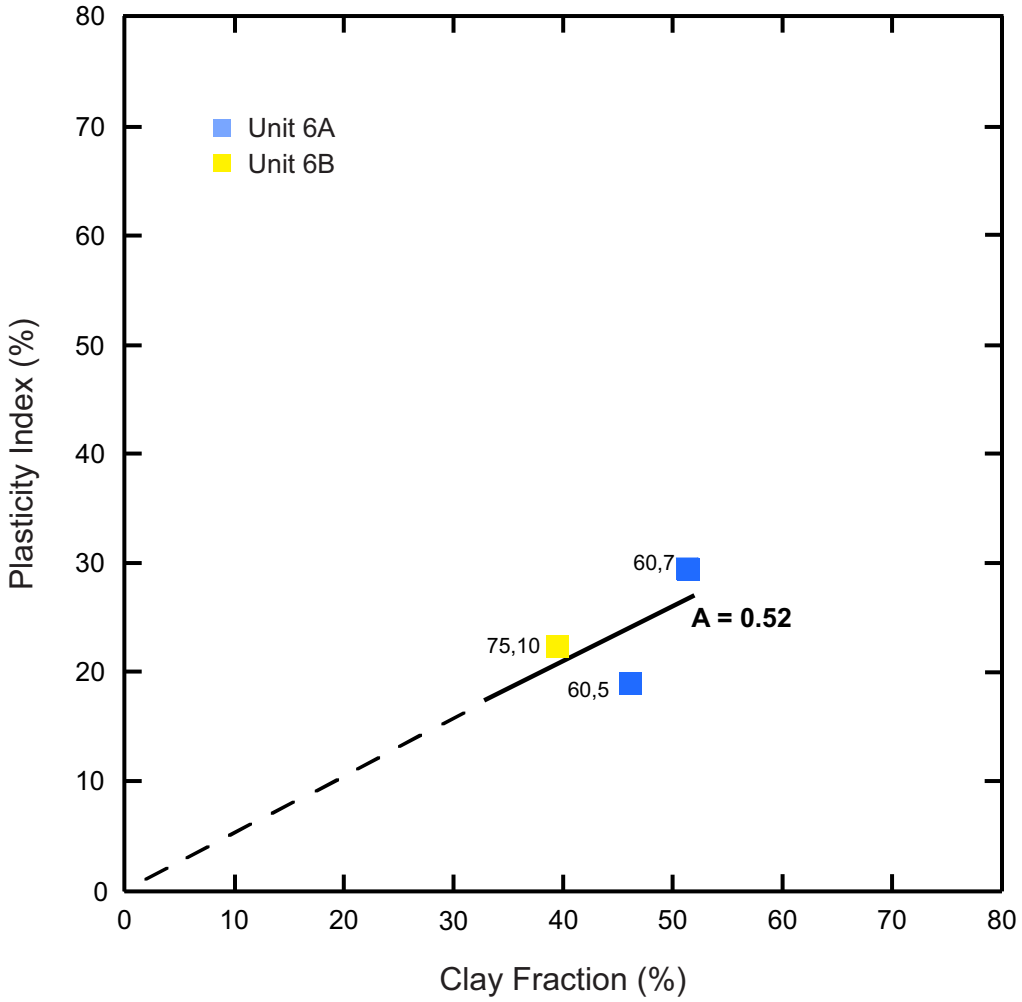

Figure 9.22. Activity chart showing results for Unit 6. The first number denotes the core number and the second number denotes the down core Atterberg limit test sequence.

Table 8.1. A summary of the number of geotechnical tests conducted for the five cores.

Core Number	Latitude (°)	Longitude (°)	Core Length (cm)	Water Contents	Atterberg limits	Grain Size	Triaxial	Consolidation
20130290048	67.605618	-61.967451	805	19	8	10	2	3
20130290060	71.867328	-70.867066	469	12	7	13	2	1
20130290075	69.547883	-64.643330	671	10	10	13	2	3
20130290077	68.308682	-63.794663	618	17	9	20	1	1
20130290082	67.781908	-59.539071	643	16	7	10	2	3

Table 8.2. Summary of Atterberg limit results for piston core 20130290048.

Depth (cm)	w_n (%)	LL (%)	PL (%)	PI (%)	LI	Classification	Zone
28-38	59.7	29.3	16.5	12.8	3.4	CL	B
162-172	26.0	20.6	13.3	7.2	1.8	CL-ML	A
190-200	68.9	40.3	21.0	19.3	2.5	CI	B
250-260	75.4	51.5	28.7	22.9	2.0	CH	-
331-346	86.9	53.9	26.7	27.2	2.2	CH	-
481-495	48.7	33.6	17.2	16.4	1.9	CL	B
638-648	47.8	35.7	19.2	16.4	1.7	CI	B
796-806	55.2	48.0	18.9	29.1	1.3	CI	-

Table 8.3. Summary of consolidation test results for piston core 201390290048.

Depth (cm)	ρ_{sat} (g/cm^3)	w_n (%)	C_c	C_r	P'_c (kPa)	OCR	k (cm/sec)	Classification
200-202.5	1.62	68.3	0.7	0.05	18.9	1.2	5.99E-08	CI
353-355.5	1.60	74.4	0.7	0.05	27.0	0.9	1.11E-07	CH
500-502.5	1.76	45.4	0.6	0.03	35.0	1.0	NA	CL

Table 8.4. Summary of triaxial test results for piston core 20130290048. Initial Young's modulus ($\mathcal{E}_i$) is calculated for the present day effective overburden stress.

Depth (cm)	e	w_n (%)	ϕ' (°)	c' (kPa)	S	A_f	$\mathcal{E}_i$ (MPa)	Classification
332-344	2.42	86.9	25.6	2.3	0.25	0.63	4.63	CH
483-495	1.32	48.7	24.9	5.0	0.27	0.48	14.04	CL

Table 8.5. Summary of FS results for piston core 20130290048.

Depth (cm)	Slope Angle (°)	Critical Angle (°)	Critical Acceleration Coefficient	Critical Height (m)	Minimum FS
794	1.42	9.27	0.06	32.73	6.42

Table 8.6. Summary of Atterberg limit results for piston core 20130290060.

Depth (cm)	w_n (%)	LL (%)	PL (%)	PI (%)	LI	Classification	Zone
17-27	45.1	25.1	14.1	11.0	2.8	CL	A
95-105	26.6	20.2	11.9	8.3	1.8	CL	A
142-154	72.5	58.8	24.1	34.7	1.4	CH	-
220-230	60.2	53.2	21.7	31.5	1.2	CH	-
298-314	32.8	38.5	19.5	18.9	0.7	CI	B
365-375	71.2	66.6	26.5	40.1	1.1	CH	-
455-465	37.3	50.4	21.0	29.5	0.6	CH	-

Table 8.7. Summary of consolidation test results for piston core 201390290060.

Depth (cm)	ρ_{sat} (g/cm^3)	w_n (%)	C_c	C_r	P'_c (kPa)	OCR	k (cm/sec)	Classification
294-296.5	1.95	32.3	0.3	0.04	48.0	2.2	1.08E-07	CI

Table 8.8. Summary of triaxial test results for piston core 20130290060. Initial Young's modulus ($\mathcal{E}_i$) is calculated for the present day effective overburden stress.

Depth (cm)	e	w_n (%)	ϕ' (°)	c' (kPa)	S	A_f	$\mathcal{E}_i$ (MPa)	Classification
142-154	1.85	266.9	22.3	2.2	0.26	0.54	3.21	CH
300-312	0.91	32.8	23.8	6.8	0.32	0.36	8.94	CI

Table 8.9. Summary of FS results for piston core 20130290060.

Depth (cm)	Slope Angle (°)	Critical Angle (°)	Critical Acceleration Coefficient	Critical Height (m)	Minimum FS
420.0	3.8	18.3	0.08	11.5	4.5

Table 8.10. Summary of Atterberg limit results for piston core 20130290075.

Depth (cm)	w_n (%)	LL (%)	PL (%)	PI (%)	LI	Classification	Zone
55-65	168.9	99.0	32.2	66.8	2.1	CE	-
200-206	121.4	79.4	29.4	50.1	1.8	CV	-
245-255	111.1	58.9	28.2	30.7	2.1	CH	-
285-295	50.5	29.4	16.3	13.1	2.6	CL	B
320-330	23.4	17.9	12.1	5.8	1.9	CL-ML	A
373-377	111.7	62.0	25.1	36.9	2.0	CH	-
416-424	31.1	21.6	12.6	9.0	2.1	CL	-
470-480	65.2	42.0	19.2	22.7	2.0	CI	-
545-555	50.9	46.2	20.5	25.7	1.2	CI	-
668-671	37.0	40.3	17.9	22.4	0.9	CI	-

Table 8.11. Summary of consolidation test results for piston core 201390290075.

Depth (cm)	ρ_{sat} (g/cm^3)	w_n (%)	C_c	C_r	P'$_c$ (kPa)	OCR	k (cm/sec)	Classification
201-203.5	1.45	120.4	1.1	0.09	8.5	1.2	2.50E-07	CV
375-377.5	1.47	111.7	1.1	0.08	14.5	0.8	4.21E-06	CH
668-670.5	1.89	37.0	0.3	0.02	39.0	0.9	1.22E-07	CI

Table 8.12. Summary of triaxial test results for piston core 20130290075. Initial Young's modulus ($\mathcal{E}_i$) is calculated for the present day effective overburden stress.

Depth (cm)	e	w_n (%)	ϕ' (°)	c' (kPa)	S	A_f	$\mathcal{E}_i$ (MPa)	Classification
206-218	3.31	125.3	18.9	0.0	0.19	0.64	1.75	CV
646-658	0.97	34.3	24.3	9.4	0.32	0.45	18.84	CI

Table 8.13. Summary of FS results for piston core 20130290075.

Depth (cm)	Slope Angle (°)	Critical Angle (°)	Critical Acceleration Coefficient	Critical Height (m)	Minimum FS
422.0	1.7	9.2	0.07	12.2	5.3

Table 8.14. Summary of Atterberg limit results for piston core 20130290077.

Depth (cm)	w_n (%)	LL (%)	PL (%)	PI (%)	LI	Classification	Zone
93-103	93.9	64.6	26.3	38.3	1.8	CH	-
142-152	19.7	19.7	13.4	6.3	1.0	CL-ML	A
170-180	113.8	72.6	30.9	41.7	2.0	CV	-
250-260	68.7	52.1	22.4	29.7	1.6	CH	-
325-335	55.2	53.5	24.1	29.5	1.1	CH	-
378-388	56.7	47.2	20.5	26.7	1.4	CI	-
440-450	58.7	49.0	23.6	25.4	1.4	CI	-
512-525	49.2	43.3	20.6	22.7	1.3	CI	-
597-613	42.5	52.4	21.5	30.9	0.7	CH	-

Table 8.15. Summary of consolidation test results for piston core 201390290077.

Depth (cm)	ρ_{sat} (g/cm^3)	w_n (%)	C_c	C_r	P'_c (kPa)	OCR	k (cm/sec)	Classification
613-615.5	1.86	40.6	0.3	0.03	23.5	0.6	1.83E-07	CH

Table 8.16. Summary of triaxial test results for piston core 20130290077. Initial Young's modulus ($\mathcal{E}_i$) is calculated for the present day effective overburden stress.

Depth (cm)	e	w_n (%)	ϕ' (°)	c' (kPa)	S	A_f	$\mathcal{E}_i$ (MPa)	Classification
598-610	1.44	54.8	25.8	2.2	0.28	0.56	9.46	CH

Table 8.17. Summary of FS results for piston core 20130290077.

Depth (cm)	Slope Angle (°)	Critical Angle (°)	Critical Acceleration Coefficient	Critical Height (m)	Minimum FS
590.0	0.8	12.8	0.09	100.9	15.9

Table 8.18. Summary of Atterberg limit results for piston core 20130290082.

Depth (cm)	w_n (%)	LL (%)	PL (%)	PI (%)	LI	Classification	Zone
55-65	69.1	41.0	19.2	21.8	2.3	CI	-
120-130	101.2	53.0	25.0	28.1	2.7	CH	-
180-185	70.2	39.7	21.7	18.0	2.7	CI	B
269-279	68.9	43.9	22.3	21.6	2.2	CI	-
339-344	56.5	33.9	19.5	14.5	2.6	CL	B
470-475	53.4	29.0	17.8	11.3	3.2	CL	A
533-543	41.5	27.6	16.9	10.7	2.3	CL	A

Table 8.19. Summary of consolidation test results for piston core 201390290082.

Depth (cm)	ρ_{sat} (g/cm^3)	w_n (%)	C_c	C_r	P'_c (kPa)	OCR	k (cm/sec)	Classification
182-184.5	1.60	70.2	0.7	0.05	9.5	1.0	NA	CI
343-345.5	1.72	56.5	0.5	0.04	16.0	0.8	9.47E-08	CL
489-491.5	1.72	52.6	0.6	0.04	35.0	1.1	3.84E-07	CL

Table 8.20. Summary of triaxial test results for piston core 20130290082. Initial Young's modulus ($\mathcal{E}_i$) is calculated for the present day effective overburden stress.

Depth (cm)	e	w_n (%)	ϕ' (°)	c' (kPa)	S	A_f	$\mathcal{E}_i$ (MPa)	Classification
188-196	1.83	66.9	30.3	0.0	0.26	0.50	6.20	CI
478-486	1.21	44.5	30.3	1.6	0.29	0.70	12.45	CL

Table 8.21. Summary of FS results for piston core 20130290082.

Depth (cm)	Slope Angle (°)	Critical Angle (°)	Critical Acceleration Coefficient	Critical Height (m)	Minimum FS
645.0	0.7	11.4	0.10	113.7	15.4

Table 9.1. Average values of physical property of geotechnical units. Standard deviation presented in brackets. Unit 6B only has one Atterberg and one grain size measurement.

Unit	ρ_{sat} (g/cm^3)	w_n (%)	LL (%)	PL (%)	PI (%)	A	Clay (%)	Silt (%)	Sand (%)	Gravel (%)	Classification
1A	1.43 (0.09)	149.3 (38.3)	75.5 (17.9)	29.0 (2.5)	46.5 (15.7)	0.68 (0.12)	53.2 (10.8)	44.9 (10.5)	1.9 (2.5)	-	CH
1B	1.58 (0.11)	81.6 (15.1)	44.6 (7.4)	21.9 (2.9)	22.6 (5.1)	0.65 (0.10)	34.9 (4.7)	58.3 (7.3)	6.8 (10.3)	-	CI, CH
2	1.91 (0.21)	45.5 (25.4)	23.5 (5.5)	14.1 (2.6)	9.4 (3.2)	0.22 (0.05)	43.8 (8.5)	46.0 (7.3)	9.7 (8.6)	0.6 (1.7)	CL, CL-ML
3	1.62 (0.06)	81.0 (17.6)	57.8 (9.1)	25.8 (3.1)	32.1 (7.6)	0.65 (0.08)	45.4 (14.0)	53.0 (13.0)	1.6 (1.7)	-	CH
4	1.83 (0.13)	57.3 (9.1)	48.2 (4.0)	21.3 (1.8)	26.9 (3.0)	0.56 (0.09)	47.4 (7.6)	49.3 (4.9)	3.3 (4.9)	-	CI, CH
5A	1.86 (0.09)	53.4 (7.4)	34.7 (4.6)	18.5 (2.0)	16.2 (2.7)	0.39 (0.03)	38.8 (9.6)	50.0 (4.4)	11.2 (8.3)	-	CL, CI
5B	1.90 (0.16)	52.7 (11.6)	28.3 (1.0)	17.3 (0.6)	11.0 (0.4)	0.44 (0.06)	21.4 (6.9)	58.1 (3.6)	20.6 (10.3)	-	CL
6A	1.85 (0.08)	35.5 (2.4)	44.4 (8.4)	20.2 (1.0)	24.2 (7.4)	0.49 (0.12)	47.6 (3.7)	32.9 (8.1)	14.3 (7.4)	5.3 (7.3)	CI,CH
6B	1.96 (0.07)	40.2 (4.2)	40.3 (-)	17.9 (-)	22.4 (-)	0.57 (-)	39.4 (-)	48.7 (-)	12.0 (-)	-	CI

Table 9.2. Summary of advanced geotechnical data.

Unit	ϕ' (°)	c' (kPa)	S	A_f	C_c	C_r	P'_c (kPa)	OCR	k (cm/sec)
1A	18.9	0.0	0.19	0.64	1.1	0.09	7.3	1.2	2.50E-07
1B	30.3	0.0	0.26	0.50	0.5	0.05	9.5	1.0	NA
2	-	-	-	-	0.5	0.04	16.0	0.8	9.47E-08
3	24.0	2.3	0.26	0.59	0.9	0.07	20.8	0.9	2.16E-06
4	25.8	2.2	0.28	0.56	0.3	0.03	23.5	0.6	1.83E-07
5A	24.9	5.0	0.27	0.48	0.6	0.04	27.0	1.1	5.99E-08
5B	30.3	1.6	0.29	0.70	0.6	0.04	35.0	1.1	3.84E-07
6A	23.8	6.8	0.32	0.36	0.3	0.04	48.0	2.2	1.08E-07
6B	24.3	9.4	0.32	0.45	0.3	0.02	39.0	0.9	1.22E-07

Figure 1.1. Location map of the 5 geotechnical cores collected during cruise 2013029 (from Google Earth).

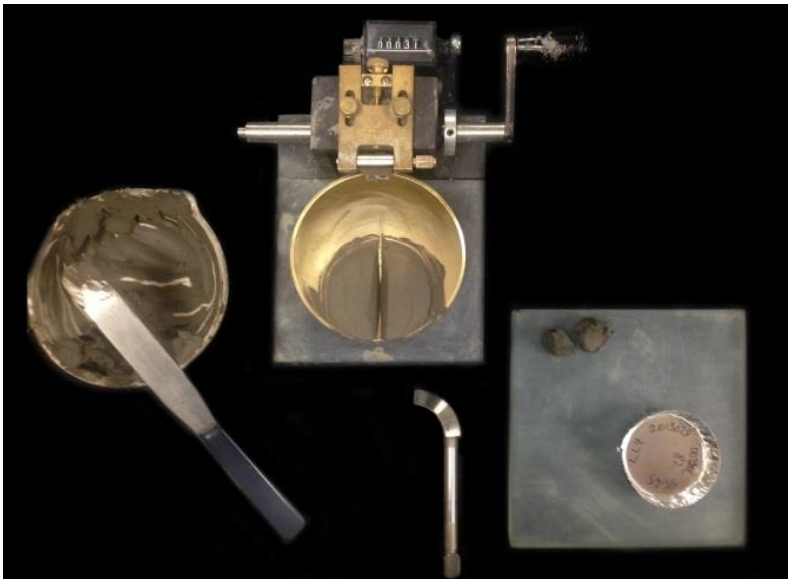

Figure 3.1. Liquid limit test apparatus.

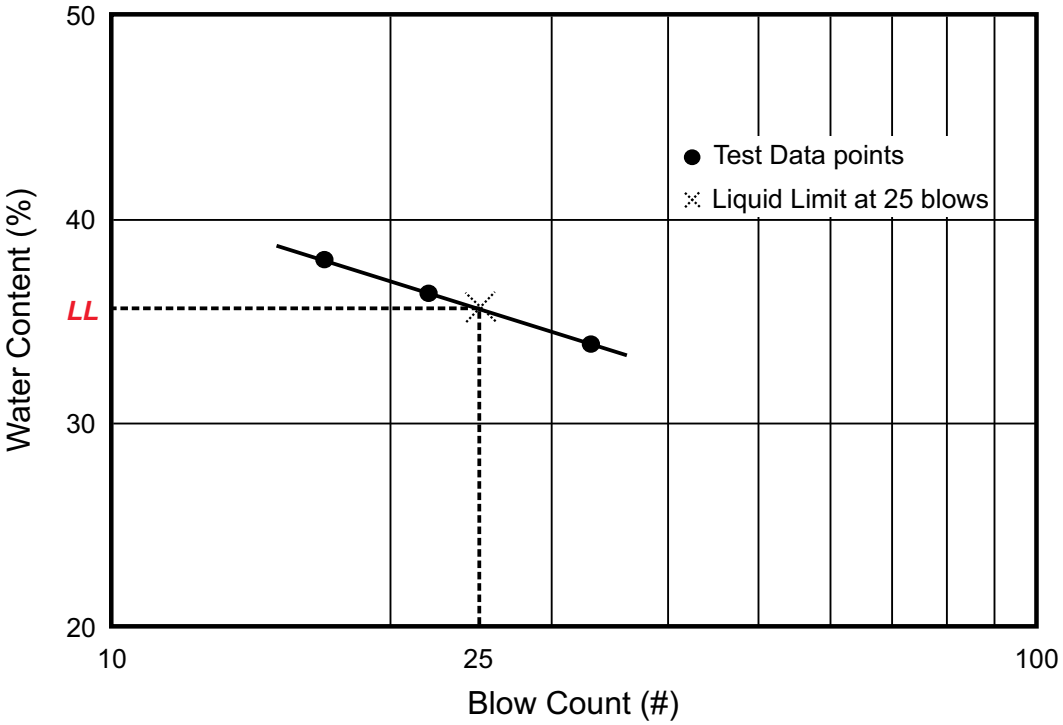

Figure 3.2. Laboratory data for determining the liquid limit of soil.

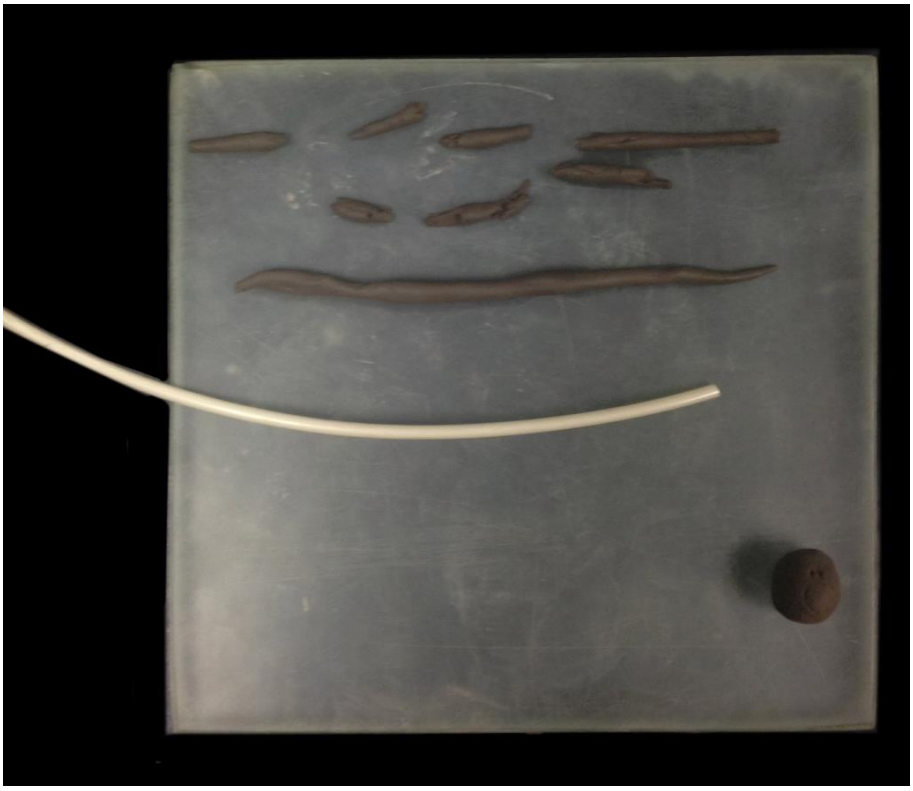

Figure 3.3. Crumbing of the soil threads at the plastic limit.

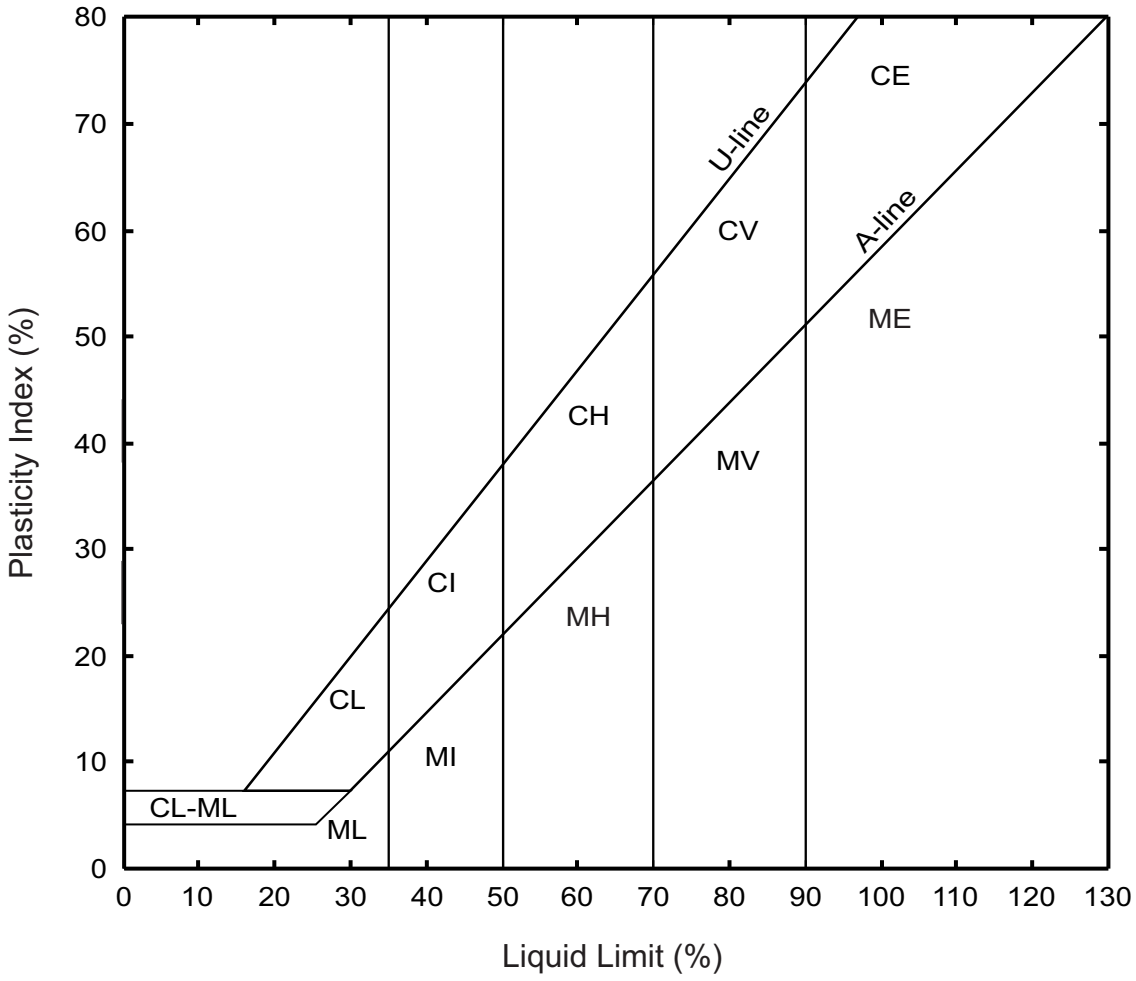

Figure 3.4. British Standard plasticity chart with A and U lines defined.

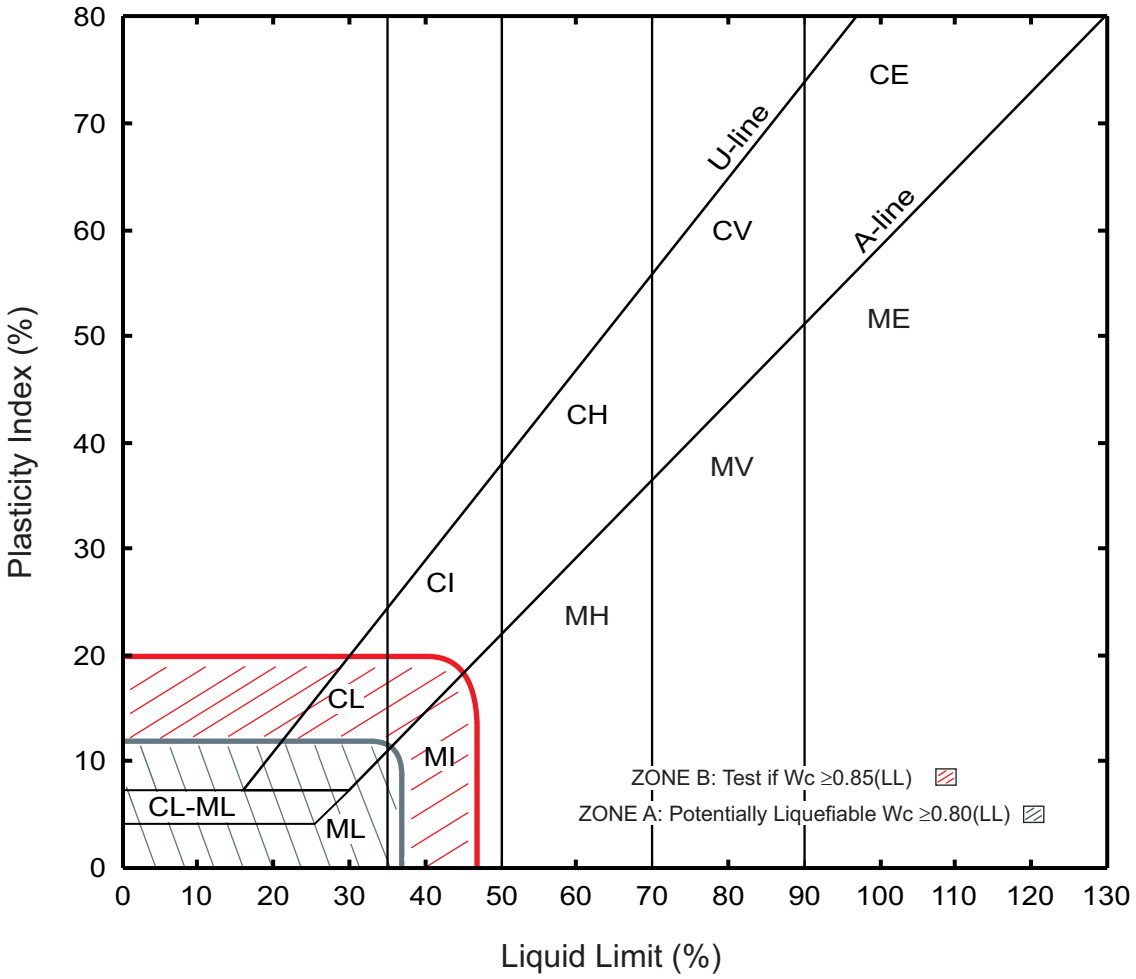

Figure 3.5. Plasticity chart with liquefaction potential zones (Seed et al., 2003).

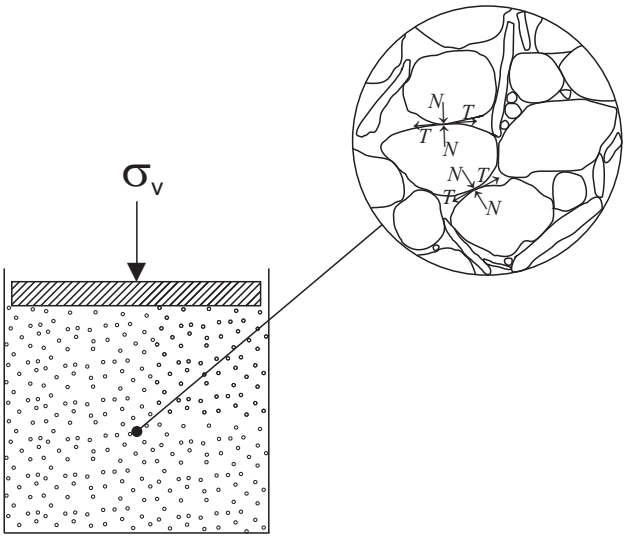

Figure 4.1. Schematic representation of normal (*N*) and tangential (*T*) force transmission through soil under an applied vertical load (σ_v) (after Lamb and Whitman, 1969).

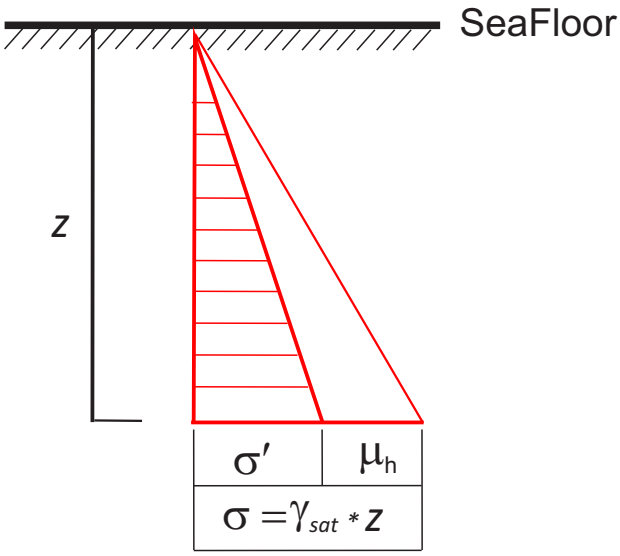

Figure 4.2. The total normal stress acting on sediment below the seafloor is a combination of effective stress and pore water pressure.

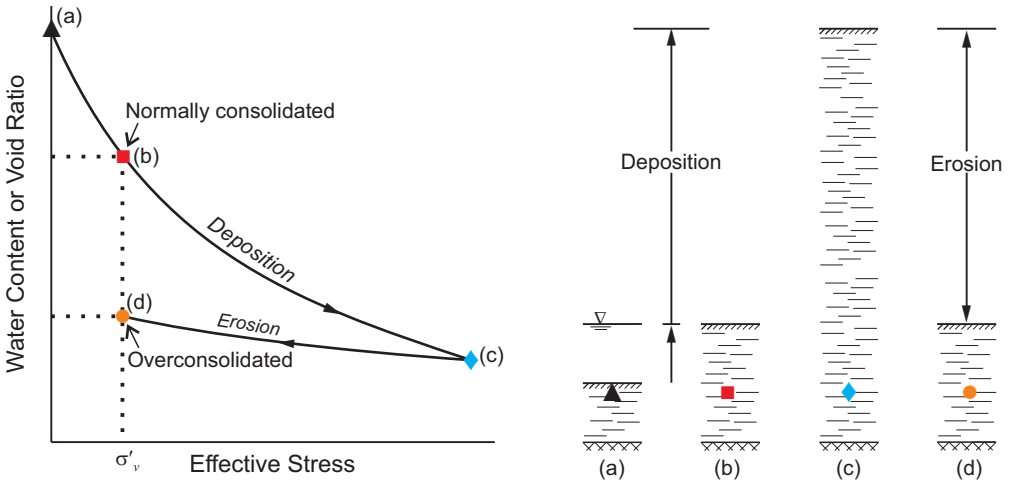

Figure 5.1. Normal and overconsolidated clays by gravitational compaction (Skempton, 1970)

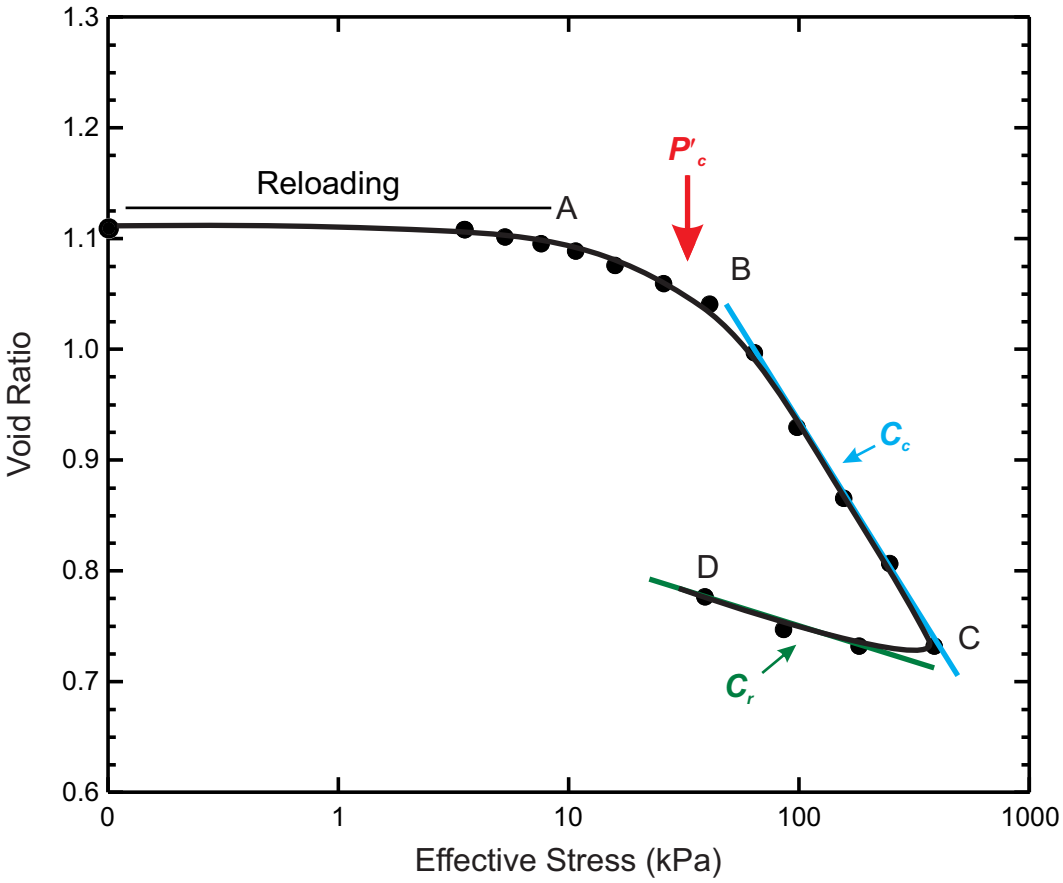

Figure 5.2. Typical consolidation e-log effective stress curve. Point A marks the end of the reloading point A to B marks the transition from reloading to new stresses, point B to C defines the virgin compression line and point C to D defines the expansion index.

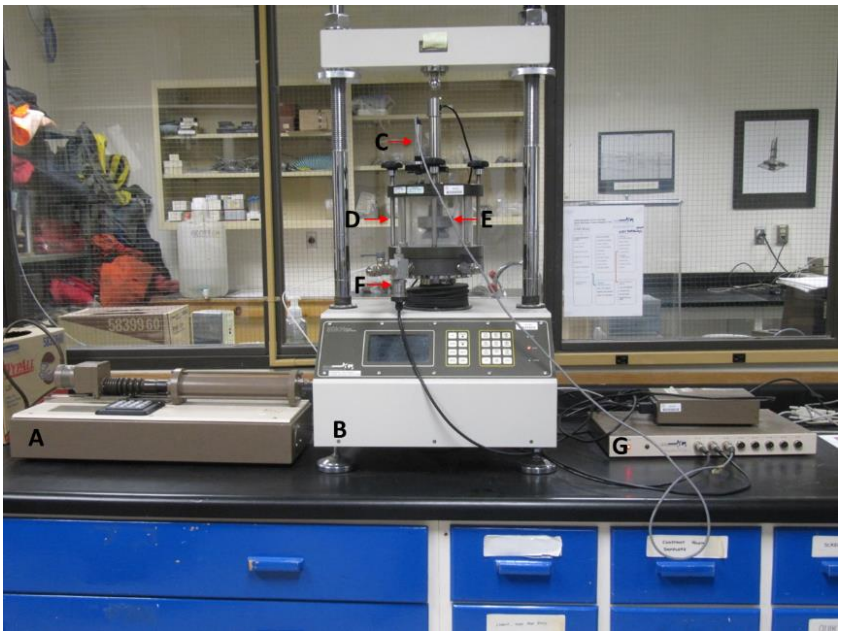

Figure 5.3. The GDS CRS consolidation system includes (A) back pressure controller, (B) 50 kN load frame, (C) axial displacement transducer, (D) CRS consolidation cell, (E) submersible load cell, (F) pore pressure transducer and (G) DAQ system.

Figure 5.4. The GDS Rowe consolidation system includes (A) back pressure controller, (B) load chamber controller, (C) Rowe consolidation cell, (D) DAQ system and (E) pore pressure transducer.

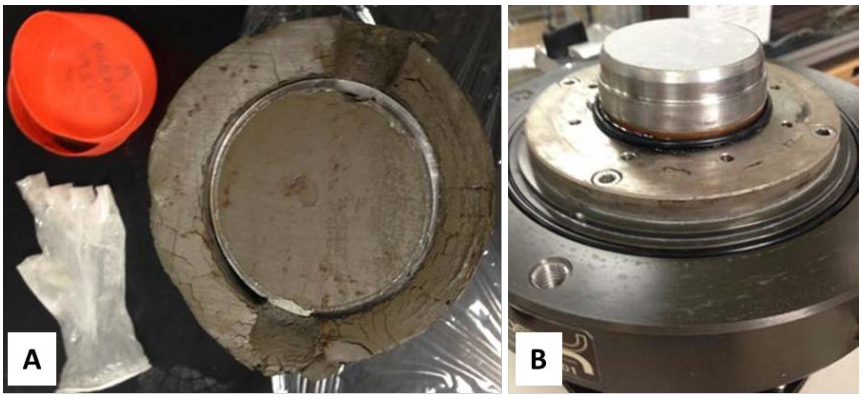

Figure 5.5. Sediment extruded into CRS consolidation ring (A) and a trimmed sample on the CRS cell base (B).

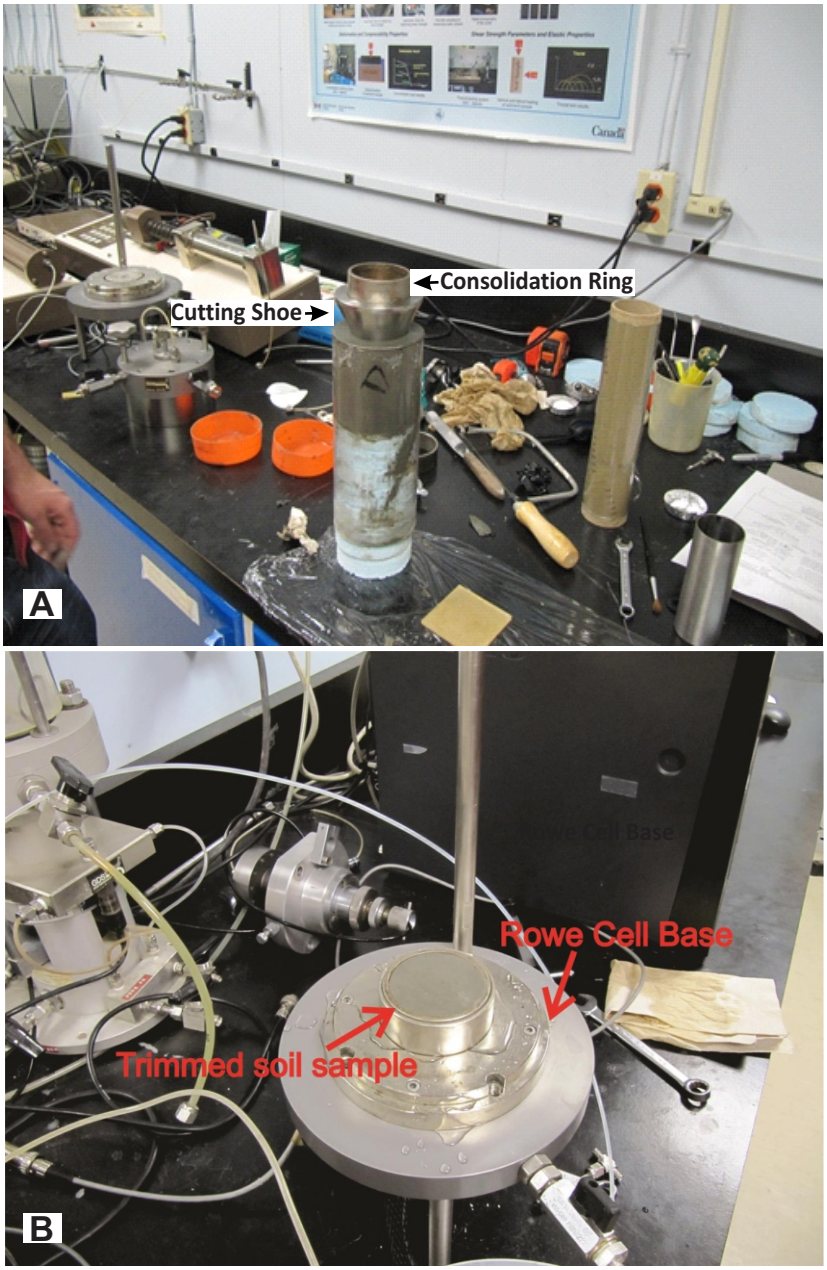

Figure 5.6. Sediment being extruded into the Rowe cell consolidation ring (A) and a trimmed sample on the Rowe cell base (B).

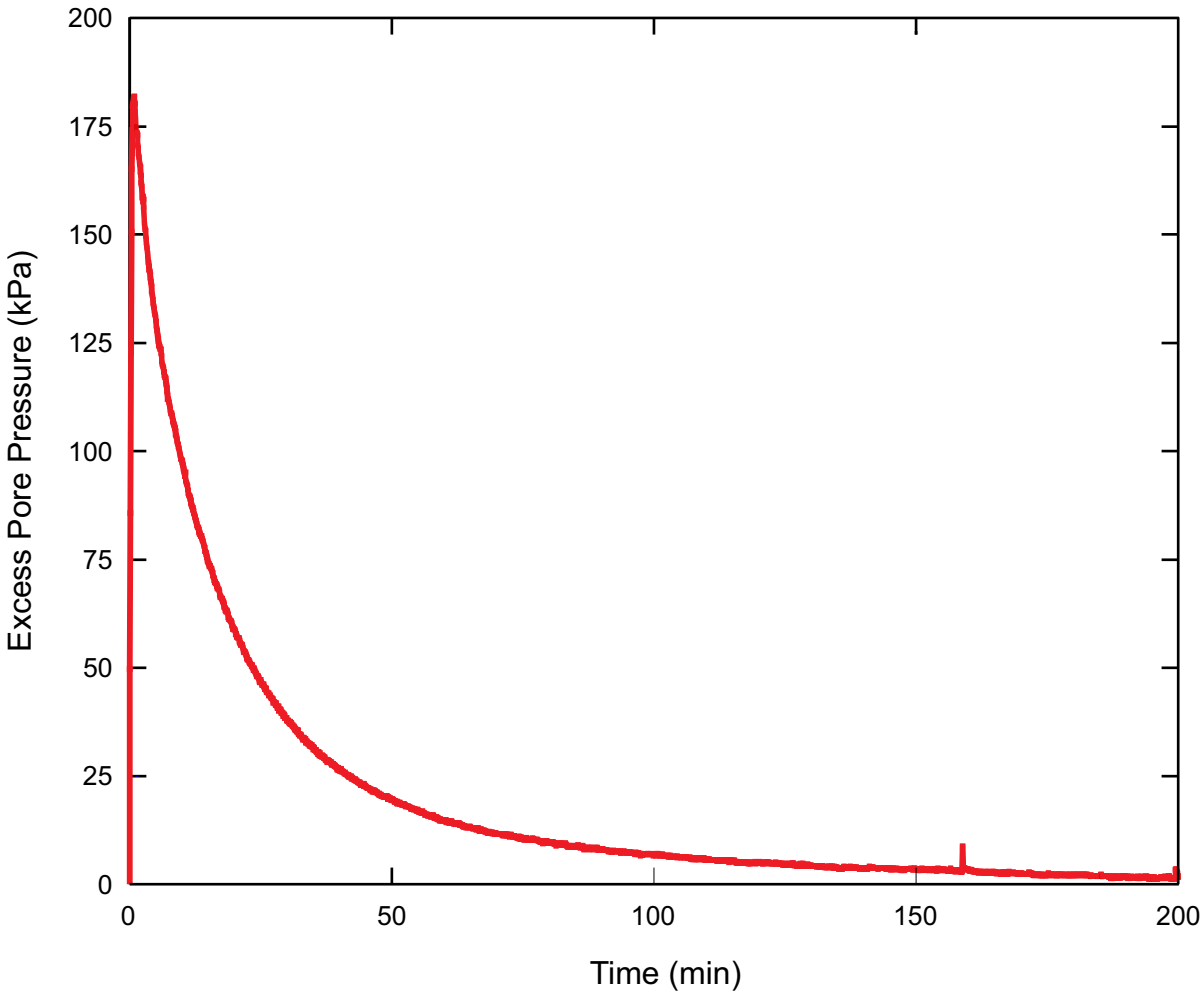

Figure 5.7 Sample pore pressure response measured at the base of the sample to a new load increment.

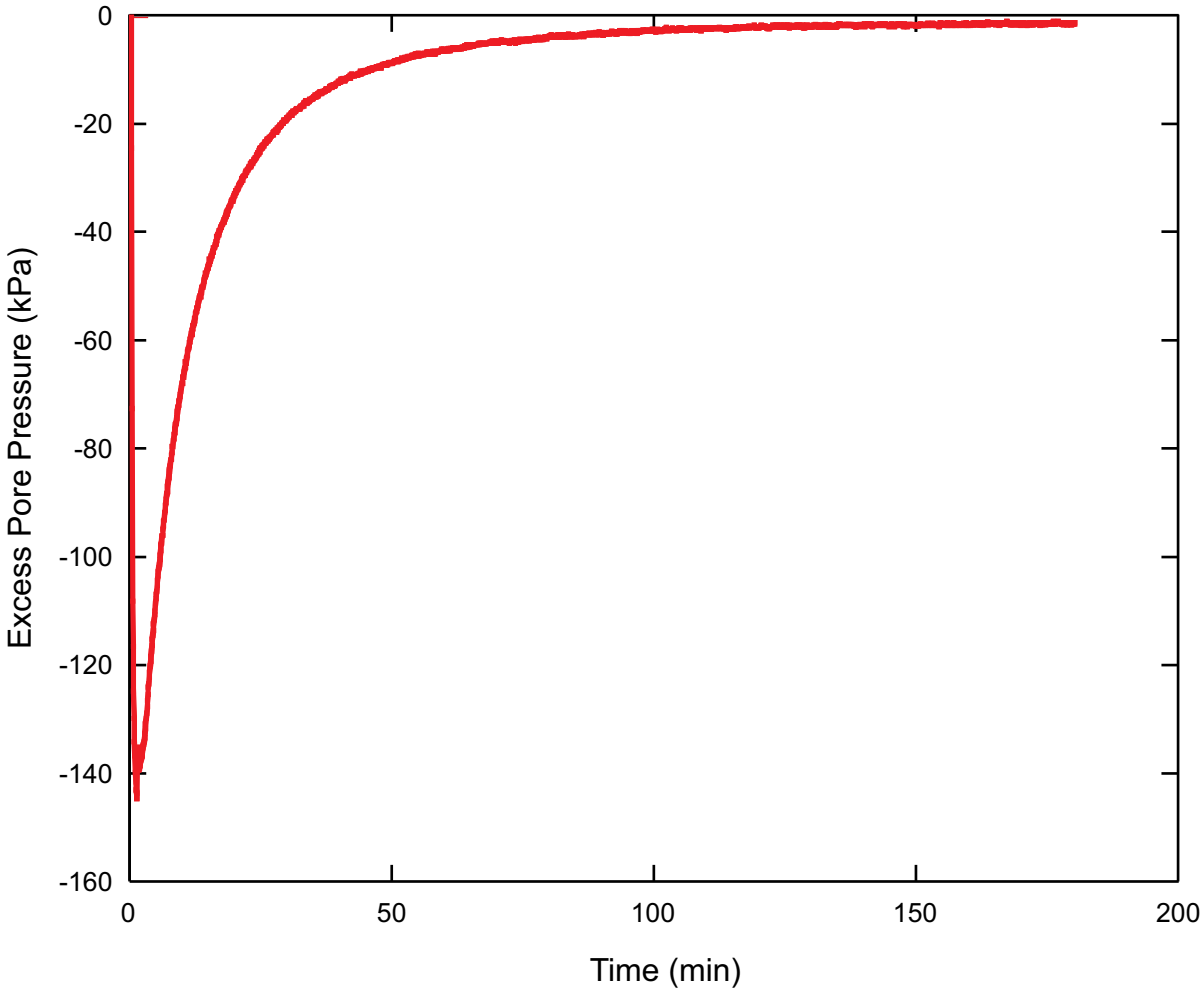

Figure 5.8. Sample pore pressure response measured at the base of the sample to a new unload increment.

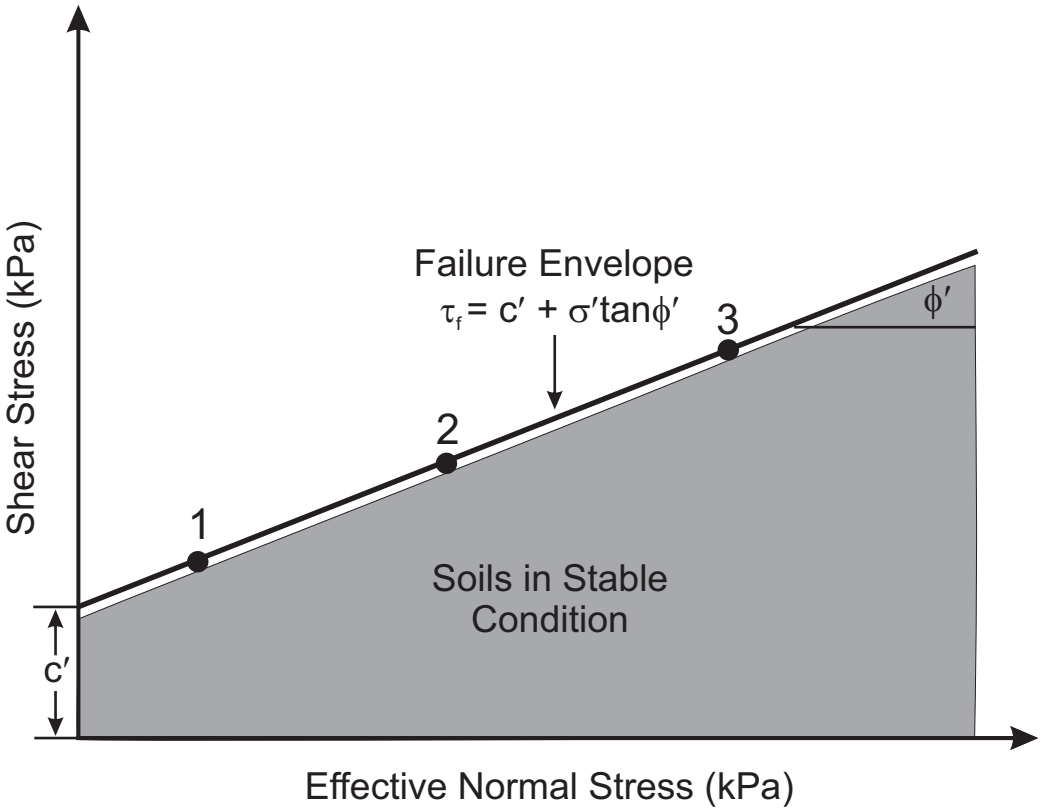

Figure 6.1. Maximum shear strength related to effective normal stress from triaxial tests.

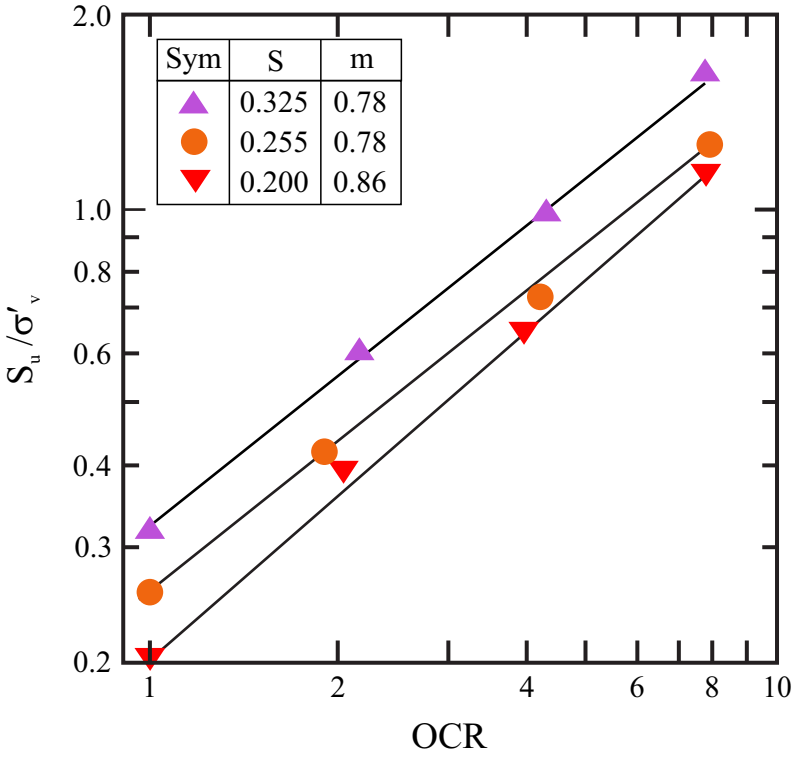

Figure 6.2. Example of a SHANSEP analysis for AGS plastic marine clay showing the OCR vs undrained strength ratio relationship (Su/σ'v) (after Ladd and DeGroot, 2003).

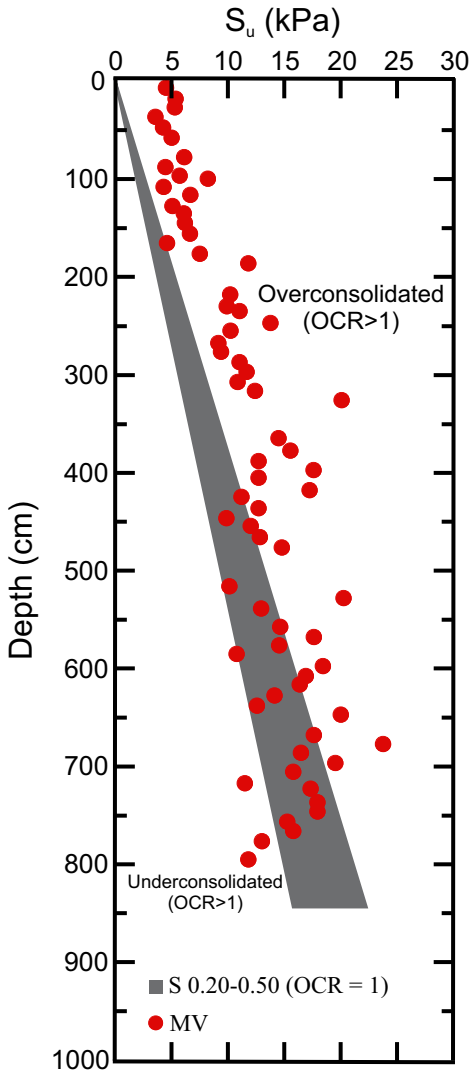

Figure 6.3. A comparison of the undrained shear strength calculated using the S ratio and the MV shear strength data

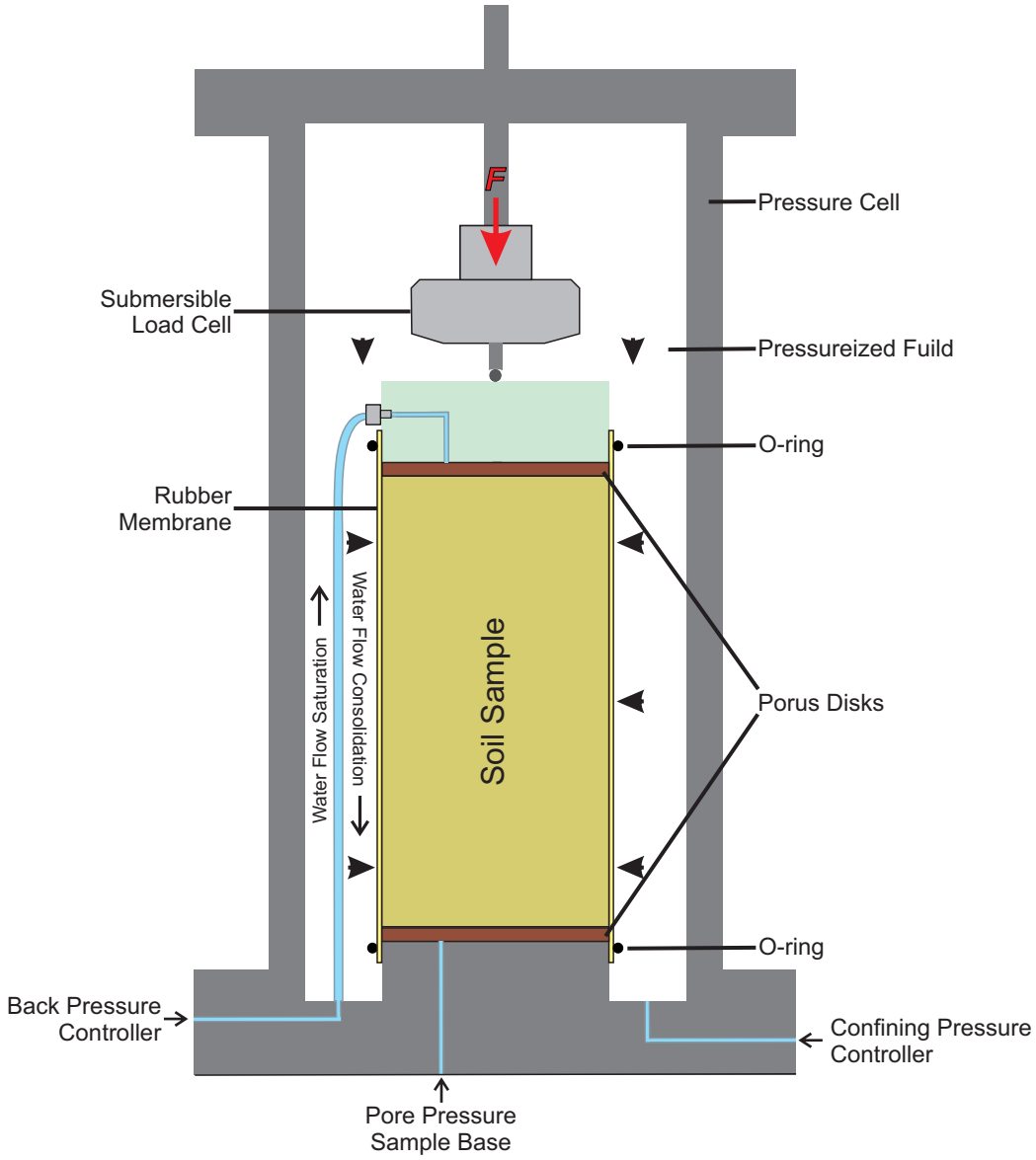

Figure 6.4. General set-up of a soil sample in a triaxial cell.

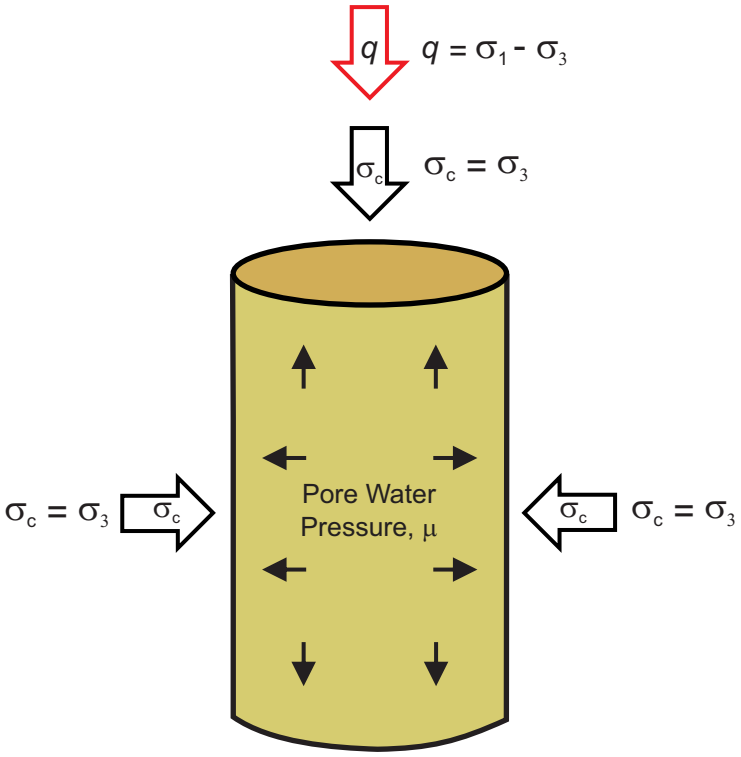

Figure 6.5. Sample stress during the shear stage where σ_c is the confining pressure that remains constant during the shear stage.

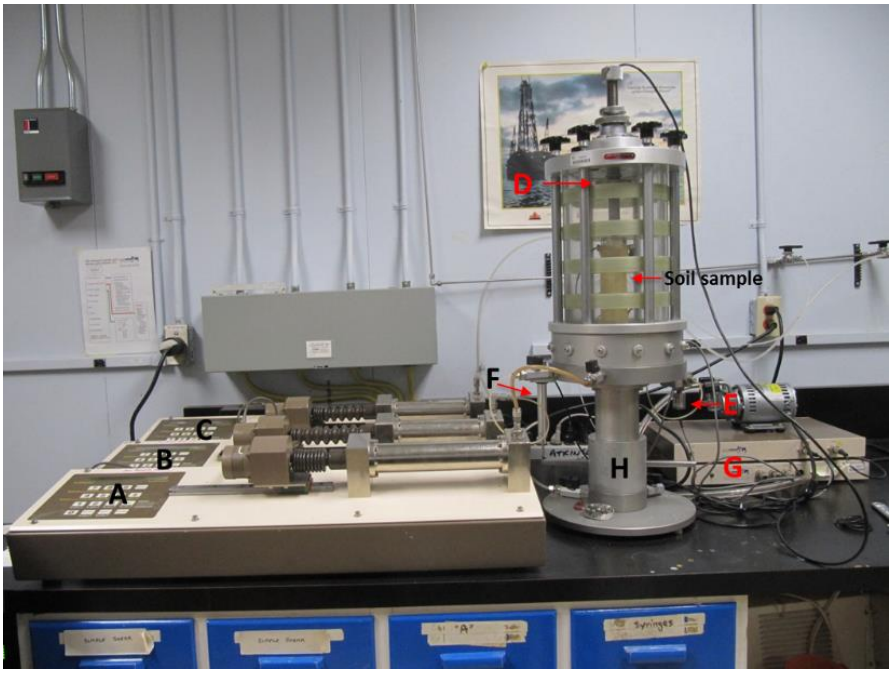

Figure 6.6. The GDS triaxial system at the GSCA geomechnical lab includes 3 2 MPa GDS pressure/volume controllers (A, B, C), submersible load cell (D), pore pressure transducer (E), linear displacement transducer (F), DAQ system (G) and Bishop & Wesley stress path triaxial cell (H).

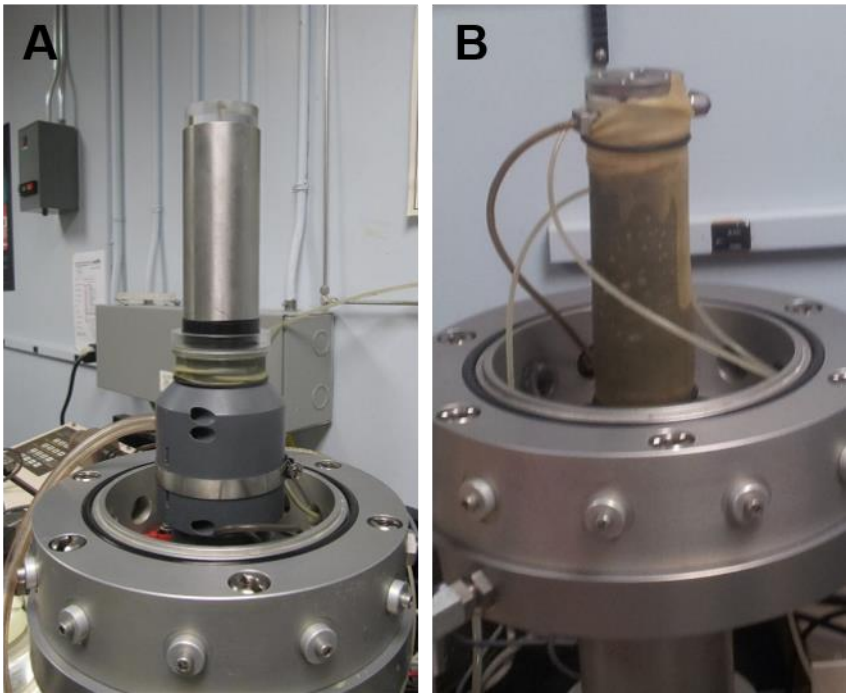

Figure 6.7. Placement of the sample into the rubber membrane in the B&W triaxial cell. A) Sampling ring with sample and split form with rubber membrane. B) Soil sample in the rubber membrane with top cap attached.

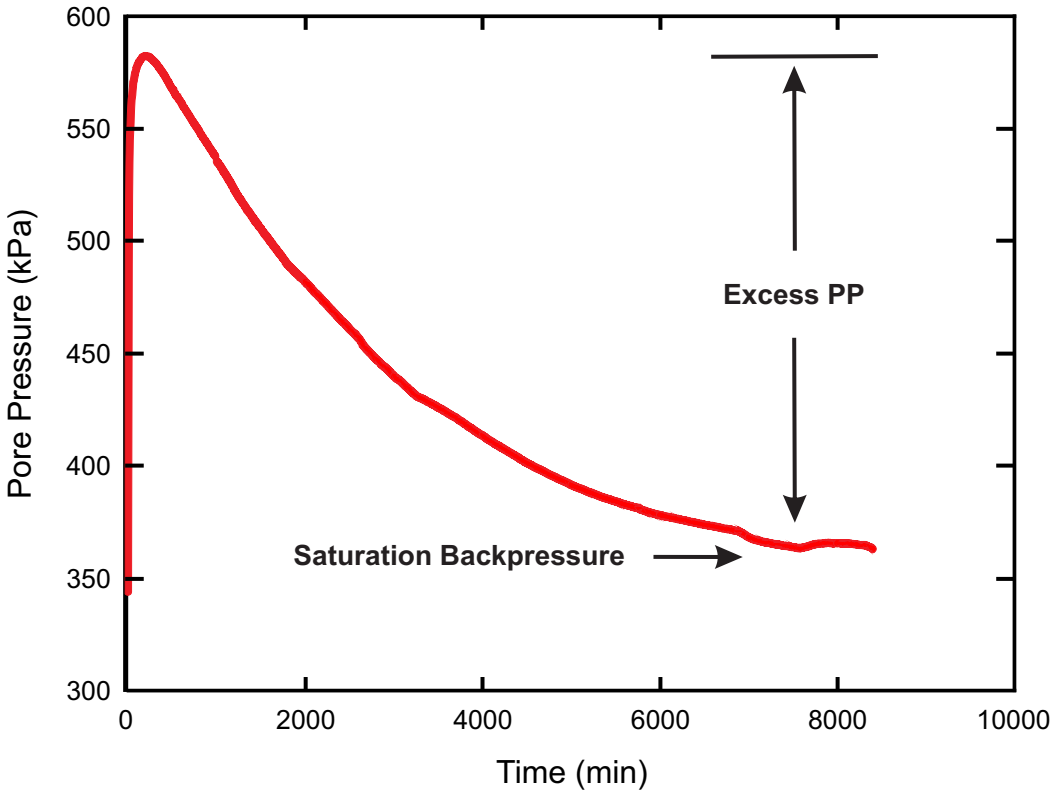

Figure 6.8. Triaxial test data illustrating pore pressure dissipation during the isotropic consolidation stage.

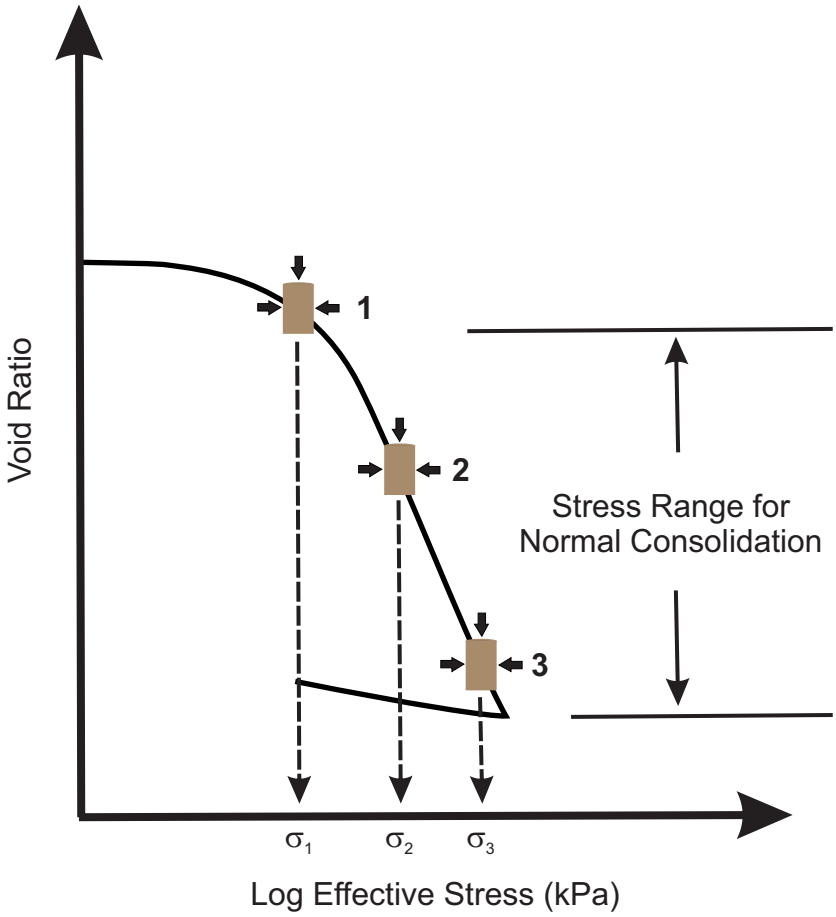

Figure 6.9. Consolidation test data illustrating the procedure for selecting 3 confining pressures for CIU triaxial testing. Note that confining pressures 2 and 3 are in the normal consolidation stress range for the sample.

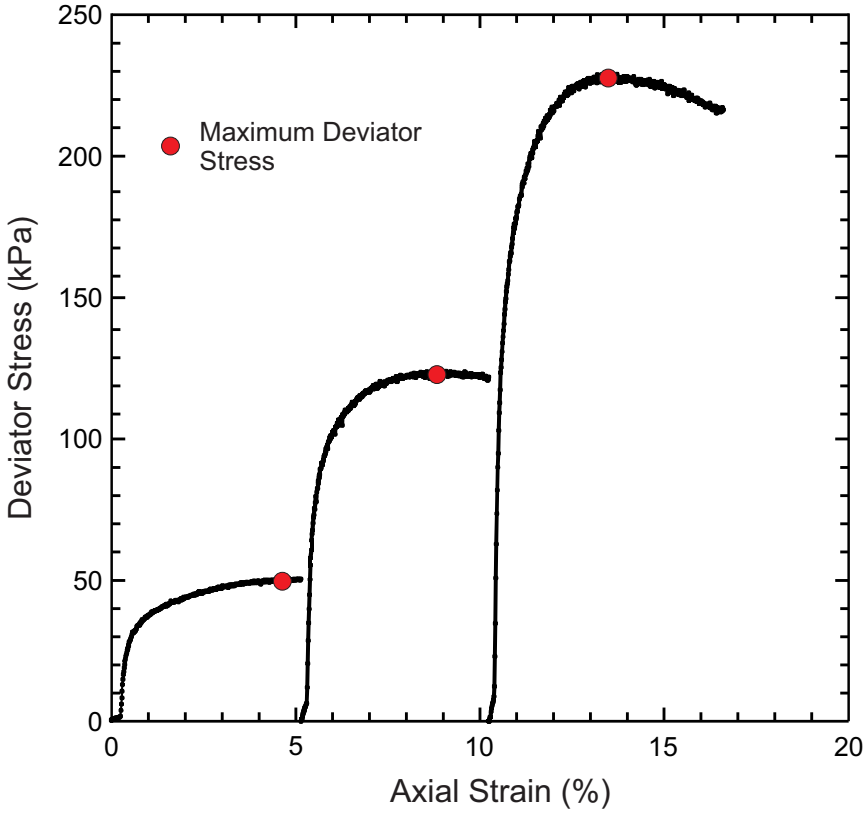

Figure 6.10. Triaxial test data illustrating the stress-strain for the 3 shear stages.

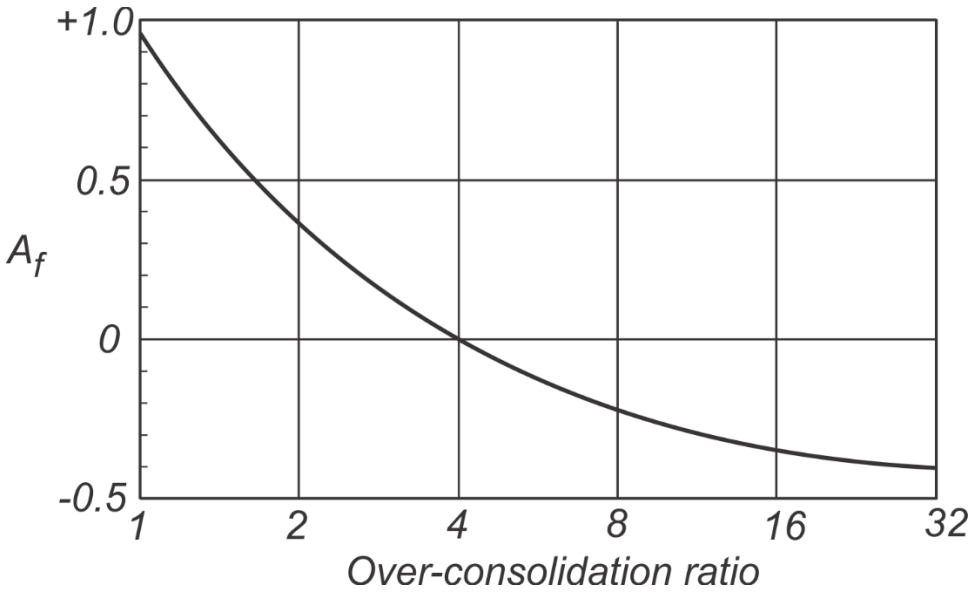

Figure 6.11. Relationship between A_f and OCR values.

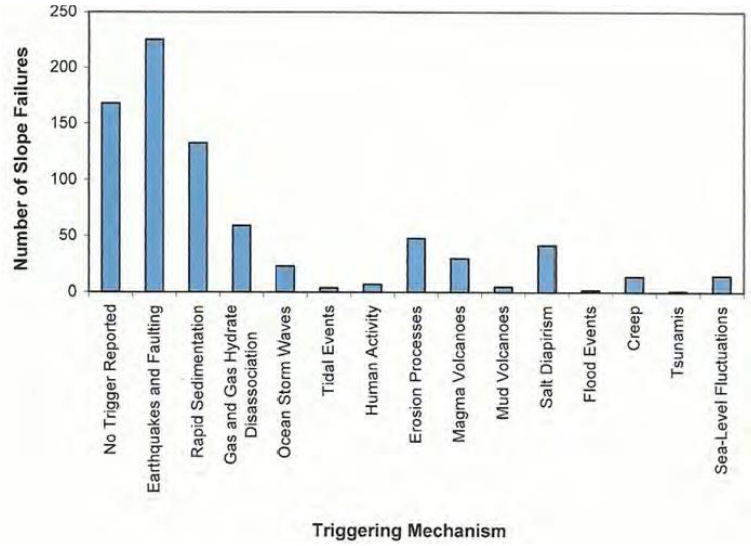

Figure 7.1. Triggering mechanisms for 534 submarine slides (Hance, 2003).

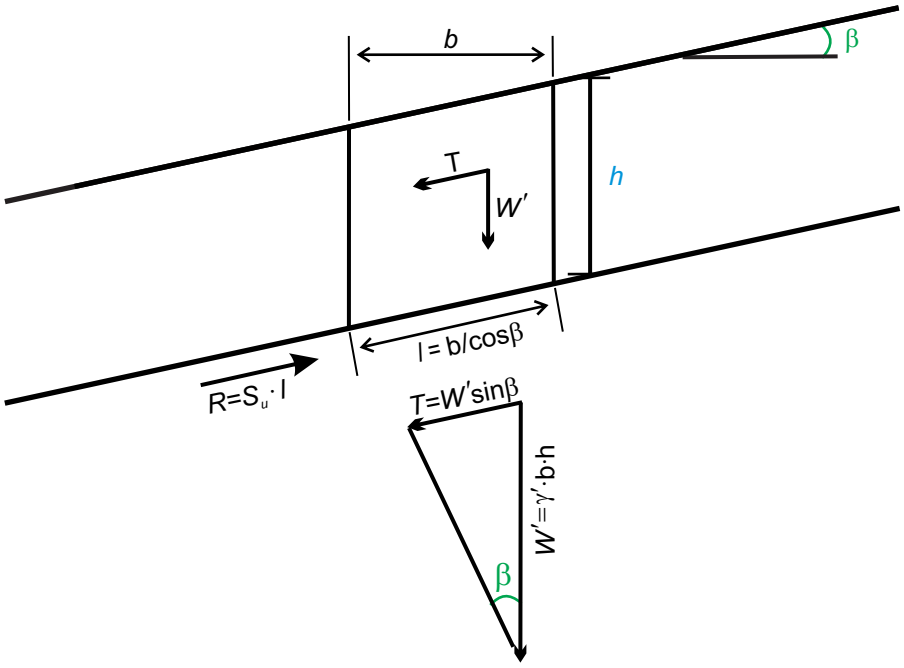

Figure 7.2. The equilibrium of an infinite slope under undrained conditions, with gravity forces, T (after Morgenstren, 1967). Only the forces used in the FS calculation are shown.

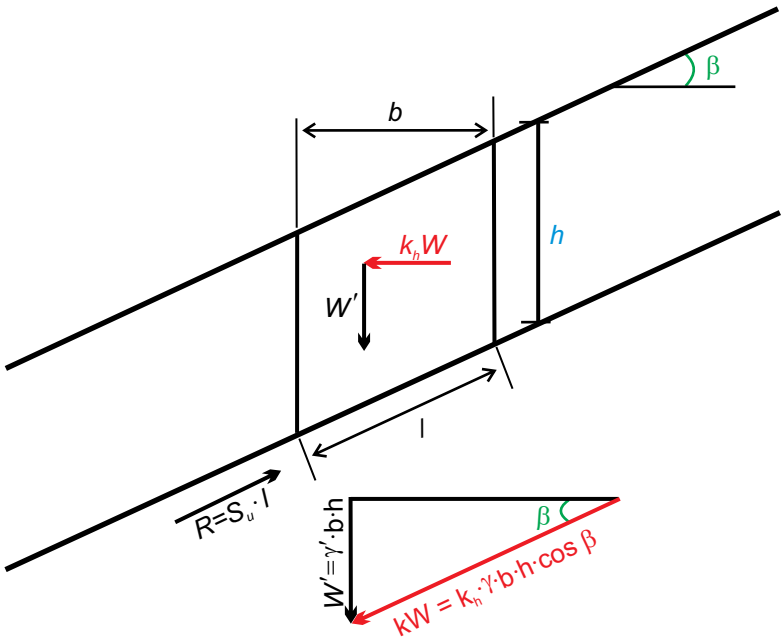

Figure 7.3. The equilibrium of an infinite slope under undrained conditions, with an earthquake force (kW, after Morgenstren, 1967). Only the forces used in the FS calculation are shown.

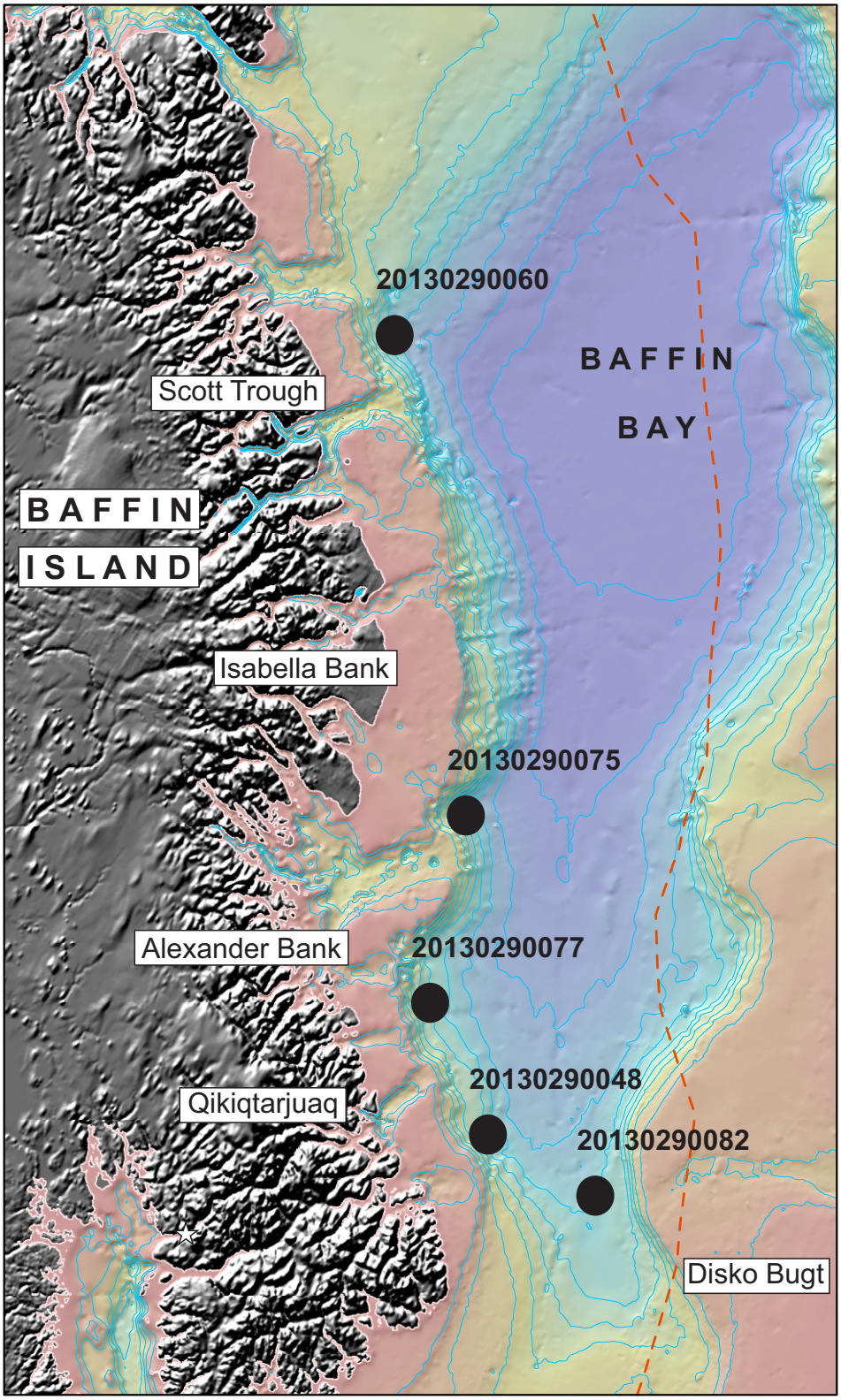

Figure 8.1. Location map of the geotechnical cores used in this study.

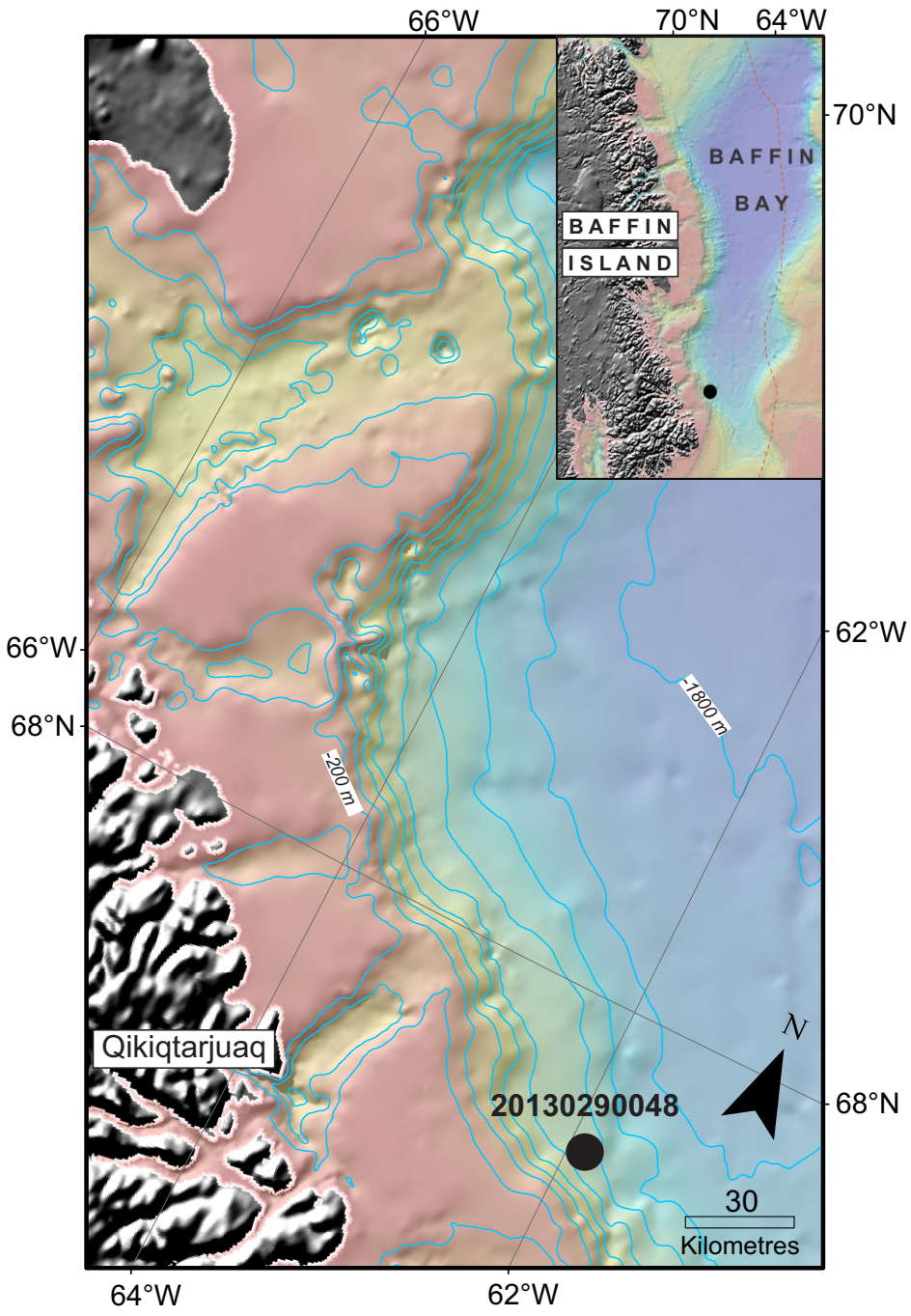

Figure 8.2. Location map of piston core 20130290048.

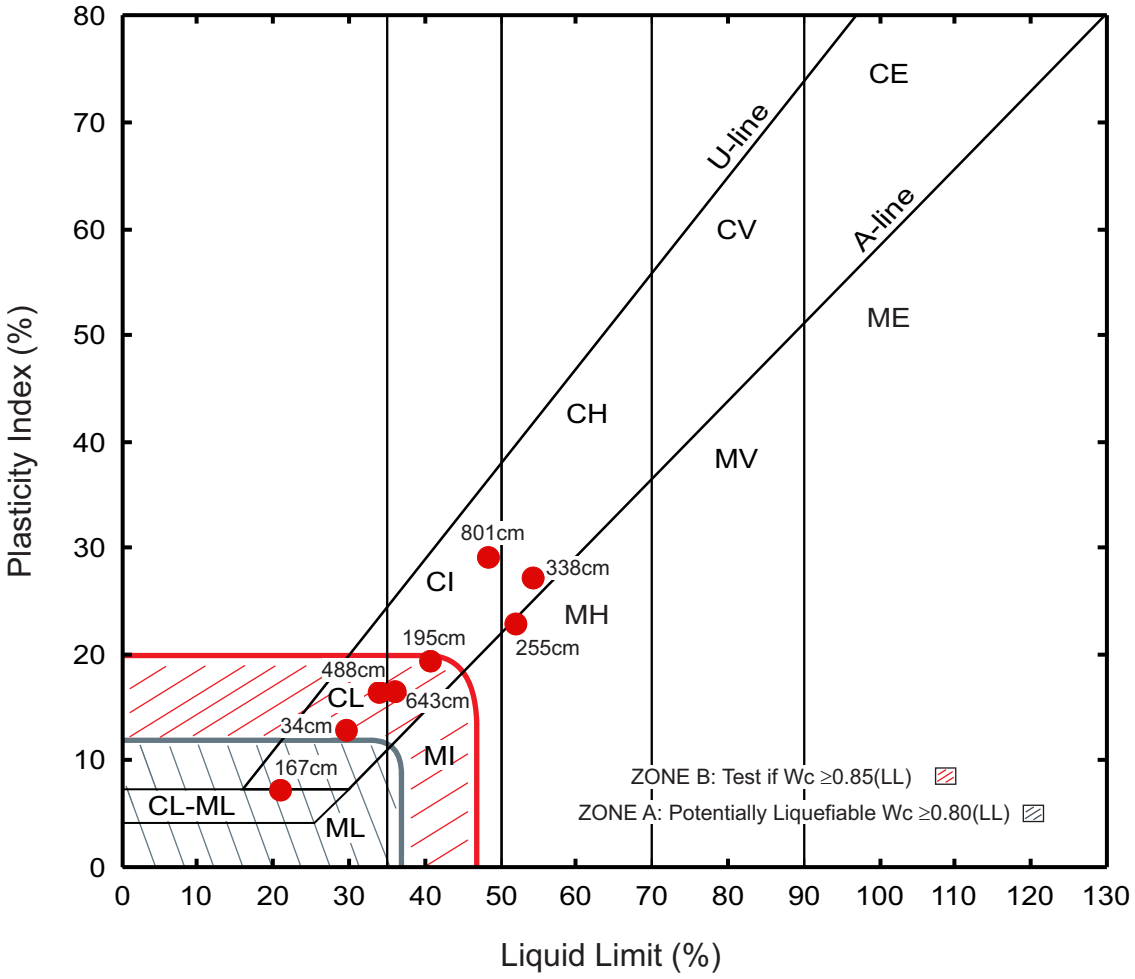

Figure 8.3. Plasticity chart showing Atterberg limit results of piston core 20130290048.

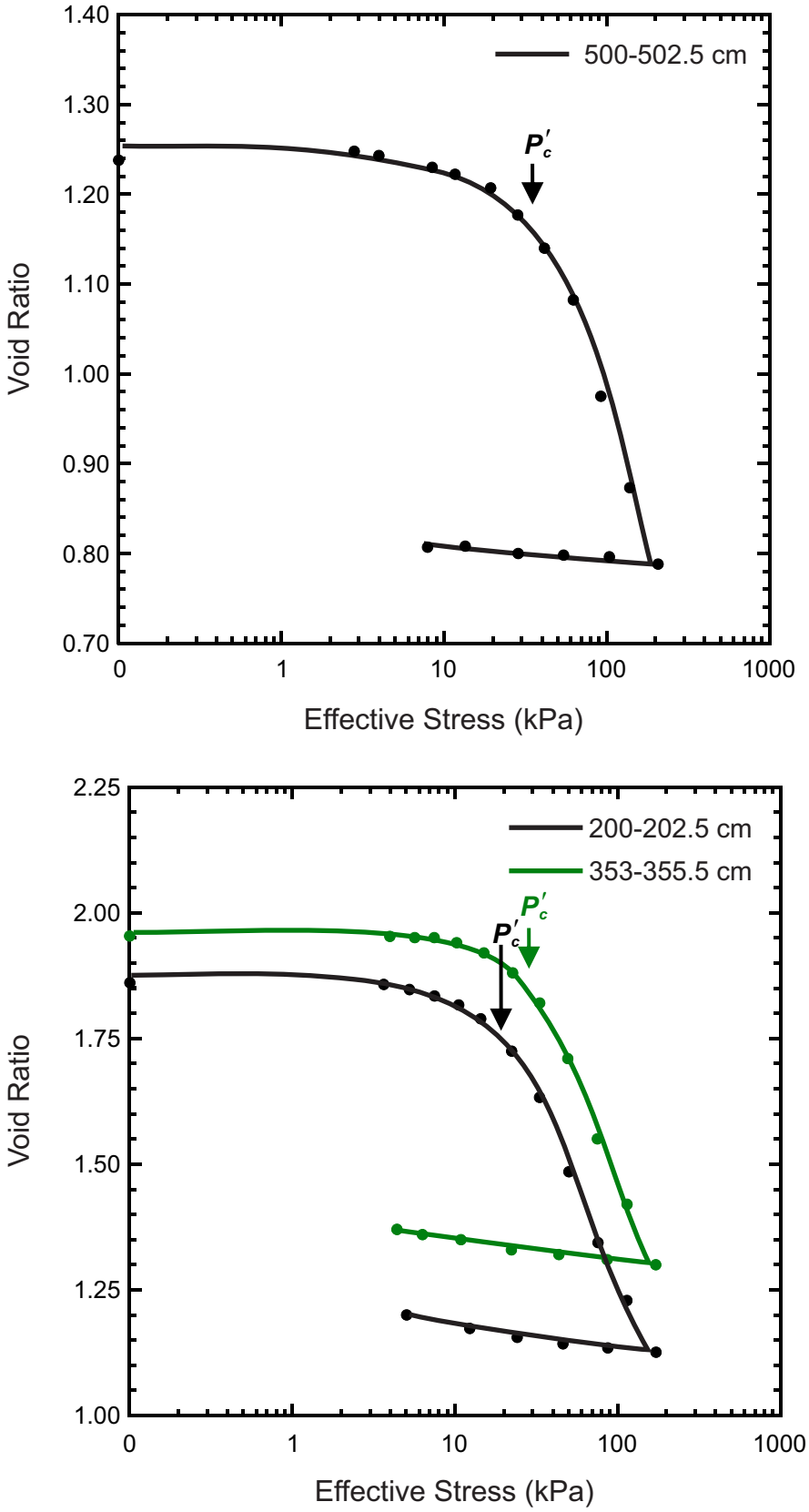

Figure 8.4. Consolidation plots for piston core 20130290048.

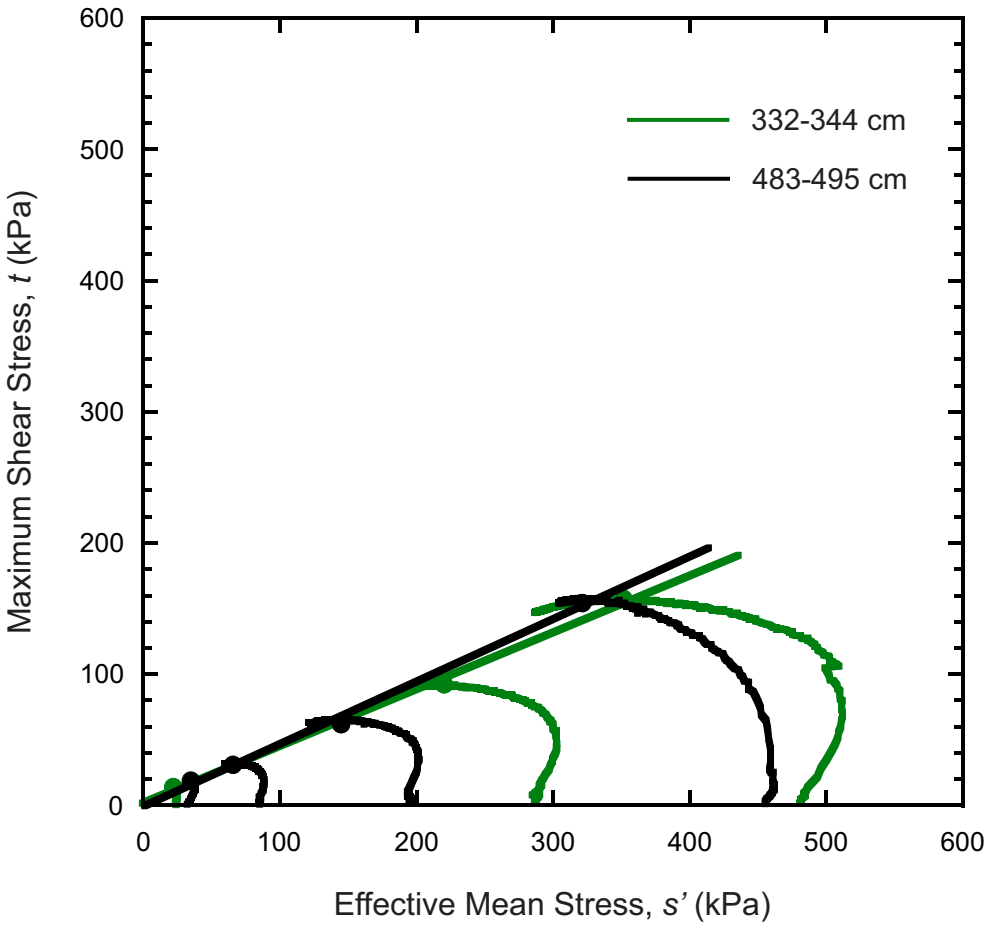

Figure 8.5. Stress paths and failure envelopes from triaxial test results for piston core 20130290048.

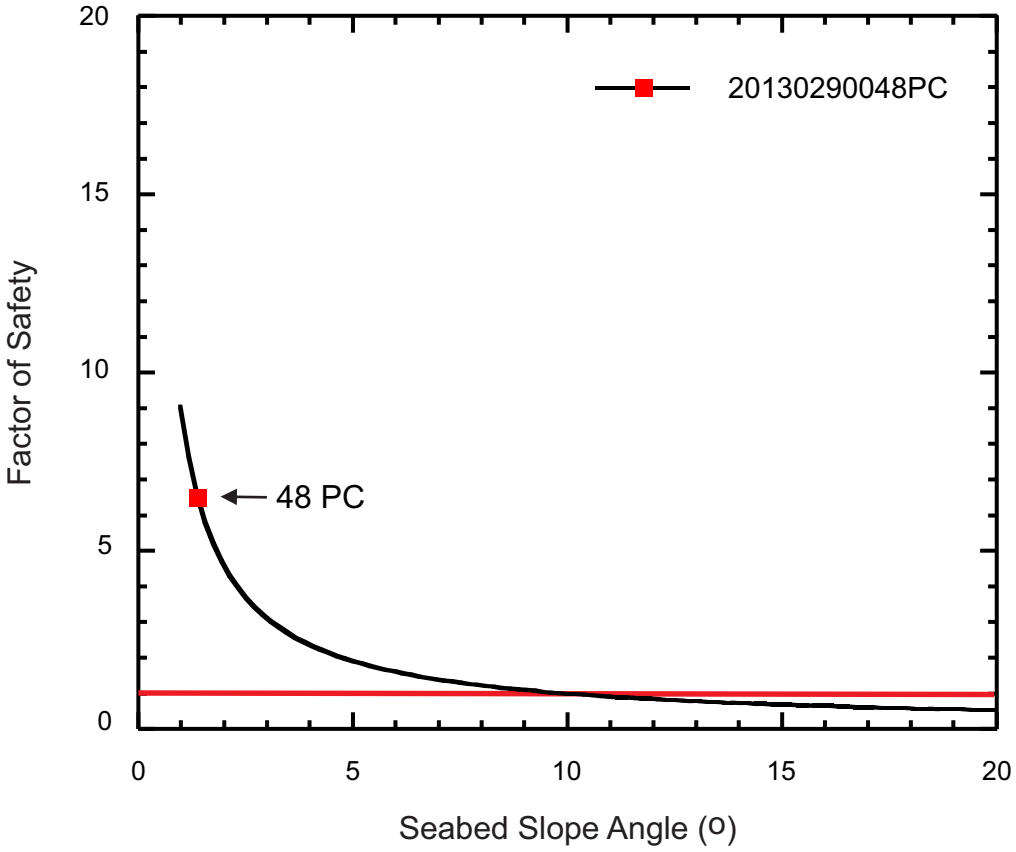

Figure 8.6. FS at various slope angles for piston core 20130290048.

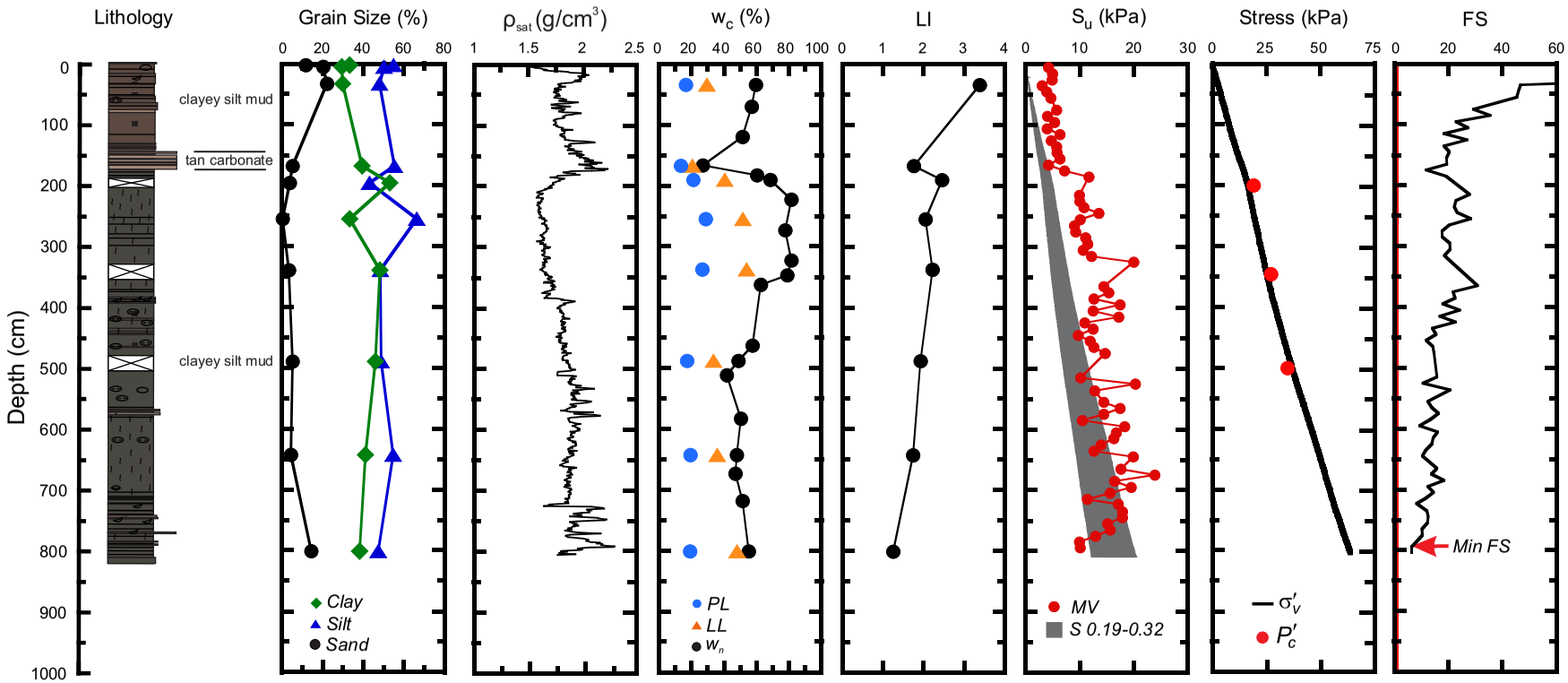

Figure 8.7. Geotechnical profile for core 20130290048 from the slope off Qikiqtarjuaq. (ρ_{sat}= saturated bulk density, w_c = water content, w_n = natural in-situ water content, *PL* = plastic limit, *LL* = liquid limit, *LI* = liquidity index, S_u = undrained shear strength, *MV* = laboratory miniature vane shear strength, *S* = shear strength calculated from the normalized strength ratio, σ'_v = effective overburden stress, P'_c = past maximum stress, *FS* = factor of safety).

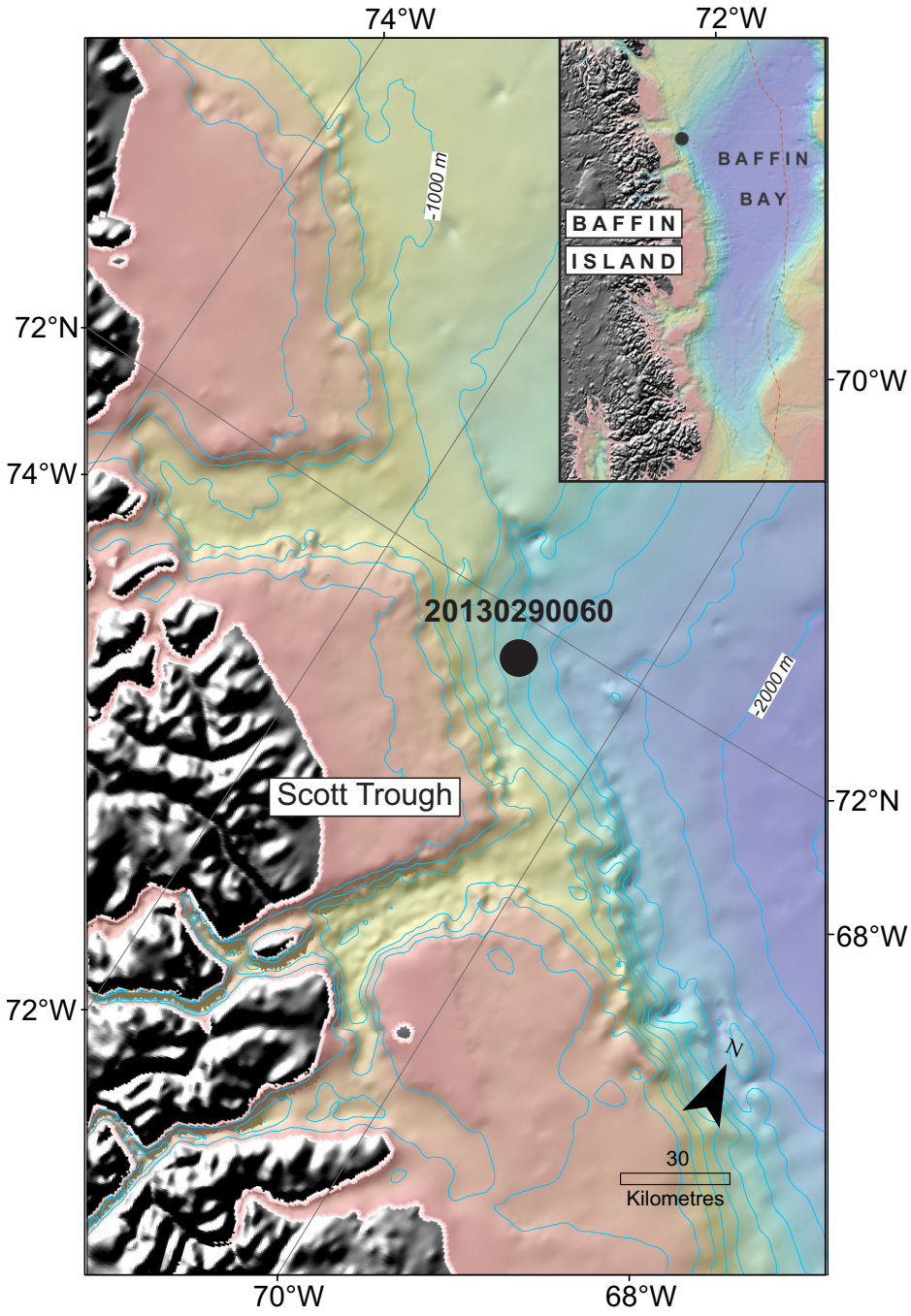

Figure 8.8. Location map of piston core 20130290060.

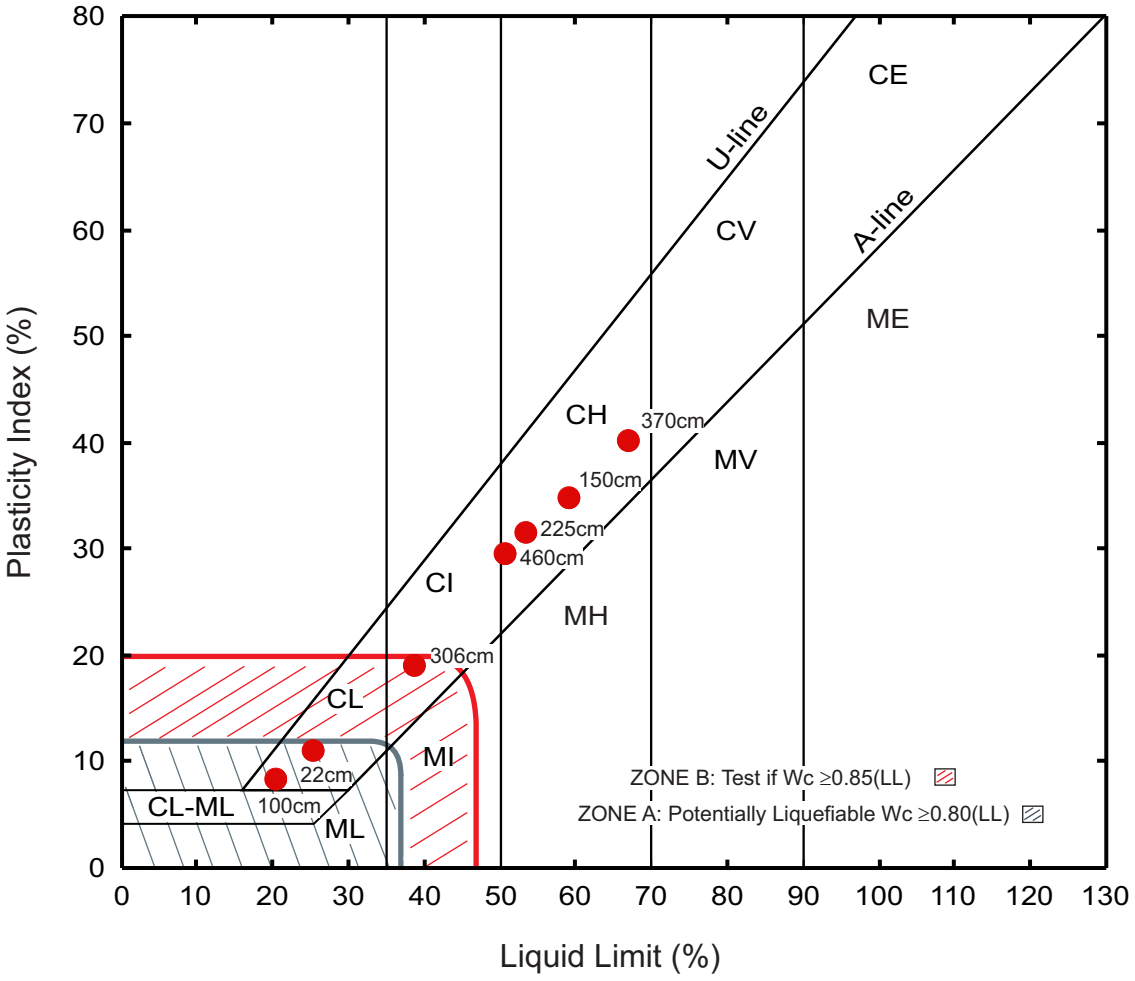

Figure 8.9. Plasticity chart showing Atterberg limit results of piston core 20130290060.

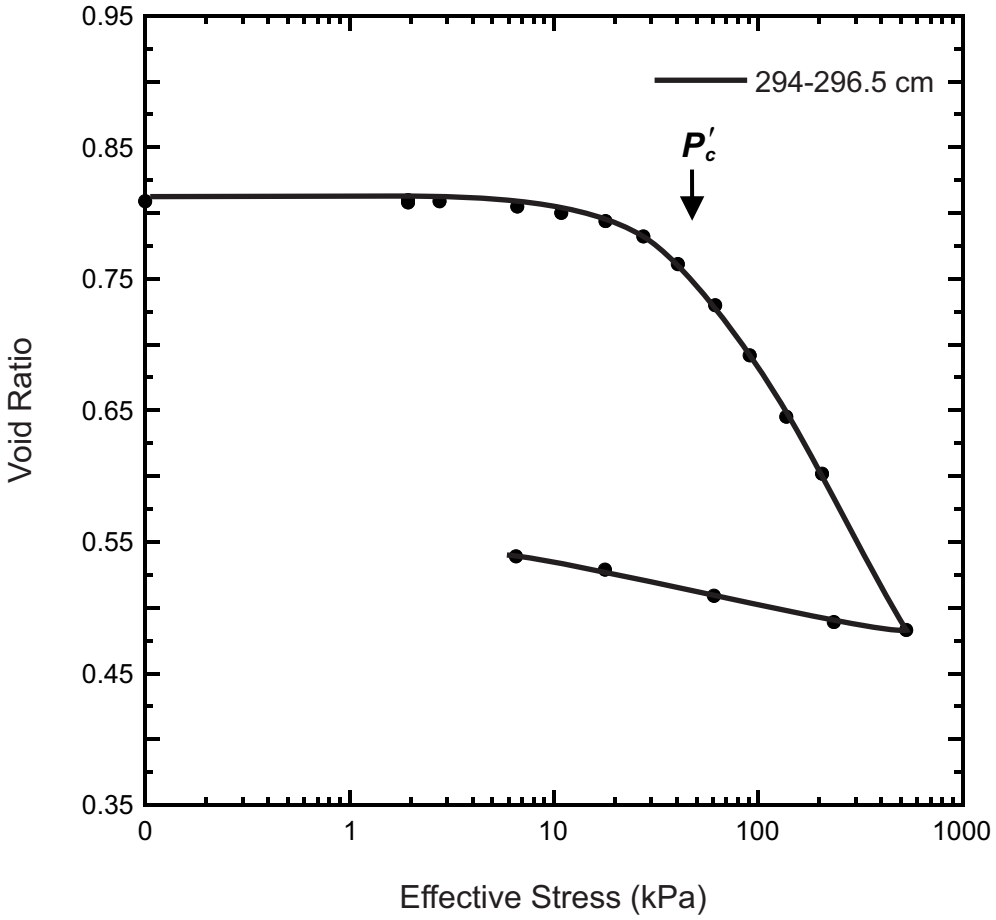

Figure 8.10. Consolidation plot for piston core 20130290060.

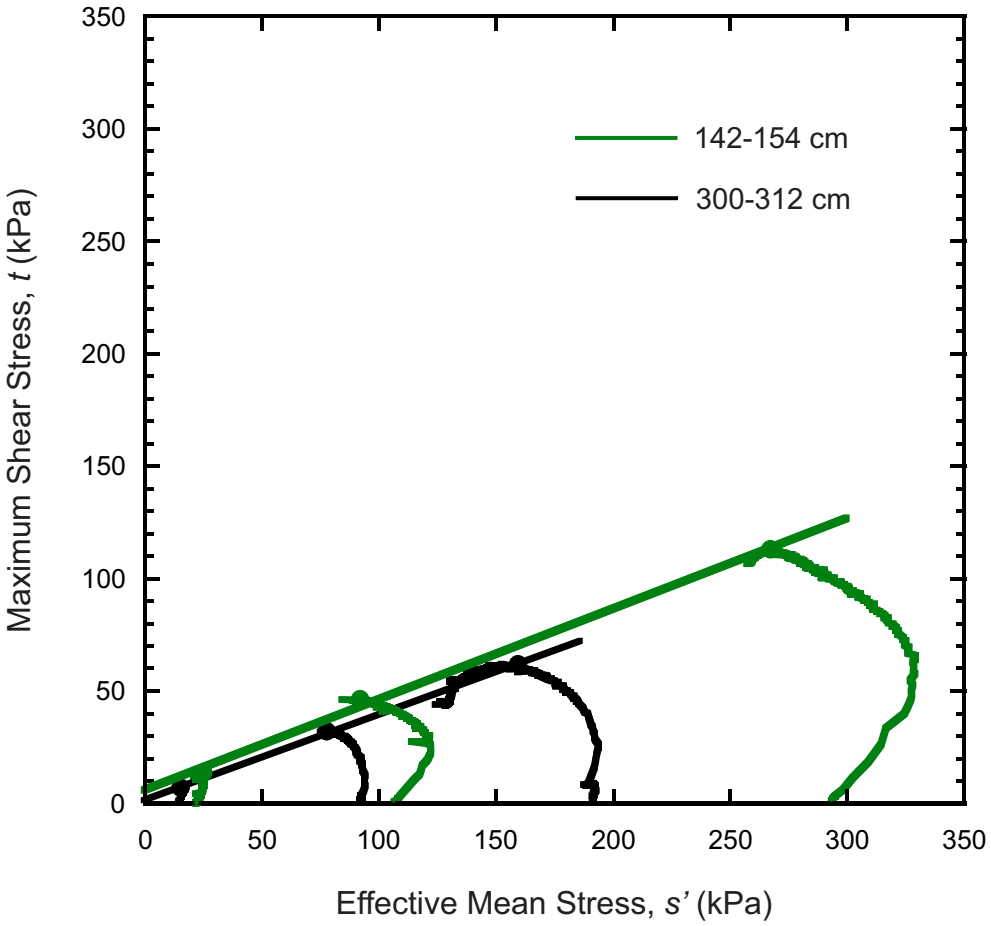

Figure 8.11. Stress paths and failure envelopes from triaxial test results for piston core 20130290060.

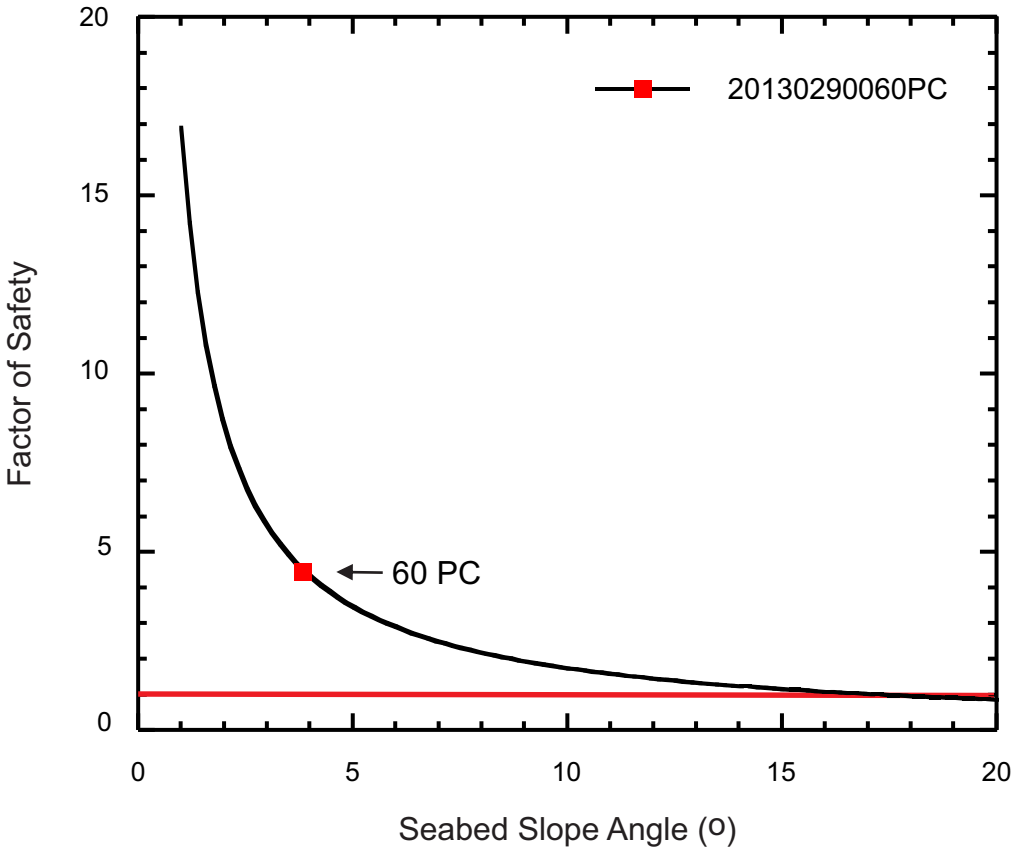

Figure 8.12. FS at various slope angles for piston core 20130290060.

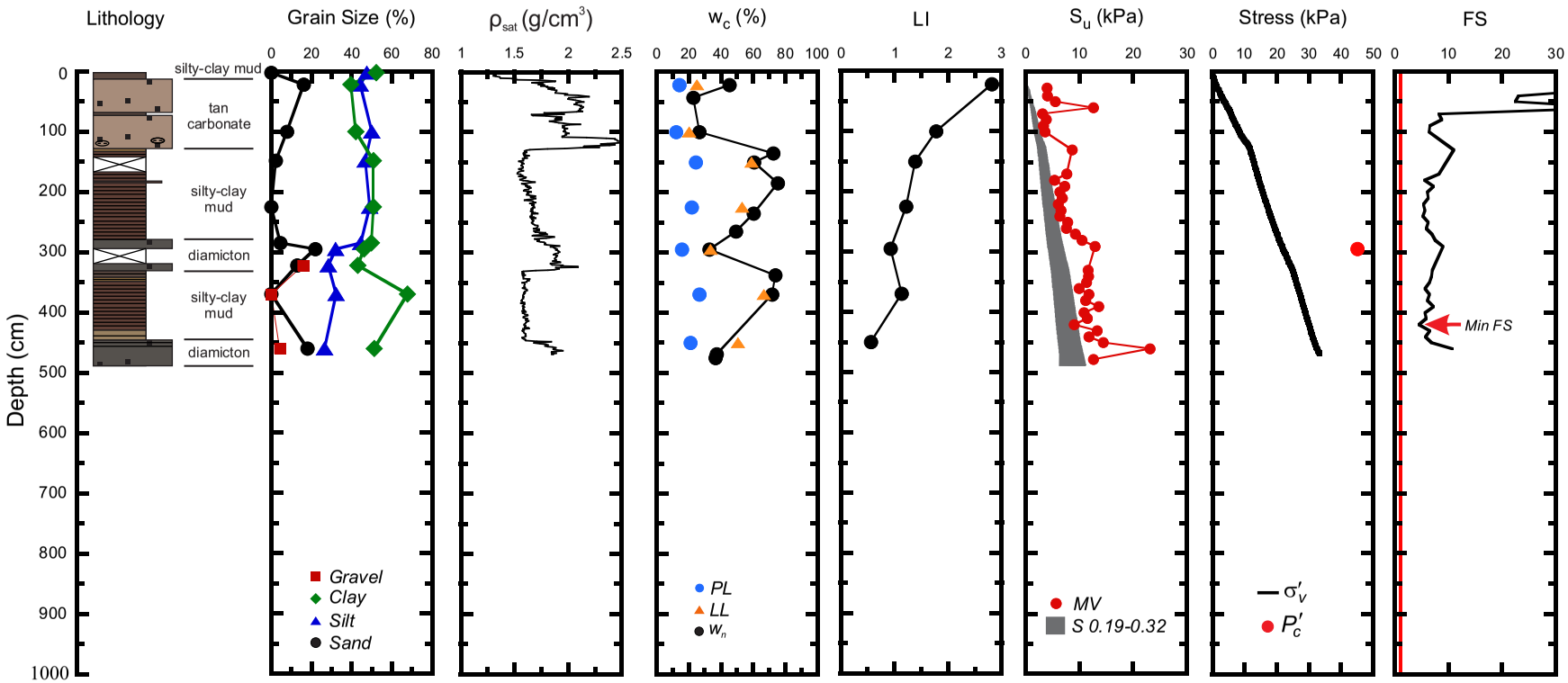

Figure 8.13. Geotechnical profile for core 20130290060 from the slope off Scott Trough. (ρ_{sat}= saturated bulk density, w_c = water content, w_n = natural in-situ water content, *PL* = plastic limit, *LL* = liquid limit, *LI* = liquidity index, S_u = undrained shear strength, *MV* = laboratory miniature vane, *S* = shear strength calculated from the normalized strength ratio, σ'_v = effective overburden stress, P'_c = past maximum stress, *FS* = factor of safety).

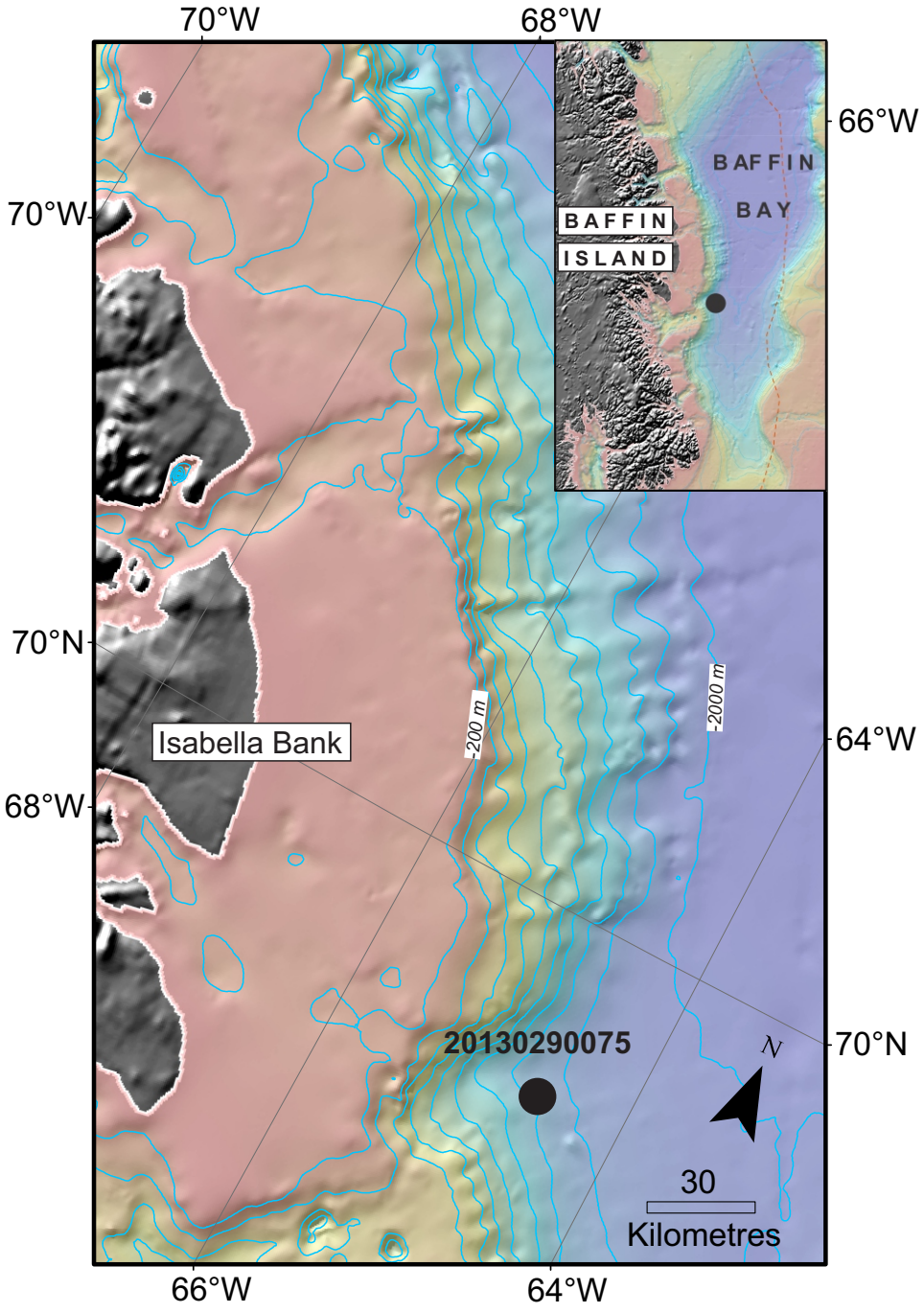

Figure 8.14. Location map of piston core 20130290075.

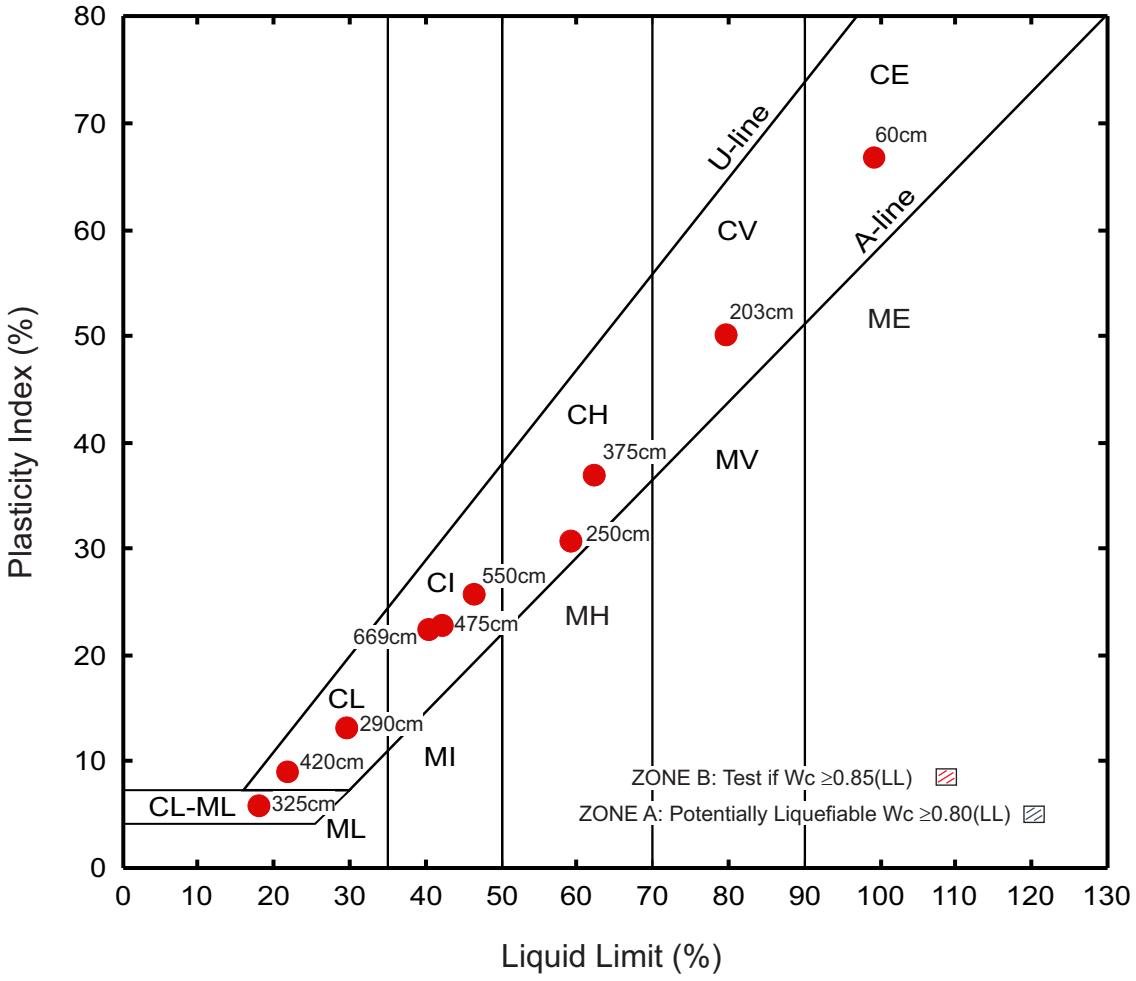

Figure 8.15. Plasticity chart showing Atterberg limit results of piston core 20130290075.

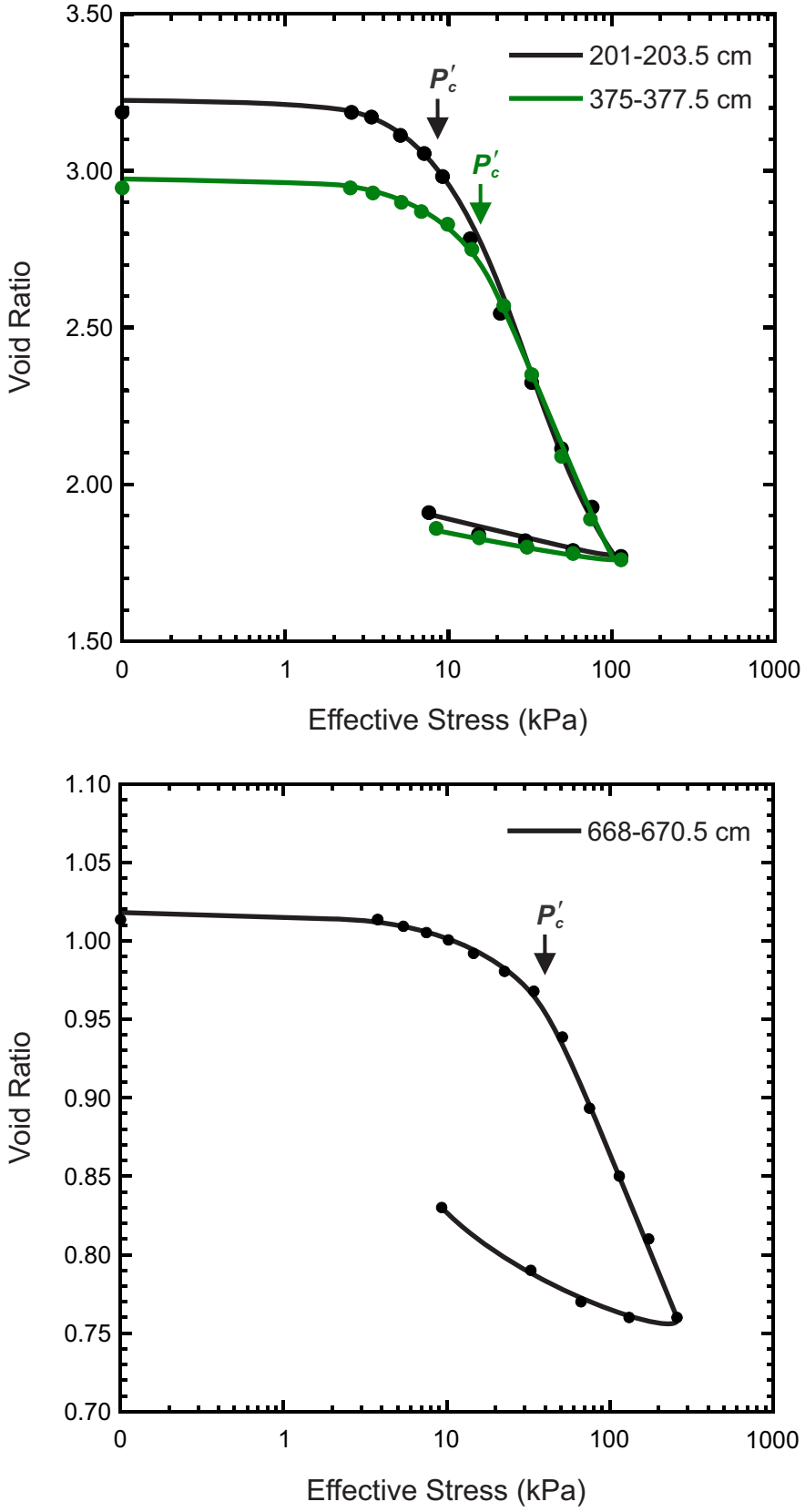

Figure 8.16. Consolidation plots for piston core 20130290075.

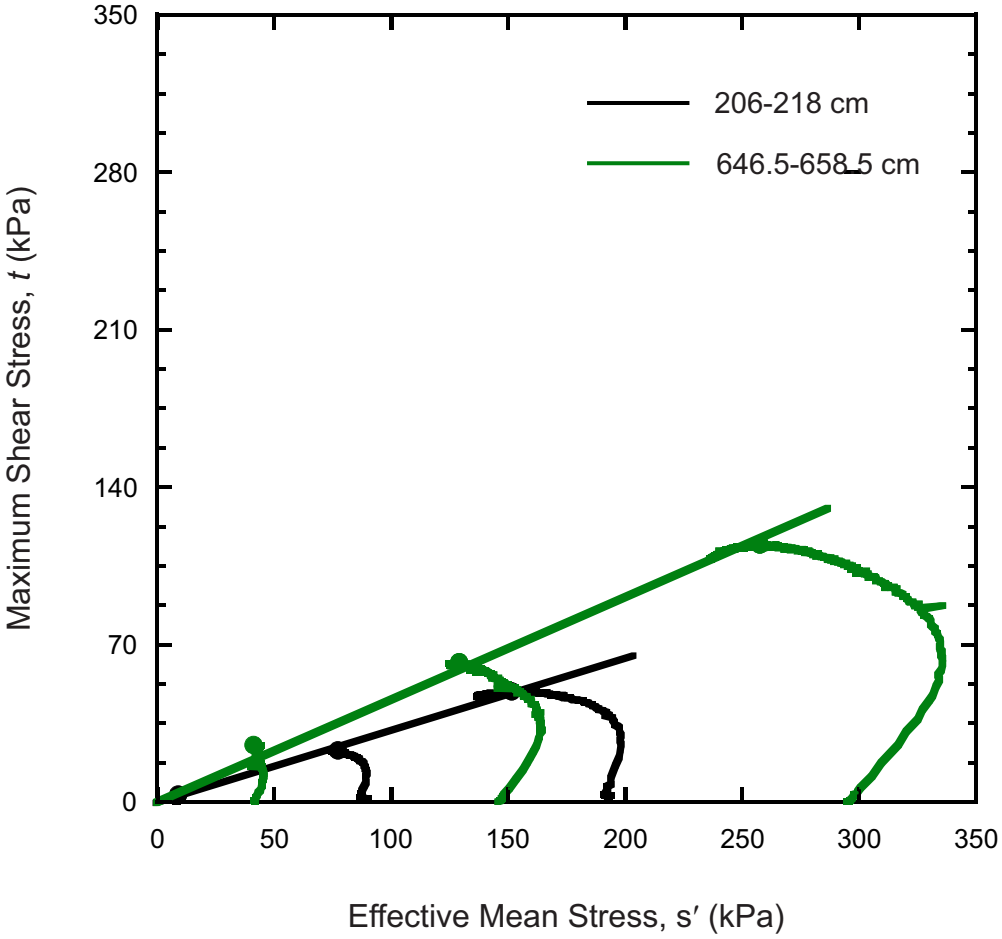

Figure 8.17. Stress paths and failure envelopes from triaxial test results for piston core 20130290075.

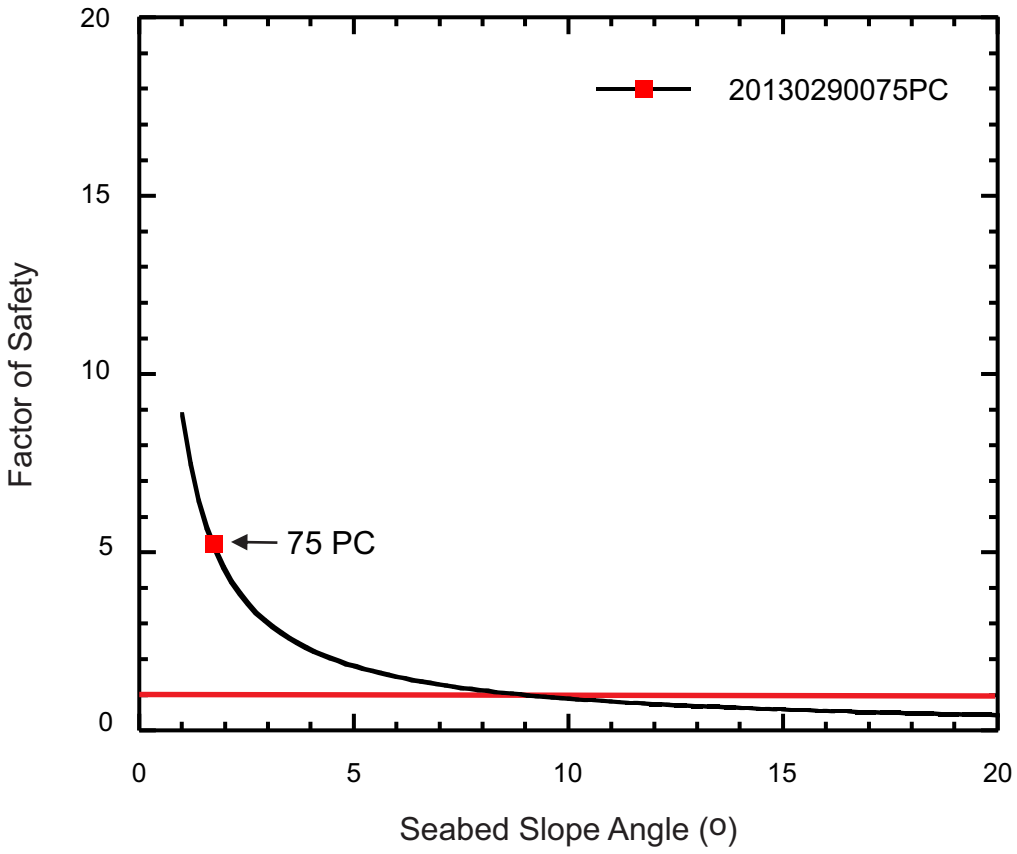

Figure 8.18. FS at various slope angles for piston core 20130290075.

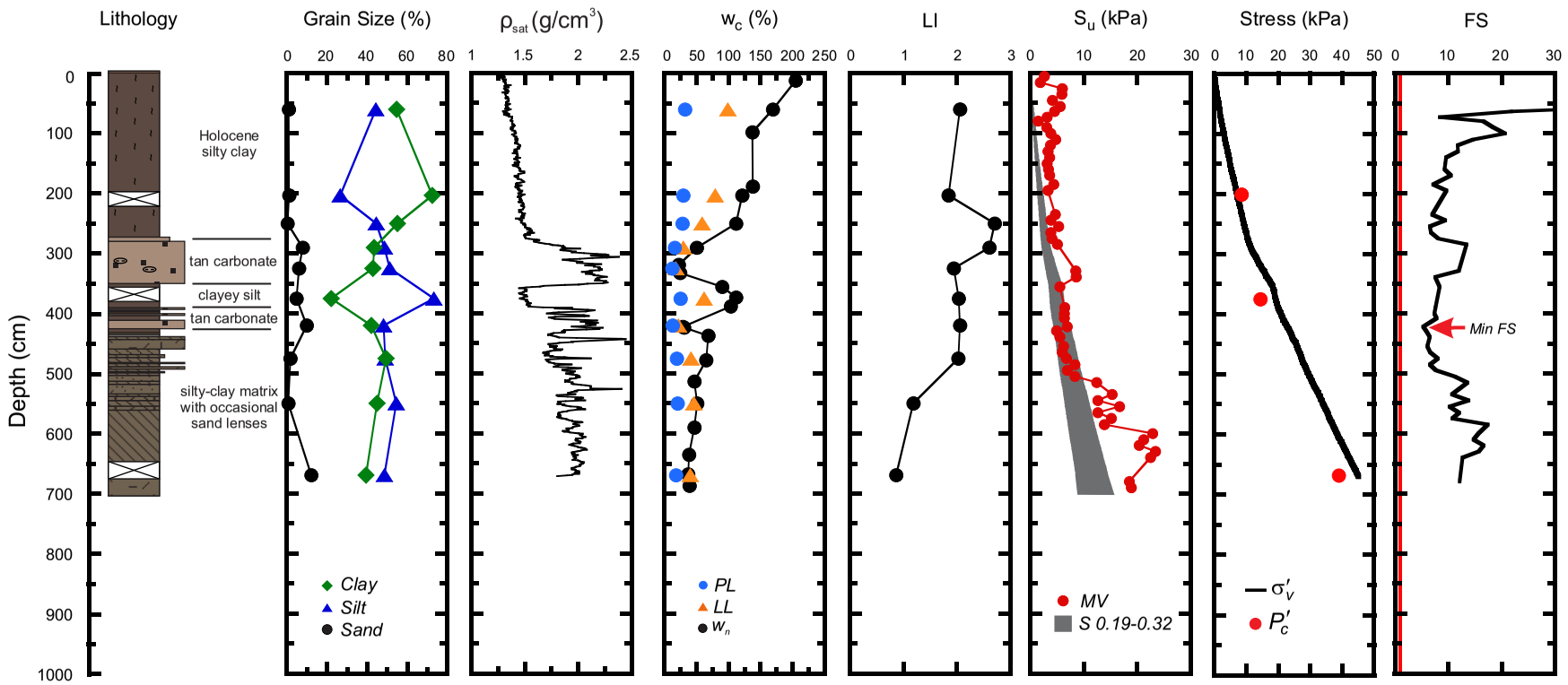

Figure 8.19. Geotechnical profile for core 20130290075 from the slope off Clyde River. (ρ_{sat} = saturated bulk density, w_c = water content, w_n = natural in-situ water content, *PL* = plastic limit, *LL* = liquid limit, *LI* = liquidity index, S_u = undrained shear strength, *MV* = laboratory miniature vane, *S* = shear strength calculated from the normalized strength ratio, σ'_v = effective overburden stress, P'_c = past maximum stress, *FS* = factor of safety).

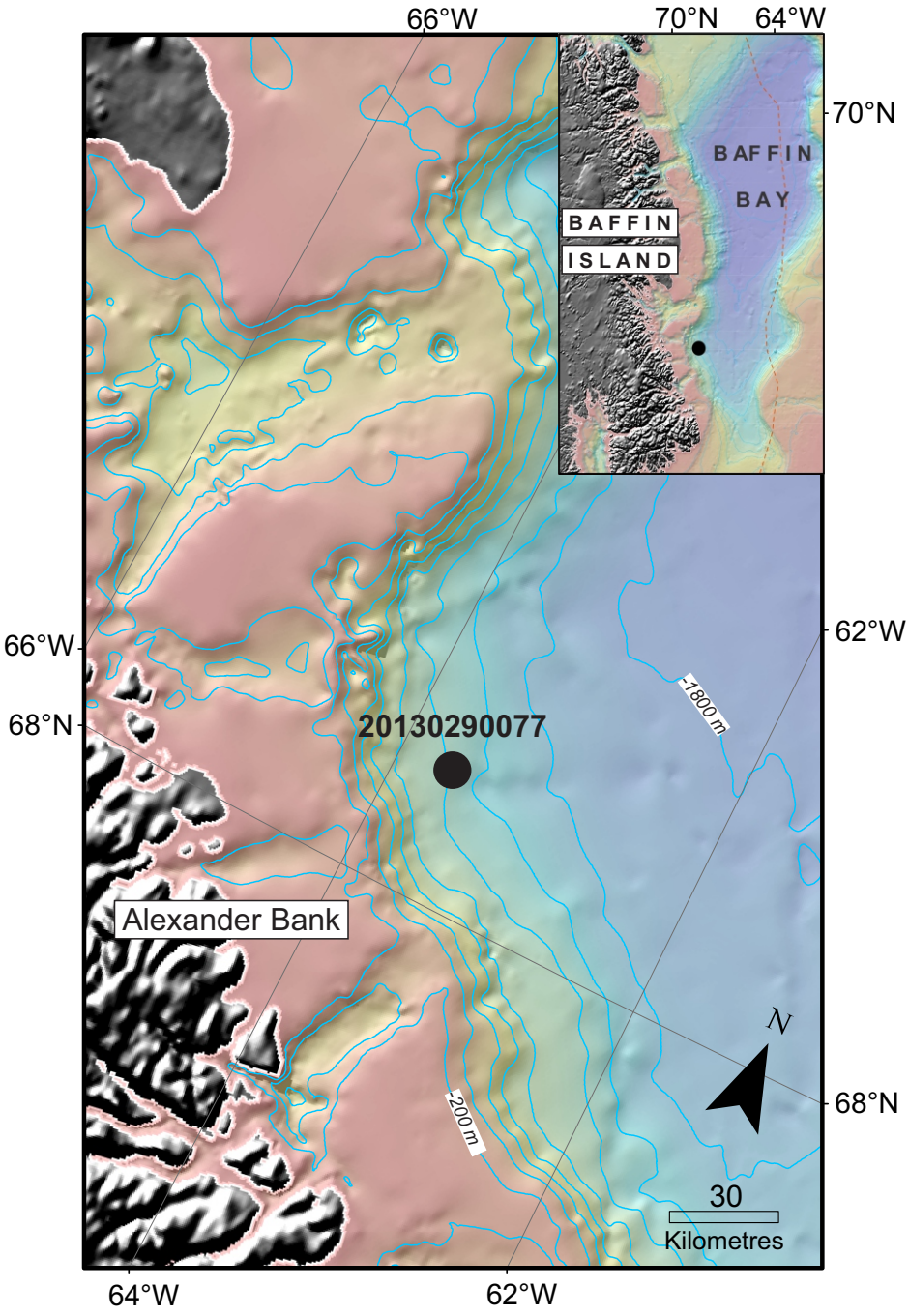

Figure 8.20. Location map of piston core 20130290077.

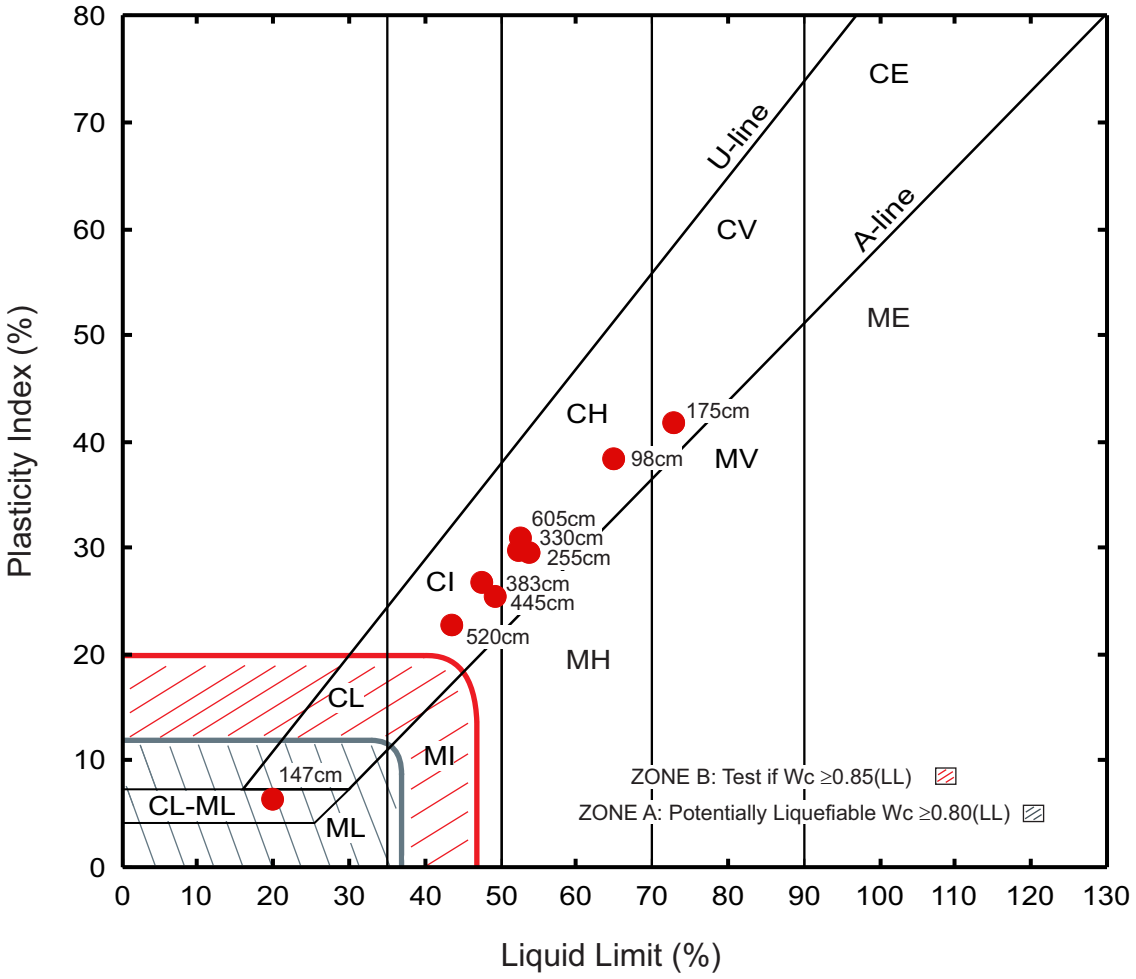

Figure 8.21. Plasticity chart showing Atterberg limit results of piston core 20130290077.

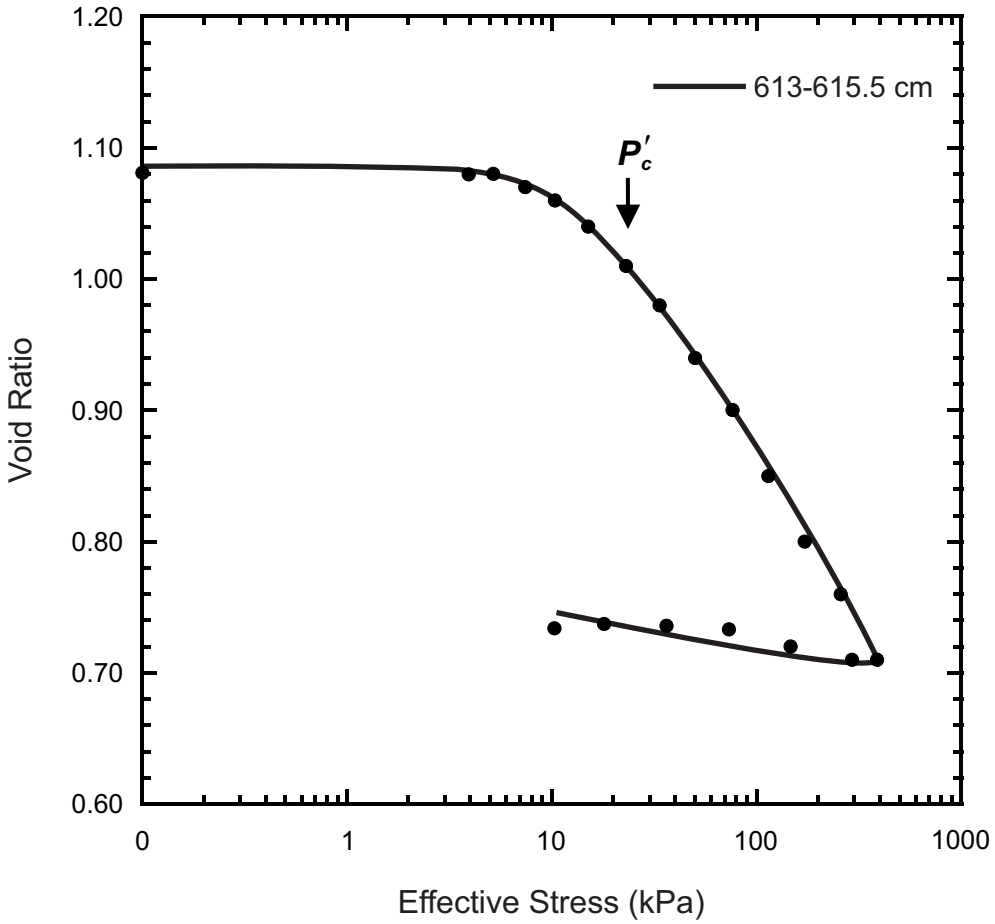

Figure 8.22. Consolidation plot for piston core 20130290077.

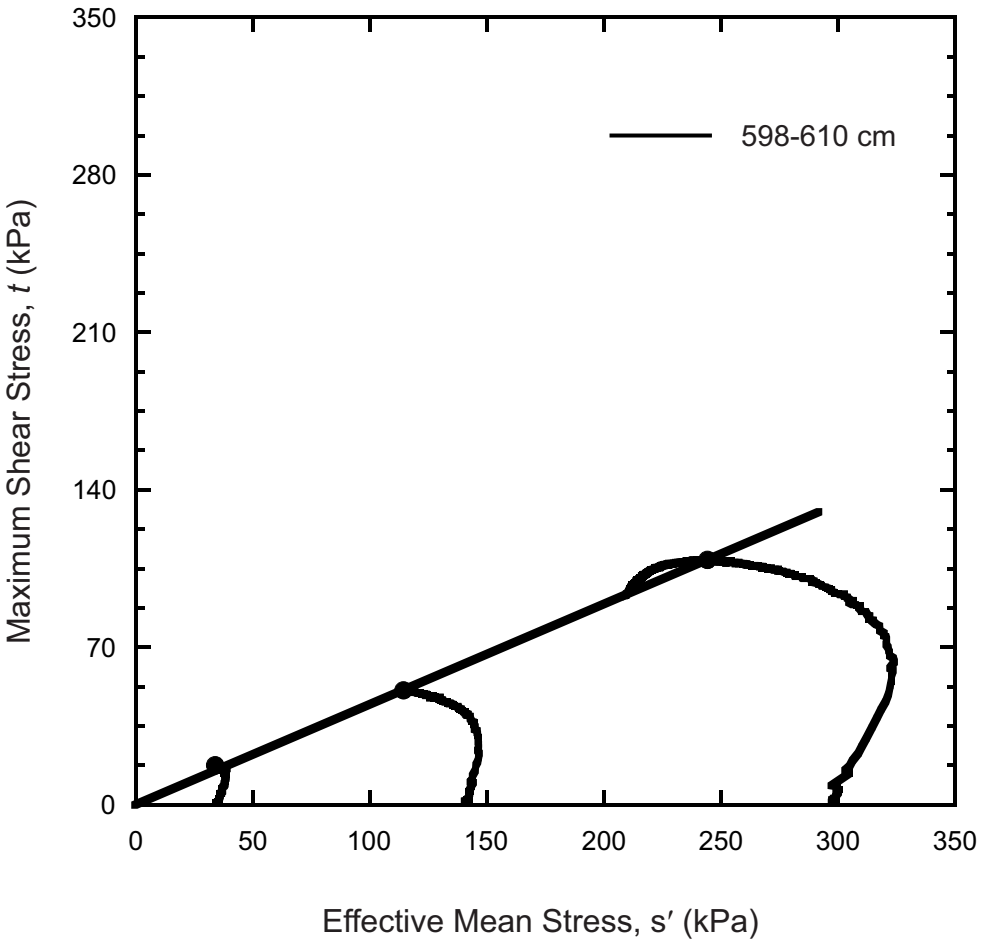

Figure 8.23. Stress path and failure envelope from triaxial test results for piston core 20130290077.

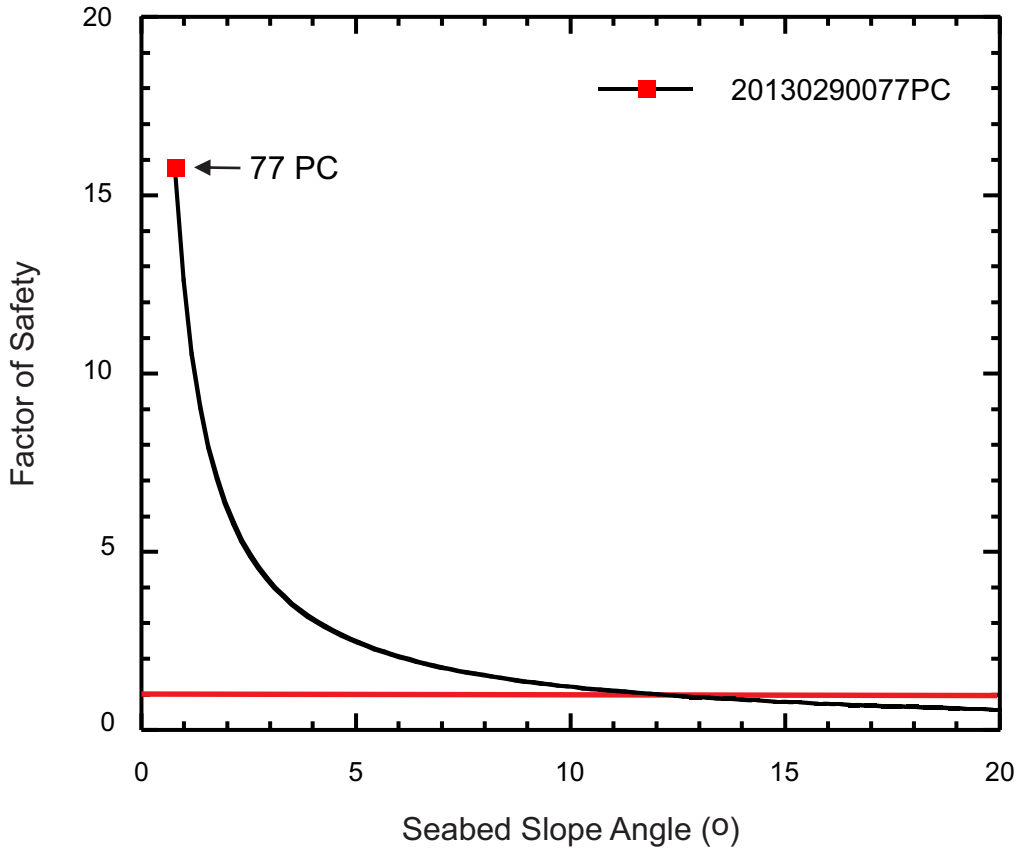

Figure 8.24. FS at various slope angles for piston core 20130290077.

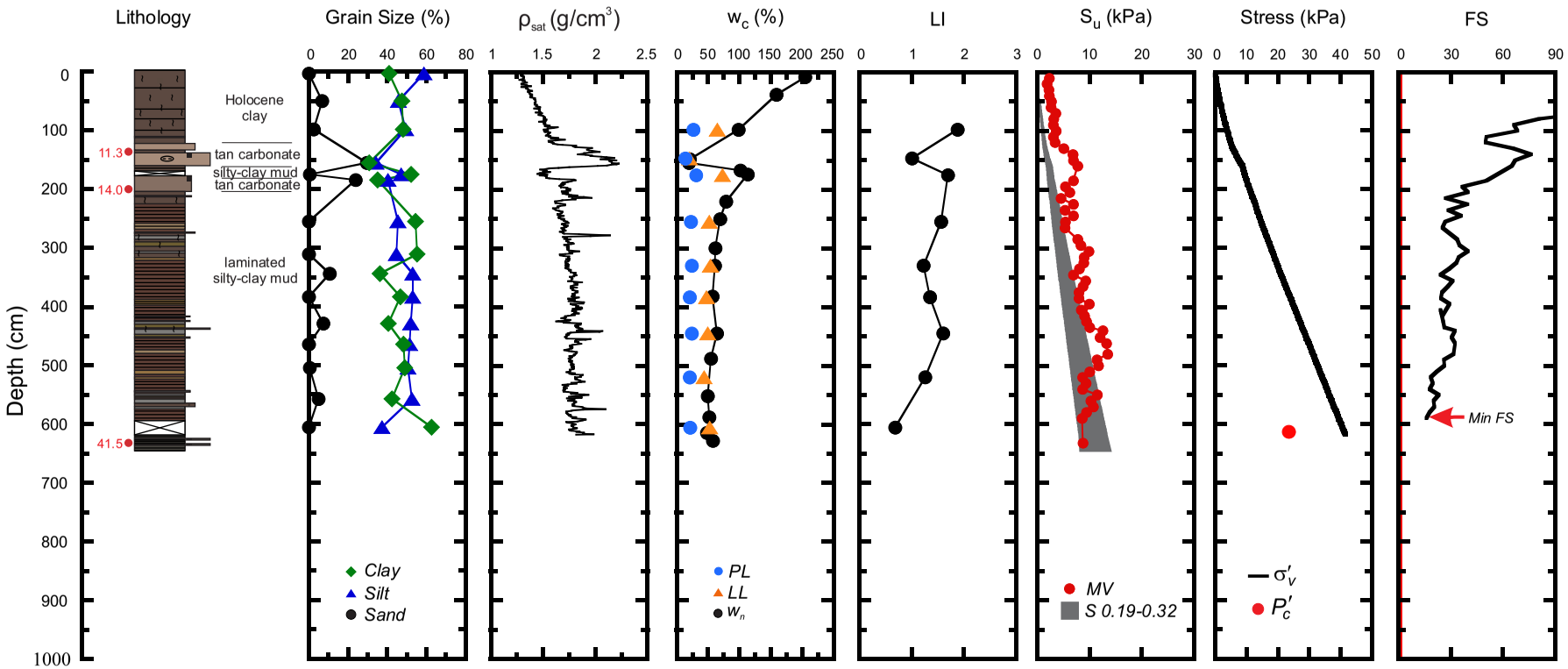

Figure 8.25. Geotechnical profile for core 20130290077 from the slope off Alexander Bank. (ρ_{sat} = saturated bulk density, w_c = water content, w_n = natural in-situ water content, *PL* = plastic limit, *LL* = liquid limit, *LI* = liquidity index, S_u = undrained shear strength, *MV* = laboratory miniature vane, *S* = shear strength calculated from the normalized strength ratio, σ'_v = effective overburden stress, P'_c = past maximum stress, *FS* = factor of safety).

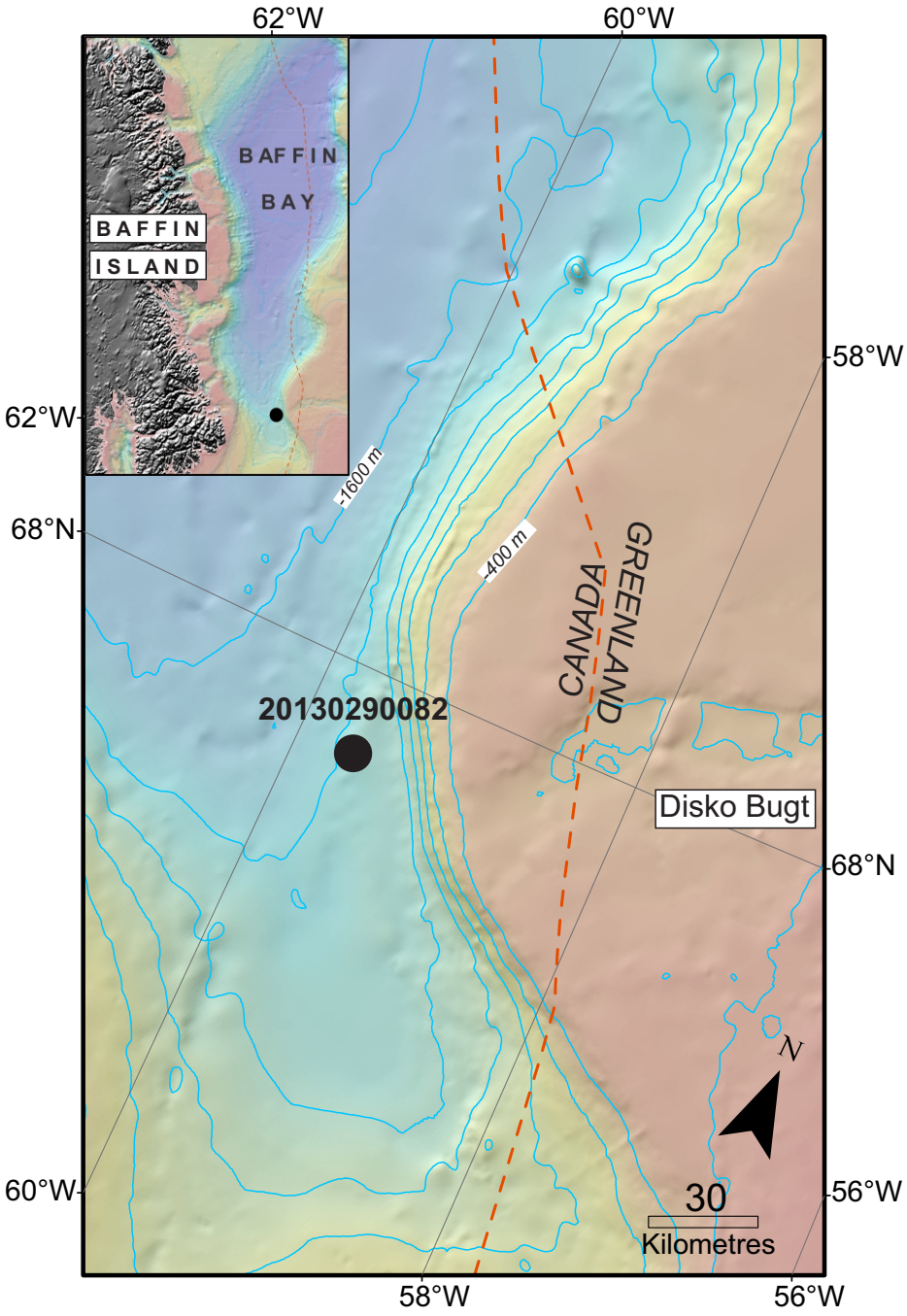

Figure 8.26. Location map of piston core 20130290082.

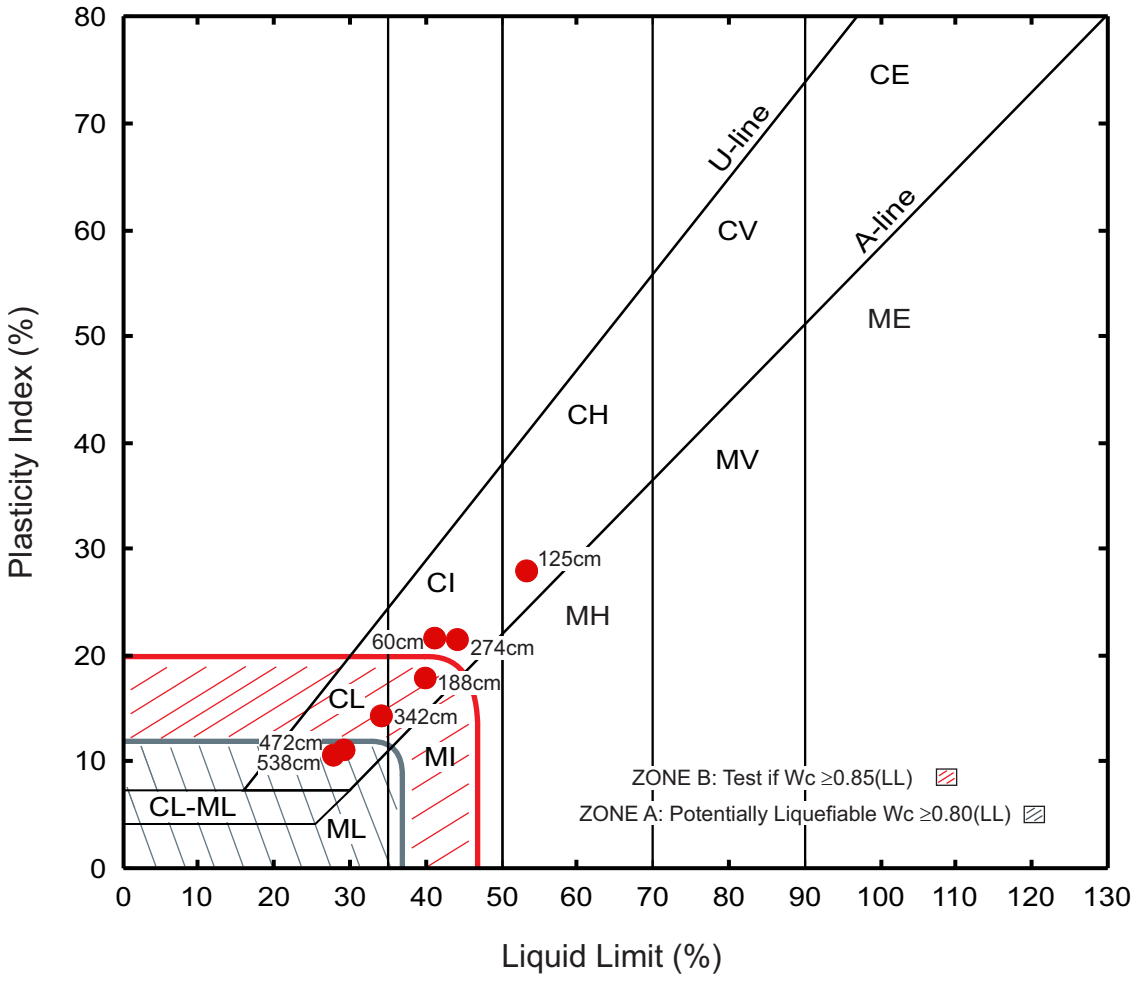

Figure 8.27. Plasticity chart showing Atterberg limit results of piston core 20130290082.

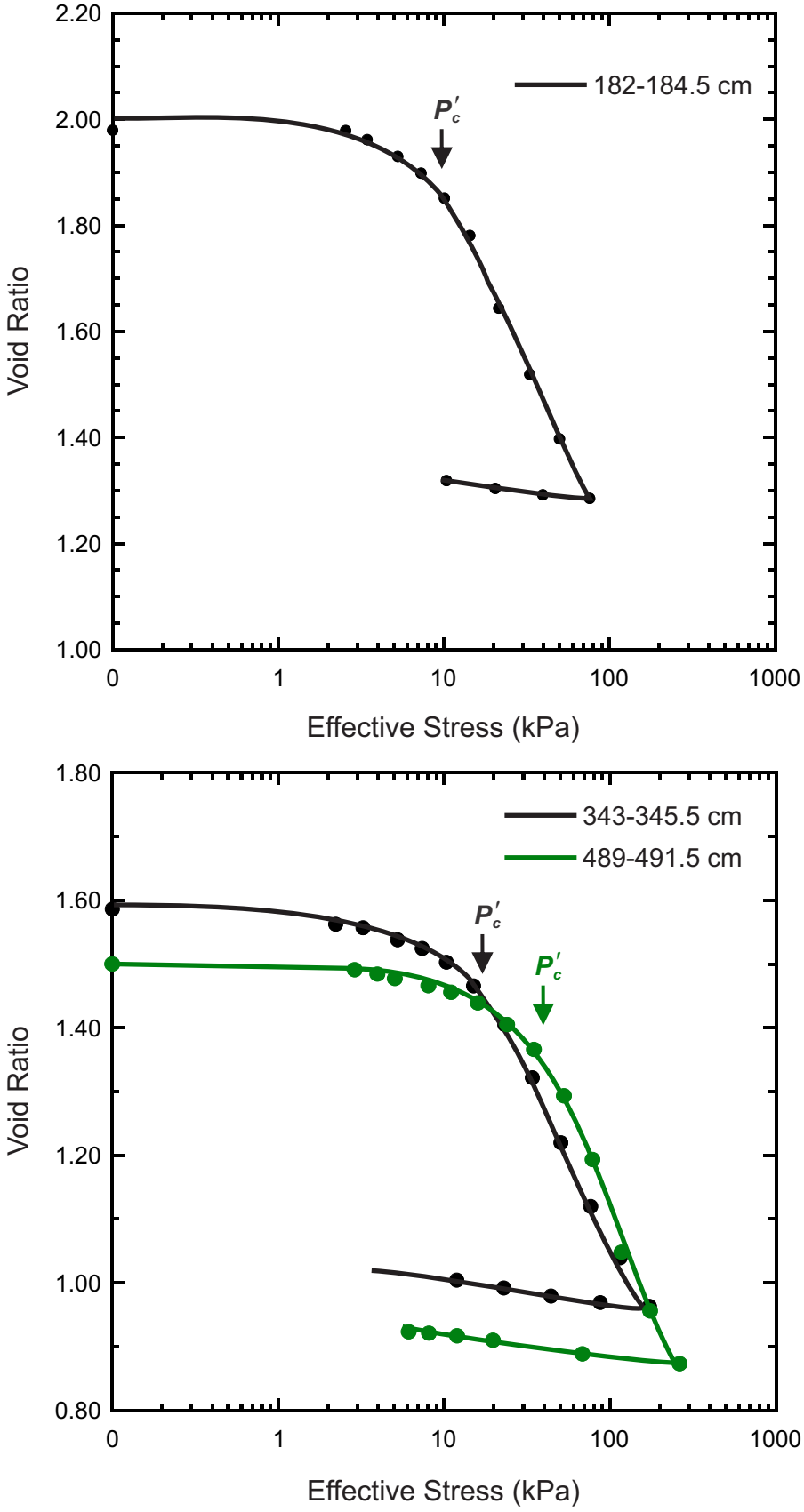

Figure 8.28. Consolidation plots for piston core 20130290082.

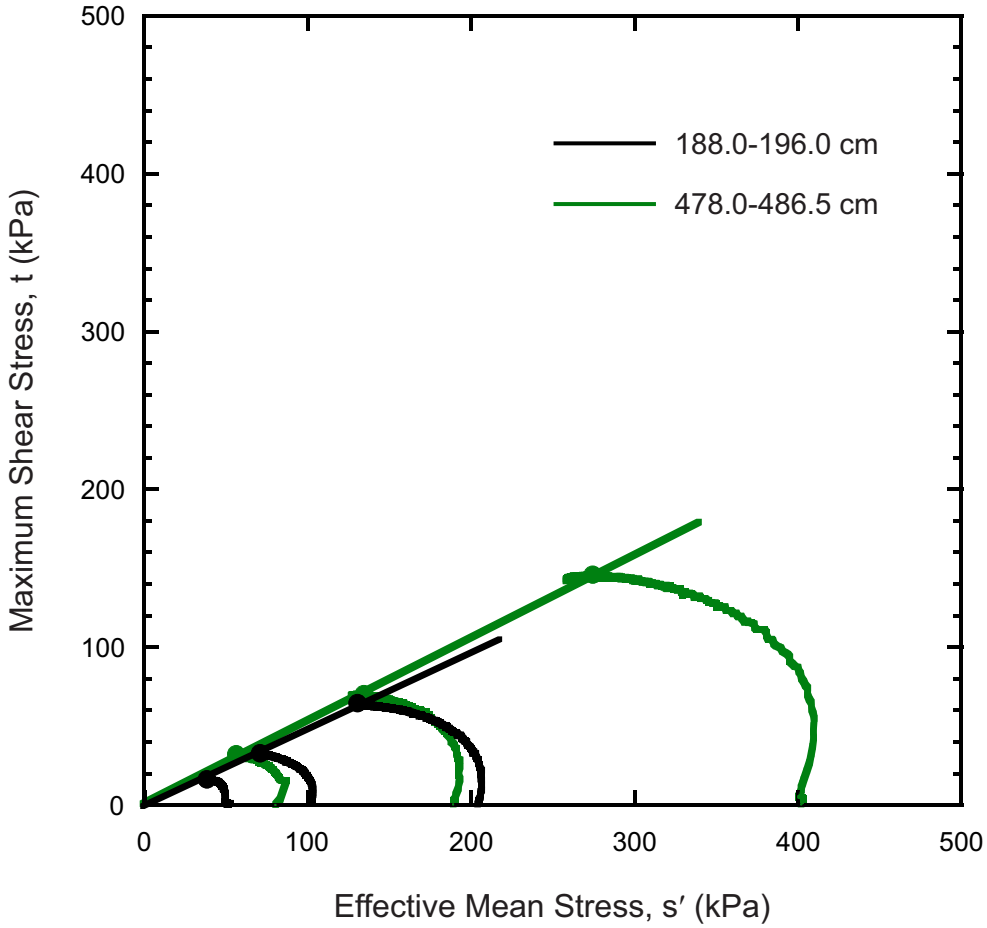

Figure 8.29. Stress paths and failure envelopes from triaxial test results for piston core 20130290082.

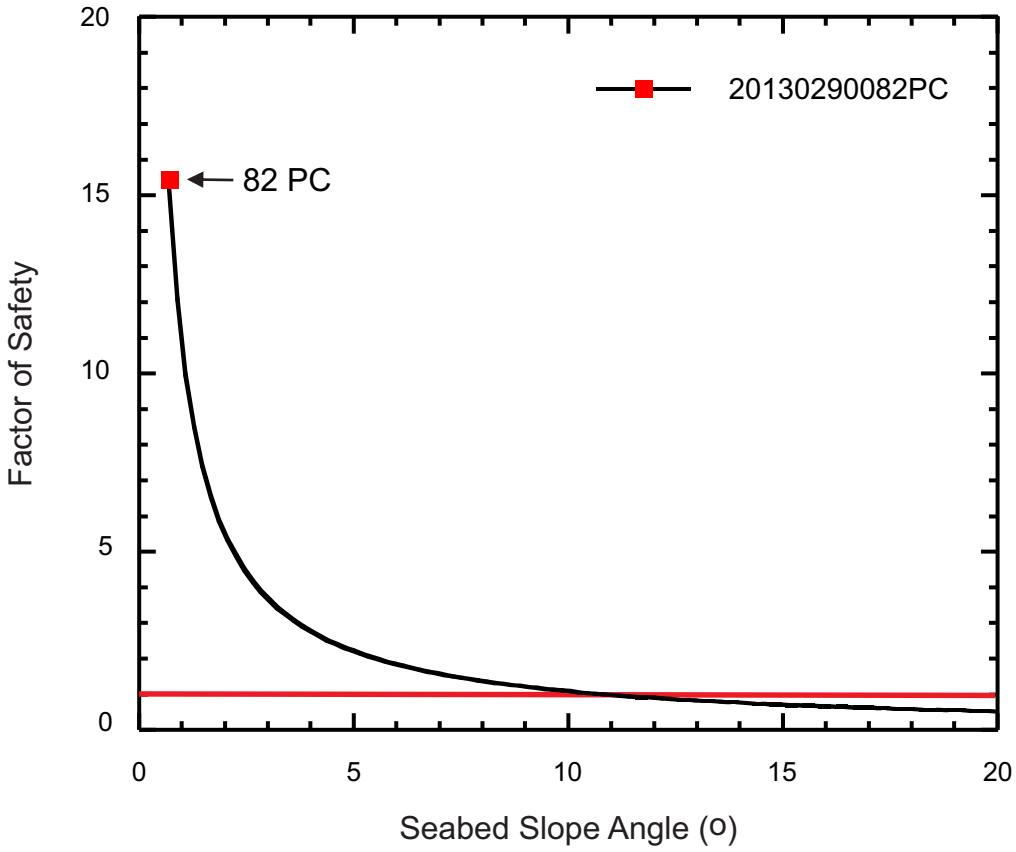

Figure 8.30. FS at various slope angles for piston core 20130290082.

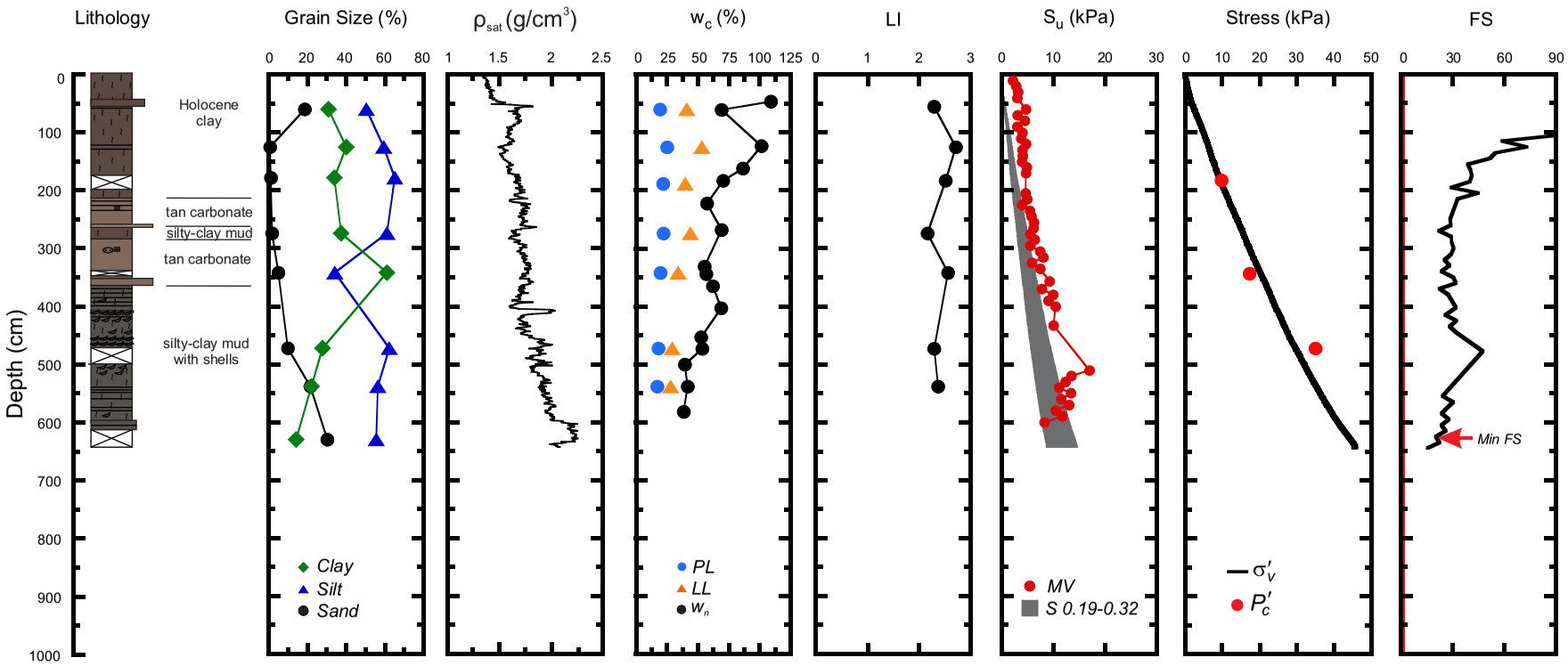

Figure 8.31. Geotechnical profile for core 20130290082 from the slope off Disko Bugt. (ρ_{sat}= saturated bulk density, w_c = water content, w_n = natural in-situ water content, *PL* = plastic limit, *LL* = liquid limit, *LI* = liquidity index, S_u = undrained shear strength, *MV* = laboratory miniature vane, *S* = shear strength calculated from the normalized strength ratio, σ'_v = effective overburden stress, P'_c = past maximum stress, *FS* = factor of safety).

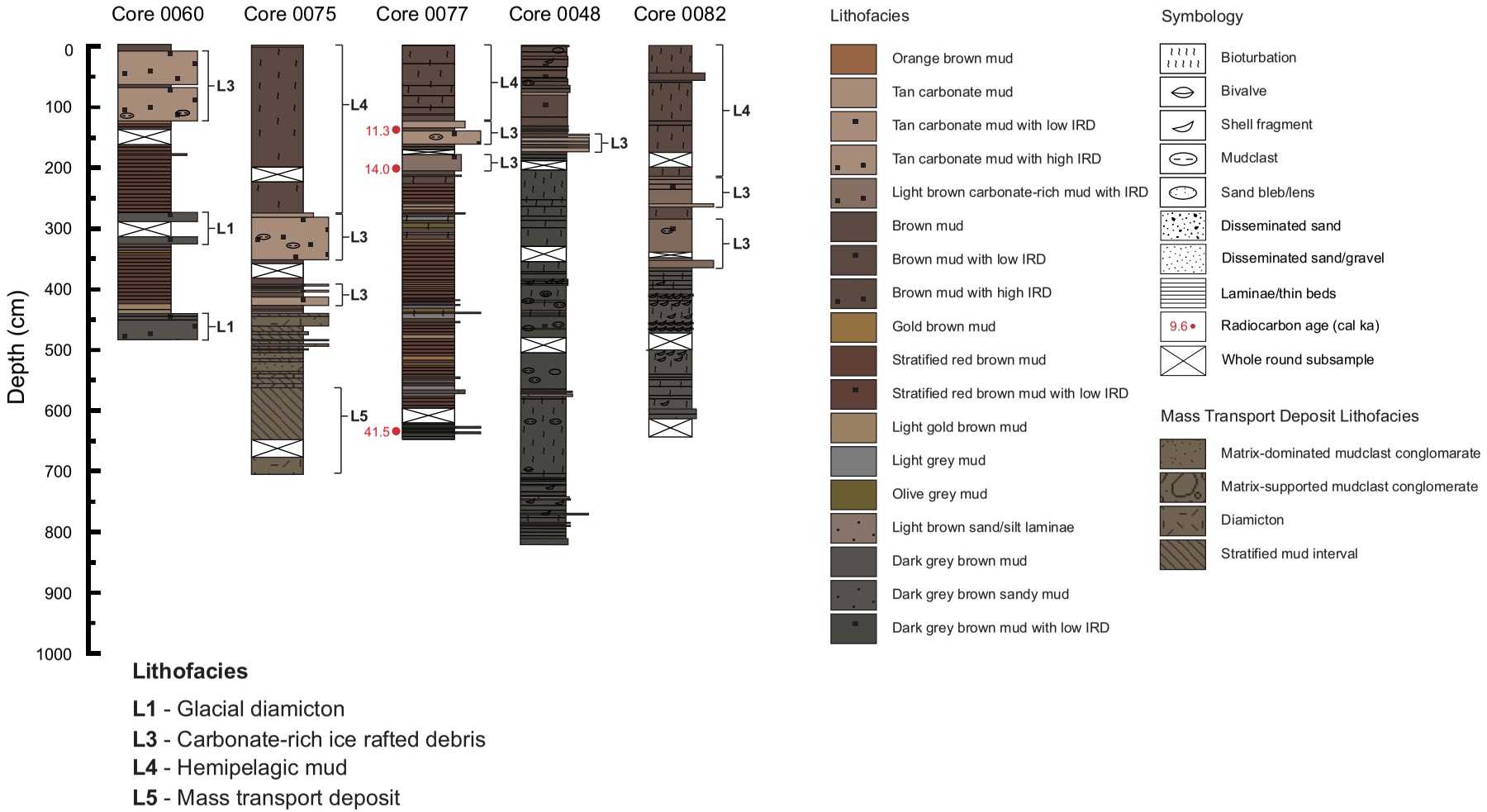

Figure 9.1. Lithofacies for the 5 geotechnical cores.

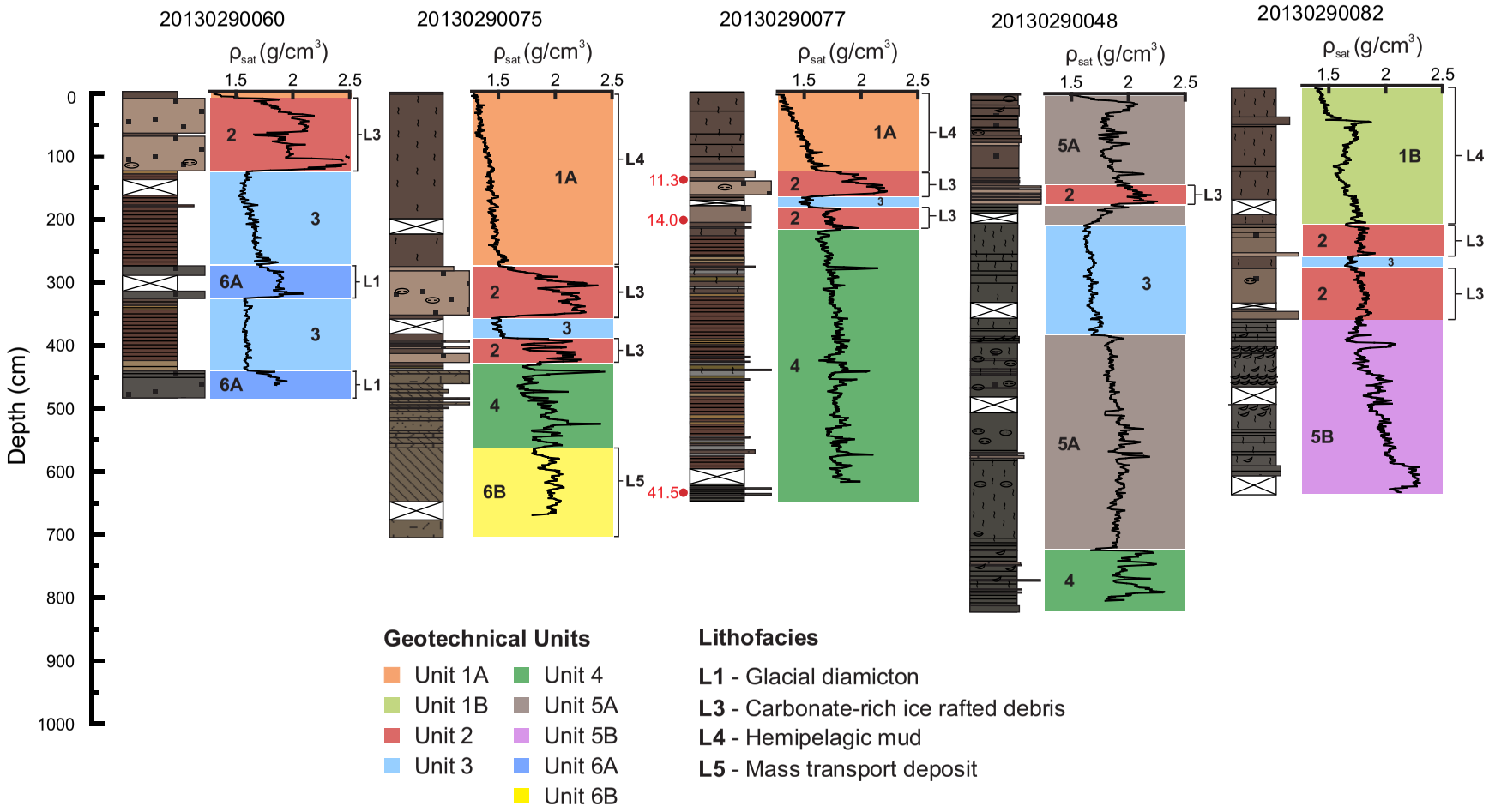

Figure 9.2. Lithologies (Jenner et al, 2018) and associated geotechnical units. Red dots signify radiocarbon age.

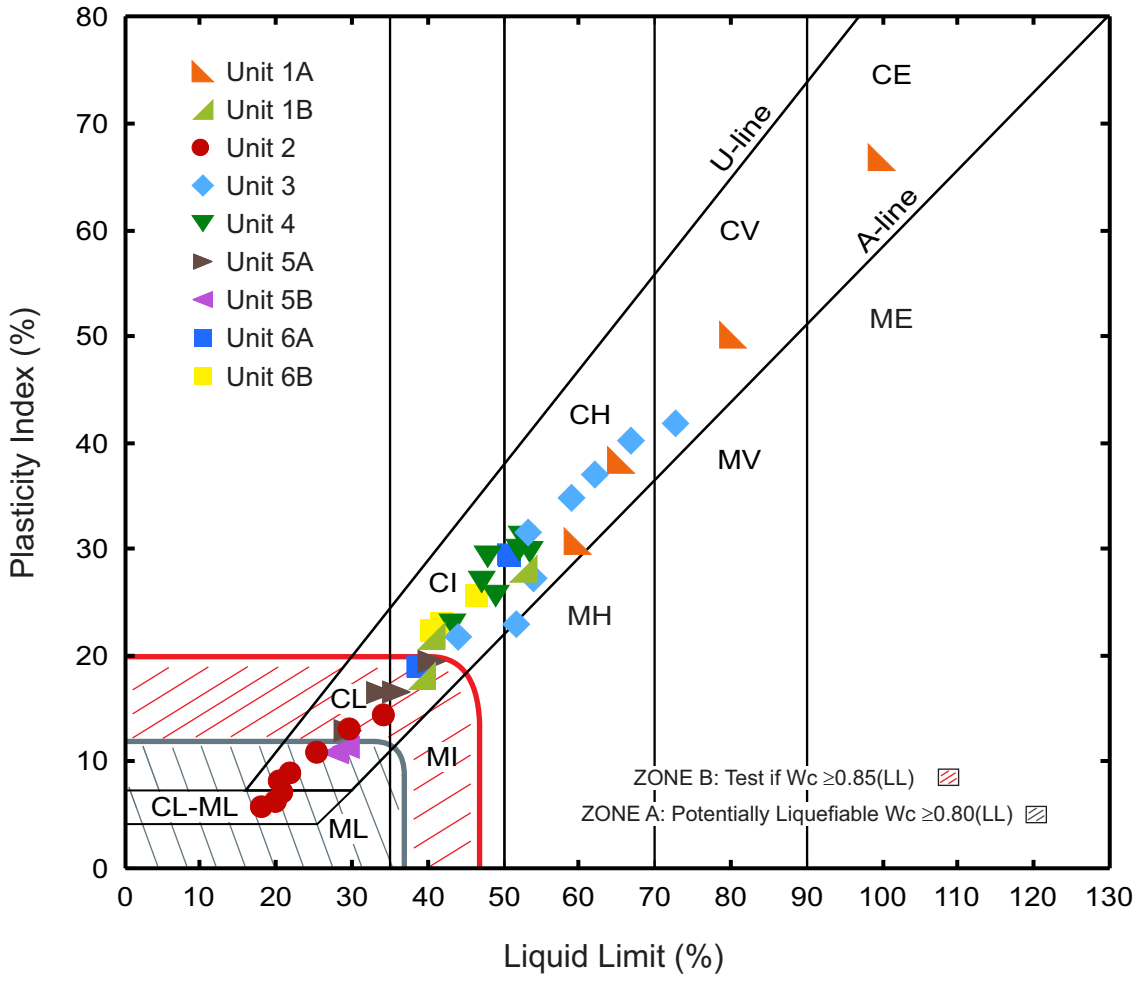

Figure 9.3. Plasticity chart showing Atterberg limit results for the geotechnical units.

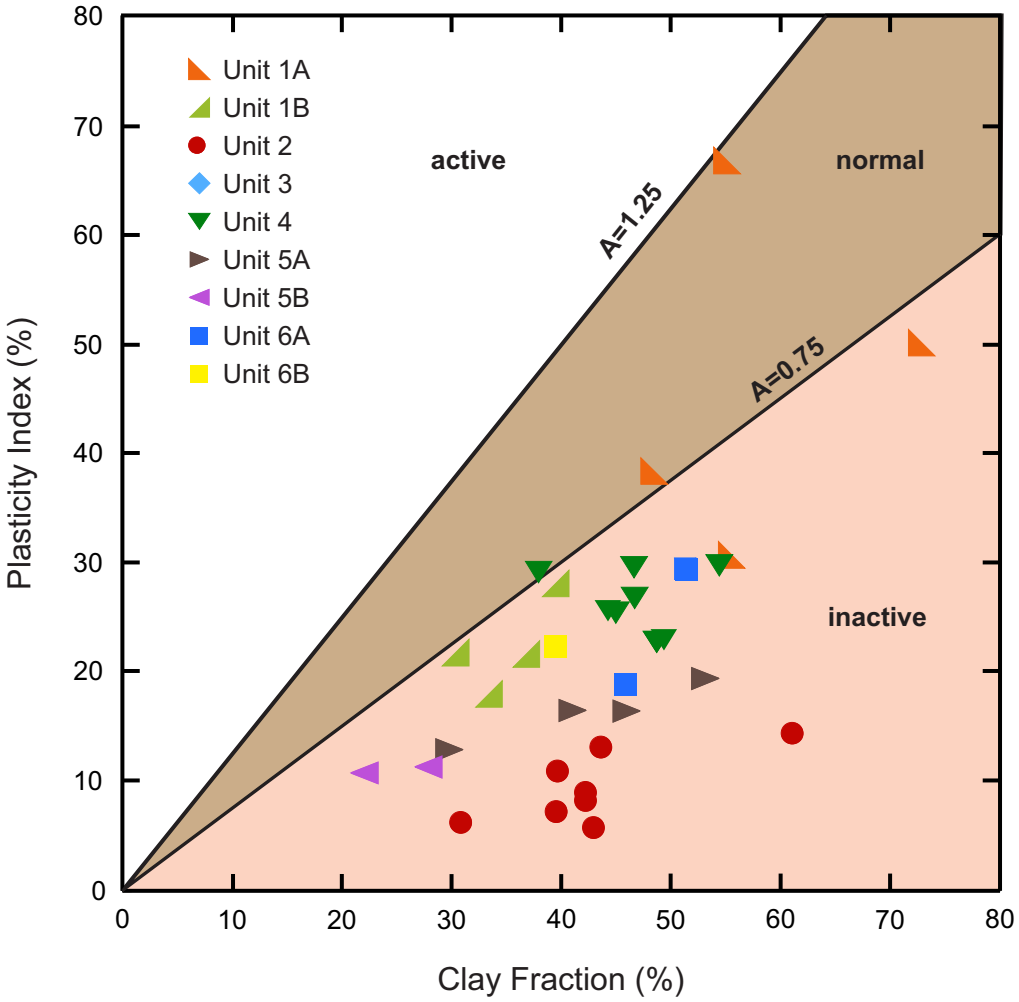

Figure 9.4. Activity chart showing results for the geotechnical units.

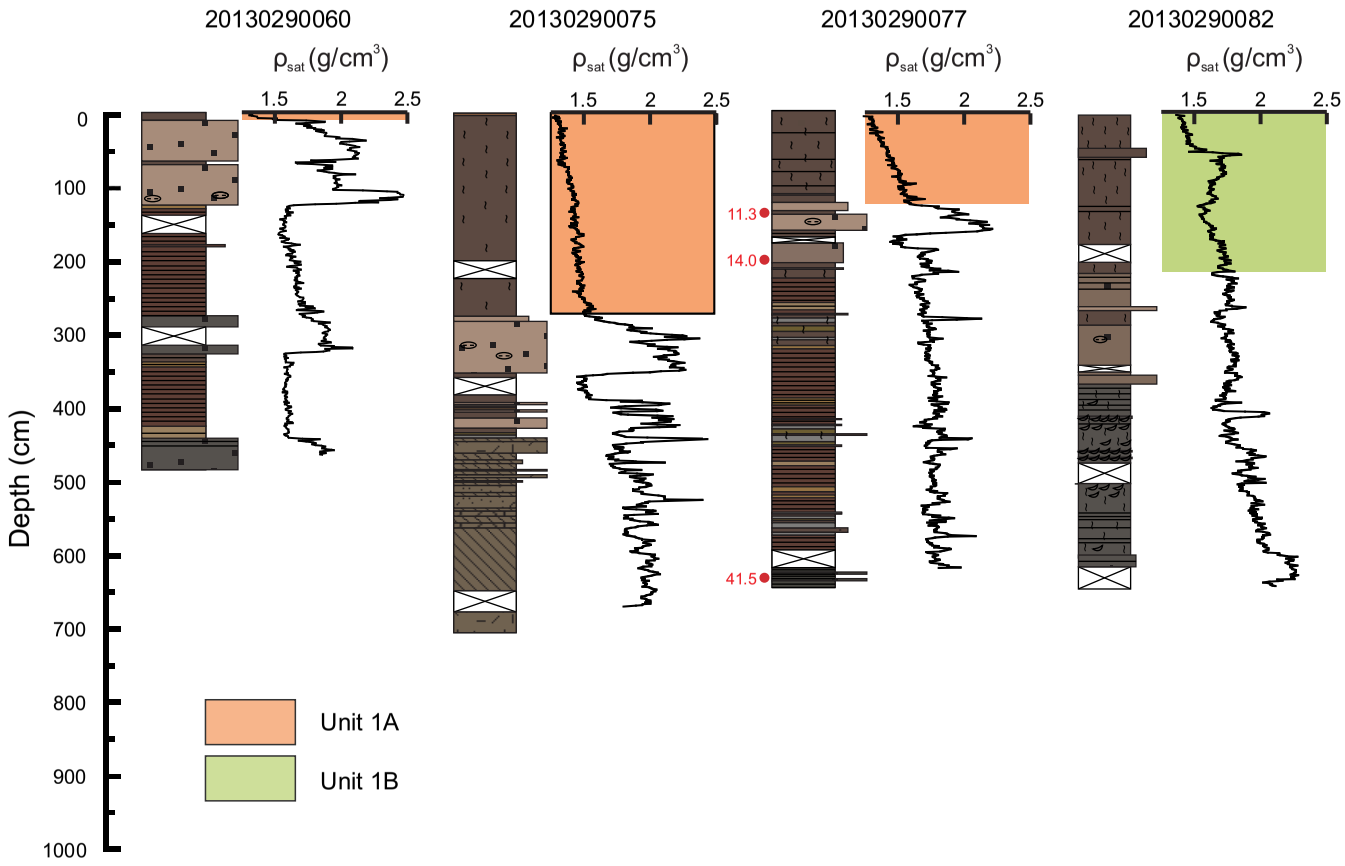

Figure 9.5. Lithology and MSCL bulk density (g/cm^3) profiles with geotechnical Unit 1A (orange rectangles) and 1B (green rectangle). The red dots signify radiocarbon ages.

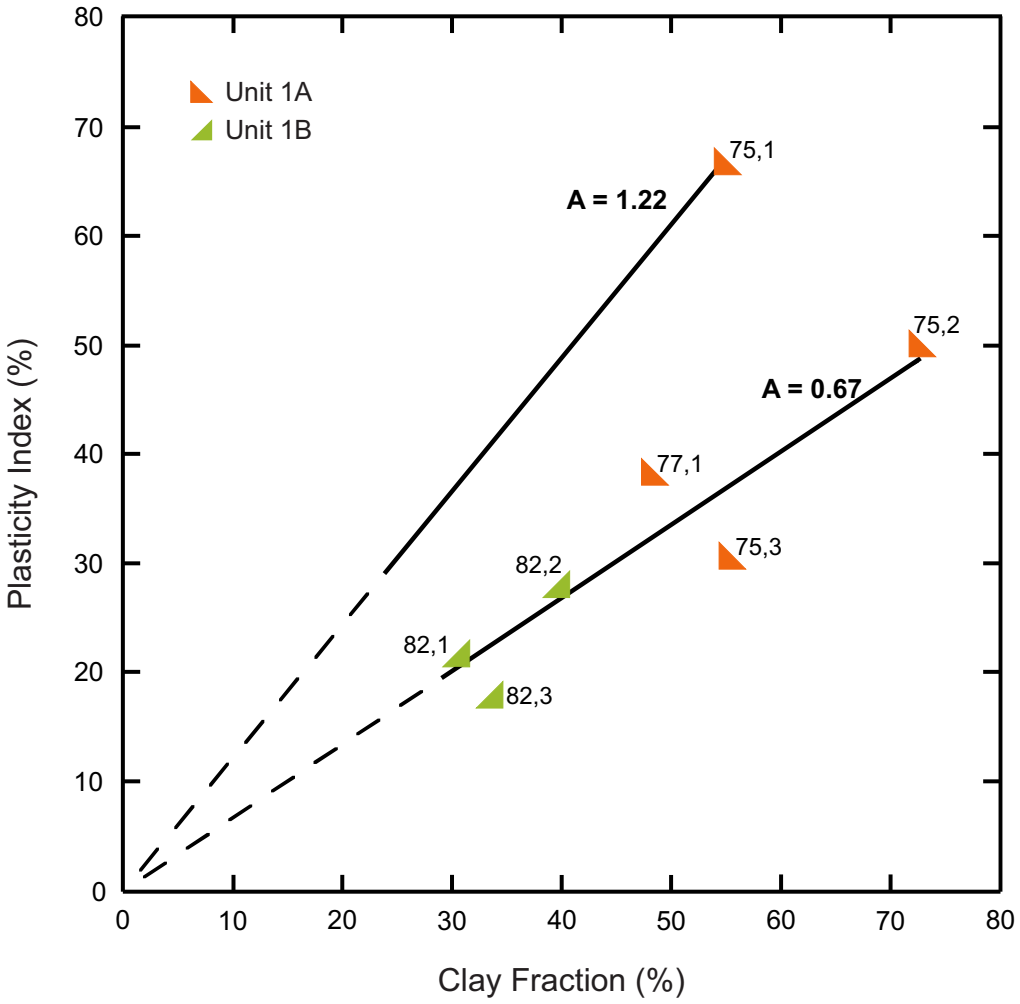

Figure 9.6. Activity chart showing results for Unit 1A and 1B. The first number denotes the core number and the second number denotes the down core Atterberg limit test sequence.

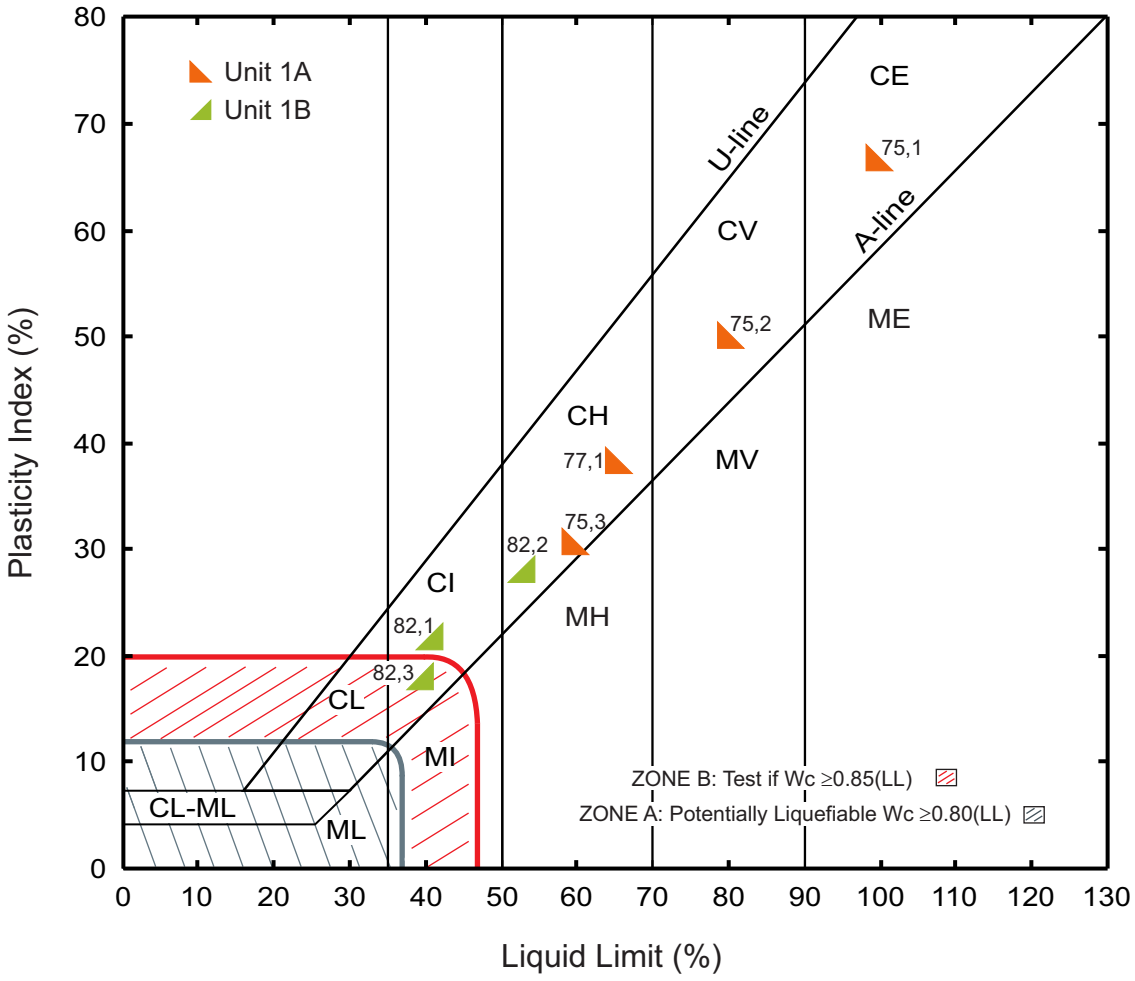

Figure 9.7. Plasticity chart showing Atterberg limit results for Unit 1A and 1B. The first number denotes the core number and the second number denotes the down core Atterberg limit test sequence.

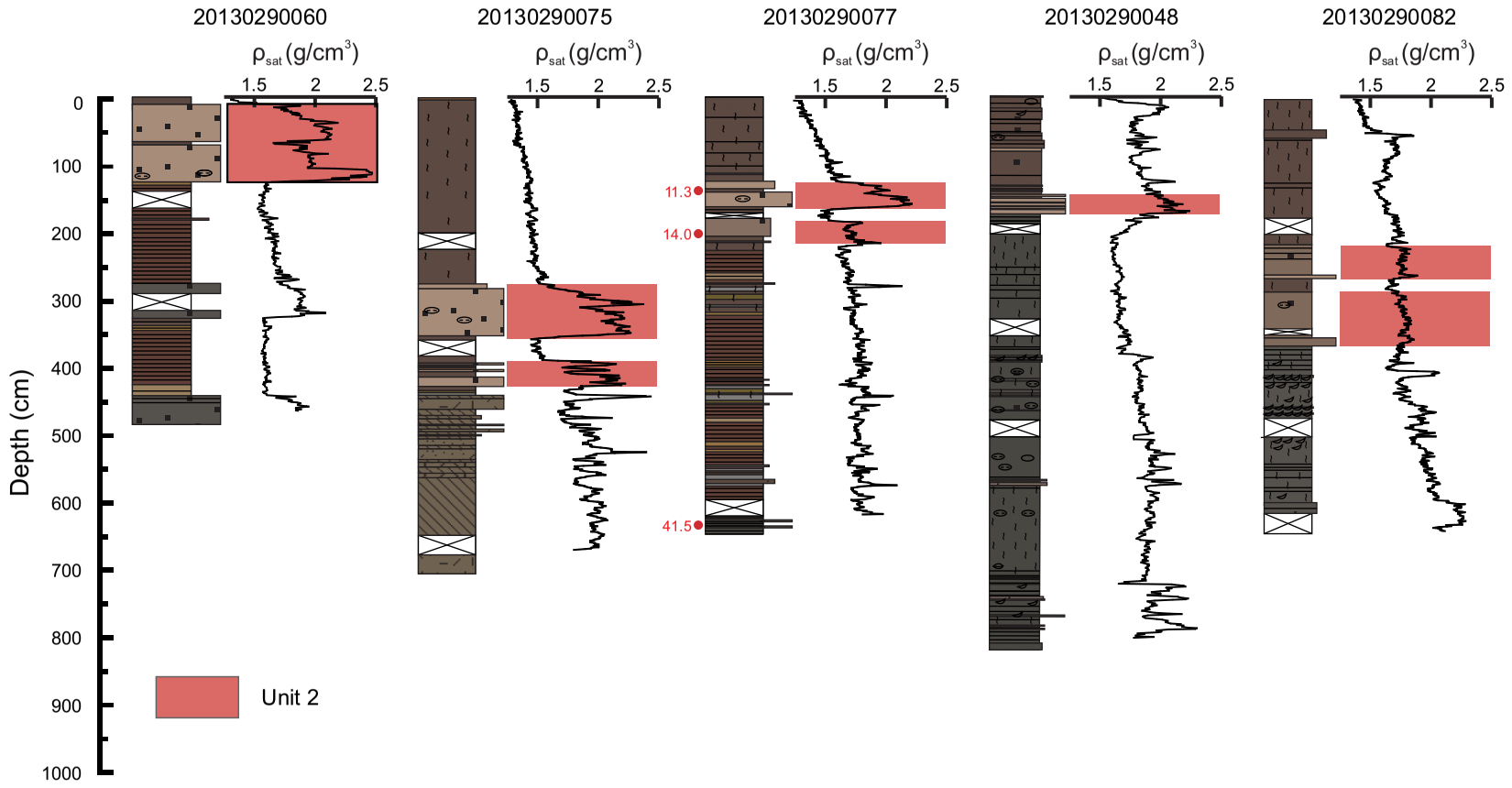

Figure 9.8. Lithology and MSCL bulk density (g/cm^3) profiles with geotechnical Unit 2 shown in red rectangles. Red dots signify radiocarbon age.

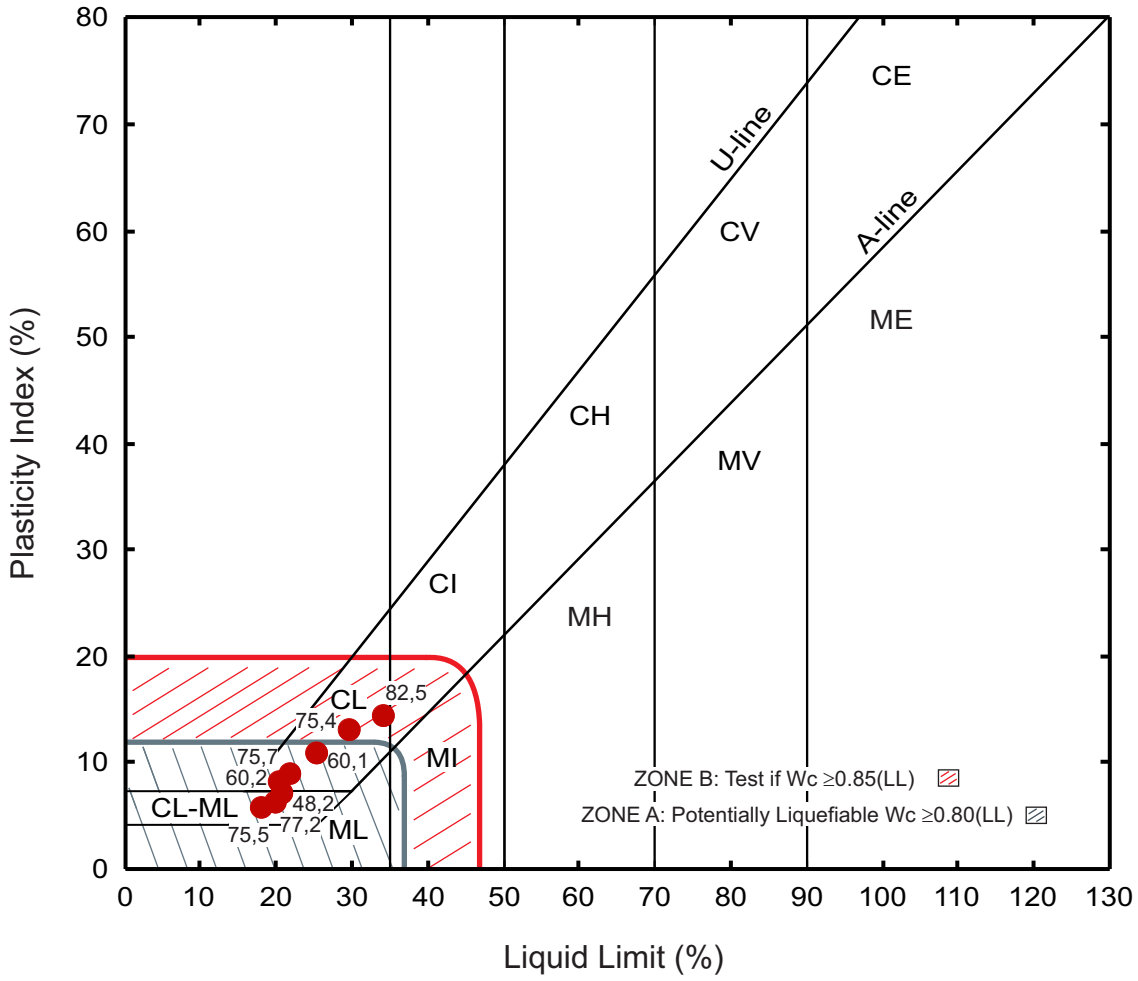

Figure 9.9. Plasticity chart showing Atterberg limit results for Unit 2. The first number denotes the core number and the second number denotes the down core Atterberg limit test sequence.

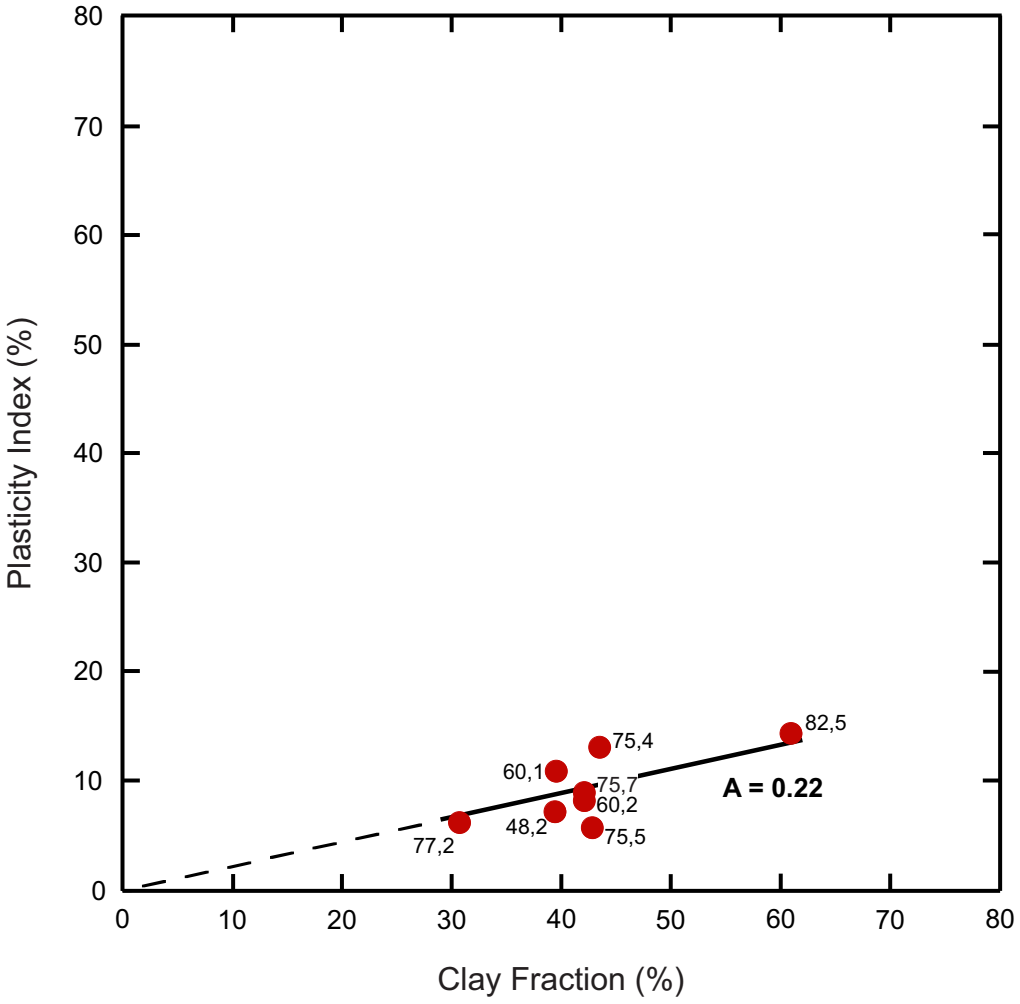

Figure 9.10. Activity chart showing results for Unit 2. The first number denotes the core number and the second number denotes the down core Atterberg limit test sequence.

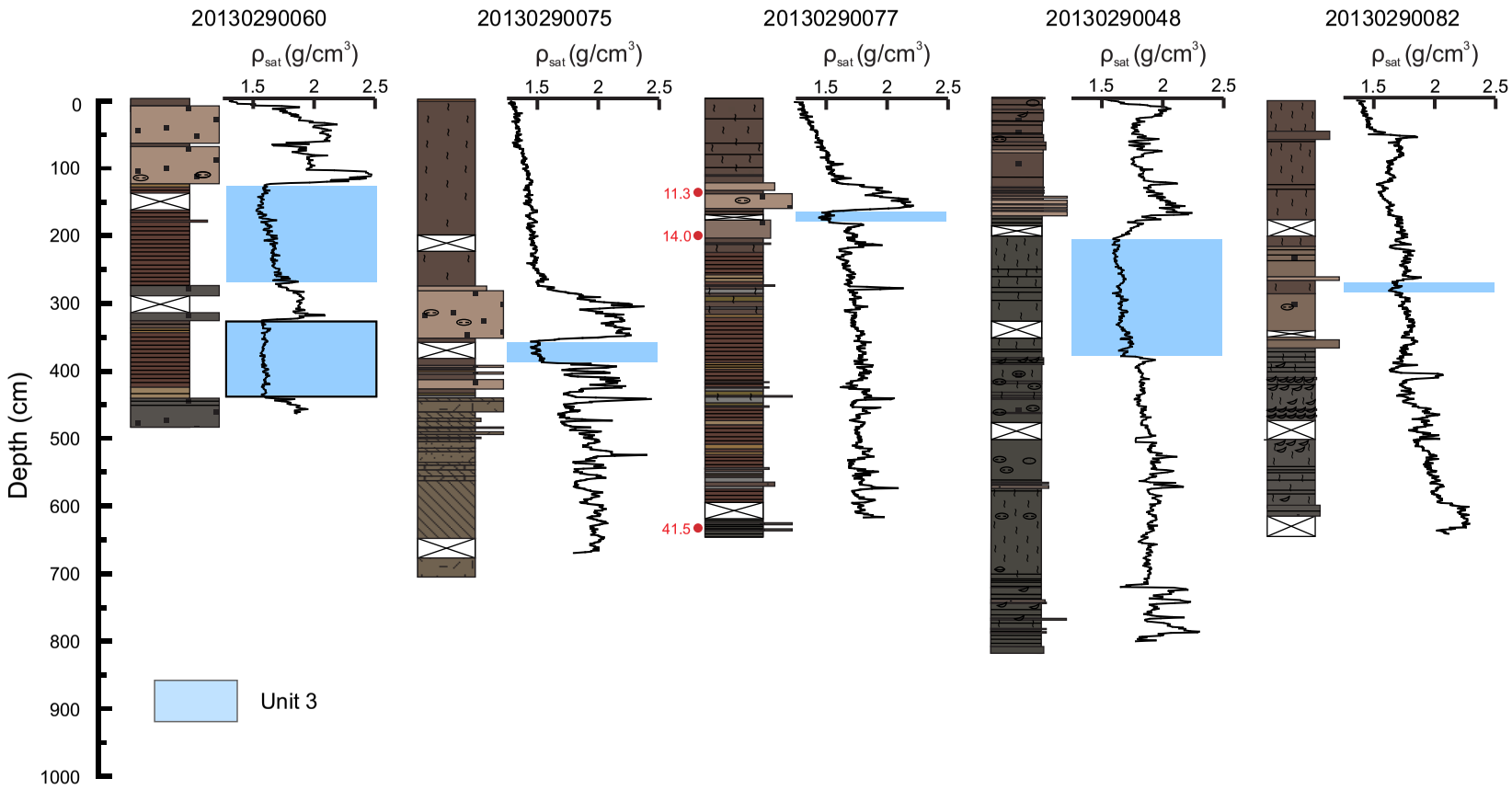

Figure 9.11. Lithology and MSCL bulk density (g/cm^3) profiles with geotechnical Unit 3 shown in blue rectangles. Red dots signify radiocarbon age.

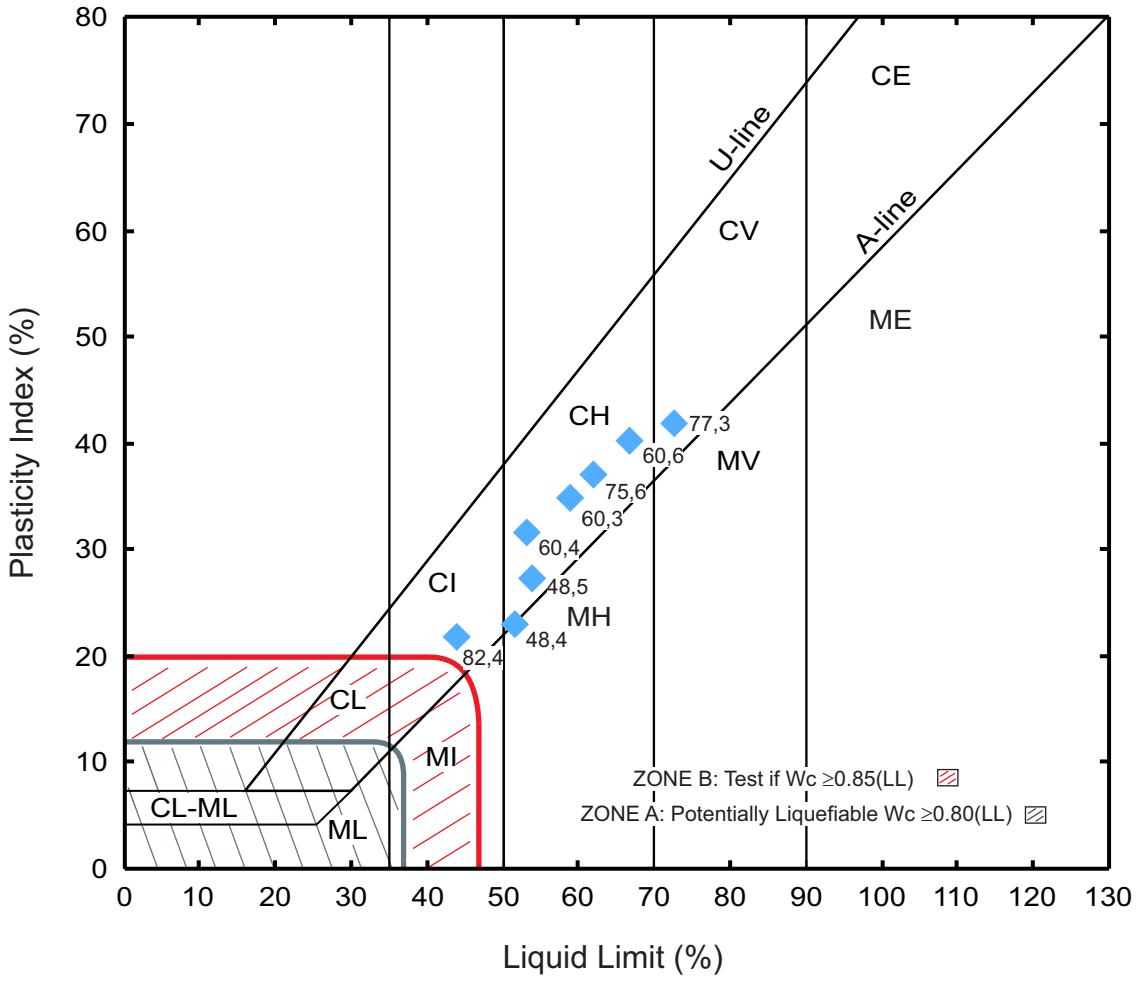

Figure 9.12. Plasticity chart showing Atterberg limit results for Unit 3. The first number denotes the core number and the second number denotes the down core Atterberg limit test sequence.

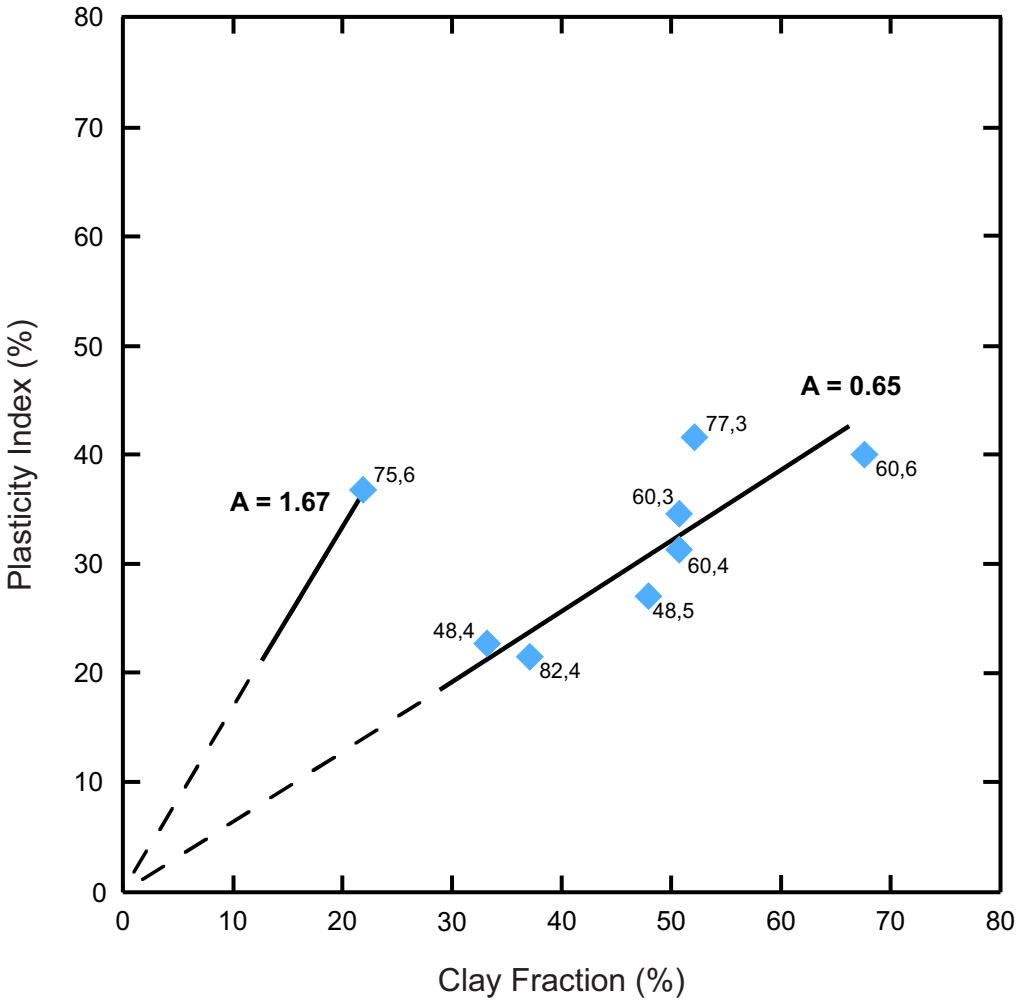

Figure 9.13. Activity chart showing results for Unit 3. The first number denotes the core number and the second number denotes the down core Atterberg limit test sequence.

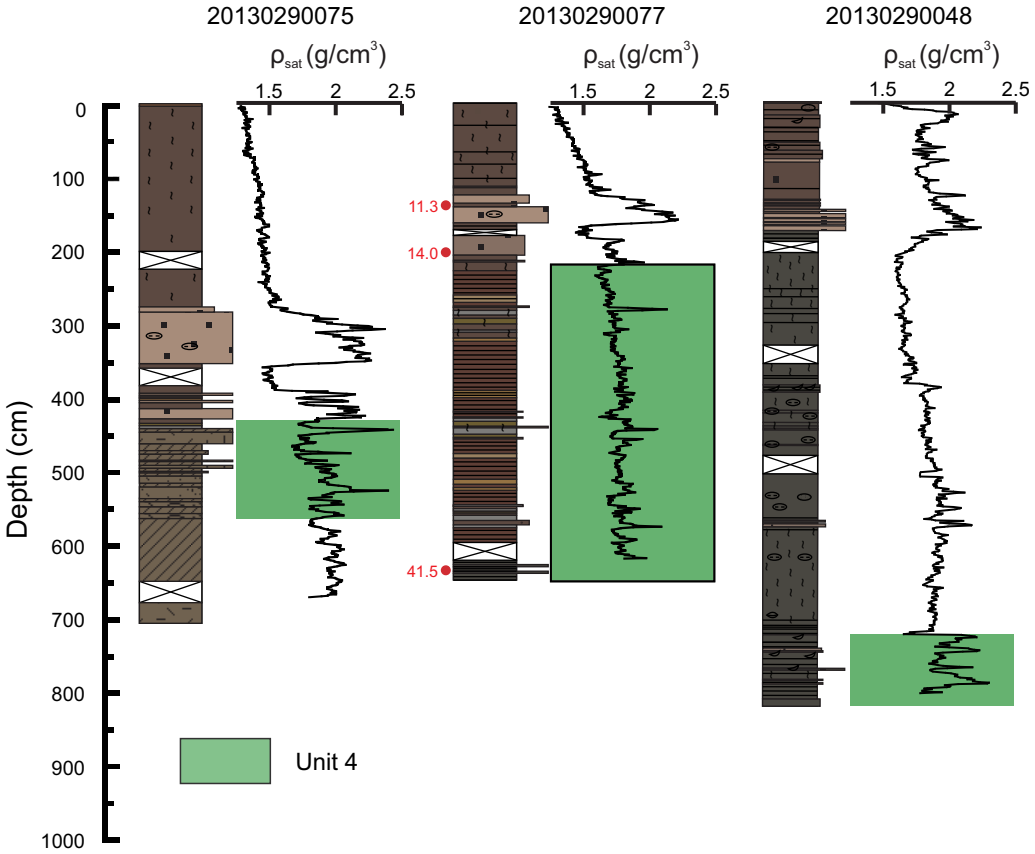

Figure 9.14. Lithology and MSCL bulk density (g/cm^3) profiles with geotechnical Unit 4 shown in green rectangles. Red dots signify radiocarbon age.

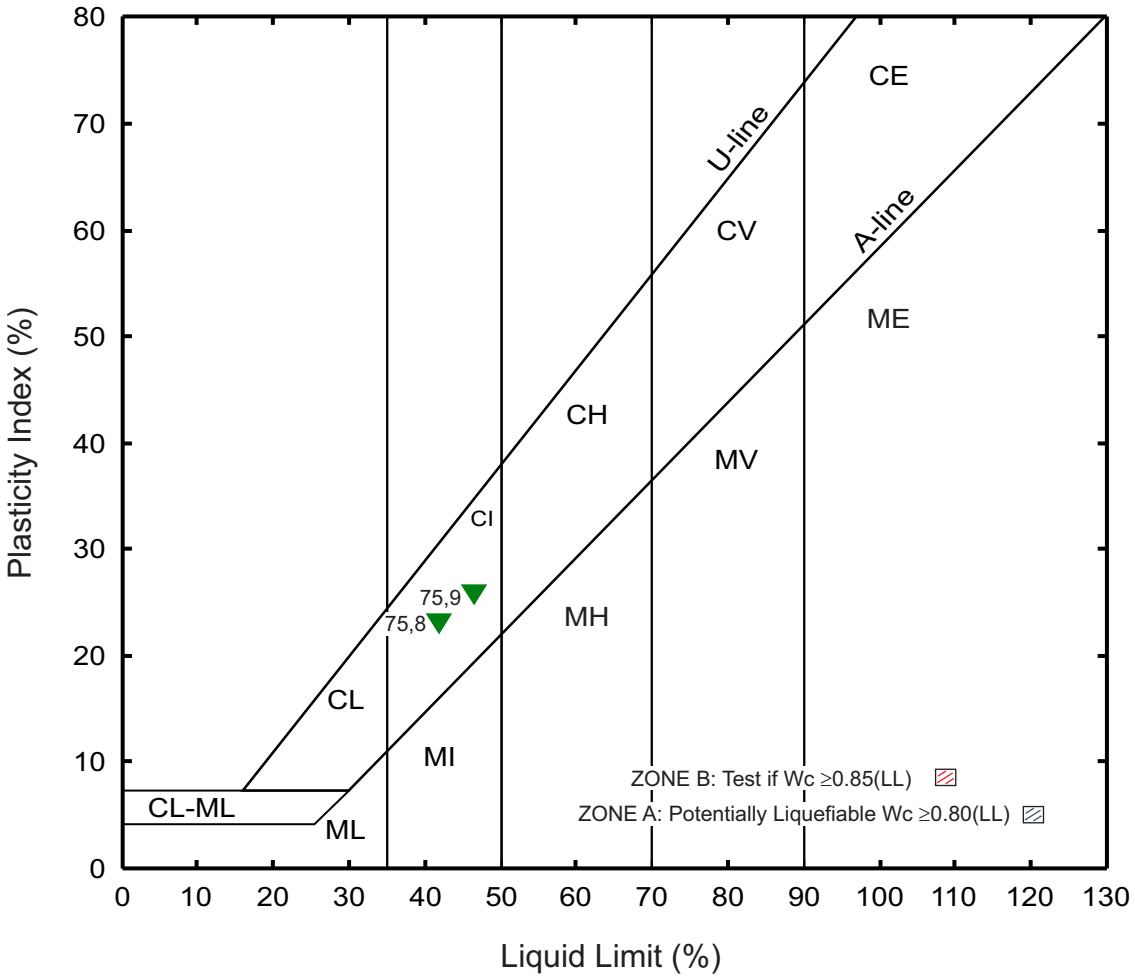

Figure 9.15. Plasticity chart showing Atterberg limit results for Unit 4. The first number denotes the core number and the second number denotes the down core Atterberg limit test sequence.

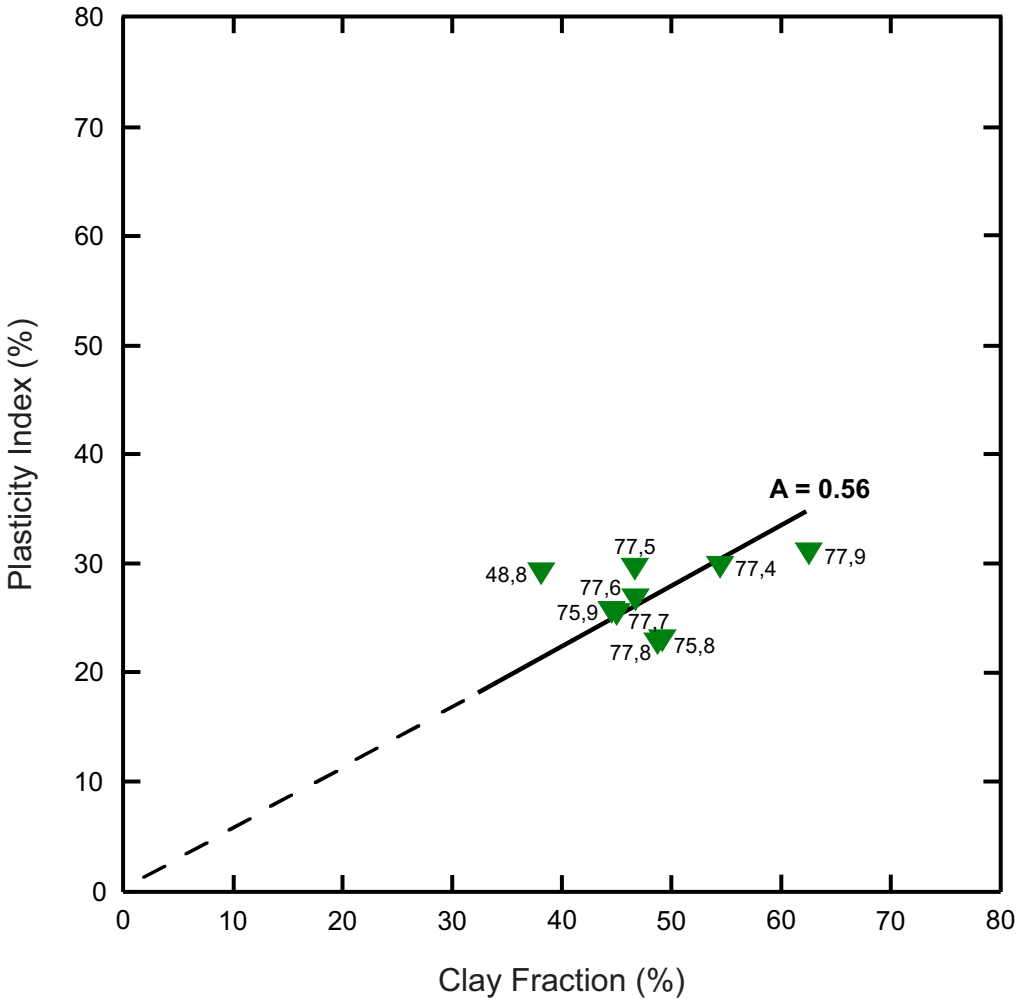

Figure 9.16. Activity chart showing results for Unit 4. The first number denotes the core number and the second number denotes the down core Atterberg limit test sequence.

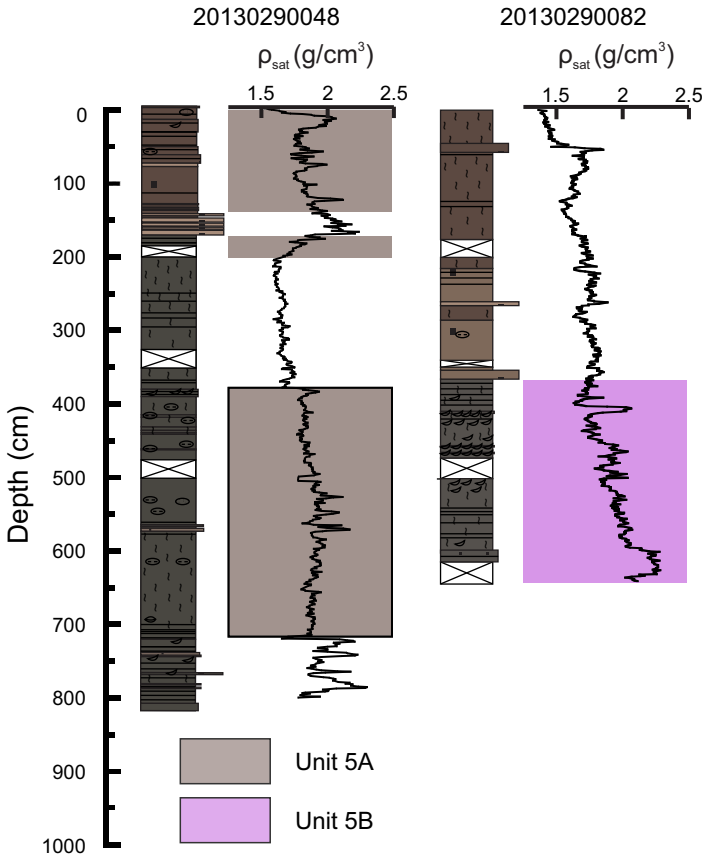

Figure 9.17. Lithology and MSCL bulk density (g/cm^3) profiles with geotechnical Unit 5A (brown rectangles) and 5B (purple rectangle).

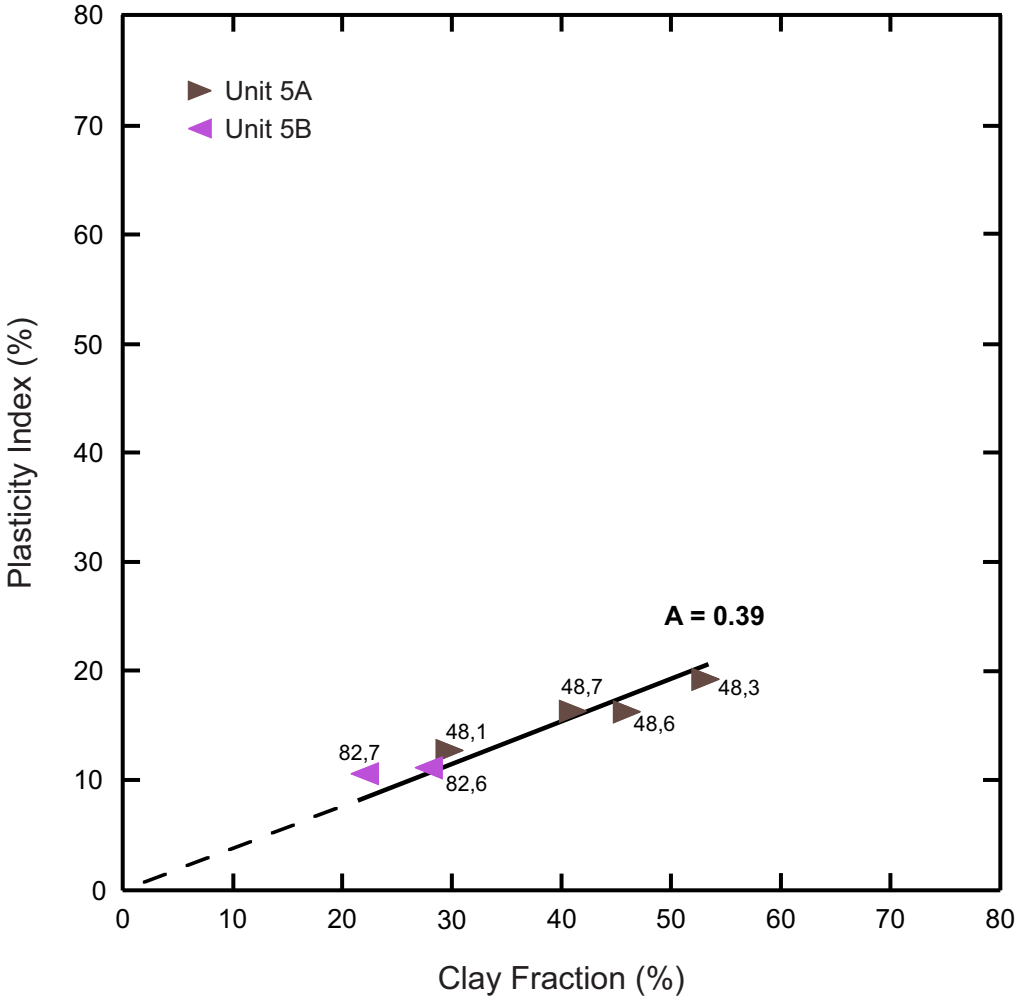

Figure 9.18. Activity chart showing results for Unit 5A and 5B. The first number denotes the core number and the second number denotes the down core Atterberg limit test sequence.

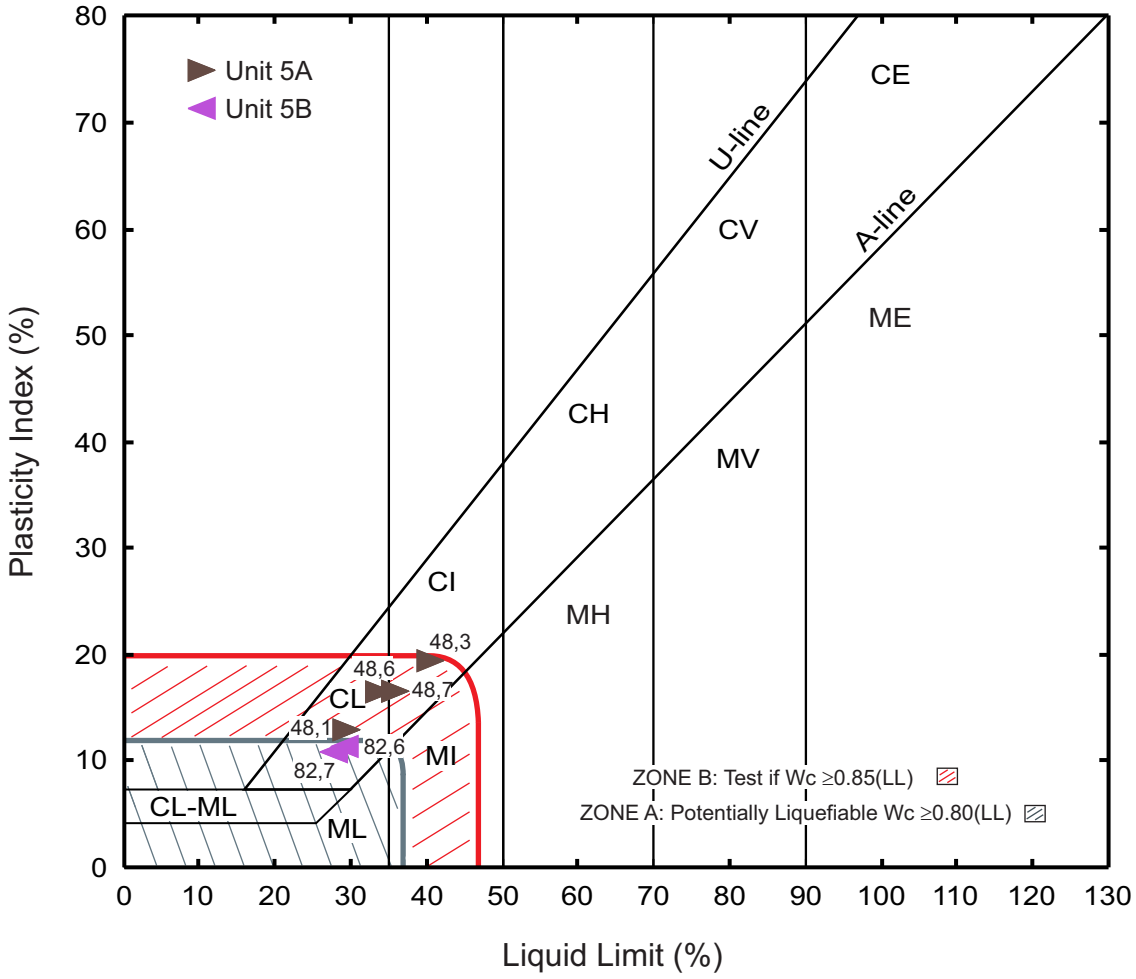

Figure 9.19. Plasticity chart showing Atterberg limit results for Unit 5A and 5B. The first number denotes the core number and the second number denotes the down core Atterberg limit test sequence.

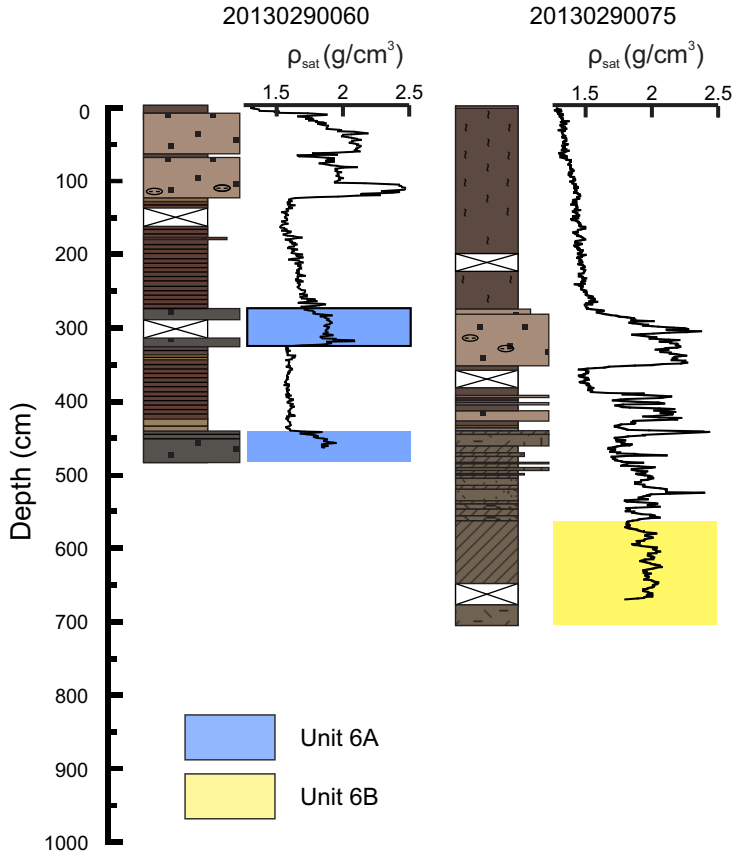

Figure 9.20. Lithology and MSCL bulk density (g/cm^3) profiles with geotechnical Unit 6A (blue rectangles) and 6B (yellow rectangle).

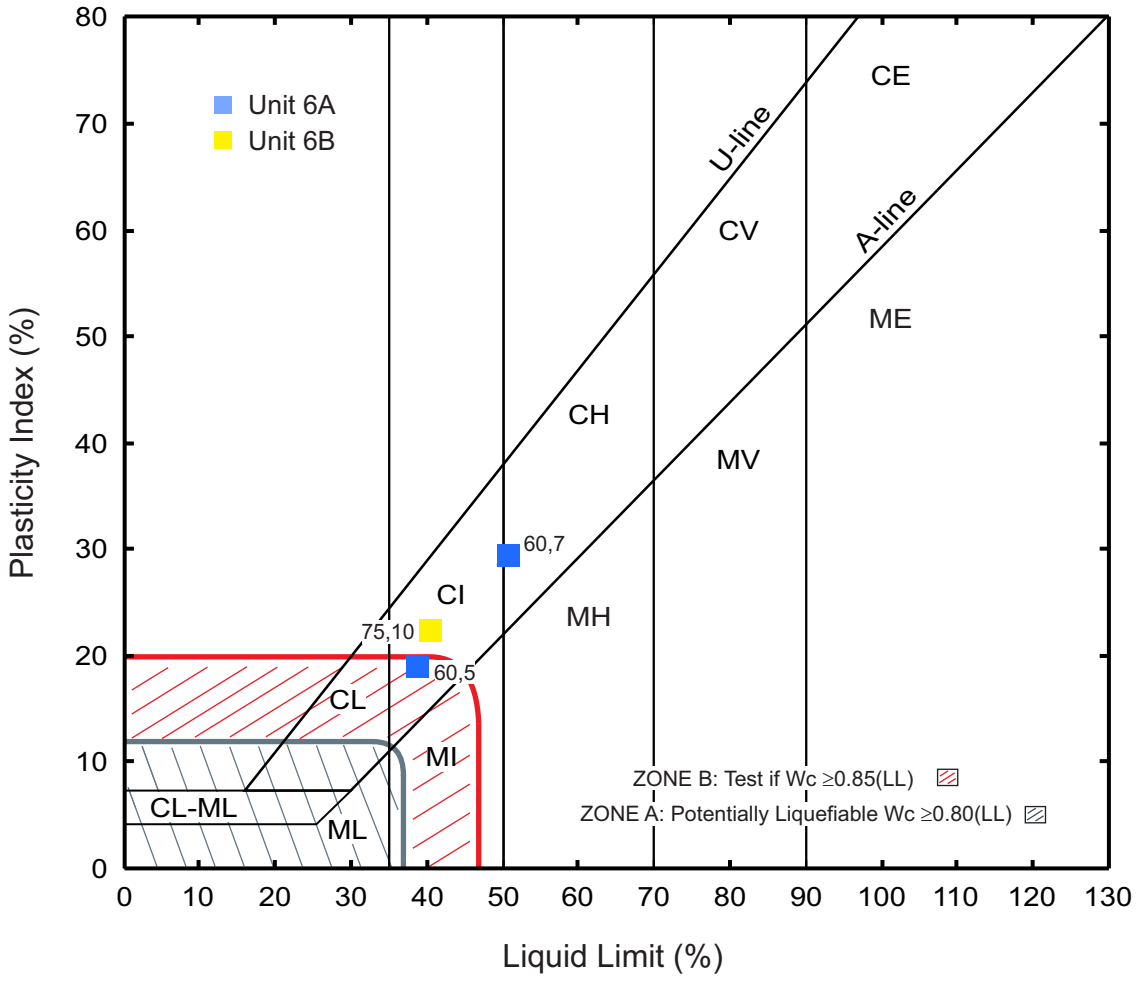

Figure 9.21. Plasticity chart showing Atterberg limit results for Unit 6. The first number denotes the core number and the second number denotes the down core Atterberg limit test sequence.

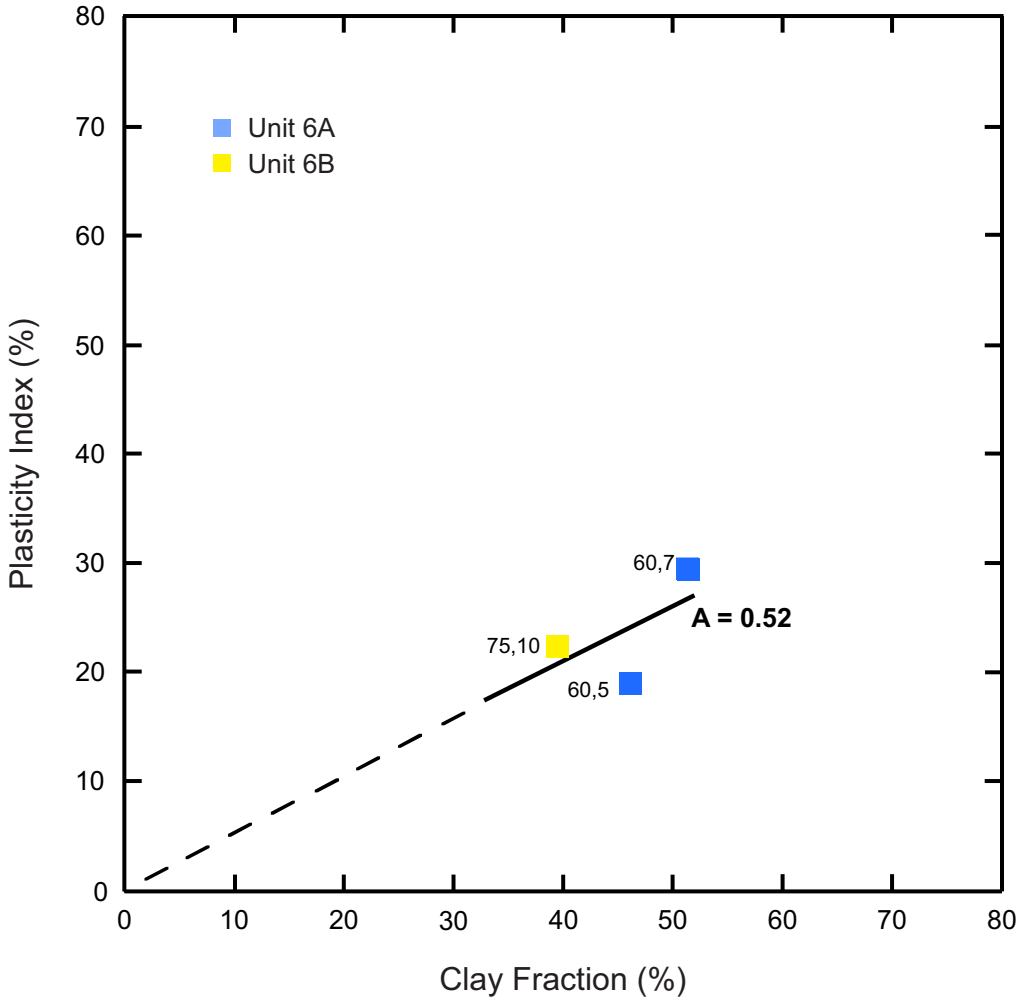

Figure 9.22. Activity chart showing results for Unit 6. The first number denotes the core number and the second number denotes the down core Atterberg limit test sequence.

Table 8.1. A summary of the number of geotechnical tests conducted for the five cores.

Core Number	Latitude (°)	Longitude (°)	Core Length (cm)	Water Contents	Atterberg limits	Grain Size	Triaxial	Consolidation
20130290048	67.605618	-61.967451	805	19	8	10	2	3
20130290060	71.867328	-70.867066	469	12	7	13	2	1
20130290075	69.547883	-64.643330	671	10	10	13	2	3
20130290077	68.308682	-63.794663	618	17	9	20	1	1
20130290082	67.781908	-59.539071	643	16	7	10	2	3

Table 8.2. Summary of Atterberg limit results for piston core 20130290048.

Depth (cm)	w_n (%)	LL (%)	PL (%)	PI (%)	LI	Classification	Zone
28-38	59.7	29.3	16.5	12.8	3.4	CL	B
162-172	26.0	20.6	13.3	7.2	1.8	CL-ML	A
190-200	68.9	40.3	21.0	19.3	2.5	CI	B
250-260	75.4	51.5	28.7	22.9	2.0	CH	-
331-346	86.9	53.9	26.7	27.2	2.2	CH	-
481-495	48.7	33.6	17.2	16.4	1.9	CL	B
638-648	47.8	35.7	19.2	16.4	1.7	CI	B
796-806	55.2	48.0	18.9	29.1	1.3	CI	-

Table 8.3. Summary of consolidation test results for piston core 201390290048.

Depth (cm)	ρ_{sat} (g/cm^3)	w_n (%)	C_c	C_r	P'_c (kPa)	OCR	k (cm/sec)	Classification
200-202.5	1.62	68.3	0.7	0.05	18.9	1.2	5.99E-08	CI
353-355.5	1.60	74.4	0.7	0.05	27.0	0.9	1.11E-07	CH
500-502.5	1.76	45.4	0.6	0.03	35.0	1.0	NA	CL

Table 8.4. Summary of triaxial test results for piston core 20130290048. Initial Young's modulus ($\mathcal{E}_i$) is calculated for the present day effective overburden stress.

Depth (cm)	e	w_n (%)	ϕ' (°)	c' (kPa)	S	A_f	$\mathcal{E}_i$ (MPa)	Classification
332-344	2.42	86.9	25.6	2.3	0.25	0.63	4.63	CH
483-495	1.32	48.7	24.9	5.0	0.27	0.48	14.04	CL

Table 8.5. Summary of FS results for piston core 20130290048.

Depth (cm)	Slope Angle (°)	Critical Angle (°)	Critical Acceleration Coefficient	Critical Height (m)	Minimum FS
794	1.42	9.27	0.06	32.73	6.42

Table 8.6. Summary of Atterberg limit results for piston core 20130290060.

Depth (cm)	w_n (%)	LL (%)	PL (%)	PI (%)	LI	Classification	Zone
17-27	45.1	25.1	14.1	11.0	2.8	CL	A
95-105	26.6	20.2	11.9	8.3	1.8	CL	A
142-154	72.5	58.8	24.1	34.7	1.4	CH	-
220-230	60.2	53.2	21.7	31.5	1.2	CH	-
298-314	32.8	38.5	19.5	18.9	0.7	CI	B
365-375	71.2	66.6	26.5	40.1	1.1	CH	-
455-465	37.3	50.4	21.0	29.5	0.6	CH	-

Table 8.7. Summary of consolidation test results for piston core 201390290060.

Depth (cm)	ρ_{sat} (g/cm^3)	w_n (%)	C_c	C_r	P'_c (kPa)	OCR	k (cm/sec)	Classification
294-296.5	1.95	32.3	0.3	0.04	48.0	2.2	1.08E-07	CI

Table 8.8. Summary of triaxial test results for piston core 20130290060. Initial Young's modulus ($\mathcal{E}_i$) is calculated for the present day effective overburden stress.

Depth (cm)	e	w_n (%)	ϕ' (°)	c' (kPa)	S	A_f	$\mathcal{E}_i$ (MPa)	Classification
142-154	1.85	266.9	22.3	2.2	0.26	0.54	3.21	CH
300-312	0.91	32.8	23.8	6.8	0.32	0.36	8.94	CI

Table 8.9. Summary of FS results for piston core 20130290060.

Depth (cm)	Slope Angle (°)	Critical Angle (°)	Critical Acceleration Coefficient	Critical Height (m)	Minimum FS
420.0	3.8	18.3	0.08	11.5	4.5

Table 8.10. Summary of Atterberg limit results for piston core 20130290075.

Depth (cm)	w_n (%)	LL (%)	PL (%)	PI (%)	LI	Classification	Zone
55-65	168.9	99.0	32.2	66.8	2.1	CE	-
200-206	121.4	79.4	29.4	50.1	1.8	CV	-
245-255	111.1	58.9	28.2	30.7	2.1	CH	-
285-295	50.5	29.4	16.3	13.1	2.6	CL	B
320-330	23.4	17.9	12.1	5.8	1.9	CL-ML	A
373-377	111.7	62.0	25.1	36.9	2.0	CH	-
416-424	31.1	21.6	12.6	9.0	2.1	CL	-
470-480	65.2	42.0	19.2	22.7	2.0	CI	-
545-555	50.9	46.2	20.5	25.7	1.2	CI	-
668-671	37.0	40.3	17.9	22.4	0.9	CI	-

Table 8.11. Summary of consolidation test results for piston core 201390290075.

Depth (cm)	ρ_{sat} (g/cm^3)	w_n (%)	C_c	C_r	P'$_c$ (kPa)	OCR	k (cm/sec)	Classification
201-203.5	1.45	120.4	1.1	0.09	8.5	1.2	2.50E-07	CV
375-377.5	1.47	111.7	1.1	0.08	14.5	0.8	4.21E-06	CH
668-670.5	1.89	37.0	0.3	0.02	39.0	0.9	1.22E-07	CI

Table 8.12. Summary of triaxial test results for piston core 20130290075. Initial Young's modulus ($\mathcal{E}_i$) is calculated for the present day effective overburden stress.

Depth (cm)	e	w_n (%)	ϕ' (°)	c' (kPa)	S	A_f	$\mathcal{E}_i$ (MPa)	Classification
206-218	3.31	125.3	18.9	0.0	0.19	0.64	1.75	CV
646-658	0.97	34.3	24.3	9.4	0.32	0.45	18.84	CI

Table 8.13. Summary of FS results for piston core 20130290075.

Depth (cm)	Slope Angle (°)	Critical Angle (°)	Critical Acceleration Coefficient	Critical Height (m)	Minimum FS
422.0	1.7	9.2	0.07	12.2	5.3

Table 8.14. Summary of Atterberg limit results for piston core 20130290077.

Depth (cm)	w_n (%)	LL (%)	PL (%)	PI (%)	LI	Classification	Zone
93-103	93.9	64.6	26.3	38.3	1.8	CH	-
142-152	19.7	19.7	13.4	6.3	1.0	CL-ML	A
170-180	113.8	72.6	30.9	41.7	2.0	CV	-
250-260	68.7	52.1	22.4	29.7	1.6	CH	-
325-335	55.2	53.5	24.1	29.5	1.1	CH	-
378-388	56.7	47.2	20.5	26.7	1.4	CI	-
440-450	58.7	49.0	23.6	25.4	1.4	CI	-
512-525	49.2	43.3	20.6	22.7	1.3	CI	-
597-613	42.5	52.4	21.5	30.9	0.7	CH	-

Table 8.15. Summary of consolidation test results for piston core 201390290077.

Depth (cm)	ρ_{sat} (g/cm^3)	w_n (%)	C_c	C_r	P'_c (kPa)	OCR	k (cm/sec)	Classification
613-615.5	1.86	40.6	0.3	0.03	23.5	0.6	1.83E-07	CH

Table 8.16. Summary of triaxial test results for piston core 20130290077. Initial Young's modulus ($\mathcal{E}_i$) is calculated for the present day effective overburden stress.

Depth (cm)	e	w_n (%)	ϕ' (°)	c' (kPa)	S	A_f	$\mathcal{E}_i$ (MPa)	Classification
598-610	1.44	54.8	25.8	2.2	0.28	0.56	9.46	CH

Table 8.17. Summary of FS results for piston core 20130290077.

Depth (cm)	Slope Angle (°)	Critical Angle (°)	Critical Acceleration Coefficient	Critical Height (m)	Minimum FS
590.0	0.8	12.8	0.09	100.9	15.9

Table 8.18. Summary of Atterberg limit results for piston core 20130290082.

Depth (cm)	w_n (%)	LL (%)	PL (%)	PI (%)	LI	Classification	Zone
55-65	69.1	41.0	19.2	21.8	2.3	CI	-
120-130	101.2	53.0	25.0	28.1	2.7	CH	-
180-185	70.2	39.7	21.7	18.0	2.7	CI	B
269-279	68.9	43.9	22.3	21.6	2.2	CI	-
339-344	56.5	33.9	19.5	14.5	2.6	CL	B
470-475	53.4	29.0	17.8	11.3	3.2	CL	A
533-543	41.5	27.6	16.9	10.7	2.3	CL	A

Table 8.19. Summary of consolidation test results for piston core 201390290082.

Depth (cm)	ρ_{sat} (g/cm^3)	w_n (%)	C_c	C_r	P'_c (kPa)	OCR	k (cm/sec)	Classification
182-184.5	1.60	70.2	0.7	0.05	9.5	1.0	NA	CI
343-345.5	1.72	56.5	0.5	0.04	16.0	0.8	9.47E-08	CL
489-491.5	1.72	52.6	0.6	0.04	35.0	1.1	3.84E-07	CL

Table 8.20. Summary of triaxial test results for piston core 20130290082. Initial Young's modulus ($\mathcal{E}_i$) is calculated for the present day effective overburden stress.

Depth (cm)	e	w_n (%)	ϕ' (°)	c' (kPa)	S	A_f	$\mathcal{E}_i$ (MPa)	Classification
188-196	1.83	66.9	30.3	0.0	0.26	0.50	6.20	CI
478-486	1.21	44.5	30.3	1.6	0.29	0.70	12.45	CL

Table 8.21. Summary of FS results for piston core 20130290082.

Depth (cm)	Slope Angle (°)	Critical Angle (°)	Critical Acceleration Coefficient	Critical Height (m)	Minimum FS
645.0	0.7	11.4	0.10	113.7	15.4

Table 9.1. Average values of physical property of geotechnical units. Standard deviation presented in brackets. Unit 6B only has one Atterberg and one grain size measurement.

Unit	ρ_{sat} (g/cm^3)	w_n (%)	LL (%)	PL (%)	PI (%)	A	Clay (%)	Silt (%)	Sand (%)	Gravel (%)	Classification
1A	1.43 (0.09)	149.3 (38.3)	75.5 (17.9)	29.0 (2.5)	46.5 (15.7)	0.68 (0.12)	53.2 (10.8)	44.9 (10.5)	1.9 (2.5)	-	CH
1B	1.58 (0.11)	81.6 (15.1)	44.6 (7.4)	21.9 (2.9)	22.6 (5.1)	0.65 (0.10)	34.9 (4.7)	58.3 (7.3)	6.8 (10.3)	-	CI, CH
2	1.91 (0.21)	45.5 (25.4)	23.5 (5.5)	14.1 (2.6)	9.4 (3.2)	0.22 (0.05)	43.8 (8.5)	46.0 (7.3)	9.7 (8.6)	0.6 (1.7)	CL, CL-ML
3	1.62 (0.06)	81.0 (17.6)	57.8 (9.1)	25.8 (3.1)	32.1 (7.6)	0.65 (0.08)	45.4 (14.0)	53.0 (13.0)	1.6 (1.7)	-	CH
4	1.83 (0.13)	57.3 (9.1)	48.2 (4.0)	21.3 (1.8)	26.9 (3.0)	0.56 (0.09)	47.4 (7.6)	49.3 (4.9)	3.3 (4.9)	-	CI, CH
5A	1.86 (0.09)	53.4 (7.4)	34.7 (4.6)	18.5 (2.0)	16.2 (2.7)	0.39 (0.03)	38.8 (9.6)	50.0 (4.4)	11.2 (8.3)	-	CL, CI
5B	1.90 (0.16)	52.7 (11.6)	28.3 (1.0)	17.3 (0.6)	11.0 (0.4)	0.44 (0.06)	21.4 (6.9)	58.1 (3.6)	20.6 (10.3)	-	CL
6A	1.85 (0.08)	35.5 (2.4)	44.4 (8.4)	20.2 (1.0)	24.2 (7.4)	0.49 (0.12)	47.6 (3.7)	32.9 (8.1)	14.3 (7.4)	5.3 (7.3)	CI,CH
6B	1.96 (0.07)	40.2 (4.2)	40.3 (-)	17.9 (-)	22.4 (-)	0.57 (-)	39.4 (-)	48.7 (-)	12.0 (-)	-	CI

Table 9.2. Summary of advanced geotechnical data.

Unit	ϕ' (°)	c' (kPa)	S	A_f	C_c	C_r	P'_c (kPa)	OCR	k (cm/sec)
1A	18.9	0.0	0.19	0.64	1.1	0.09	7.3	1.2	2.50E-07
1B	30.3	0.0	0.26	0.50	0.5	0.05	9.5	1.0	NA
2	-	-	-	-	0.5	0.04	16.0	0.8	9.47E-08
3	24.0	2.3	0.26	0.59	0.9	0.07	20.8	0.9	2.16E-06
4	25.8	2.2	0.28	0.56	0.3	0.03	23.5	0.6	1.83E-07
5A	24.9	5.0	0.27	0.48	0.6	0.04	27.0	1.1	5.99E-08
5B	30.3	1.6	0.29	0.70	0.6	0.04	35.0	1.1	3.84E-07
6A	23.8	6.8	0.32	0.36	0.3	0.04	48.0	2.2	1.08E-07
6B	24.3	9.4	0.32	0.45	0.3	0.02	39.0	0.9	1.22E-07